

QUANTITATIVE MIXING MEASUREMENTS OF A SUPERSONIC INJECTION COIL NOZZLE WITH TRIP JETS

Carrie A. Noren

13 June 2008

Final Report

APPROVED FOR PUBLIC RELEASE; DISTRIBUTION IS UNLIMITED.



**AIR FORCE RESEARCH LABORATORY
Directed Energy Directorate
3550 Aberdeen Ave SE
AIR FORCE MATERIEL COMMAND
KIRTLAND AIR FORCE BASE, NM 87117-5776**

NOTICE AND SIGNATURE PAGE

Using Government drawings, specifications, or other data included in this document for any purpose other than Government procurement does not in any way obligate the U.S. Government. The fact that the Government formulated or supplied the drawings, specifications, or other data does not license the holder or any other person or corporation; or convey any rights or permission to manufacture, use, or sell any patented invention that may relate to them.

This report was cleared for public release by the Air Force Research Laboratory [insert TD site] Public Affairs Office and is available to the general public, including foreign nationals. Copies may be obtained from the Defense Technical Information Center (DTIC) (<http://www.dtic.mil>).

AFRL-RD-PS-TR-2008-1099 HAS BEEN REVIEWED AND IS APPROVED FOR PUBLICATION IN ACCORDANCE WITH ASSIGNED DISTRIBUTION STATEMENT.

//signed//

CARRIE A. NOREN, DR-I
Project Officer

//signed//

WALLACE T. CLARK III, DR-IV
Chief, Laser Division

This report is published in the interest of scientific and technical information exchange, and its publication does not constitute the Government's approval or disapproval of its ideas or findings.

REPORT DOCUMENTATION PAGE				Form Approved OMB No. 0704-0188	
Public reporting burden for this collection of information is estimated to average 1 hour per response, including the time for reviewing instructions, searching existing data sources, gathering and maintaining the data needed, and completing and reviewing this collection of information. Send comments regarding this burden estimate or any other aspect of this collection of information, including suggestions for reducing this burden to Department of Defense, Washington Headquarters Services, Directorate for Information Operations and Reports (0704-0188), 1215 Jefferson Davis Highway, Suite 1204, Arlington, VA 22202-4302. Respondents should be aware that notwithstanding any other provision of law, no person shall be subject to any penalty for failing to comply with a collection of information if it does not display a currently valid OMB control number. PLEASE DO NOT RETURN YOUR FORM TO THE ABOVE ADDRESS.					
1. REPORT DATE (DD-MM-YYYY) 13-06-2008		2. REPORT TYPE Final Report		3. DATES COVERED (From - To) 01 Oct 03 - 13 Jun 2008	
4. TITLE AND SUBTITLE Quantitative Mixing Measurements of a Supersonic Injection COIL Nozzle with Trip Jets				5a. CONTRACT NUMBER In House (DF299896)	
				5b. GRANT NUMBER	
				5c. PROGRAM ELEMENT NUMBER 62605F	
6. AUTHOR(S) Carrie A. Noren				5d. PROJECT NUMBER 4866	
				5e. TASK NUMBER LB	
				5f. WORK UNIT NUMBER 11	
7. PERFORMING ORGANIZATION NAME(S) AND ADDRESS(ES)				8. PERFORMING ORGANIZATION REPORT NUMBER	
9. SPONSORING / MONITORING AGENCY NAME(S) AND ADDRESS(ES) Air Force Research Laboratory 3550 Aberdeen Ave SE Kirtland AFB, NM 87117-5776				10. SPONSOR/MONITOR'S ACRONYM(S)	
				11. SPONSOR/MONITOR'S REPORT NUMBER(S) AFRL-RD-PS-TR-2008-1099	
12. DISTRIBUTION / AVAILABILITY STATEMENT Approved for Public Release; Distribution is Unlimited.					
13. SUPPLEMENTARY NOTES Public Release approved by 377ABW, RD08-0207.					
14. ABSTRACT A supersonic nozzle with supersonic iodine injection was designed and studied with Planar Laser-Induced Fluorescence (PLIF). The nozzle simulates Chemical Oxygen Iodine Laser (COIL) flow conditions with non-reacting, cold flows. A laser sheet near 565 nm excited the iodine, and the fluorescence was imaged with an intensified and gated CCD camera. Streamwise and semi-spanwise (oblique-view) images were taken, where the presence of injected flow was highlighted. With these images, the flow structures were identifiable and the mixing quality between the primary and injected flow was quantitatively measured with histograms, structure size measurements, and jet penetration. Four different injection scenarios are investigated. The first scenario includes a single injector positioned downstream of the nozzle throat. To enhance the mixing between the flows, trip jets were placed in the wake of the single jet. The trip jets, significantly smaller than the primary iodine jet, are intended to destabilize the counter-rotating vortex pair (CRVP) of the primary jet. Three different trip jet configurations are compared for their ability to enhance mixing between the oxygen and iodine flows. While the mixedness between the injected and primary flows was not optimized, the comparison between the four different injection scenarios may aid in future nozzle design and mixing optimization.					
15. SUBJECT TERMS PLIF, COIL, jet penetration, mixedness, jet in crossflow, trip jets, injection					
16. SECURITY CLASSIFICATION OF:			17. LIMITATION OF ABSTRACT SAR	18. NUMBER OF PAGES 170	19a. NAME OF RESPONSIBLE PERSON Carrie A. Noren
a. REPORT UNCLASSIFIED	b. ABSTRACT UNCLASSIFIED	c. THIS PAGE UNCLASSIFIED			19b. TELEPHONE NUMBER (include area code) 505-853-2685

This page intentionally left blank

TABLE OF CONTENTS

Section	Page
1.0 SUMMARY	1
2.0 INTRODUCTION	2
2.1 Chemical Oxygen Iodine Lasers	2
2.2 Fluid Mechanics Related to COIL Nozzles.....	4
2.2.1 Jet in Crossflow Structure	4
2.2.2 Perturbation of Injected Flow	7
2.3 COIL Diagnostics	11
2.4 Thesis Overview	14
3.0 DESCRIPTION OF EXPERIMENTAL SYSTEM	16
3.1 Introduction	16
3.2 Gas Delivery System	16
3.3 Nozzle Design	17
3.3.1 Pressure and Mach Number Measurements	20
3.3.2 Injector Design	22
4.0 PLIF DIAGNOSTICS	24
4.1 Introduction	24
4.2 Lasers.....	24
4.2.1 Dye Laser Calibration	25
4.2.2 Iodine Fluorescence Lifetime	33
4.3 Optics.....	42
5.0 PLIF IMAGE ANALYSIS OF SINGLE INJECTOR.....	46
5.1 Introduction	46
5.2 Ensemble Averaging	47
5.2.1 Streamwise Images.....	47
5.2.2 Oblique Images.....	51
5.3 Histograms.....	56
5.3.1 Streamwise Images.....	57
5.3.2 Oblique Images.....	58
5.4 Structure Size	59
6.0 MULTIPLE INJECTORS	64
6.1 Introduction	64
6.2 Streamwise-View Ensemble Averages	67
6.2.1 Trip Scenario A	68
6.2.2 Trip Scenario B	75
6.2.3 Trip Scenario C	82
6.3 Oblique-View Ensemble Averages	89
6.3.1 Trip Scenario A	89
6.3.2 Trip Scenario B	93

6.3.3	Trip Scenario C	98
6.4	Streamwise-View Histograms	102
6.4.1	Trip Scenario A	102
6.4.2	Trip Scenario B	103
6.4.3	Trip Scenario C	104
6.5	Oblique-View Histograms.....	105
6.5.1	Trip Scenario A	106
6.5.2	Trip Scenario B	106
6.5.3	Trip Scenario C	107
6.6	Structure Size	108
6.7	Jet Penetration	110
7.0	CONCLUSION AND RECOMMENDATIONS	112
7.1	Summary of Results and Conclusions.....	112
7.2	Recommendations for Future Work	116
REFERENCES		118
Appendix A: Flow Rate Measurement and Uncertainty.....		123
Appendix B: Flow Straightener		140
Appendix C: Nozzle Design		144

LIST OF FIGURES

Figure	Page
1. Cartoon depicting the four types of vortical structures associated with a jet-in-crossflow. ¹³	6
2. A three-dimensional schematic of the structures in a compressible (supersonic) JICF system. ²³	7
3. The nozzle contour, from the plenum to the exit of the nozzle.....	18
4. Nozzle frame with top contour insert installed.	19
5. Nozzle frame with top and bottom contour inserts, shown after installation.....	19
6. Nozzle installed on test stand. The polycarbonate side plates are visible along with the pressure taps on the top and bottom of the nozzle.	19
7. Mach number, measured and calculated with 3-D CFD.	21
8. Wall static pressures, as measured, calculated with 3-D CFD, and calculated using isentropic relationships.	22
9. Schematic of a single injector, units are given in millimeters.	23
10. A schematic of the hollow cathode lamp (HCL) setup. PS is the power supply, R is a resistor, C is the capacitor, BC is the box controller, and PC is the computer.....	26
11. Normalized neon lamp voltage versus dye laser wavelength.	27
12. Normalized photodiode response versus an adjusted dye laser wavelength. The normalized iodine spectrum is also plotted for comparison.	28
13. Photodiode response, iodine spectrum, and individual spectral lines versus wavelength. The dye laser bandwidth and operating wavelength are shown.	29
14. Boltzmann distribution for the ground-state vibration and rotational levels that are excited in the bandwidth of the dye laser at 565.095nm.	32
15. Boltzmann distribution with constant temperature and $v''=0$	32
16. Intensity versus time for a single image pixel, located 0.48 cm downstream of the nozzle throat, at the nozzle half-height. The blue line is the normalized intensity while the green line is an exponential fit to the data. The lifetime is measured from the peak intensity to 1/e of the peak intensity.	35
17. Intensity versus time for a single image pixel, located 5.86 cm downstream of the nozzle throat, at the nozzle half-height. The blue line is the normalized intensity while the green line is an exponential fit to the data. The lifetime is measured from the peak intensity to 1/e of the peak intensity.	36
18. Two-point moving average of the iodine fluorescence lifetime versus downstream distance from throat. The lifetime is the average for an image field of view along the centerline, where the distance from the nozzle throat is measured at the image center.....	37
19. Averaged integrated normalized fluorescence lifetime versus downstream distance from the throat. The error bars are plus/minus one standard deviation of the integrated normalized lifetime for each image.	38

20. Averaged integrated normalized fluorescence lifetime versus iodine molar flow rate.	39
21. Contour plots of the fluorescence lifetimes (color bar units are nanoseconds) at four overlapping locations in the nozzle. Spatial dimension units in plots are in mm, x-location is measured from the nozzle throat, and y-location is measured from the nozzle half-height.	40
22. 3-D Navier-Stokes simulation results for temperature contours within a 2-D planar slice through the center of the jet.⁴⁷	41
23. Contour plots of the integrated normalized lifetimes (color bar units are nanoseconds*normalized lifetime) at four overlapping locations in the nozzle. Spatial dimension units in plots are in mm, x-location is measured from the nozzle throat, and y-location is measured from the nozzle half-height.....	42
24. A schematic of the laser and optics setup. The lenses are annotated with SL for spherical lens, CL for cylindrical lens, and M for mirror. In this schematic, the lasers and optics are situated to acquire images in the oblique view.	43
25. A schematic of the lasers and optics setup to acquire streamwise images. The laser sheet is aimed up the back end of the nozzle through a window.....	44
26. Schematic of the nozzle with shaded boxes indicating the locations of the five streamwise PLIF images taken (Figures 27 through 31).	48
27. Ensemble average of the streamwise images at the jet exit. Note that the iodine fluorescence is reflected onto the bottom wall of the nozzle, shown under the red line. Color bar units are pixel intensity.	49
28. Ensemble average of the streamwise images of the jet from ~22 mm to ~36 mm downstream of the nozzle throat. Color bar units are pixel intensity.	49
29. Ensemble average of the streamwise images of the jet from ~29 mm to ~43 mm downstream of the nozzle throat. Color bar units are pixel intensity.	50
30. Ensemble average of the streamwise images of the jet from ~53 mm to ~67 mm downstream of the nozzle throat. Color bar units are pixel intensity.	50
31. Ensemble average of the streamwise images of the jet from ~82 mm to ~96 mm downstream of the nozzle throat. Color bar units are pixel intensity.	51
32. Schematic of the x-, x45-, and y-axes with respect to the nozzle and camera. The x45-axis is along the direction of the laser sheet.	52
33. Ensemble average of the oblique images at x~13 mm. Color bar units are pixel intensity.....	53
34. Ensemble average of the oblique images at x~23 mm. Color bar units are pixel intensity.....	53
35. Ensemble average of the oblique images at x~35 mm. Color bar units are pixel intensity.....	54
36. Ensemble average of the oblique images at x~45 mm. Color bar units are pixel intensity.....	54
37. Ensemble average of the oblique images at x~55 mm. Color bar units are pixel intensity.....	55

38. Ensemble average of the oblique images at $x \sim 65$ mm. Color bar units are pixel intensity.....	55
39. Ensemble average of the oblique images at $x \sim 75$ mm. Color bar units are pixel intensity.....	56
40. Histograms of the ensemble-averaged streamwise images from Figures 27 to 31. The intensity of each image is normalized by the maximum intensity in Figure 27. The x -location is measured at the center of the image.	58
41. Histograms of the ensemble-averaged oblique images from Figures 33 to 39. The intensity of each image is normalized by the maximum intensity in Figure 33.	59
42. Black and white image of the oblique structure at $x \sim 75$ mm.	60
43. Areas of the oblique image structures versus downstream distance from the nozzle throat.	61
44. Outline of the black and white image from Figure 42.	62
45. Interface lengths of the oblique image structures versus downstream distance from the nozzle throat.	62
46. Top- and side-view schematic of the injector and trip jet for Trip Scenario A. Units are in millimeters and the primary flow is left to right.....	65
47. Top- and side-view schematic of the injector and trip jet for Trip Scenario B. Units are in millimeters and the primary flow is left to right.....	66
48. Top- and side-view schematic of the injector and trip jet for Trip Scenario C. Units are in millimeters and the primary flow is left to right.....	66
49. Ensemble average of the streamwise images at the jet exit for Trip Scenario A. Note that the iodine fluorescence is reflected from the bottom wall of the nozzle, shown under the red line. Color bar units are pixel intensity.	68
50. Ensemble average of the streamwise images of the jet from ~ 8 mm to ~ 22 mm downstream of the nozzle throat, for Trip Scenario A. Color bar units are pixel intensity.....	69
51. Ensemble average of the streamwise images of the jet from ~ 15 mm to ~ 29 mm downstream of the nozzle throat, for Trip Scenario A. Color bar units are pixel intensity.	69
52. Ensemble average of the streamwise images of the jet from ~ 22 mm to ~ 36 mm downstream of the nozzle throat, for Trip Scenario A. Color bar units are pixel intensity.	70
53. Ensemble average of the streamwise images of the jet from ~ 29 mm to ~ 43 mm downstream of the nozzle throat, for Trip Scenario A. Color bar units are pixel intensity.	70
54. Ensemble average of the streamwise images of the jet from ~ 36 mm to ~ 50 mm downstream of the nozzle throat, for Trip Scenario A. Color bar units are pixel intensity.	71
55. Ensemble average of the streamwise images of the jet from ~ 43 mm to ~ 57 mm downstream of the nozzle throat, for Trip Scenario A. Color bar units are pixel intensity.	71
56. Ensemble average of the streamwise images of the jet from ~ 49 mm to ~ 63 mm downstream of the nozzle throat, for Trip Scenario A. Nozzle wall is not present in image. Color bar units are pixel intensity.	72

57. Ensemble average of the streamwise images of the jet from ~57 mm to ~71 mm downstream of the nozzle throat, for Trip Scenario A. Nozzle wall is not present in image. Color bar units are pixel intensity.....	72
58. Ensemble average of the streamwise images of the jet from ~64 mm to ~78 mm downstream of the nozzle throat, for Trip Scenario A. Nozzle wall is not present in image. Color bar units are pixel intensity.	73
59. A mosaic of the streamwise images for Trip Scenario A.	74
60. Ensemble average of the streamwise images at the jet exit, for Trip Scenario B. Color bar units are pixel intensity.	75
61. Ensemble average of the streamwise images of the jet from ~4 mm to ~18 mm downstream of the nozzle throat, for Trip Scenario B. Color bar units are pixel intensity.	76
62. Ensemble average of the streamwise images of the jet from ~11 mm to ~25 mm downstream of the nozzle throat, for Trip Scenario B. Color bar units are pixel intensity.....	76
63. Ensemble average of the streamwise images of the jet from ~18 mm to ~32 mm downstream of the nozzle throat, for Trip Scenario B. Color bar units are pixel intensity.	77
64. Ensemble average of the streamwise images of the jet from ~25 mm to ~39 mm downstream of the nozzle throat, for Trip Scenario B. Color bar units are pixel intensity.	77
65. Ensemble average of the streamwise images of the jet from ~32 mm to ~46 mm downstream of the nozzle throat, for Trip Scenario B. Color bar units are pixel intensity.	78
66. Ensemble average of the streamwise images of the jet from ~39 mm to ~53 mm downstream of the nozzle throat, for Trip Scenario B. Color bar units are pixel intensity.	78
67. Ensemble average of the streamwise images of the jet from ~45 mm to ~60 mm downstream of the nozzle throat, for Trip Scenario B. Color bar units are pixel intensity.	79
68. Ensemble average of the streamwise images of the jet from ~53 mm to ~67 mm downstream of the nozzle throat, for Trip Scenario B. Color bar units are pixel intensity.	79
69. Ensemble average of the streamwise images of the jet from ~60 mm to ~74 mm downstream of the nozzle throat, for Trip Scenario B. Color bar units are pixel intensity.	80
70. A mosaic of the streamwise images for Trip Scenario B.	81
71. Ensemble average of the streamwise images at the jet exit, for Trip Scenario C. Color bar units are pixel intensity.	82
72. Ensemble average of the streamwise images of the jet from ~5 mm to ~19 mm downstream of the nozzle throat, for Trip Scenario C. Color bar units are pixel intensity.	83
73. Ensemble average of the streamwise images of the jet from ~9 mm to ~24 mm downstream of the nozzle throat, for Trip Scenario C. Color bar units are pixel intensity.	83
74. Ensemble average of the streamwise images of the jet from ~16 mm to ~31 mm downstream of the nozzle throat, for Trip Scenario C. Color bar units are pixel intensity.	84
75. Ensemble average of the streamwise images of the jet from ~22 mm to ~37 mm downstream of the nozzle throat, for Trip Scenario C. Color bar units are pixel intensity.	84

76. Ensemble average of the streamwise images of the jet from ~30 mm to ~45 mm downstream of the nozzle throat, for Trip Scenario C. Color bar units are pixel intensity.....	85
77. Ensemble average of the streamwise images of the jet from ~36 mm to ~52 mm downstream of the nozzle throat, for Trip Scenario C. Color bar units are pixel intensity.....	85
78. Ensemble average of the streamwise images of the jet from ~42 mm to ~58 mm downstream of the nozzle throat, for Trip Scenario C. Color bar units are pixel intensity.	86
79. Ensemble average of the streamwise images of the jet from ~49 mm to ~65 mm downstream of the nozzle throat, for Trip Scenario C. Color bar units are pixel intensity.....	86
80. Ensemble average of the streamwise images of the jet from ~56 mm to ~72 mm downstream of the nozzle throat, for Trip Scenario C. Color bar units are pixel intensity.....	87
81. Ensemble average of the streamwise images of the jet from ~62 mm to ~77 mm downstream of the nozzle throat, for Trip Scenario C. Color bar units are pixel intensity.....	87
82. A mosaic of the streamwise images for Trip Scenario C.....	88
83. Ensemble average of oblique images at $x \sim 10$ mm, for Trip Scenario A. Color bar units are pixel intensity.	89
84. Ensemble average of oblique images at $x \sim 13$ mm, for Trip Scenario A. Color bar units are pixel intensity.	90
85. Ensemble average of oblique images at $x \sim 25$ mm, for Trip Scenario A. Color bar units are pixel intensity.	90
86. Ensemble average of oblique images at $x \sim 35$ mm, for Trip Scenario A. Color bar units are pixel intensity.	91
87. Ensemble average of oblique images at $x \sim 45$ mm, for Trip Scenario A. Color bar units are pixel intensity.	91
88. Ensemble average of oblique images at $x \sim 55$ mm, for Trip Scenario A. Color bar units are pixel intensity.	92
89. Ensemble average of oblique images at $x \sim 65$ mm, for Trip Scenario A. Color bar units are pixel intensity.	92
90. Ensemble average of oblique images at $x \sim 75$ mm, for Trip Scenario A. Color bar units are pixel intensity.	93
91. Ensemble average of oblique images at $x \sim 12.3$ mm, for Trip Scenario B. Color bar units are pixel intensity....	94
92. Ensemble average of oblique images at $x \sim 25$ mm, for Trip Scenario B. Instantaneous images were centered. Color bar units are pixel intensity.....	95
93. Ensemble average of oblique images of the jet at $x \sim 35$ mm, for Trip Scenario B. Instantaneous images were centered. Color bar units are pixel intensity.	95
94. Ensemble average of oblique images at $x \sim 45$ mm, for Trip Scenario B. Instantaneous images were centered. Color bar units are pixel intensity.....	96
95. Ensemble average of oblique images at $x \sim 55$ mm, for Trip Scenario B. Instantaneous images were centered. Color bar units are pixel intensity.....	96
96. Ensemble average of oblique images of the jet at $x \sim 65$ mm, for Trip Scenario B. Instantaneous images were centered. Color bar units are pixel intensity.	97

97. Ensemble average of oblique images at $x \sim 75$ mm, for Trip Scenario B. Instantaneous images were centered. Color bar units are pixel intensity.....	97
98. Ensemble average of oblique images at $x \sim 7$ mm, for Trip Scenario C. Color bar units are pixel intensity.....	98
99. Ensemble average of oblique images at $x \sim 10.5$ mm, for Trip Scenario C. Color bar units are pixel intensity....	99
100. Ensemble average of oblique images at $x \sim 25$ mm, for Trip Scenario C. Instantaneous images were centered. Color bar units are pixel intensity.....	99
101. Ensemble average of oblique images at $x \sim 35$ mm, for Trip Scenario C. Instantaneous images were centered. Color bar units are pixel intensity.....	100
102. Ensemble average of oblique images at $x \sim 45$ mm, for Trip Scenario C. Instantaneous images were centered. Color bar units are pixel intensity.....	100
103. Ensemble average of oblique images at $x \sim 55$ mm, for Trip Scenario C. Color bar units are pixel intensity...	101
104. Ensemble average of oblique images at $x \sim 65$ mm, for Trip Scenario C. Color bar units are pixel intensity...	101
105. Ensemble average of oblique images at $x \sim 75$ mm, for Trip Scenario C. Instantaneous images were centered. Color bar units are pixel intensity.....	102
106. Histograms of the ensemble-averaged streamwise images from Figures 49 to 58, Trip Scenario A. The intensity of each image is normalized by the maximum intensity in Figure 49. The x -location is measured at the center of the image.	103
107. Histograms of the ensemble-averaged streamwise images from Figures 60 to 69, Trip Scenario B. The intensity of each image is normalized by the maximum intensity in Figure 60. The x -location is measured at the center of the image.	104
108. Histograms of the ensemble-averaged streamwise images from Figures 71 to 81, Trip Scenario C. The intensity of each image is normalized by the maximum intensity in Figure 71. The x -location is measured at the center of the image.	105
109. Histograms of the ensemble-averaged oblique images from Figures 83 to 90, Trip Scenario A. The intensity of each image is normalized by the maximum intensity in Figure 83.....	106
110. Histograms of the ensemble-averaged oblique images from Figures 91 to 97, Trip Scenario B. The intensity of each image is normalized by the maximum intensity in Figure 91.....	107
111. Histograms of the ensemble-averaged oblique images from Figures 98 to 105, Trip Scenario C. The intensity of each image is normalized by the maximum intensity in Figure 98.	108
112. Structure area versus downstream distance for the single jet and Trip Scenarios A, B, and C.....	109
113. Interface length versus downstream distance for the single jet and Trip Scenarios A, B, and C.....	110
114. Jet penetration versus downstream distance for the single jet and Trip Scenarios A, B, and C. Penetration measurements are taken from the ensemble-averaged streamwise images.....	111

1.0 SUMMARY

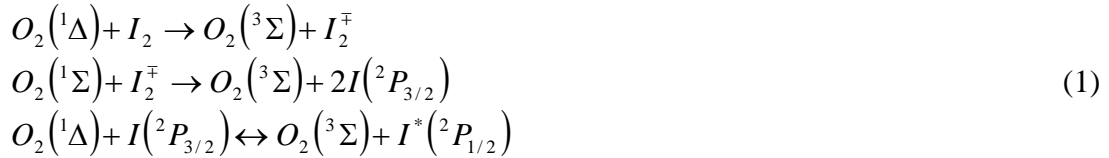
A supersonic nozzle with supersonic iodine injection was designed and studied with Planar Laser-Induced Fluorescence (PLIF). The nozzle simulates Chemical Oxygen Iodine Laser (COIL) flow conditions with non-reacting, cold flows. A laser sheet near 565 nm excited the iodine, and the fluorescence was imaged with an intensified and gated CCD camera. Streamwise and semi-spanwise (oblique-view) images were taken, where the presence of injected flow was highlighted. With these images, the flow structures were identifiable and the mixing quality between the primary and injected flow was quantitatively measured with histograms, structure size measurements, and jet penetration.

Four different injection scenarios are investigated. The first scenario includes a single injector positioned downstream of the nozzle throat. To enhance the mixing between the flows, trip jets were placed in the wake of the single jet. The trip jets, significantly smaller than the primary iodine jet, are intended to destabilize the counter-rotating vortex pair (CRVP) of the primary jet. Three different trip jet configurations are compared for their ability to enhance mixing between the oxygen and iodine flows. While the mixedness between the injected and primary flows was not optimized, the comparison between the four different injection scenarios may aid in future nozzle design and mixing optimization.

2.0 INTRODUCTION

2.1 Chemical Oxygen Iodine Lasers

In 1977, the Air Force Weapons Laboratory demonstrated the Chemical Oxygen Iodine Laser (COIL).¹ McDermott and coworkers passed chlorine gas vapor through a rotating disk device, which contained basic hydrogen peroxide as a fuel, to obtain the excited state of molecular oxygen, $O_2(^1\Delta)$. Molecular iodine was injected into the gaseous flow of excited oxygen, $O_2(^1\Delta)$ and $O_2(^1\Sigma)$, and ground-state oxygen, $O_2(^3\Sigma)$, to produce the excited state of atomic iodine. The $^2P_{1/2} - ^2P_{3/2}$ transition of atomic iodine produces an output wavelength of 1.315 μm . The whole transition is pumped by the singlet delta excited state of molecular oxygen $O_2(^1\Delta)$, triggering the following sequence of reaction equations:



Truesdell et al., Avizonis and Neumann, and Avizonis and Truesdell give detailed descriptions of the COIL chemistry and mechanics.^{2,3,4}

The gases are typically mixed in a supersonic nozzle, with excited oxygen and a diluent (usually helium) in the primary flow and iodine and a diluent (helium) in the injected flow. Supersonic nozzles are used to maximize the temperature drop downstream of the throat of the nozzle (and thus move the state of the flow farther away from thermodynamic equilibrium, facilitating lasing) and to increase the flow per unit nozzle throat area. The low temperature of a supersonic nozzle optimizes the production of $I^*(^2P_{1/2})$.³ Historically, the iodine and its diluent have been injected into the subsonic region of the nozzle upstream of the throat. Injecting the

iodine in the subsonic region promotes mixing between the injected iodine and the primary oxygen flows, whereas diffusive mixing is difficult in the supersonic region because of compressibility effects. A well-mixed medium increases the interaction between $O_2(^1\Delta)$ and iodine, to produce more $I^*(^2P_{1/2})$. A well-mixed medium also produces a more uniform laser beam profile. Numerical studies have been performed for chemical lasers with iodine injection in the subsonic region of the nozzle by Madden and Miller, Miller et al., Madden and Solomon, and Masuda et al.⁵⁻⁹ These simulations were performed to investigate the spatial and temporal gradients in the flowfield, which impact the laser beam quality.

While the injection of iodine has traditionally been in the subsonic region of the nozzle, there are advantages to injecting the iodine in the supersonic region of the nozzle. Designs in which iodine is injected in the supersonic region have the potential to provide improved performance. Injecting the iodine downstream of the nozzle throat decouples the injected flow from the Singlet Oxygen Generator (SOG), the device that chemically makes and delivers $O_2(^1\Delta)$. This decoupling allows changes to be made to the injected mass flow without affecting the pressure upstream in the flow from the SOG. When injected into the subsonic region, the iodine and diluent gases are a significant portion of the SOG molar flow. By injecting the iodine and diluent helium into the supersonic region, the pressure increase and velocity decrease associated with injection are avoided, reducing the loss of $O_2(^1\Delta)$ to quenching processes. Lower pressure and increased velocity decrease the rate of $O_2(^1\Delta)$ loss, and a greater velocity decreases the time it takes to transport $O_2(^1\Delta)$ downstream of the throat, providing more $O_2(^1\Delta)$ downstream for laser power extraction.

Injecting the iodine in the supersonic region does hinder the mixing between the primary flow of oxygen and the injected iodine flow. Mixing between supersonic streams is more

difficult because of the increased flow stability associated with compressible flows and shock losses that decrease jet penetration. The supersonic nozzle and the iodine injectors must be designed to provide adequate penetration of the iodine stream into the oxygen flow and adequate mixing between the oxygen and iodine flows to completely dissociate the iodine molecules.¹⁰ The process of dissociation of the iodine molecules by $O_2(^1\Delta)$ is sensitive to the rate of mixing. If the local molecular iodine concentration drops too rapidly, dissociation is decreased and laser performance drops. COIL nozzle designs with supersonic injection of iodine have been studied numerically by Madden and coworkers and experimentally by Rosenwaks and coworkers and Barmashenko and coworkers.¹⁰⁻¹²

2.2 Fluid Mechanics Related to COIL Nozzles

The flow physics of iodine injection into the oxygen flow of a COIL nozzle are very similar to those of a fundamental problem of a jet in crossflow (JICF). There have been extensive studies of JICF structures and methods used to perturb the stability of the dominant structures to enhance mixing. This research and methods of perturbation are directly applicable to COIL nozzles, with a caveat that COIL nozzles operate under relatively low pressures when compared to many other flow regimes.

2.2.1 Jet in Crossflow Structure

Fric and Roshko give a thorough description of four structures present when an incompressible jet enters a crossflow, with emphasis on the structure in the wake of the jet.¹³ They experimentally studied the jet in crossflow with smoke-wire visualization, which places closely-spaced streaklines into the flow. In their experiments, the crossflow Reynolds

number ranged from 3800 to 11,400 and the jet-to-crossflow velocity ratio ranged from 2 to 10. They refuted the common assumption that there is a strong similarity between the near wake of a jet and that of a circular cylinder. In their experiments, they identified four types of coherent structures in the near field of the jet: 1) jet shear-layer vortices; 2) system of horseshoe vortices; 3) counter-rotating vortex pair (CRVP); and 4) wake vortices. These structures are illustrated in Figure 1. Initially, the jet shear-layer vortices are the dominant flow structures. They result from the Kelvin-Helmholtz instability of the annular shear layer that lies on the leading edge of the jet orifice. The horseshoe vortices arise from the adverse pressure gradient upstream of the jet interacting with the approaching low-momentum fluid in the wall boundary layer. The CRVP is the dominant system of primary-secondary flow interaction and persists far downstream. In the development of the CRVP, the crossflow skirts laterally around the jet, shearing the jet fluid along its edges and then folding the face of the jet over itself to form the CRVP. Finally, the wake vortices are formed in the region downstream of the jet (between the jet and the wall). Each wake vortex has a termination on the wall and on the jet, whereas with a circular cylinder the wake vortices terminate only on the wall.

Fric and Roshko noted that it was essential to establish the source of vorticity of the wake structures to understand them. From their smoke visualization, they found that the vortical structures in the wake of a jet are formed from the vorticity originating in the boundary layer of the crossflow wall. Alternating separation events occur on each side of the jet, on the crossflow wall, resulting in eruptions of boundary layer fluid and vorticity that interact with the jet fluid. Fric and Roshko conclude that the wake vortices may affect unsteady components of the CRVP structure.

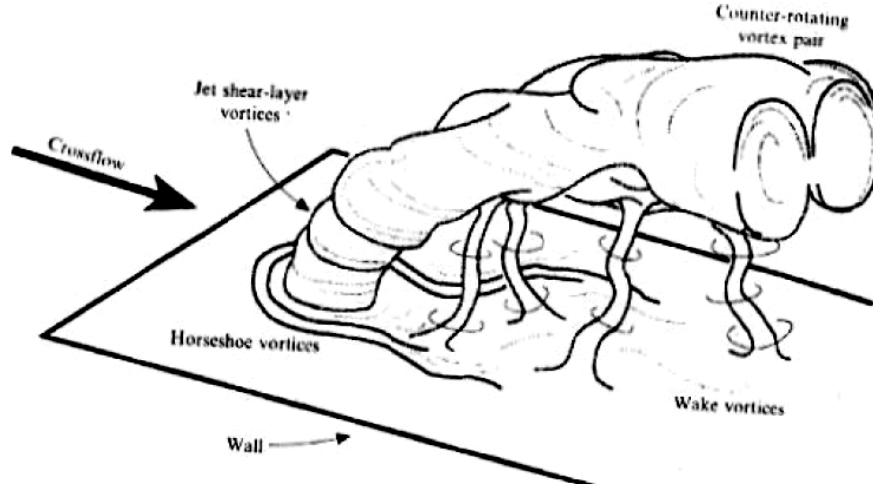


Figure 1. Cartoon depicting the four types of vortical structures associated with a jet-in-crossflow.¹³

Rivero et al. also performed an experimental study to identify the incompressible JICF structures.¹⁴ They performed hot-wire measurements and PLIF flow visualization on a JICF with a velocity ratio of 3.8 and crossflow Reynolds number of 6600. They concluded that three structures (folded vortex rings, horseshoe vortices, and handle-like structures) contribute to a coherent velocity field. The folded vortex rings result from the roll-up process of the shear layer, as in the shear-layer vortices of Fric and Roshko's work.¹³ The handle-like structures link the boundary layer vorticity with the CRVP through the upright wake vortices. The CRVP is strongly modulated by this coherent velocity field. Their results indicate that the CRVP is not a steady feature of the jet in crossflow, but the intensity of each counter-rotating vortex has fluctuations driven by Kármán-like vortices present in the jet wake.

Though the studies by Fric and Roshko and Rivero et al. detail the structures of a jet issuing into a *subsonic* crossflow, the description of the jet structures still applies to *supersonic* flows.¹³⁻¹⁴ Gruber et al., in their studies of the compressibility effects of a supersonic JICF, developed a three-dimensional schematic of the flow structures, as shown in

Figure 2.¹⁵ Because the crossflow is supersonic, a bow shock forms just upstream of the jet, increasing the jet stability. The jet is supersonic and forms a shock structure (Mach disk) downstream of the jet exit. The wake region, horseshoe vortex region, and the CRVP are all present with a supersonic jet issuing into a supersonic crossflow.

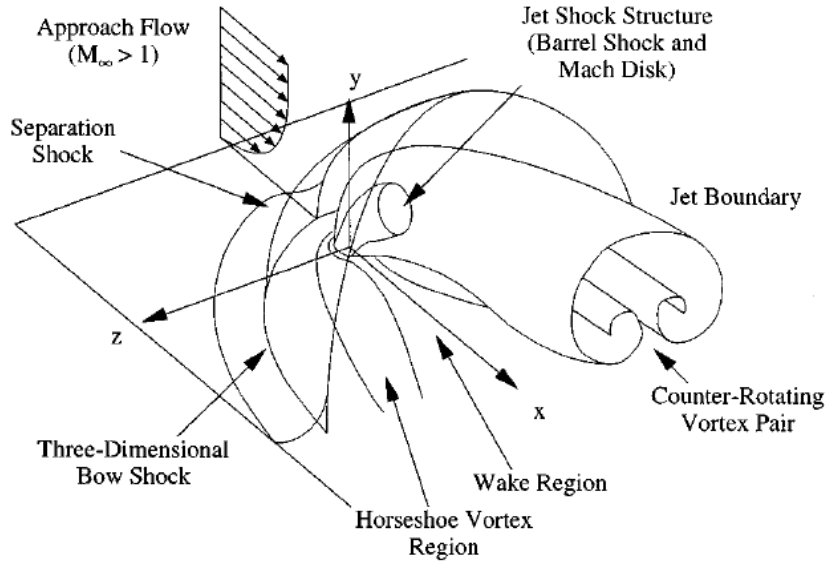


Figure 2. A three-dimensional schematic of the structures in a compressible (supersonic) JICF system.¹⁵

2.2.2 Perturbation of Injected Flow

The jet structures, mainly the CRVP, can be perturbed to produce unsteadiness or altered in shape to increase the mixing between the jet and crossflow. Voignier et al. studied three different methods to perturb the jet structure, motivated by the need to stretch the mixing interface in a deuterium fluoride (DF) combustion driven chemical laser and increase mixing.¹⁶ They compared small signal gain profiles from different perturbation methods: trip jet nozzles, ramp nozzles, and deflector nozzles. The trip jets used either inert gas or cavity fuel and were injected transversely between reactant streams through small orifices. In that study, the metric for comparing the performance of the trip jets to the ramp and deflector nozzles involved both performance and manufacturing costs. To compare the

mixing enhancement capability, the small signal gain and the distance of positive gain after the nozzle exit plane (NEP) were measured. With no trip jets, ramps, or deflectors, the maximum small signal gain was 1.5%/cm and the distance of positive gain was 40 mm from the NEP. The nozzle with the trip jets produced the largest small signal gain, with a maximum of 7%/cm, with positive gain measured for over 30 mm from the NEP. The deflector and ramp nozzles had lower small signal gain and the region of positive gain was less than 20 mm. With the trip jet nozzle having a higher peak gain and longer region of positive gain, it was concluded that the mixing rate was higher than that of the ramp and deflector nozzles.

Cenkner and Driscoll used Planar Laser-Induced Fluorescence (PLIF) and Laser Doppler Velocimetry (LDV) to study supersonic cold-flow mixing of nozzles that employ gas trips.¹⁷ Their nozzle simulated chemical laser flow conditions, with the reacting species being injected adjacently in a nozzle. The trip jets were positioned near the NEP of both nozzles of the reacting species and utilized nonreacting flow. Cenkner and Driscoll conclude that there are three convective mechanisms that could contribute to the enhanced mixing of adjacent gas streams: 1) a low-pressure wake of the trip jets that draws gas from the adjacent flow; 2) a high-pressure region that is established in the adjacent flow, that pushes this flow into the main flow; and 3) a trip-jet induced breakup that possibly triggers a spreading effect in the adjacent flow. They also concluded that trip jets did not increase the maximum turbulence intensity, but instead spread the low-level turbulence in the wake of the base region into the core of the nozzle flows.

Driscoll published experimental results comparing ramp and trip jet nozzles applicable to DF chemical laser nozzles.¹⁸ The trip jets supplied inert gas into an inert gas

layer separating the reactant streams, retarding the molecular mixing. The inert gas also perturbed the density in the laser cavity, potentially degrading the laser beam uniformity. Driscoll's LIF (laser-induced fluorescence) experimental results indicate that the ramp and trip jet nozzles (with inert gas) produce similar levels of mixing enhancement. The ramp and trip nozzles both doubled the reactant interface length within a centimeter of the NEP. However, because of the possible inert gas layer formed by the trip jets in that case, in future work it may be advantageous to use a reactant gas in the trip jet.

While Voigneir et al., Cenker and Driscoll, and Driscoll employed trip jets to destabilize both the primary and secondary flows, Takeuchi et al. employed trip jets with a reactant gas to destabilize the secondary flow.¹⁶⁻¹⁹ An ejector COIL consisting of two-dimensional slit nozzles with trip jet iodine injection was designed and tested. The trip jets were located at the NEP of the nitrogen nozzle (which was adjacent to the oxygen nozzle). The iodine was mixed into the nitrogen flow via the trip jets and then the nitrogen/iodine flow was mixed into the adjacent oxygen flow. They used a horizontal Pitot scan to experimentally demonstrate that the mixing ability of the trip jets was sufficient. While the slit nozzle design is not similar to the supersonic injection scheme studied here, it does demonstrate the mixing enhancement of trip jets, because they not only injected the iodine, but also were able to enhance the mixing between the nitrogen and oxygen flows.

The injected flow may also be altered by means other than ramps, deflectors, and trip jets. The jet may be influenced by forcing the injected flow at a selected frequency or imparting the jet with a swirling component before it issues into the cross stream flow. A forcing frequency acts upon existing instabilities in the flow, whereas a swirling jet introduces a new instability. Murugappan et al. used Rayleigh/Mie scattering from naturally

occurring ice crystals to study the mixing and penetration of a forced jet in a Mach 2 cross stream.²⁰ They forced the underexpanded jet into the cross stream with a high-frequency actuator at three different frequencies (0 Hz, 900 Hz, and 5 kHz). They found that both of the forced cases provided superior mixing characteristics and higher penetration of large-scale structures into the freestream than the unforced case. In a subsequent study, Murugappan et al. used Rayleigh/Mie scattering and NO (nitric oxide) PLIF to study the mixing and penetration characteristics of a swirling injector that consisted of two independent streams.²¹ One stream was annular with swirl vanes at the exit to impart swirl on the jet. The other stream was a central jet to control the penetration of the jet into the freestream and prevent early vortex breakdown. The optimal case that was tested showed an increase of 16% in mixing area with the streamwise images and an increase of 78% in total area contained within the jet boundary with the cross-stream images.

The shape of the injector also affects penetration and large-scale structure size of the jet in crossflow. Gruber et al. and Gruber et al. used planar Rayleigh/Mie scattering to study two sonic transverse injectors.²²⁻²³ The experiment of Gruber et al., involving a circular injector, was simulated, with comparable results, using the Reynolds Averaged Navier Stokes (RANS) equations, by Palekar et al.^{22,24} Of the two sonic transverse injectors studied by Gruber et al., one injector was circular and the other was elliptical (with the major axis aligned in the lateral direction).²² Both injectors were directed perpendicular to the crossflow. The elliptical jet was found to spread more rapidly in the lateral direction than the circular jet, indicating an axis switching phenomenon within the jet. However, the elliptical jet did suffer a 20% reduction in penetration compared to the circular jet. The elliptical jet was wide and flat with the counter-rotating vortices spread farther apart than the vortices

from the circular jet. This spread in vortices provided a larger central entrainment region where freestream fluid may be entrained into the jet core. Though the penetration of the jet suffered, the increased entrainment region enhanced the mixing of the jet and crossflow. Blanchard et al. and Landman and Saffman discuss the nature of a JICF using elliptical geometry.²⁵⁻²⁶ They conclude that the elliptical cross section of a CRVP, regardless of orifice shape, can cause the loss of jet stability. This loss in stability would also have the potential to enhance the mixing between the jet and crossflow.

The work by Viti et al. examines the use of smaller jets to alter the flow behind a primary jet, though it does not elaborate on the structural interactions between a primary jet and an array of smaller jets.²⁷ Viti et al. numerically simulated and experimentally studied a primary jet issuing into a Mach 4 crossflow with an array of smaller injectors downstream of the primary. The jets were all sonic and injected perpendicular to the crossflow, with the smaller injectors injecting 0.5 to 1% of the mass flow rate of the primary jet. They used pressure sensitive paint to measure the pressure field and Schlieren photographs for imaging. The numerical simulation was done with RANS equations and the Wilcox $k-\omega$ turbulence model. They did not measure the impact the smaller jets had on fluid mixing, but did find that the smaller injectors reduced the size and intensity of the low-pressure region downstream of the primary jet.

2.3 COIL Diagnostics

Nonintrusive imaging of the interaction between the oxygen and iodine flows can be used to determine the degree of mixing between the primary and secondary flows, the concentration of the iodine flow, and the temperature, pressure, and velocity of the flows. Knowing the

thermodynamic characteristics and the mixing quality between the oxygen and iodine flows can be useful in optimizing the COIL mixing nozzle.

There are several different types of flow imaging, including Particle Image Velocimetry (PIV), Rayleigh/Mie scattering, Schlieren imaging, and Planar Laser-Induced Fluorescence (PLIF). As an example of PIV in a similar application, Borg et al. used PIV to measure particle velocity in a low-pressure turbulent jet.²⁸ The jet fluid was seeded with tracer particles that were illuminated by a plane sheet of light. A charge-coupled device (CCD) camera acquired images pairs with a known time separation. This allowed for particle displacement mapping from one image to the next. To make such mapping possible, the time separation between images must be small enough that the particle movement is a small fraction of the image size.

Rayleigh/Mie scattering is similar to PIV in that it uses a laser sheet to illuminate the flow. Rayleigh scattering is observed directly off tracer gas (e.g., biacetyl) molecules, whereas Mie scattering is produced by light scatter from tracer particles in particle-seeded flow. A CCD camera is used to capture the scattered light. The image intensities are directly related to the tracer concentration, as long as the tracer behaves as a passive scalar during the mixing process. An example is the work of Gruber et al., who studied JICF flowfields using silicon dioxide particles as tracers.¹⁵

Schlieren photography is also used to image density gradients in the flow and is good for imaging the boundary of a JICF, for example. Ben-Yakar and Hanson used fast-framing Schlieren photography to study the time evolution of JICF structures.²⁹ A drawback to Schlieren imaging is that while it can be used to identify structures along the edges of a jet, it cannot discern the internal features. Another limitation is that it integrates the density gradients along the beam propagation path, unlike the previously-discussed methods that use a thin sheet of light

to illuminate a planar section of the flow, and integration occurs only through the thickness of the light sheet.

PLIF is an imaging technique where a thin planar sheet of laser light is used to induce fluorescence in a species carried by the flow. The fluorescent light (with the wavelength distinct from that of the laser light) is then captured with a CCD camera. The laser wavelength used is chosen based on the absorption spectrum of the fluorescing species. Some common fluorescing species are acetone³⁰⁻³¹, nitric oxide³², OH for reacting flows³³, and iodine. The fluorescing species is chosen based on ease of use, level of toxicity, or whether it is already present in the system to be imaged.

Hiller and Hanson discuss the use of iodine in PLIF fluid mechanic experiments.³⁴ They argue that saturating the fluorescence, with the use of a continuous-wave excitation laser, allows the fluorescence signal to be independent of the quenching rate and laser intensity, which is desirable. With non-saturated fluorescence and a continuous-wave excitation laser, the PLIF signal, S_f , is a function of the excitation laser power, I , fluorescence decay rate, A_{21} , collisional quenching rate, Q , Boltzmann population fraction, F_1 , number density of the iodine species being irradiated, N_{I_2} , and a correction for the optical collection geometry and molecular transition, C ³⁵

$$S_f = CI \frac{A_{21}}{A_{21} + Q} F_1 N_{I_2} \quad (2)$$

This direct relationship allows the determination of the number density of the fluorescing iodine molecules, which directly relates to concentration of the injectant.

Iodine PLIF has been successfully used to measure temperature, pressure, and velocity in a compressible flow field. Hartfield et al. used the fluorescence broadband to determine temperature, and the shape and position of the fluorescence spectrum to determine velocity and pressure in a compressible flowfield.³⁶ Their uncertainties were quite reasonable with 6% for

temperature, 5% for pressure, and 25 m/s for velocity. Iodine PLIF can also be used to measure injectant mole fraction and iodine concentration in a flowfield.^{35,34}

With iodine present in COIL systems, using PLIF with iodine as the fluorescing species is an obvious choice for fluid imaging. There are several benefits to using iodine: it has a large absorption cross section, it fluoresces strongly in the visible, it has a high vapor pressure, and it has numerous transition lines across a large range of frequencies allowing the use of different laser wavelengths for excitation.³⁷

2.4 Thesis Overview

The JICF structure analyses of Fric and Roshko and Rivero et al. suggest that the CRVP can be destabilized or stretched by producing a disturbance in the wake of the jet that mimics wake vortices.¹³⁻¹⁴ The wake vortices occur in the downstream region of the jet and connect the crossflow boundary layer to the CRVP. A ramp, deflector, or small trip jet could create a disturbance in this portion of the flow to enhance the action of the wake vortices or create additional wake vortices to perturb the CRVP. In this study, trip jet interactions with a single jet will be investigated. The trip jet(s) will be located in the subsonic wake region of the jet to connect with the CRVP.

The trip jet designs for DF and COIL chemical lasers, as tested by Voignier et al., Cenker and Driscoll, Driscoll, and Takeuchi et al., demonstrated the capability of the trip jets to enhance mixing between two components of the flow.¹⁶⁻¹⁹ It was noted that using reactants in the trip jets reduces the chance of having an inert gas layer present between the two reacting species, an effect that would inhibit mixing (and thus decrease the chemical laser efficiency). However, trip jets were not the only tools studied to enhance mixing with injected flow. Though

trip jets seem like a natural device to stretch the structures in the issuing jets, the flow may be disturbed or influenced by forced injection of the jet with a high-frequency actuator, or swirl could be imparted to the jet at its exit.²⁰⁻²¹

The objective of this thesis is to investigate injection penetration and mixedness with supersonic iodine injection in the supersonic region of a nozzle. A nozzle was designed with COIL chemistry considerations and was tested using non-reacting flows. A single jet of iodine and diluent helium was positioned just downstream of the nozzle throat and the injected iodine was imaged using PLIF. Using the PLIF images, the jet penetration and mixedness of the oxygen and iodine flows were determined. To enhance the mixing between the flows, trip jets were placed in the wake of the single jet. The trip jets, significantly smaller than the primary iodine jet, were placed with the intent of destabilizing the CRVP of the primary jet. Different configurations of the trip jet(s) are compared for their ability to enhance mixing between the oxygen and iodine flows.

The next chapter discusses the experimental system used in this effort, including the gas delivery system and the nozzle design, verification of the nozzle design, and the specifications of the single injector. The specifics of the PLIF diagnostics are detailed in Chapter 4. Chapter 5 presents the PLIF results with the single injector, while Chapter 6 presents the results of the single injector with three different trip jet scenarios. Chapter 7 concludes the thesis and presents recommendations for future work.

3.0 DESCRIPTION OF EXPERIMENTAL SYSTEM

3.1 Introduction

This chapter describes the gas delivery system and the nozzle designed for experimentation. The gas delivery system includes a vacuum pump, delivery of the primary gases to the plenum of the nozzle, and delivery of iodine and carrier helium to the injector(s) of the nozzle. The nozzle was designed according to Chemical Oxygen Iodine Laser (COIL) gas flow specifications, with a design Mach number of 2.2. The nozzle was tested to verify the Mach number and static pressures with COIL gas flow rates. The design for a single injector is also discussed.

3.2 Gas Delivery System

This experiment uses COIL gas flow ratios to accurately represent the fluid mechanics in a COIL nozzle. In a COIL nozzle, typical molar gas flows are 4:1 helium to oxygen in the primary flow, with a plenum (stagnation) pressure of 65 Torr.³⁸ Injected with helium as a carrier gas, the iodine molar flow rate is 1.5% of the oxygen flow rate. The primary flows are delivered at room temperature (300K). To determine the molar flow rates of the primary flow, Eqn. A.10 (from Appendix A) is used. The throat and span of the nozzle are 1 cm and 5 cm respectively, giving a throat area of 5 cm² (see Section 3.3 for design details). The molecular weight for the helium and oxygen mixture is 9.6 kg/kmol and the ratio of specific heats is 1.587, giving a total molar flow rate of about 640 mmol/s, with 514 mmol/s of helium and 129 mmol/s of oxygen.

The injected flow is 129 mmol/s of helium and 1.5 mmol/s of iodine. The molar flow rate measurement technique and the uncertainties are detailed in Appendix A.

The oxygen and helium gases flow through an in-line mixer upstream of the nozzle, sufficient to fully mix the two gases. To ensure the uniformity of the primary gas flow and to dissipate any vortical structures in it, a flow straightener was placed downstream of the in-line mixer and just upstream of nozzle plenum. The flow straightener is a series of honeycomb and fine mesh screens to take out both axial and lateral turbulence. The flow straightener design is discussed in Appendix B. The nozzle is pumped with a vacuum system that has a capacity of 793 m³/min and can pump to a pressure as low as 0.2 Torr.

3.3 Nozzle Design

The nozzle was designed with a Mach number of 2.2 at the nozzle exit plane (NEP). Mach 2.2 decreases the static temperature from 300 K at the plenum to less than 150 K. The contour of the nozzle was designed using a computer program developed at the University of Illinois at Urbana-Champaign.³⁹ The nozzle is contoured on the top and bottom, while the sidewalls are flat polycarbonate plates. The contour has been adjusted to compensate for a boundary layer build-up along the contours and sidewalls. A thorough description of the nozzle design and the boundary layer correction is given in Appendix C. The throat of the nozzle is 1 cm, while the span is 5 cm. The NEP is 4.3 cm downstream of the nozzle throat. The contour profile is then extended to 22.5 cm downstream of the throat at a constant 2-degree angle, matching the contour angle at the NEP. The nozzle profile from the plenum to the exit of the nozzle is displayed in Figure 3.

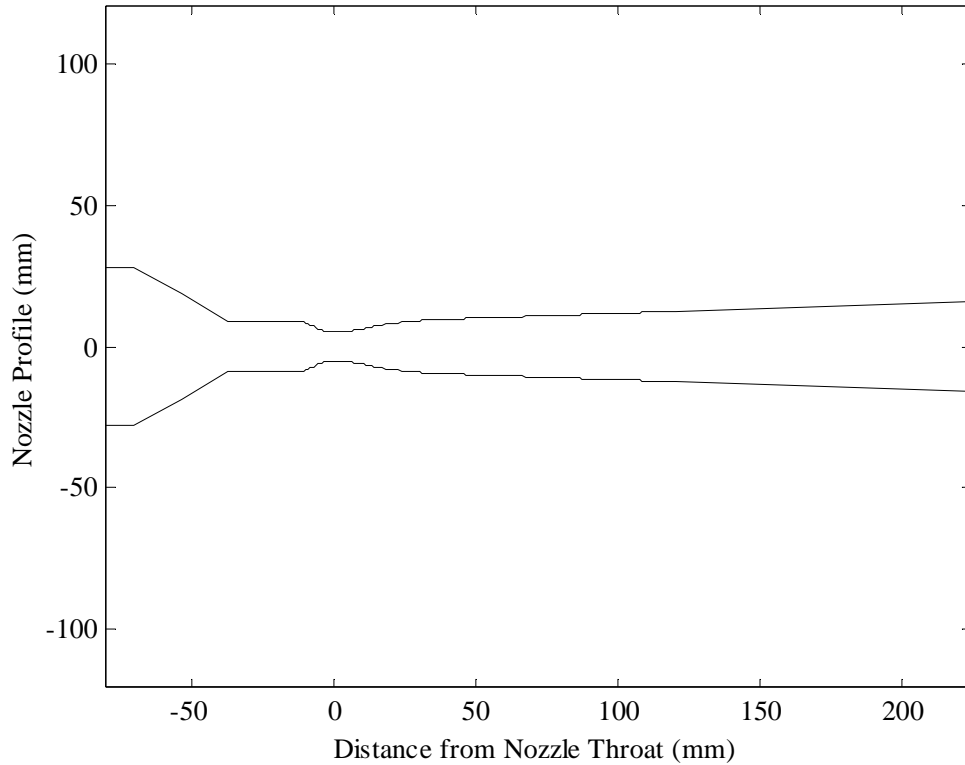


Figure 3. The nozzle contour, from the plenum to the exit of the nozzle.

The nozzle consists of a stainless steel main body frame, top and bottom stainless steel contour inserts, and polycarbonate sidewalls. Multiple inserts, each with an injector plenum, were made so that different iodine injector scenarios could be tested. The injectors were fabricated by Wire-Tech, Inc. after the inserts were complete, using sinker EDM (Electrical Discharge Machining). Three holes penetrate the inserts in the spanwise direction around the injector plenum (which is near the throat of the nozzle). Heaters are placed in these holes to keep the nozzle block warm so that the gaseous iodine does not freeze out in the plenum or injectors. Figure 4 is a picture of the nozzle frame with only one insert installed, while Figure 5 is a picture of the frame and inserts after installation. Figure 6 is a picture of the nozzle on the test stand, where the polycarbonate side plates and pressure taps are visible.

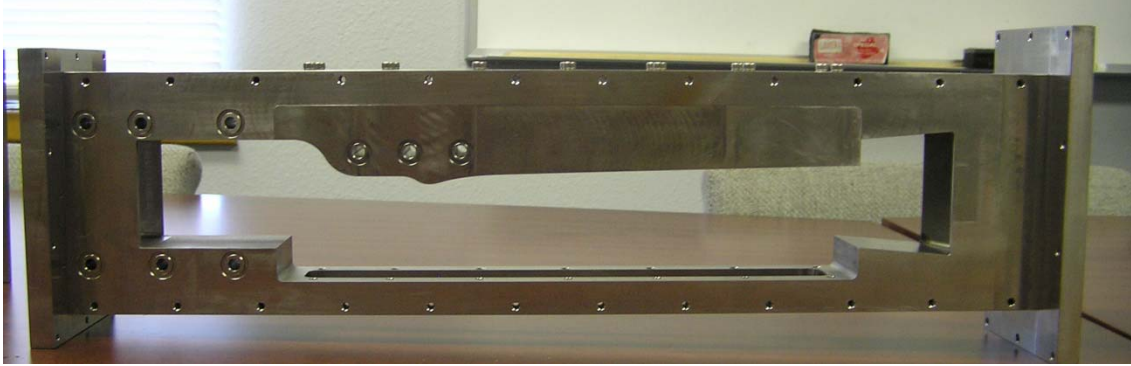


Figure 4. Nozzle frame with top contour insert installed.



Figure 5. Nozzle frame with top and bottom contour inserts, shown after installation.

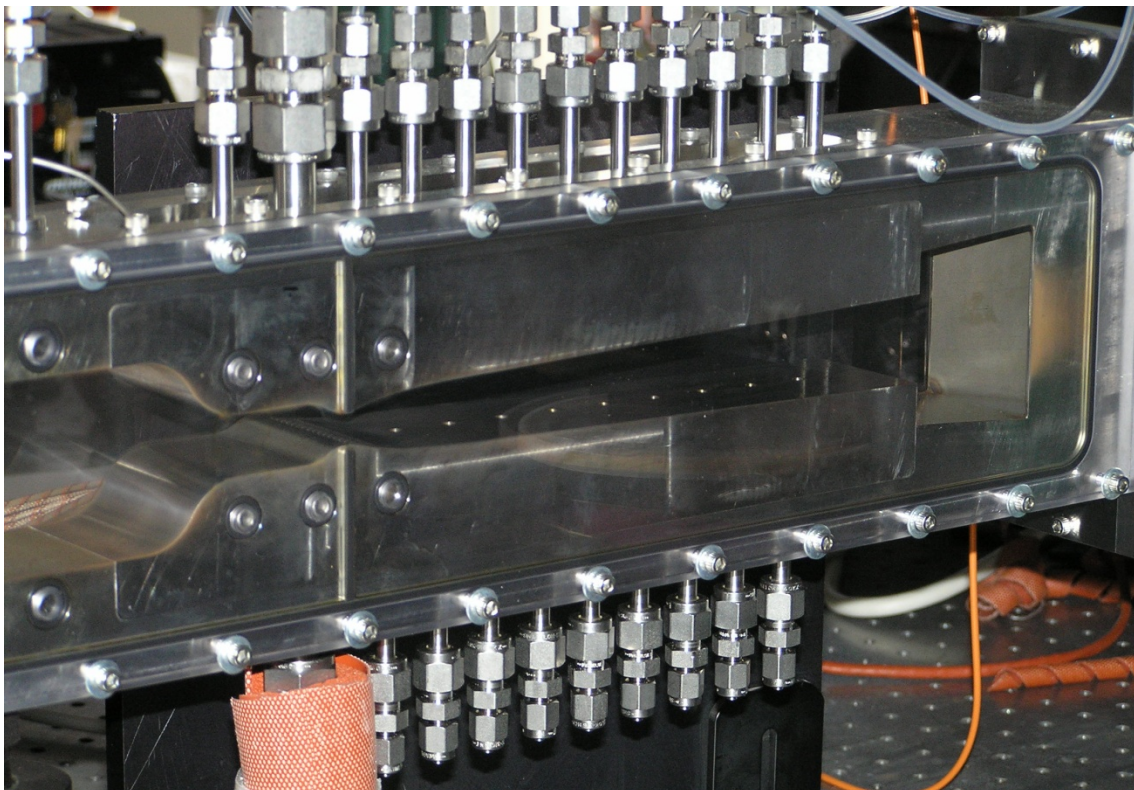


Figure 6. Nozzle installed on test stand. The polycarbonate side plates are visible along with the pressure taps on the top and bottom of the nozzle.

3.3.1 Pressure and Mach Number Measurements

To verify the nozzle design, pressure measurements were made without iodine injection. One of the smooth polycarbonate walls was replaced with a polycarbonate wall that had fittings at 2.5-cm increments. A Pitot tube was inserted in these fittings. Because the flow is supersonic, the stagnation pressures upstream and downstream of the shock wave formed by the Pitot tube were used to calculate the Mach number in the flow. The isentropic relationship for pressure and Mach number and the relationship for Mach numbers up- and downstream of a normal shock were used to determine the Mach number from the ratio of stagnation pressures. From Lifshitz and Landau, the relationship between the Mach number upstream of the normal shock wave, M_1 , and the ratio of stagnation pressures, where P_{01} is the stagnation pressure upstream of the normal shock and P_{02} is the stagnation pressure downstream of the normal shock, is⁴⁰

$$\frac{P_{02}}{P_{01}} = \left[\left(\frac{\gamma+1}{2} M_1^2 \right) / \left(1 + \frac{\gamma-1}{2} M_1^2 \right) \right]^{\gamma/(\gamma-1)} \left(\frac{2\gamma}{\gamma+1} M_1^2 - \frac{\gamma-1}{\gamma+1} \right)^{1/(\gamma-1)} \quad (3)$$

The stagnation pressure upstream of the normal shock was measured in the plenum of the nozzle, whereas the stagnation pressure downstream of the normal shock wave was measured by the Pitot tube. The Pitot tube was placed along the centerline of the nozzle. The ratio of specific heats, γ , is assumed constant (1.587) in this calculation. The Mach number distribution, as determined from the measured stagnation pressures, is displayed in Figure 7. At the NEP, the Mach number is close to the design number of 2.2. Along with the experimental results, Figure 7 displays the Mach number from a three dimensional computational fluid dynamics (CFD) calculation for this nozzle, which agrees with the measured values.⁴¹

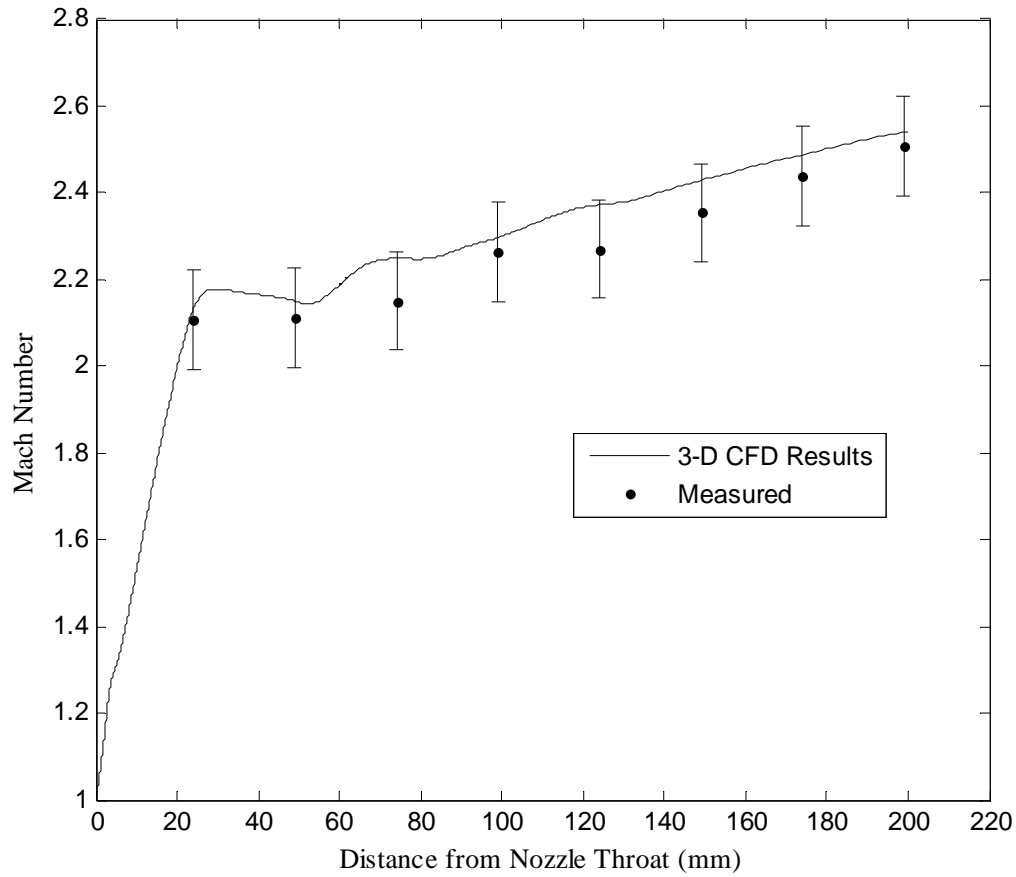


Figure 7. Mach number, measured and calculated with 3-D CFD.

Static pressure measurements were made along the top and bottom walls of the nozzle. As can be seen in Figure 6, there are pressure taps along the top and bottom contours. The taps are staggered from top to bottom and are 2 cm apart, allowing static pressure measurements to be made in 1-cm increments. The measured static pressures, along with 3-D CFD results and the isentropic prediction are shown in Figure 8.⁴¹ The 3-D CFD calculation matches well with the measured results.

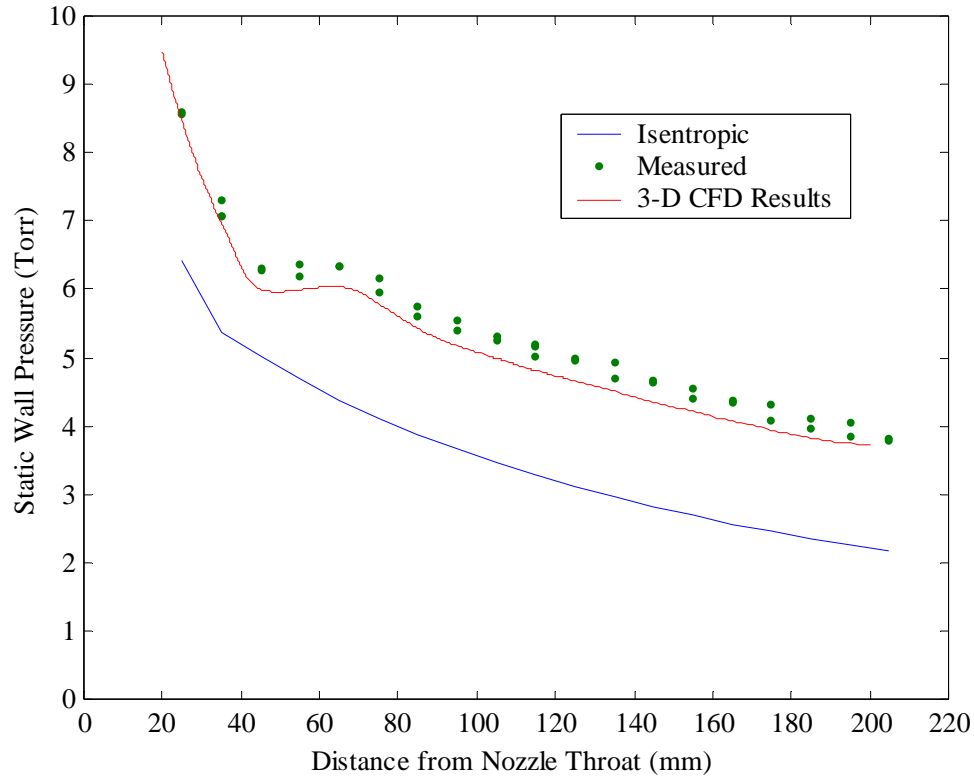


Figure 8. Wall static pressures, as measured, calculated with 3-D CFD, and calculated using isentropic relationships.

3.3.2 Injector Design

The contour inserts were designed so that injectors were machined after the inserts were manufactured. The first injection scenario is a single injector positioned on the centerline of the bottom contour, 0.25 cm from the nozzle throat. It is angled 45° to the primary flow. The throat of the injector is 0.51 mm in diameter, while the minor axis of the jet exit (which is elliptical because of the wall curvature) is 1.0 mm. The area ratio of the injector gives a jet exit Mach number of 3.4. The 45° angle and the high Mach number of 3.4 are designed to provide substantial jet penetration into the supersonic crossflow. Though these may not be the optimum parameters, this is the design to be studied here. Figure 9 is a schematic of the injector.

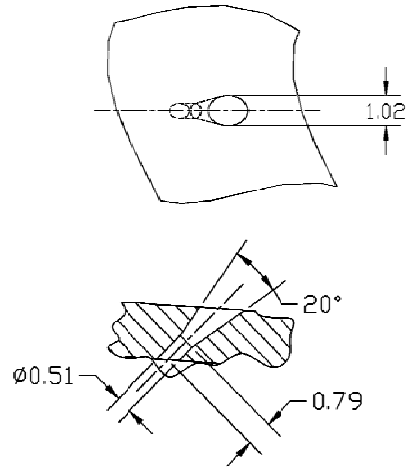


Figure 9. Schematic of a single injector, units are given in millimeters.

4.0 PLIF DIAGNOSTICS

4.1 Introduction

The PLIF system consists of a Neodymium:Yttrium-Aluminum-Garnet (Nd:YAG) laser, tunable dye laser, laser-sheet-forming optics, and an intensified charge-coupled device (ICCD) camera. This chapter will present the laser specifications and the optical setup in detail.

4.2 Lasers

For this experiment, a Nd:YAG laser is used to pump a tunable dye laser. The Nd:YAG laser is operated at the second harmonic (532 nm), with 400 mJ/pulse. It has a 10-Hertz pulse rate and an 8- to 10-ns pulse width. Rhodamine 6G is used in the dye laser, giving a laser wavelength range of 559 to 576 nm. The pulse width is 10 ns and the pulse energy is about 100 mJ.

Temperature variation in the nozzle can affect the iodine spectral lines that are being pumped and the iodine fluorescence lifetime, both of which can impact the fluorescence intensity. Fluorescence intensity, for the purposes of this study, is directly related to the concentration of the injected flow. Because the temperature variation in nozzle is considerable, by as much as 300 K from the nozzle throat to the exit, it is essential to determine the wavelength and bandwidth at which the laser is operated and the fluorescence lifetime throughout the nozzle. To verify the laser wavelength and bandwidth, the laser was calibrated with a Hollow Cathode Discharge Lamp (HCL), as discussed in Section 4.2.1. Section 4.2.2 discusses the method to measure the iodine fluorescence lifetime and maps the fluorescence lifetime throughout the

nozzle. During the PLIF experiments, the dye laser was operated at 565.095 nm with a bandwidth of 0.024 nm. At this wavelength and bandwidth, eight iodine spectral lines were pumped. Two primary spectral lines are being pumped throughout the temperature range. Because the same lines are being pumped throughout the jet of the nozzle, intensity adjustments are not required to accurately compare PLIF images. The fluorescence lifetime has the largest variance at the exit of the jet, where the temperature gradient is the greatest. This large variance in lifetime must be considered when analyzing the PLIF images.

4.2.1 Dye Laser Calibration

The optogalvanic effect was exploited using an HCL to determine the bandwidth and approximate wavelength correction of the dye laser. Optogalvanic wavelength calibration with an HCL is discussed by Zhu et al.⁴² The optogalvanic effect is the impedance change of a discharge tube when illuminated by a second discharge tube or tunable dye laser. The voltage across the discharge tube is measured while the dye laser is tuned to the wavelength of transition of a species present in the discharge of the lamp. In this experiment, a neon/gold lamp is used as the HCL. Unfortunately, neon does not have a strong transition near the peak dye laser wavelength of 565 nm. However, neon does have a strong transition with an excitation wavelength of 588.1895 nm, which is still achievable with the Rhodamine 6G dye. The laser bandwidth and an approximate wavelength correction will be determined at this wavelength. To determine the dye laser wavelength correction at the laser reading of 564.7077 nm (as used in the experiments), iodine fluorescence response, as measured with a photodiode, is plotted versus laser reading wavelength. This plot is compared to and adjusted to match the iodine spectrum.

A schematic of the lamp setup is shown in Figure 10. The lamp is powered by a low-amperage, high-voltage power supply. About 350 volts and 1 mA were needed to start the lamp, though only 170 volts were needed to operate the lamp after startup.

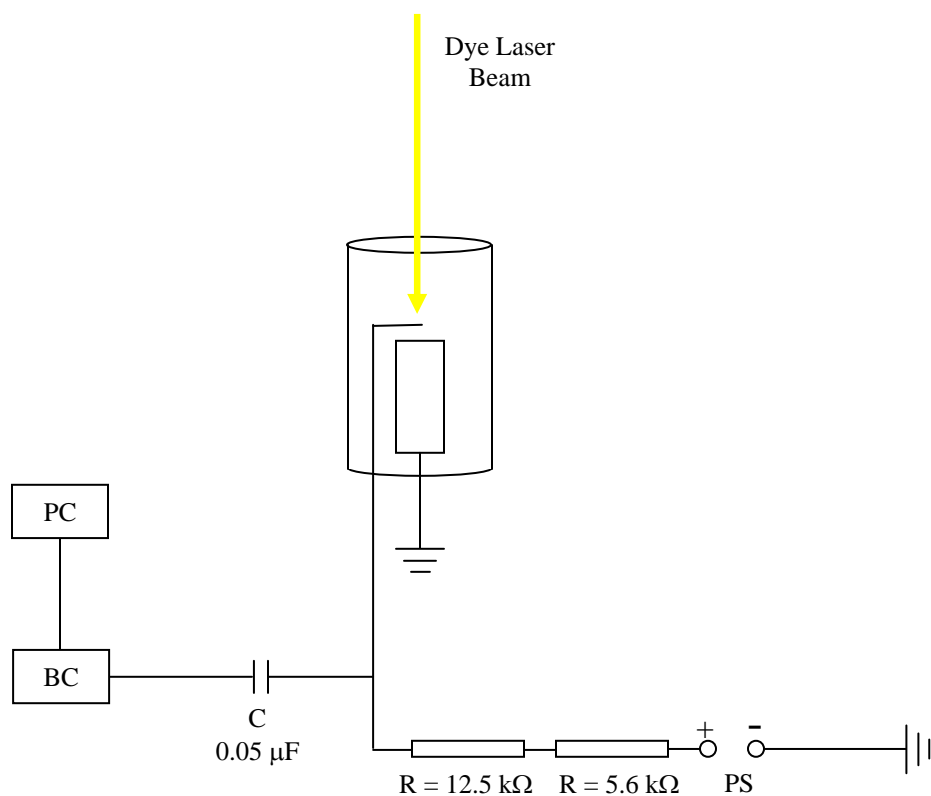


Figure 10. A schematic of the hollow cathode lamp (HCL) setup. PS is the power supply, R is a resistor, C is the capacitor, BC is the box controller, and PC is the computer.

To capture the 588.1895 nm transition, the dye laser was set up to step over a wavelength range that would include the transition. This first pass was crude and was used to find a range of wavelengths that included the 588.1895 nm transition. The lamp had an increase in voltage between the dye laser settings of 587.9 nm and 588.05 nm. The dye laser was then setup to scan from 587.9000 nm to 588.0500 nm in 0.0001-nm increments. A computer recorded the wavelength and the lamp voltage at each increment. The lamp voltage versus wavelength is plotted in Figure 11. The lamp voltage peaked when the dye

laser was tuned to 587.9631 nm, rather than the published 588.1895-nm peak for neon. The dye laser wavelength, therefore, is incorrect by 0.2264 nm at 588.1895 nm. The correction for the laser is not linear, so this is only an estimate for the calibration at the operating laser wavelength during testing (where the laser is set at 564.7077 nm). From Fig. 3.2, the bandwidth is noted by the full-width, half-maximum (FWHM) of the lamp voltage response. The bandwidth is 0.024 nm, compared to the specified bandwidth of 0.002 nm at 570 nm.⁴³ This is a large enough bandwidth to excite multiple iodine transitions.

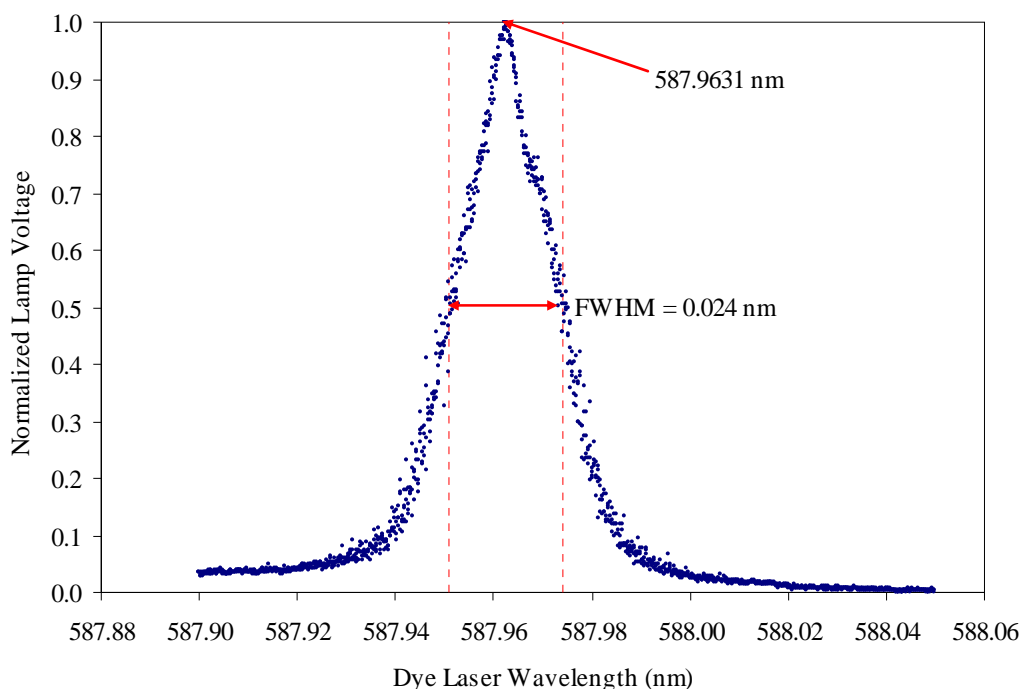


Figure 11. Normalized neon lamp voltage versus dye laser wavelength.

The dye laser wavelength must be calibrated over the wavelength used during the PLIF tests. Because the lamp does not have strong transitions over the operating wavelength of the laser, a glass cell with iodine crystals (under vacuum) was set up to monitor iodine excitation. The dye laser passed through the cell, while a photodiode (with a band pass filter fitted to only pass the iodine fluorescence) monitored the iodine fluorescence. The dye laser wavelength was scanned in 0.0002-nm increments over a large wavelength range. The

normalized photodiode response versus dye laser wavelength (after a 0.387 nm correction) is plotted in Figure 12. The dye laser needed to be adjusted by 0.387 nm to match the iodine spectrum. Therefore, the wavelength of 564.7077 nm used during the PLIF tests is actually 565.0947 nm.

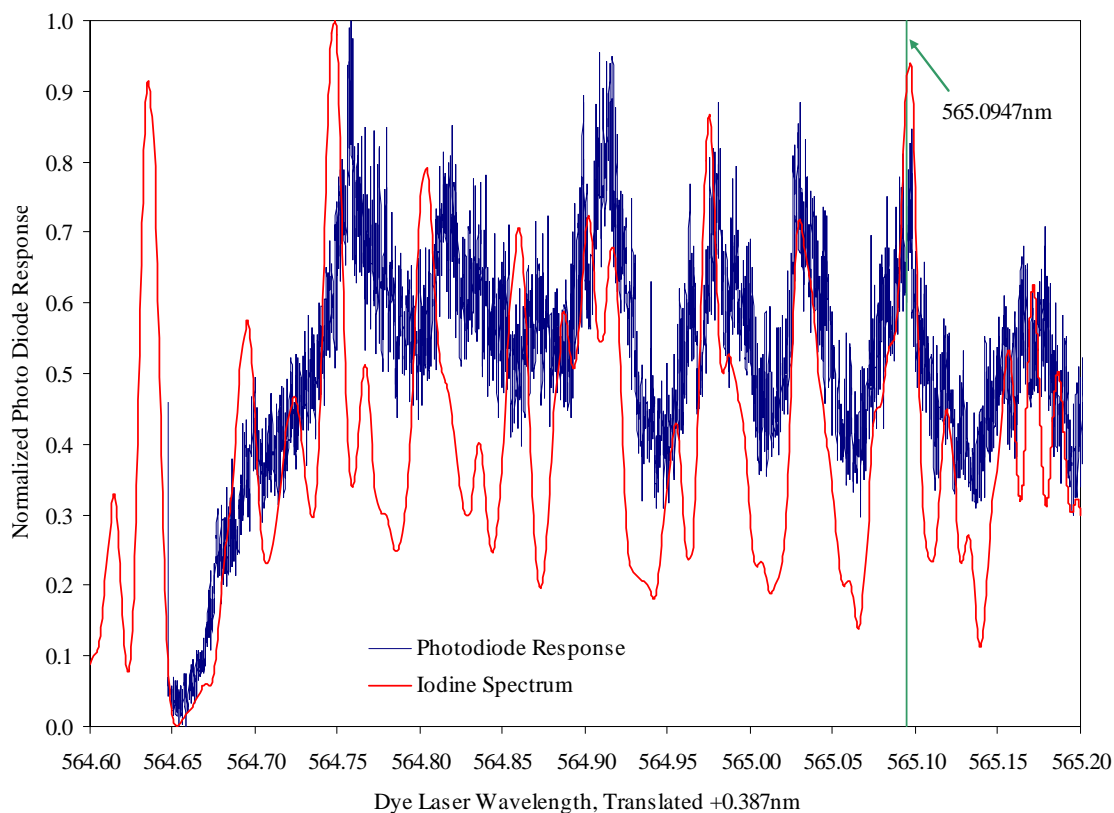


Figure 12. Normalized photodiode response versus an adjusted dye laser wavelength. The normalized iodine spectrum is also plotted for comparison.

To identify which iodine lines are being excited, the photodiode response and iodine spectrum are plotted for a smaller wavelength range centered on 565.095 nm. Figure 13 shows the photodiode response, the iodine spectrum, and the peaks of the individual iodine spectral lines. The bandwidth is noted so that the spectral lines that are excited are evident. Within the bandwidth, there are eight strong spectral lines. These spectral lines are defined in Table 1. The ground and excited states for vibration and rotation are given, where v'' is the ground-state (X electronic state) vibration level and v' is the excited-state (B electronic state)

vibration level. Likewise, J'' is the ground-state rotational level and J' is the excited state rotational level.

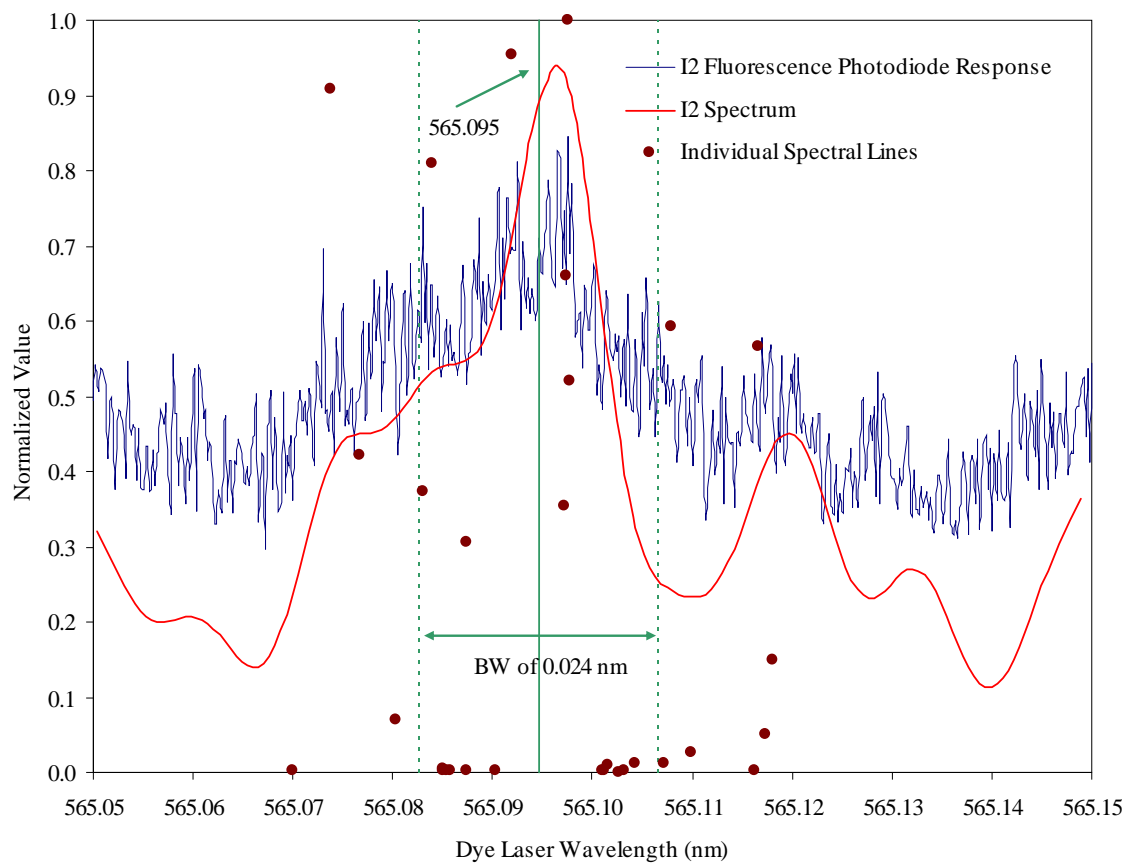


Figure 13. Photodiode response, iodine spectrum, and individual spectral lines versus wavelength. The dye laser bandwidth and operating wavelength are shown.

Table 1. Wavelength, relative absorption values, and vibration and rotational transitions for the spectral lines included in the bandwidth centered around 565.095 nm.⁴⁴

λ (nm)	Normalized Absorption	X State		B State	
		v''	J''	v'	J'
565.0830	0.07	1	115	22	116
565.0840	0.81	0	29	18	28
565.0873	0.31	0	129	20	130
565.0918	0.96	1	79	21	80
565.0971	0.35	0	125	20	124
565.0974	0.66	0	34	18	35
565.0975	1.00	1	75	21	74
565.0977	0.52	0	96	19	97

The injected flow temperature ranges from 100 K to 400 K. The population of the molecules in a particular ground state change with temperature. The ground state population, N , is⁴⁵

$$N \propto (2J + 1)e^{-(G+F)/kT} \quad (4)$$

The population is dependent on the degeneracy of the rotational level, $(2J + 1)$, the energy of the v vibration level, G , and the energy of the J rotational level, F . For a vibrating rotator, the rovibrational energy is⁴⁵

$$G(v) + F_v(J) = \omega_e \left(v + \frac{1}{2} \right) - \omega_e x_e \left(v + \frac{1}{2} \right)^2 + B_v J(J + 1) - D_v J^2(J + 1)^2 + HOT \quad (5)$$

In this equation, ω_e is the equilibrium vibration frequency, $\omega_e x_e$ is an anharmonicity constant, B_v is the rotational constant, D_v is the centrifugal distortion constant, and HOT are higher-order terms. The rotational and centrifugal distortion constants are determined by⁴⁵

$$B_v = B_e - \alpha_e \left(v + \frac{1}{2} \right) + HOT \quad (6)$$

$$D_v = D_e - \beta_e \left(v + \frac{1}{2} \right) + HOT \quad (7)$$

$$D_e = \frac{4B_e^3}{\omega_e^2} \quad (8)$$

$$\beta_e = D_e \left(\frac{8\omega_e x_e}{\omega_e} - \frac{5\alpha_e}{B_e} - \frac{\alpha_e^2 \omega_e}{24B_e^3} \right) \quad (9)$$

The constants ω_e , $\omega_e x_e$, B_e , and α_e are tabulated in Herzberg for the iodine molecule in ground state as 214.57 cm^{-1} , 0.6127 cm^{-1} , 0.03735 cm^{-1} , and 0.000117 cm^{-1} , respectively.⁴⁵

With the vibration and rotational levels known, the population as a function of temperature can be plotted. Figure 14 shows the populations for the ground-state levels that are pumped within the bandwidth of the dye laser. Though the population units are arbitrary, the plot illustrates the population trend with increasing temperature. It is evident that the $v'' = 0$, $J'' = 29$ and $v'' = 0$, $J'' = 34$ are the strongest transition lines being pumped by the dye laser within the entire temperature range of the jet. Figure 15 displays the population fraction as a function of the ground-state rotational level, for $v''=0$ and varying temperatures. For the dominant transition lines pumped by the laser ($J'' = 29$ and 34), the population fraction can change by as much as 0.01 from 100K to 500K, which would not drastically alter the iodine fluorescence intensity. From the Boltzmann distributions, the iodine fluorescence wavelength is consistent throughout the jet of the nozzle and intensity adjustments are not required to accurately compare PLIF images.

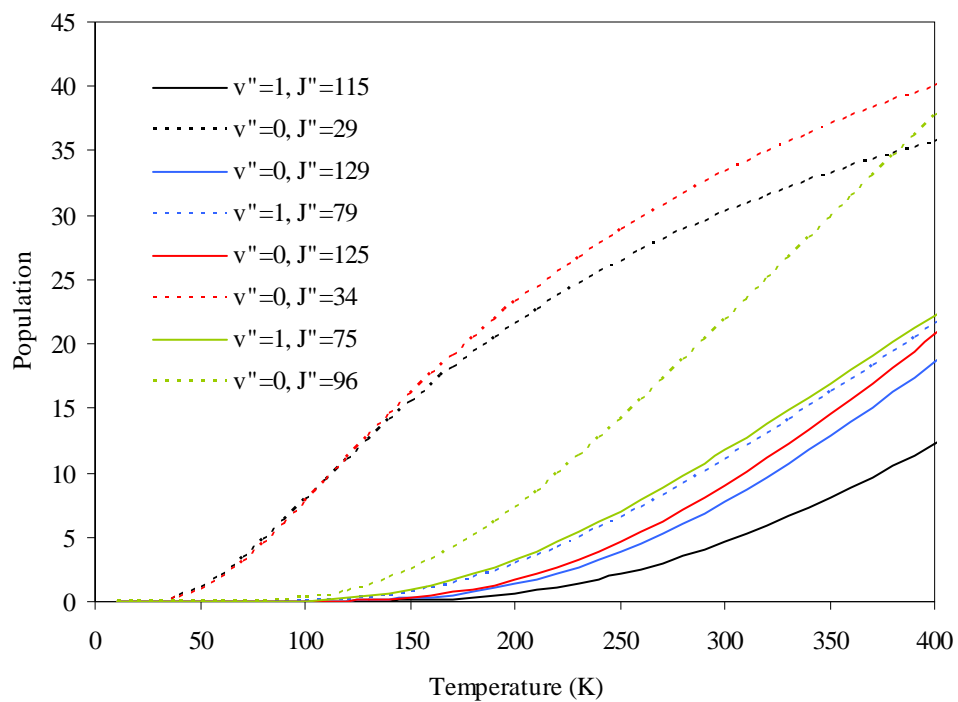


Figure 14. Boltzmann distribution for the ground-state vibration and rotational levels that are excited in the bandwidth of the dye laser at 565.095nm.

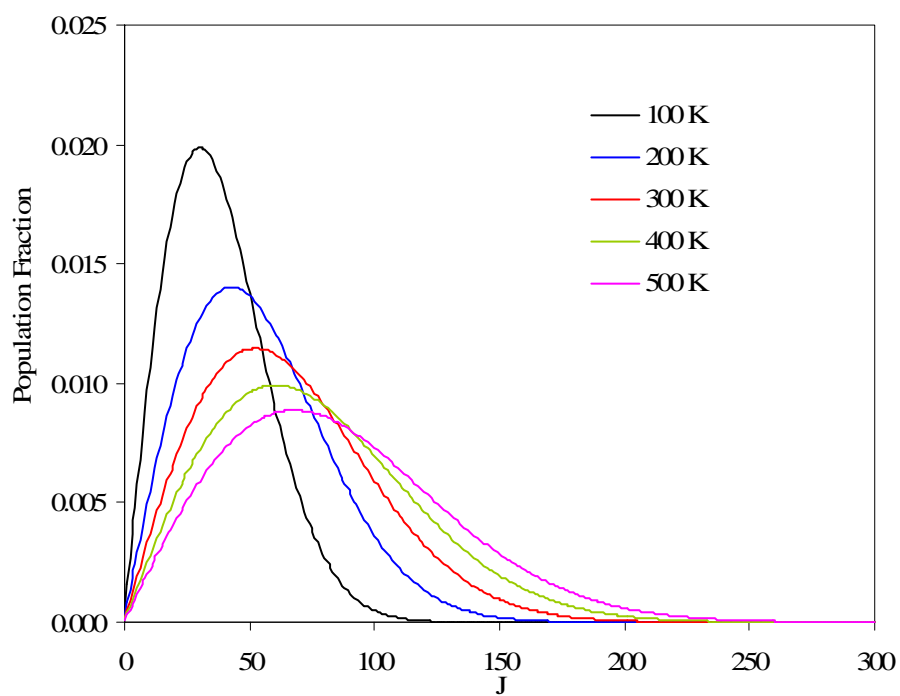


Figure 15. Boltzmann distribution with constant temperature and $v''=0$.

4.2.2 Iodine Fluorescence Lifetime

Another factor that influences the collected fluorescence intensity is the iodine fluorescence lifetime. Iodine fluorescence lifetime is most affected by the temperature and pressure in the nozzle, both of which influence the number of molecular collisions. The temperature in the jet of the nozzle decreases by as much as 300 K from the jet exit to the nozzle exit, whereas the pressure decreases by as much as 3500 Pa (see Fig. C.5). Capelle and Broida published fluorescence lifetimes and quenching cross sections of an excited state of the iodine molecule.⁴⁶ They produced the following relationship between the observed fluorescence lifetime τ_{obs} and pressure and temperature:

$$\frac{1}{\tau_{obs}} = \frac{1}{\tau_o} + \sigma_s \left(\frac{16\pi}{m_{I_2} kT} \right)^{1/2} P_{I_2} + \sigma_{He} \left(\frac{8\pi}{\mu_{He} kT} \right)^{1/2} P_{He} + \sigma_{O_2} \left(\frac{8\pi}{\mu_{O_2} kT} \right)^{1/2} P_{O_2} \quad (10)$$

where τ_o is the natural lifetime of molecular iodine. The collisional cross sections for self- and foreign gas quenching (helium and oxygen) are represented by σ_s , σ_{He} , and σ_{O_2} , respectively. The iodine, helium, and oxygen pressures are P_{I_2} , P_{He} , and P_{O_2} , respectively. m_{I_2} is the mass of an iodine molecule, μ is the reduced mass for an I_2 foreign gas molecular collision (μ_{He} and μ_{O_2} for helium and oxygen, respectively), and k is the Boltzmann constant. To isolate the effects that temperature and pressure have on the fluorescence lifetime, it is useful to use the ideal gas law, $P = \rho RT$. Replacing temperature with $P/\rho R$ and assuming the density is constant gives a $P^{1/2}$ relationship to $1/\tau_{obs}$, which indicates that a decrease in pressure increases the fluorescence lifetime. Replacing pressure with ρRT gives a $T^{1/2}$ relationship to $1/\tau_{obs}$, which indicates that a decrease in temperature would increase the

iodine fluorescence lifetime. With the dramatic decreases in pressure and temperature from the jet exit to the nozzle exit, the fluorescence lifetime is expected to increase.

PLIF imaging was used to determine the iodine fluorescence lifetime in different sections of the nozzle. The ICCD camera has the capability of capturing a series of images with increasing delay from an external trigger. Gaseous iodine was seeded in the primary flow of the nozzle, with the primary gas flow rates matching normal test conditions. The nozzle contour inserts were blank so that there were no injectors present in this study.

The camera was aimed perpendicular to the flow direction, capturing streamwise images of the flow with a 2-ns gate. The camera collected images at the same rate as the lasers (10 Hz) and was triggered by the Nd:YAG laser. The camera delay was set such that the first image was captured before the laser pulse. Each progressive image was delayed by 1 ns, such that the final image had a total delay of at least 100 ns (depending on the fluorescence lifetime at that location). The images captured the excitation laser, the most intense iodine fluorescence, the progressive decrease in fluorescence intensity, and zero intensity (after the lifetime of the iodine fluorescence). Figure 16 presents the normalized intensity versus time for a single image pixel. The pixel location is 0.48 cm downstream of the nozzle throat and at the nozzle half-height. The fluorescence lifetime is the time between the peak intensity and $1/e$ fraction of the peak intensity. At this location, the fluorescence lifetime is approximately 50 ns.

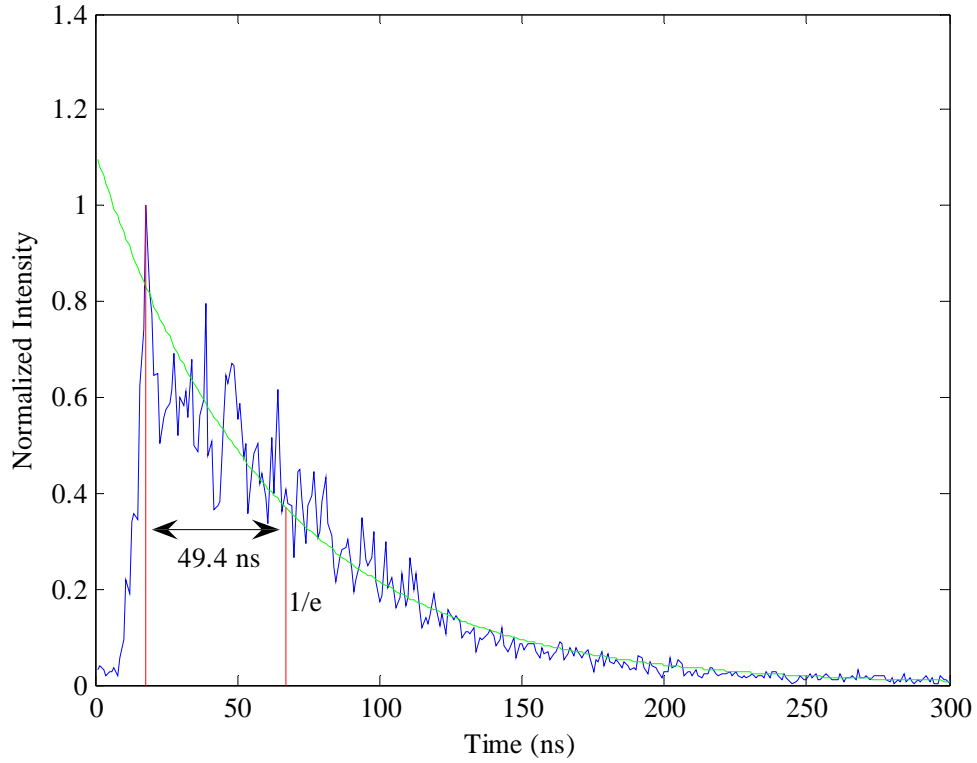


Figure 16. Intensity versus time for a single image pixel, located 0.48 cm downstream of the nozzle throat, at the nozzle half-height. The blue line is the normalized intensity while the green line is an exponential fit to the data. The lifetime is measured from the peak intensity to $1/e$ of the peak intensity.

Figure 17 presents the normalized intensity versus time for an image pixel located 5.86 cm downstream of the throat (at the nozzle half-height). The fluorescence lifetime at this location is about 120 ns. This is a much greater lifetime than at 0.48 cm downstream of the nozzle throat. To map fluorescence lifetimes versus downstream distance from the throat of the nozzle, the pixel lifetimes were averaged over the center of the nozzle (30 pixels along the centerline for the 512 pixels in image width) for each image. The average fluorescence lifetime for each image is displayed in Figure 18. The fluorescence lifetime increases from about 55 ns to 140 ns, which is significant.

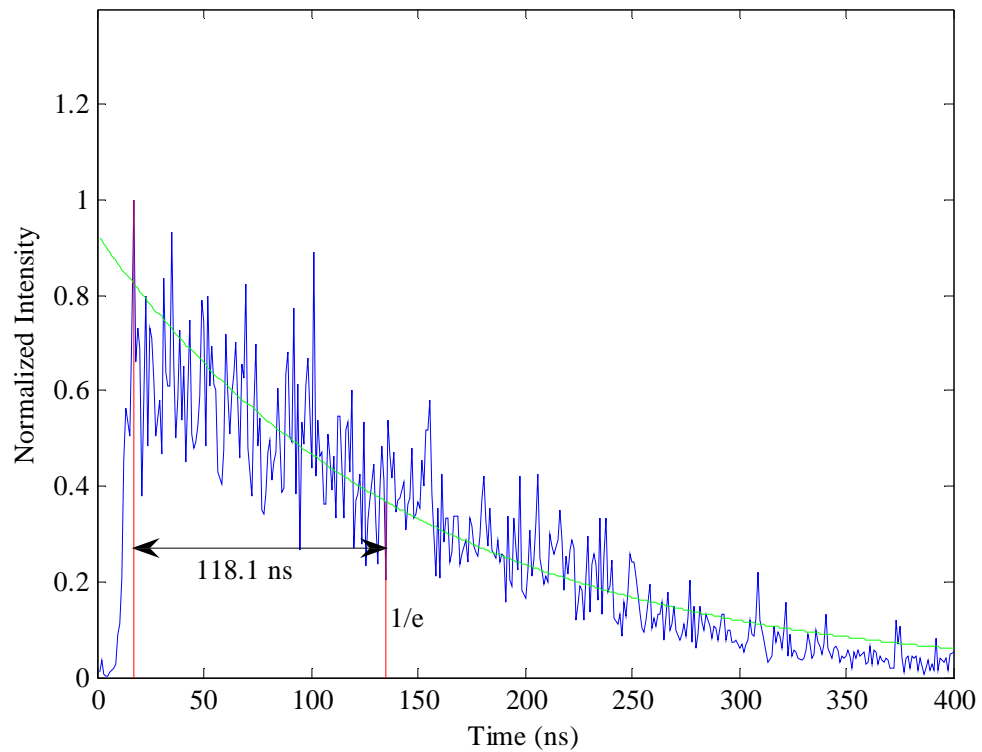


Figure 17. Intensity versus time for a single image pixel, located 5.86 cm downstream of the nozzle throat, at the nozzle half-height. The blue line is the normalized intensity while the green line is an exponential fit to the data. The lifetime is measured from the peak intensity to $1/e$ of the peak intensity.

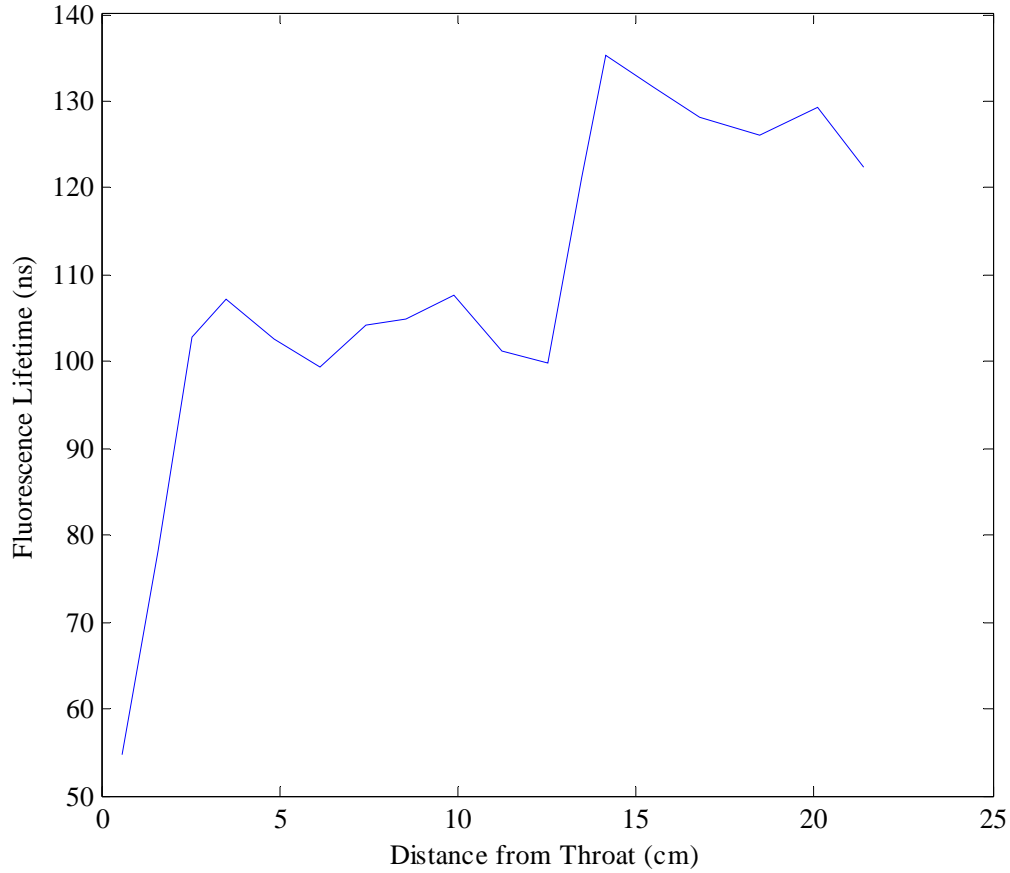


Figure 18. Two-point moving average of the iodine fluorescence lifetime versus downstream distance from throat. The lifetime is the average for an image field of view along the centerline, where the distance from the nozzle throat is measured at the image center.

To assess the collected intensity of an image, the area under the exponential curve for a 20-ns gate, 10 ns after the peak intensity, can be calculated. Using intensities that have not been normalized by the maximum image intensity, the areas are 33,285 ns·count for the 0.48-cm location and 67,257 ns·count at the 5.86-cm location. From the normalized images, where 2775 counts is the maximum intensity for the 0.48-cm location and 4668 counts for the 5.86-cm location, the areas are 12 ns·normalized counts and 14.4 ns·normalized counts, respectively. Figure 19 displays the integrated normalized lifetime versus distance from the nozzle throat. Each data point is averaged along the centerline of each image, as was done in Figure 18. However, an error bar is shown to depict plus/minus one standard deviation from

the image mean. From this plot, there is not a strong correlation between the integrated normalized lifetime and downstream distance from the nozzle throat.

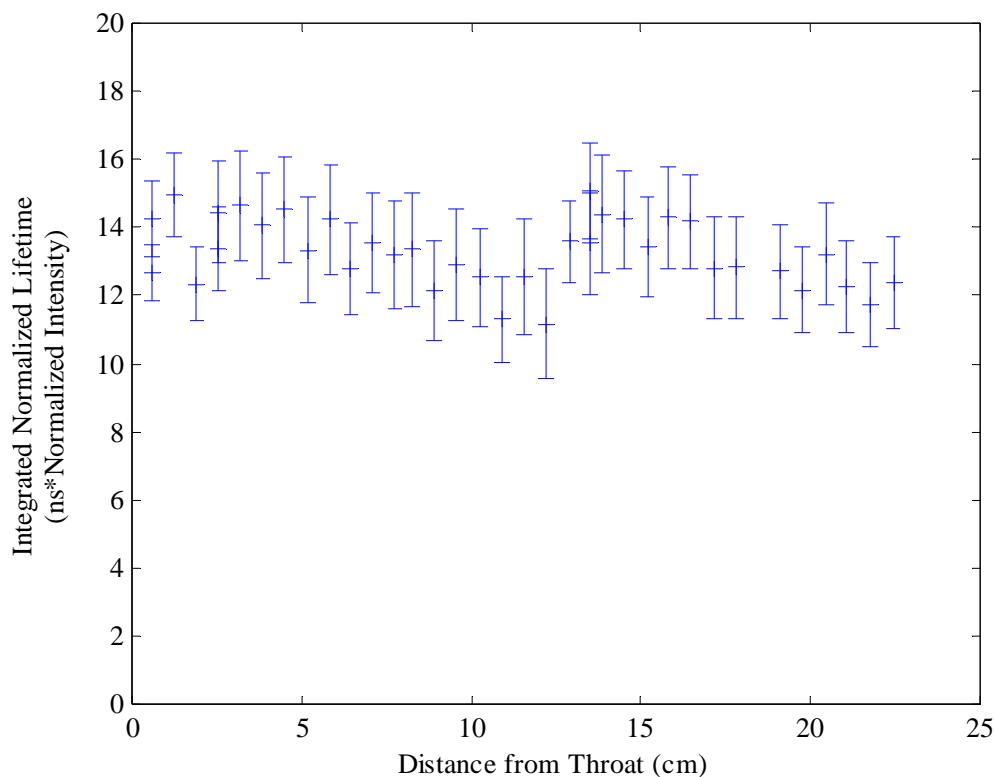


Figure 19. Averaged integrated normalized fluorescence lifetime versus downstream distance from the throat. The error bars are plus/minus one standard deviation of the integrated normalized lifetime for each image.

In collecting the lifetime images, there were fluctuations in the molar flow rate of the iodine in the flow. This fluctuation could affect the lifetime data, so the integrated normalized lifetime was plotted versus the average iodine molar flow rate, shown in Figure 20. There is not a strong correlation between the integrated normalized lifetime and iodine molar flow rate.

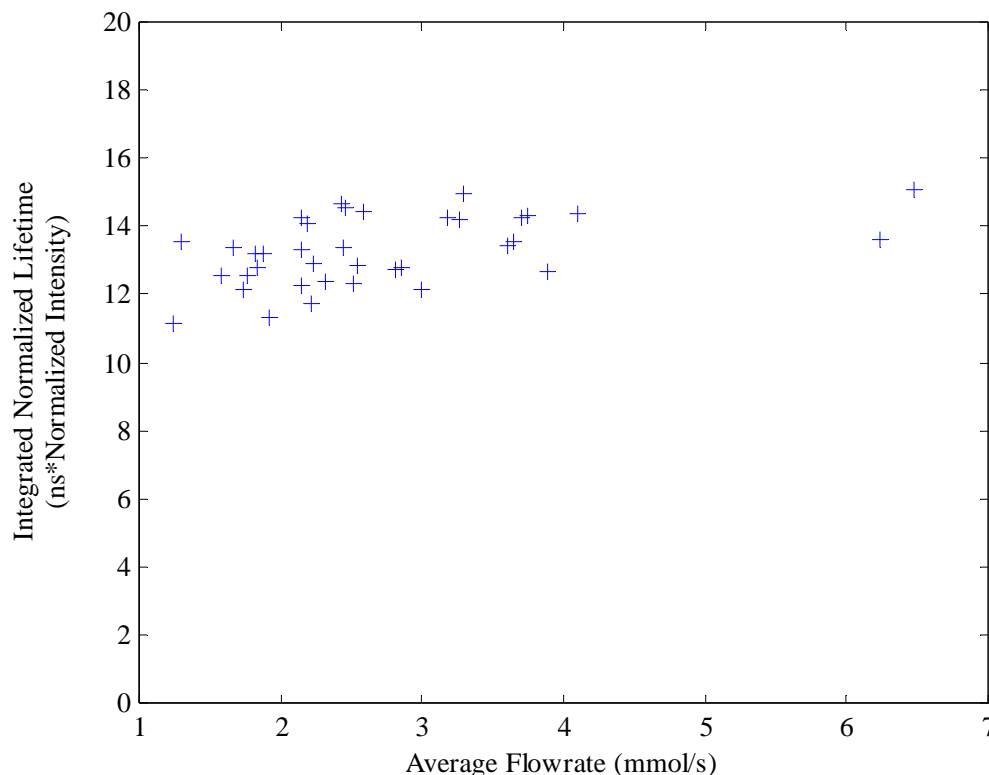


Figure 20. Averaged integrated normalized fluorescence lifetime versus iodine molar flow rate.

The lifetime data presented thus far is with the iodine seeded in the primary flow of the nozzle. The iodine that is present in the jet flow is injected at a higher temperature of 430 K and static pressure of about 1600 Pa. The jet flow also has a greater concentration of iodine, which could result in greater self-quenching. To accurately represent the fluorescence lifetime in the jet, lifetime measurements were made with a single injector and iodine seeded only in the injector. A contour plot of fluorescence lifetime for four different downstream locations is shown in Figure 21.

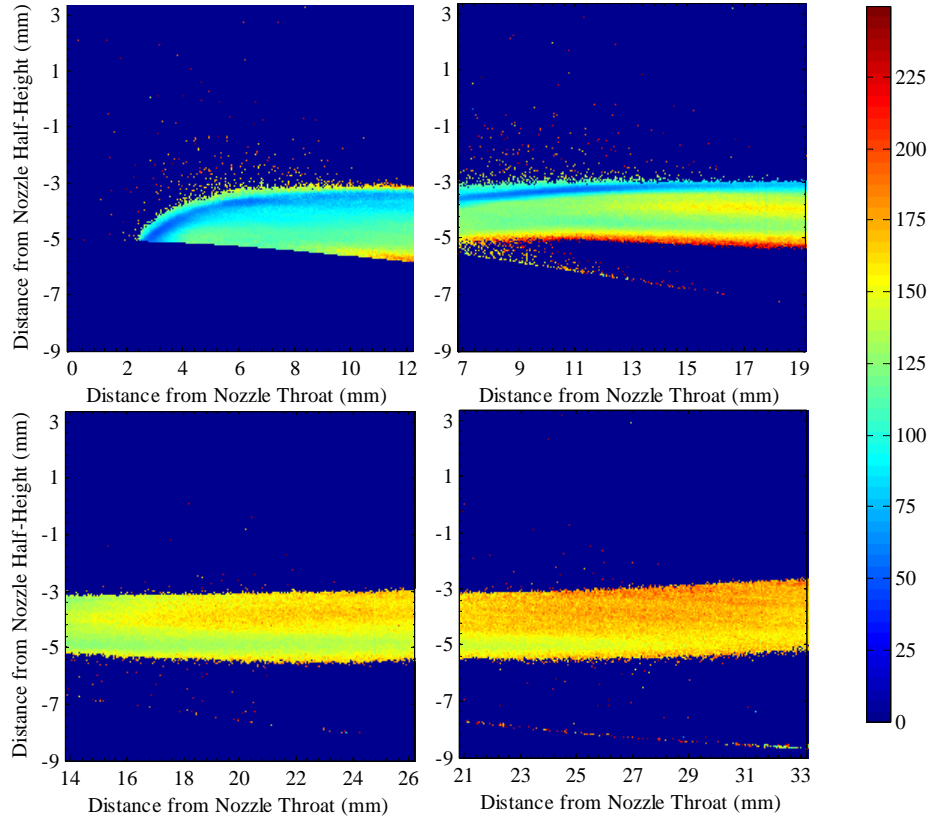


Figure 21. Contour plots of the fluorescence lifetimes (color bar units are nanoseconds) at four overlapping locations in the nozzle. Spatial dimension units in plots are in mm, x -location is measured from the nozzle throat, and y -location is measured from the nozzle half-height.

Fluorescence lifetime was obtained over the entire length of the nozzle. Close to the injector, the location and height of the jet do not fluctuate during data collection, but these begin to fluctuate with increasing downstream distance due to inherent unsteadiness of the jet flow. Because of this variance in location and height, the fluorescence lifetime data is distorted. Figure 21 gives a good representation of the fluorescence lifetime range in the injected flow. The largest lifetime gradient is seen at the exit of the injector, where the lifetime ranges from 50 to 170 ns. This variation is most likely from the large temperature variation at the jet exit. A 3-D computational fluid dynamic (CFD) simulation of this nozzle has been done by Madden et al., where the temperature variation is plotted within this single jet (shown in Figure 22).⁴⁷ The temperature is the lowest in the core of the jet but increases

toward the outer edges. As the jet issues downstream, the temperature remains relatively constant, where the fluorescence lifetime remains within the range of 150 to 170 ns.

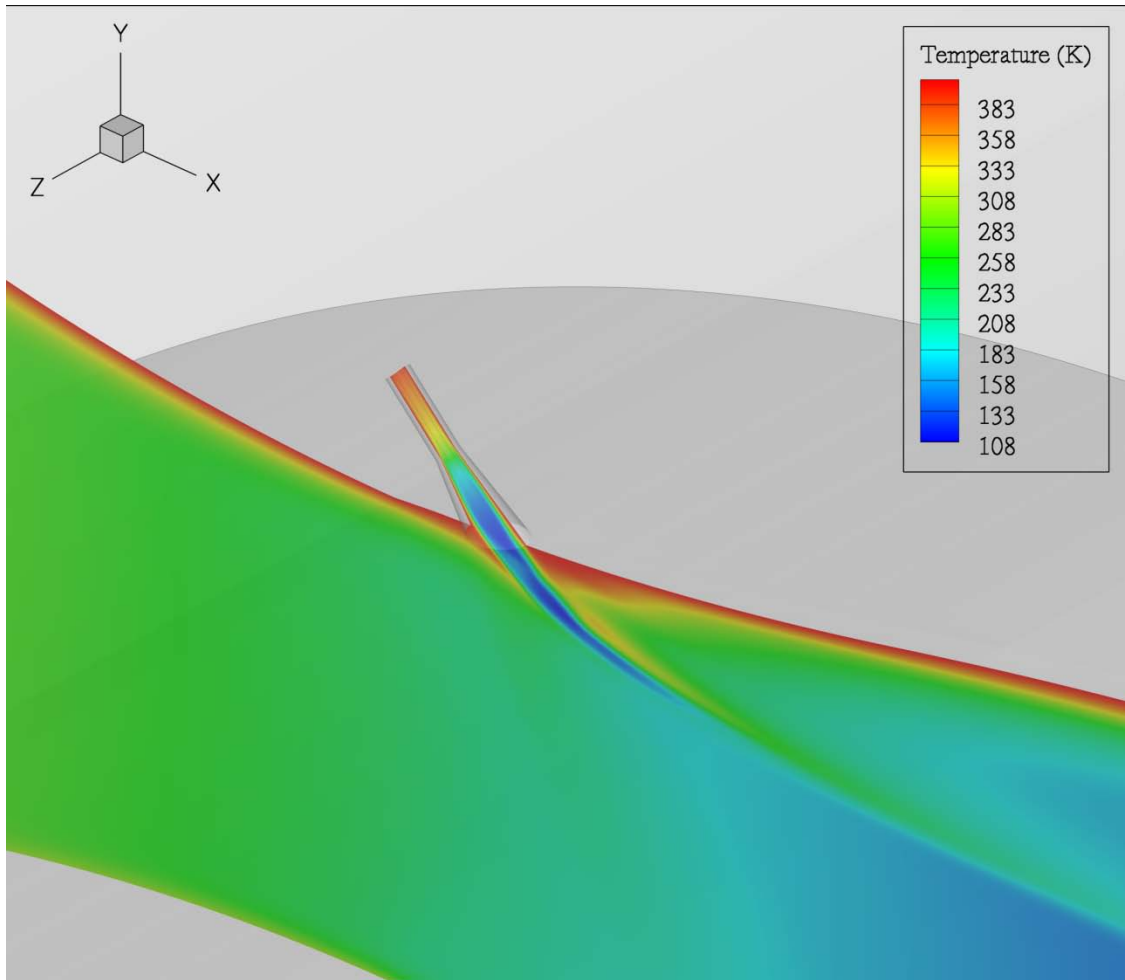


Figure 22. 3-D Navier-Stokes simulation results for temperature contours within a 2-D planar slice through the center of the jet.⁴⁷

As with the fluorescence lifetime calculations for the primary flow seeded with iodine, plotting the integrated normalized lifetime will give a better picture of what the ICCD camera actually sees. Figure 23 presents the integrated normalized lifetimes at the same four downstream locations as Figure 21. The integrated normalized lifetime is relatively constant in the core of the jet, but is significantly less at the outer edges of the jet near the orifice. This variance in the integrated normalized lifetime is most likely caused by the increased

temperatures (and decreased fluorescence lifetimes) at those edges. This variation at the jet exit should be considered when analyzing the PLIF images.

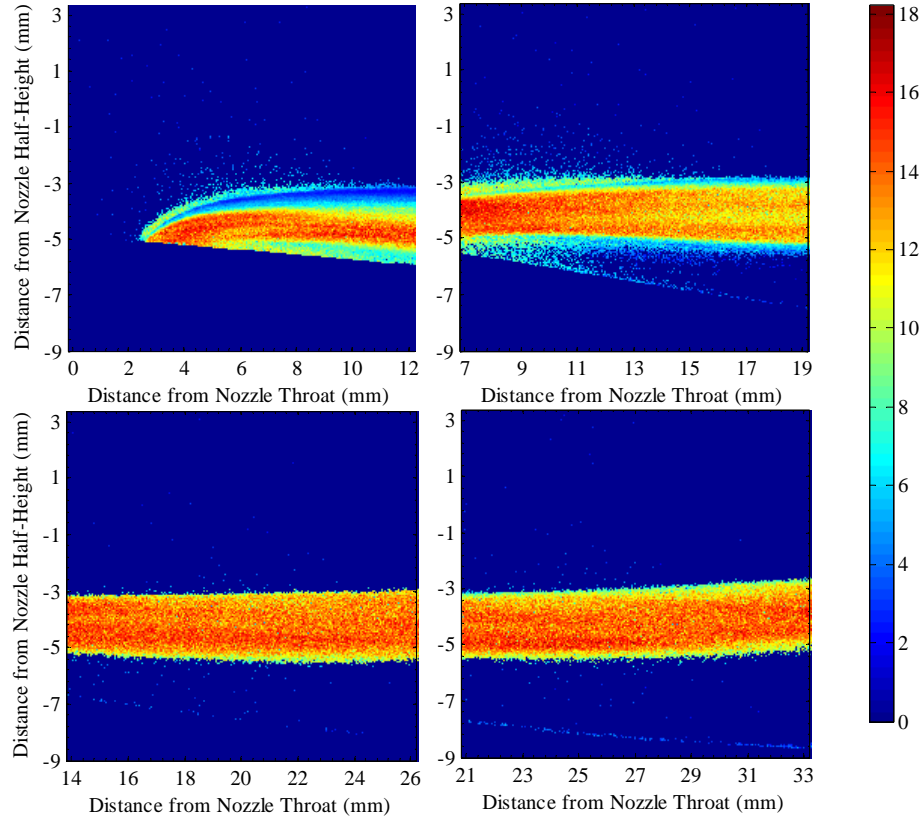


Figure 23. Contour plots of the integrated normalized lifetimes (color bar units are nanoseconds*normalized lifetime) at four overlapping locations in the nozzle. Spatial dimension units in plots are in mm, x -location is measured from the nozzle throat, and y -location is measured from the nozzle half-height.

4.3 Optics

The beam of the Nd:YAG laser is aimed directly into the dye laser. The beam from the dye laser is turned, using a BK7 prism, into a series of three lenses to collimate and expand the beam into a rectangular sheet with minimal thickness ($\sim 600 \mu\text{m}$). A schematic of the laser and optics setup is shown in Figure 24, where the lasers and camera are positioned to acquire oblique images in the flow. Spherical lenses are used to collimate the beam; each has a focal length of 8 cm. The collimated beam then passes through a cylindrical lens, with a focal length of 14 cm, to

form a laser sheet with minimal thickness and a height of ~ 4 cm. Two mirrors are used to direct the beam into the nozzle at a 45-degree angle. Before the laser sheet enters the nozzle, it passes through another cylindrical lens, with a focal length of 30 cm, to further decrease the sheet thickness.

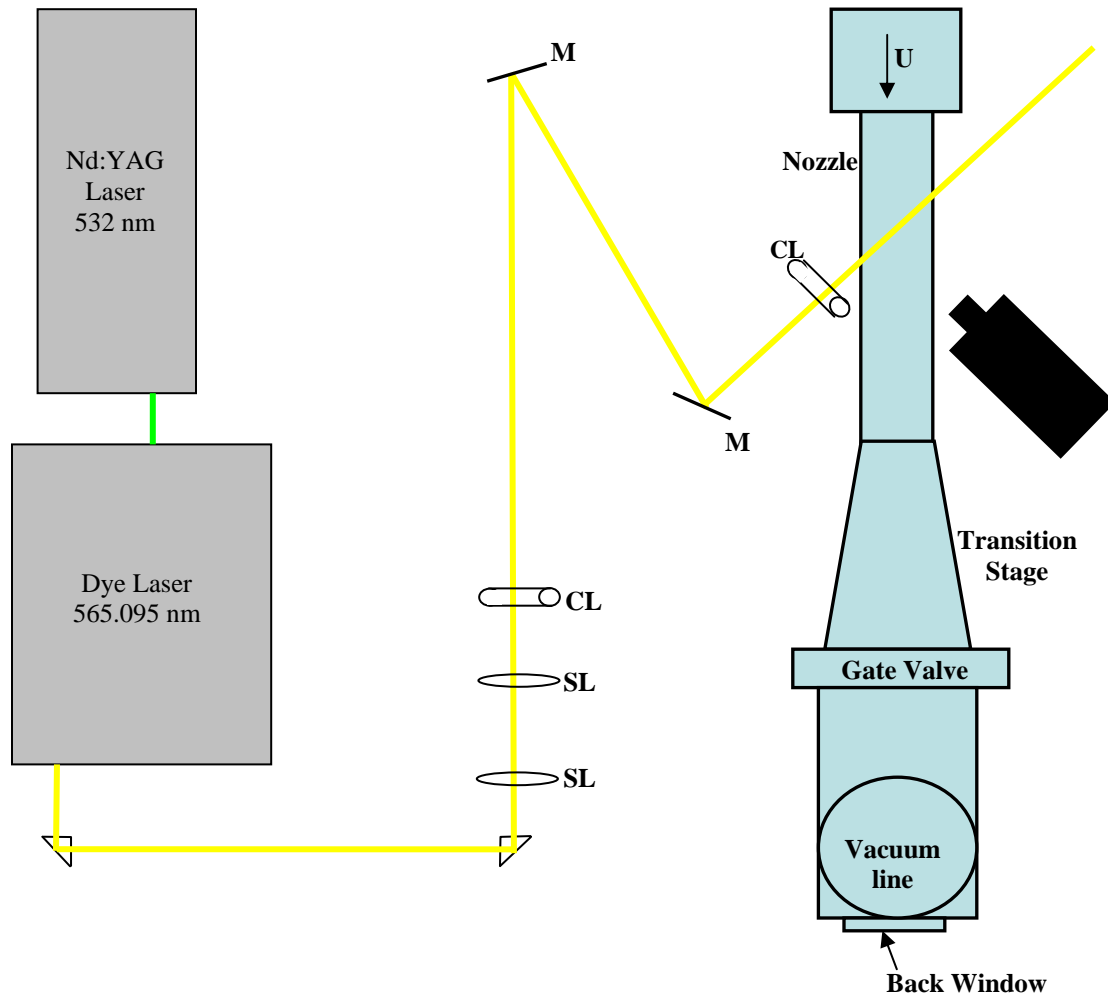


Figure 24. A schematic of the laser and optics setup. The lenses are annotated with SL for spherical lens, CL for cylindrical lens, and M for mirror. In this schematic, the lasers and optics are situated to acquire images in the oblique view.

Along with oblique images, streamwise images were captured. Figure 25 is a schematic of the laser and optics setup for streamwise imaging. The laser enters through a window in the vacuum line and is aimed down the centerline of the nozzle, in the opposite direction of the gas flow. The laser sheet is ~ 600 μm thick and is the height of the nozzle. The camera is positioned

perpendicular to the laser sheet and is on a translation stage to easily obtain pictures from the injector to the nozzle exit.

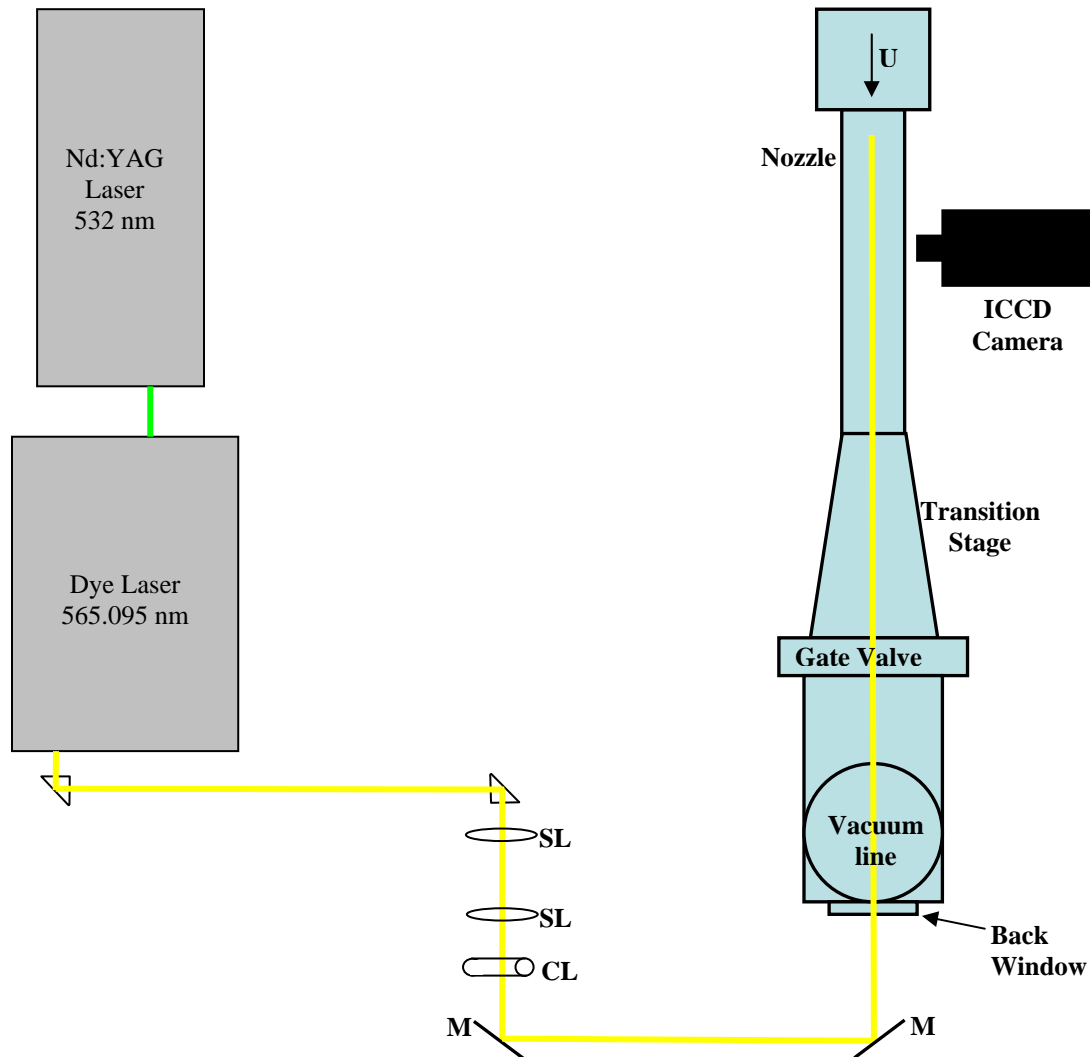


Figure 25. A schematic of the lasers and optics setup to acquire streamwise images. The laser sheet is aimed up the back end of the nozzle through a window.

The Princeton Instruments Acton ICCD camera has a Generation III photo intensifier, with GaAs as the photocathode material.⁴⁸ The camera is able to gate as fast as 2 ns and can operate at a 10-Hz frequency. The camera resolution is 512 x 512 pixels. During the tests, a Sigma 50 mm F2.8 Macro camera lens is used, allowing a resolution of ~ 0.03 mm/pixel for streamwise images and ~ 0.05 mm/pixel for oblique images. The camera gate time was set to 20

ns, which is sufficient to collect enough fluorescence yet is fast enough to capture minute gas movement. At the exit of the nozzle, where the gases are traveling with the highest velocity of approximately 900m/s (see Fig. C.4), an element in the gas translates only 0.018 mm in 20 ns. This movement is less than a pixel width.

5.0 PLIF IMAGE ANALYSIS OF SINGLE INJECTOR

5.1 Introduction

The first nozzle design studied is a nozzle with a single injector on the bottom wall of the nozzle (as described in Chapter 3). To visualize the flow, PLIF images were collected in ensembles of 100. The images were taken at progressive downstream locations with two different camera views (streamwise or oblique). The laser and camera configurations for both the oblique and streamwise views are shown in Figures 24 and 25, respectively. The streamwise view is a side view of the jet flowing from left to right, where images were taken along the nozzle centerline. The oblique-view images the jet at a 45-degree angle, displaying the spanwise structure of the jet.

The injected flow is highlighted by the iodine fluorescence. The flow with the highest fluorescence intensity is the unmixed counter-rotating vortex pair, while the less intense portion of the flow is a mixed portion of the primary and injected gasses, and the portion of the image with no intensity is the primary flow.

Ensemble averages were computed for both the streamwise and oblique views. Histogram analysis was performed on the ensemble averages of both views to map the intensity variance, which lends insight into the mixing quality between the injected and primary flows. With the oblique images, the structure size is measured to quantify the jet growth and diffusive properties.

5.2 Ensemble Averaging

Averages were taken of each image ensemble (of 100 images) for both the streamwise and oblique PLIF images.

5.2.1 Streamwise Images

A schematic of the streamwise locations of the PLIF images is displayed in Figure 26, and ensemble averages of the streamwise images are displayed in Figures 27 through 31. In each image, the flow is from left to right, the nozzle wall is drawn in red, the x -value is the distance from the nozzle throat, and the y -value is the distance from the nozzle half-height. The images display the single injector from the nozzle throat to 9.6 cm downstream of the throat. Intensity streaks in the images are caused by optical aberrations when forming the excitation laser-sheet. Most of the streamwise images were taken with a camera gain of 200, though the streamwise image in Figure 29 was taken with a camera gain of 100. To account for this difference, the overlapping section of the images in Figures 28 and 29 (30 – 36 mm) was used to determine an intensity multiplier. Each ensemble average was normalized by the maximum intensity at the exit of the injector (24,072 counts).

In general, with progressive downstream distance, the jet is penetrating farther into the centerline of the nozzle. After the nozzle exit plane (NEP), the jet began to fluctuate vertically in time. This fluctuation can be seen in a sequence of instantaneous images at a streamwise location, where the jet height is continuously changing. The fluctuations become more intense with downstream distance. Ensemble averaging the fluctuating images does not accurately convey the maximum jet penetration. Figure 30 is evidence of the jet fluctuation where the penetration is much less than in Figures 29 and 31.

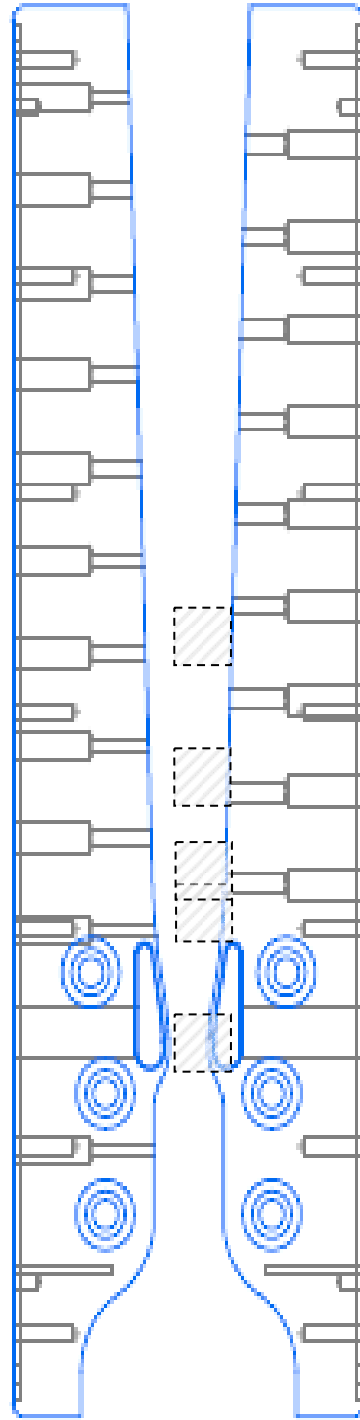


Figure 26. Schematic of the nozzle with shaded boxes indicating the locations of the five streamwise PLIF images taken (Figures 27 through 31).

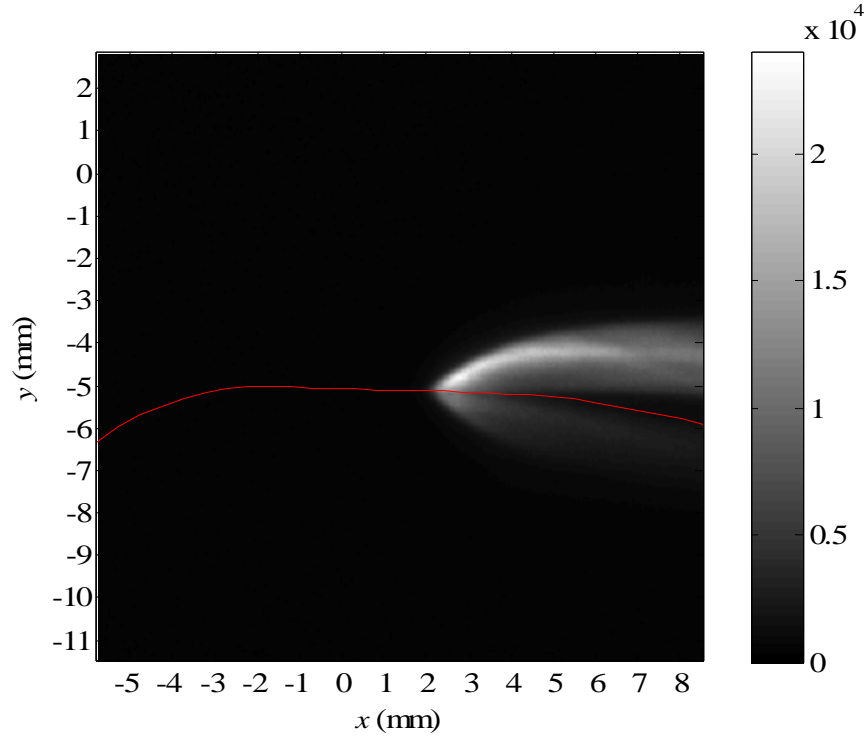


Figure 27. Ensemble average of the streamwise images at the jet exit. Note that the iodine fluorescence is reflected onto the bottom wall of the nozzle, shown under the red line. Color bar units are pixel intensity.

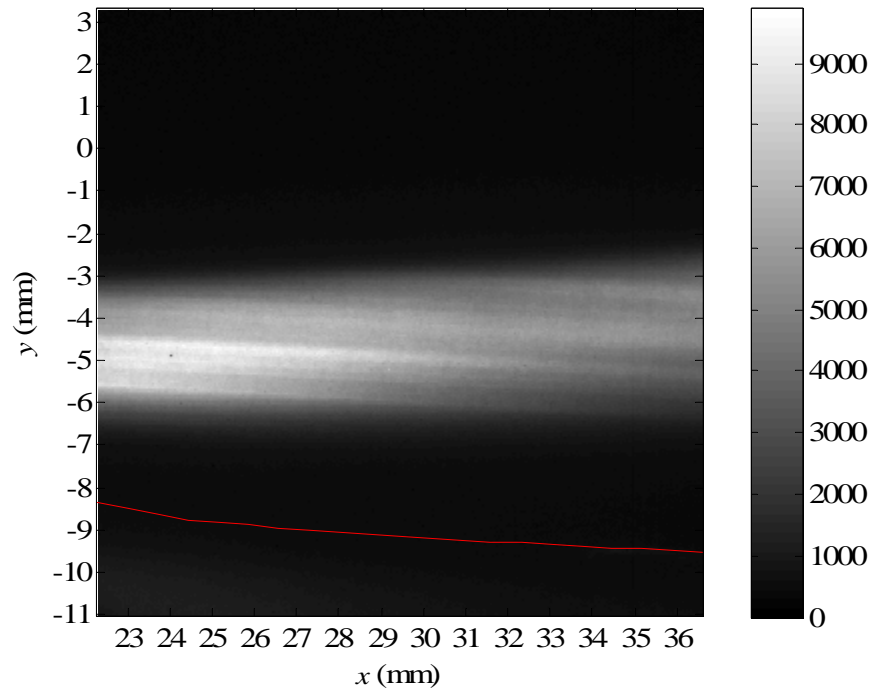


Figure 28. Ensemble average of the streamwise images of the jet from ~22 mm to ~36 mm downstream of the nozzle throat. Color bar units are pixel intensity.

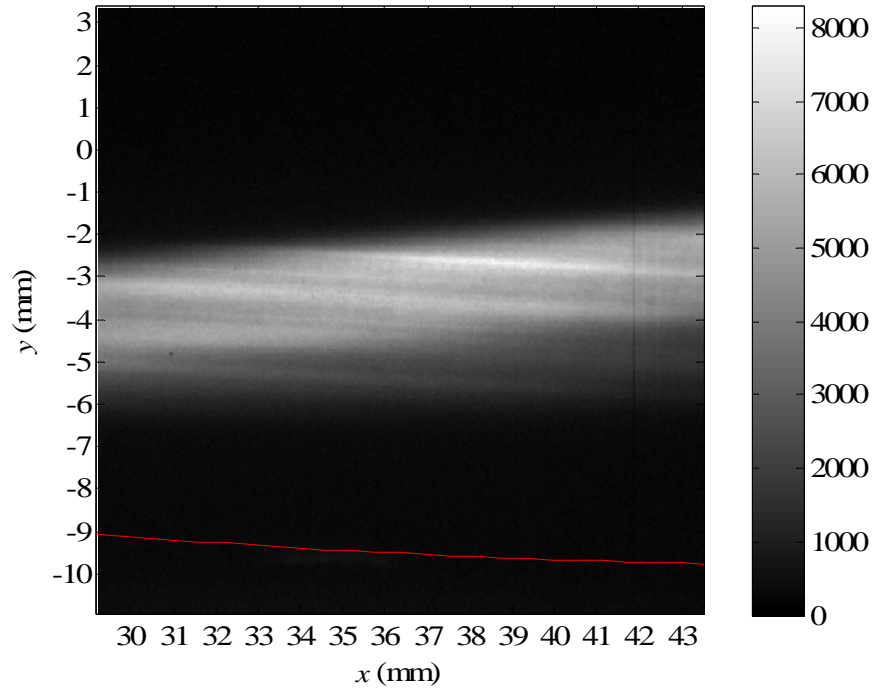


Figure 29. Ensemble average of the streamwise images of the jet from ~29 mm to ~43 mm downstream of the nozzle throat. Color bar units are pixel intensity.

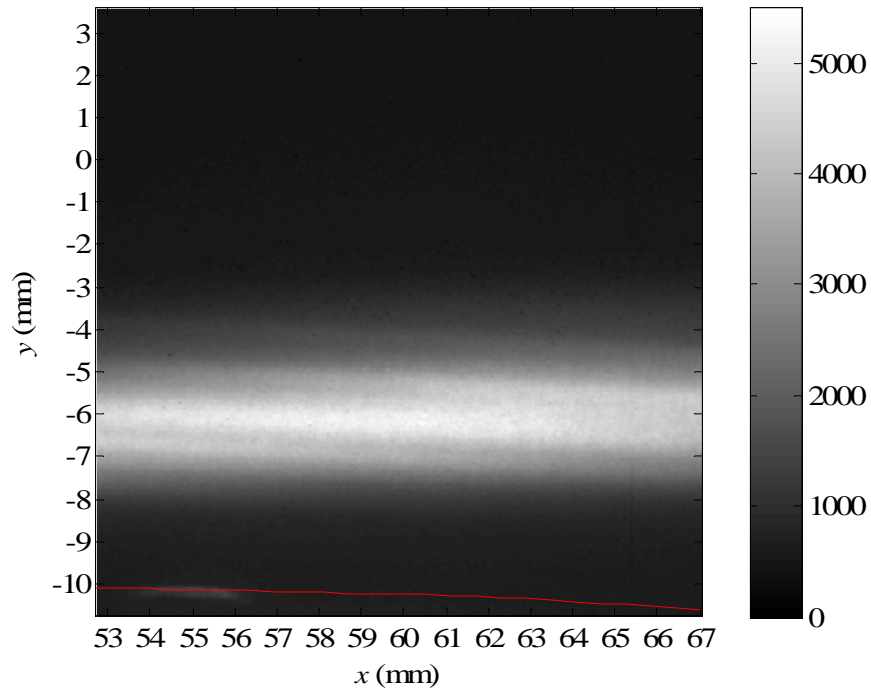


Figure 30. Ensemble average of the streamwise images of the jet from ~53 mm to ~67 mm downstream of the nozzle throat. Color bar units are pixel intensity.

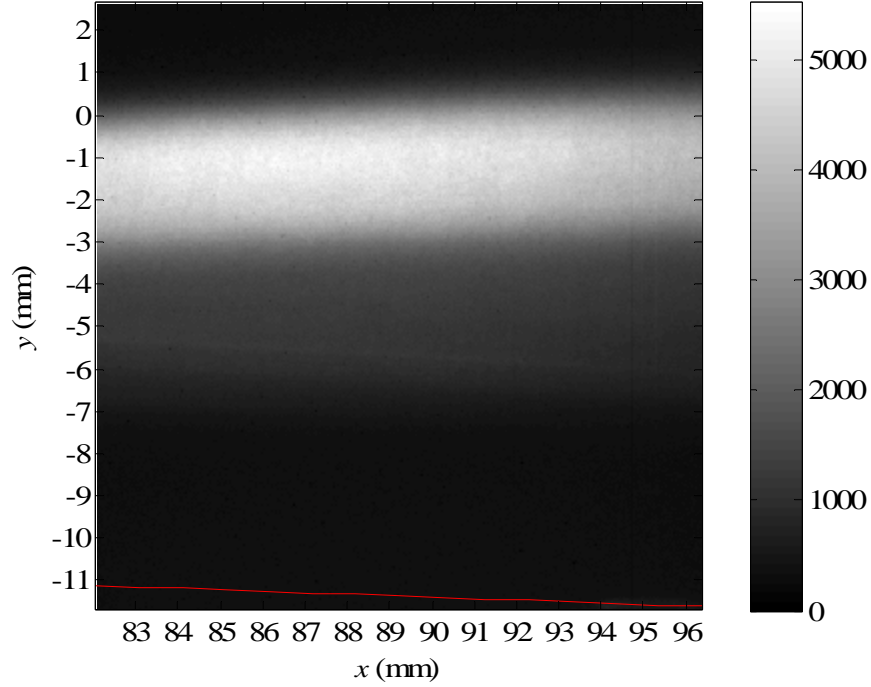


Figure 31. Ensemble average of the streamwise images of the jet from ~82 mm to ~96 mm downstream of the nozzle throat. Color bar units are pixel intensity.

5.2.2 Oblique Images

To study the spanwise structure of the jet, oblique-view images were taken. Figure 32 is a schematic of the axes used in notating the oblique view. The schematic is a top-view of the nozzle with gas flowing from top to bottom. The throat, shown with a dashed line, is where $x = 0$. The y -axis is out-of the page, starting at the nozzle half-height. The $x45$ -axis begins at the x -axis and follows the laser sheet. The camera view is typically 24 to 30 mm wide, centered at the intersection of the $x45$ - and x -axes. Because of the oblique view, the left-hand-side of each image is downstream of the right-hand-side. If the structure size is 4 mm wide, the left-hand-side is 2.8 mm downstream of the right-hand-side.

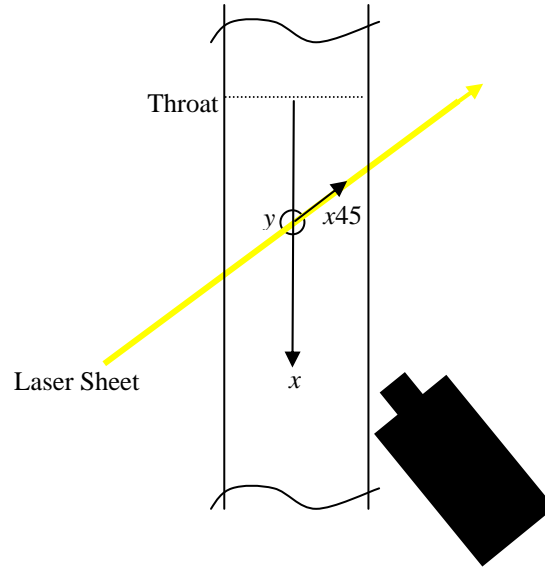


Figure 32. Schematic of the x -, $x45$ -, and y -axes with respect to the nozzle and camera. The $x45$ -axis is along the direction of the laser sheet.

Ensemble averages of the oblique images are displayed in Figures 33 through 39. The upstream to downstream separation of each 45° plane is approximately 10 mm, from 13 mm to 75 mm downstream from the nozzle throat. The oblique images were taken with a camera gain of 100. The ensemble averages are normalized by the maximum intensity in Figure 33 (5898 counts). The top and bottom walls of the nozzle are indicated by red dashes.

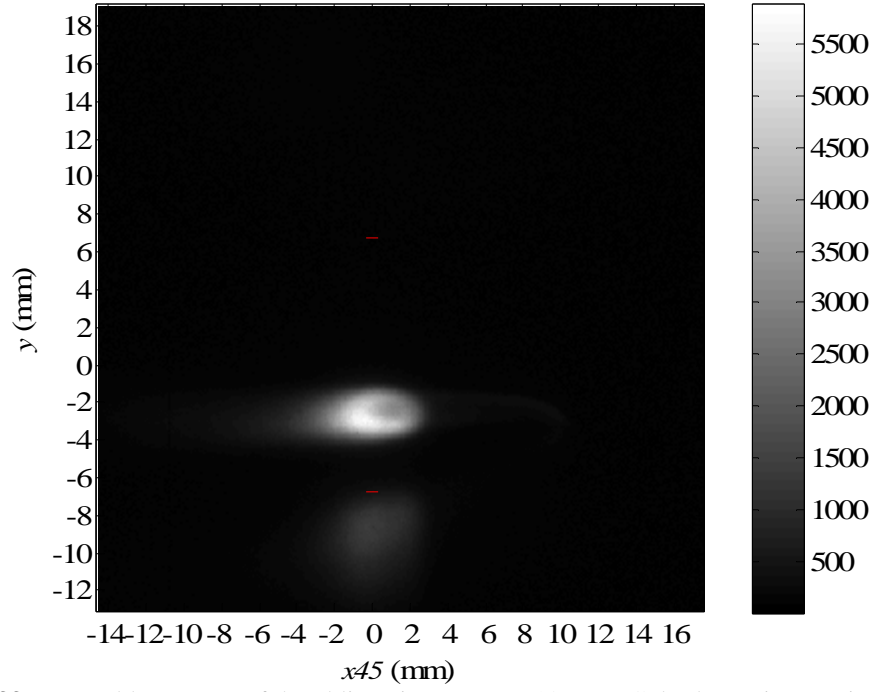


Figure 33. Ensemble average of the oblique images at $x \sim 13$ mm. Color bar units are pixel intensity.

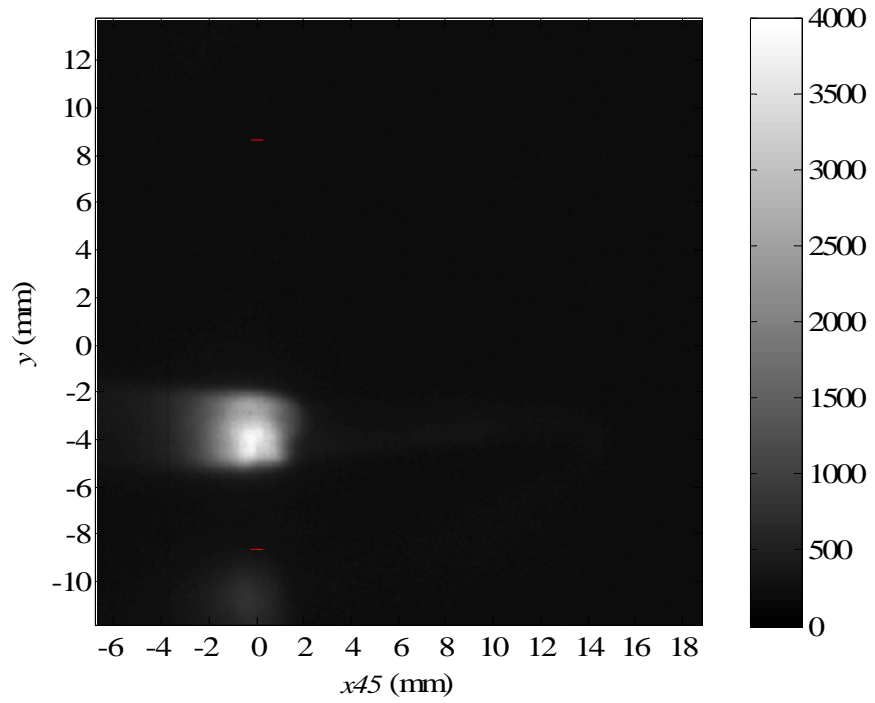


Figure 34. Ensemble average of the oblique images at $x \sim 23$ mm. Color bar units are pixel intensity.

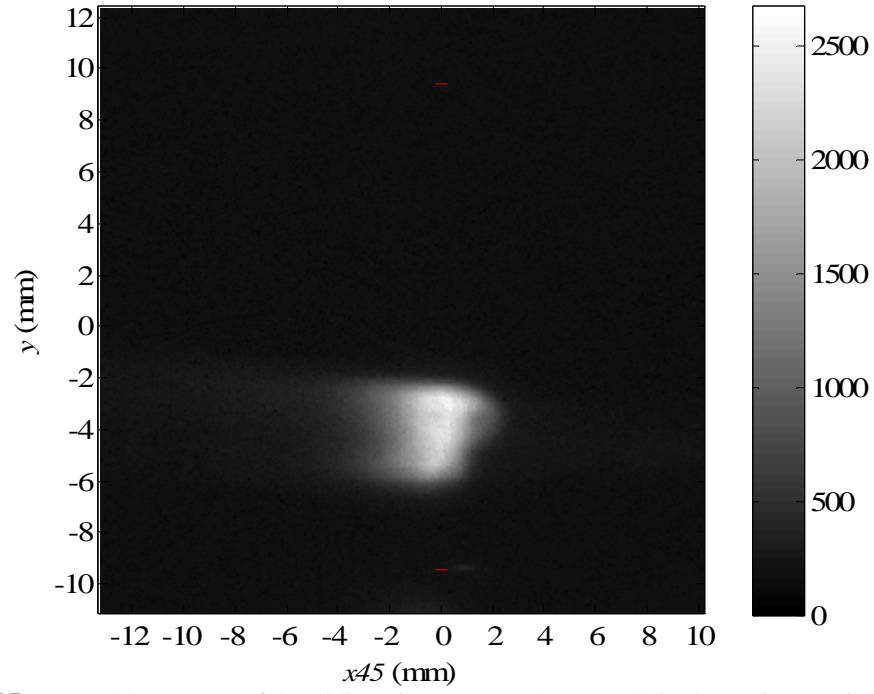


Figure 35. Ensemble average of the oblique images at $x \sim 35$ mm. Color bar units are pixel intensity.

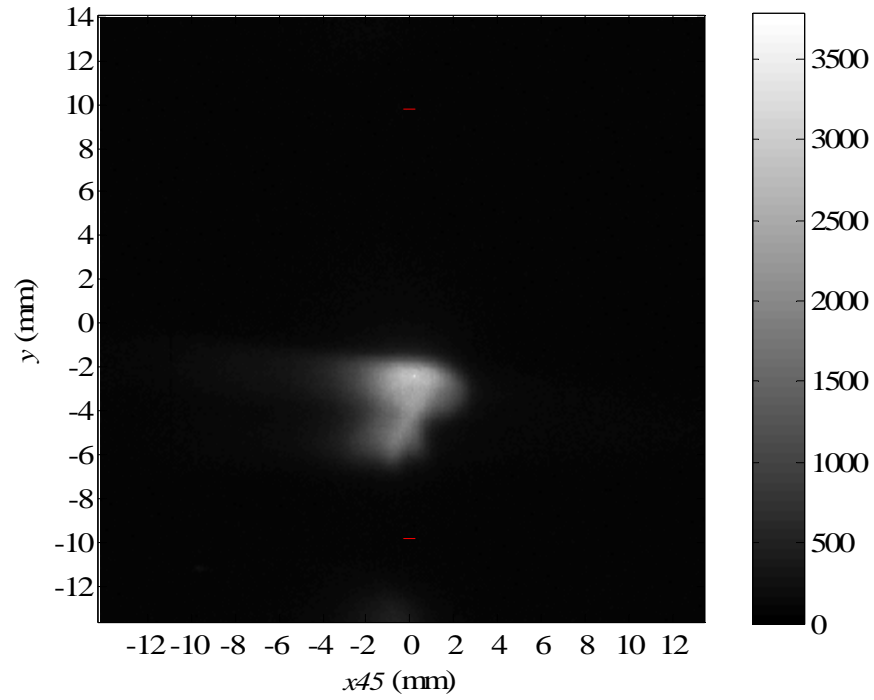


Figure 36. Ensemble average of the oblique images at $x \sim 45$ mm. Color bar units are pixel intensity.

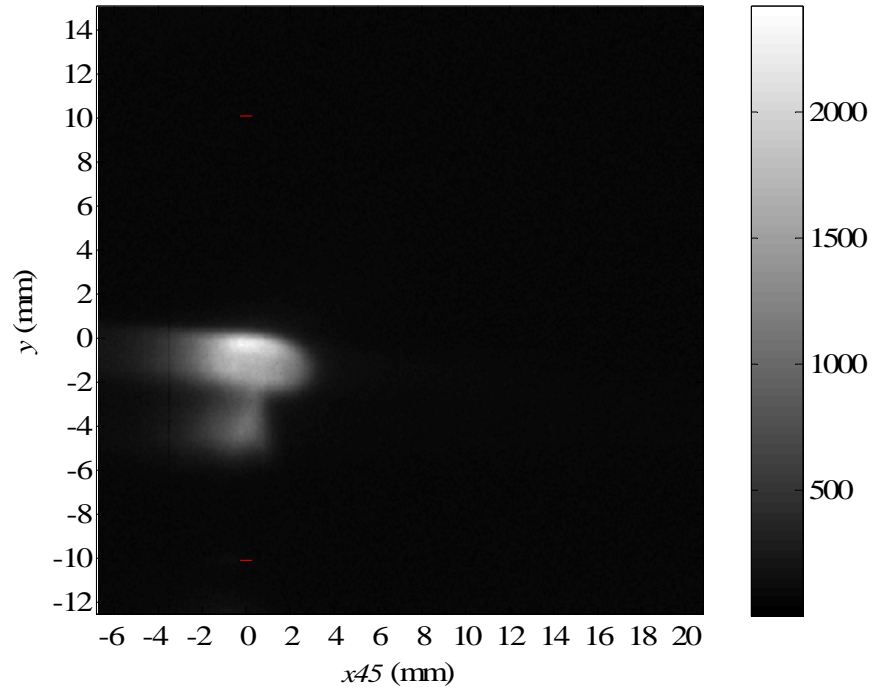


Figure 37. Ensemble average of the oblique images at $x \sim 55$ mm. Color bar units are pixel intensity.

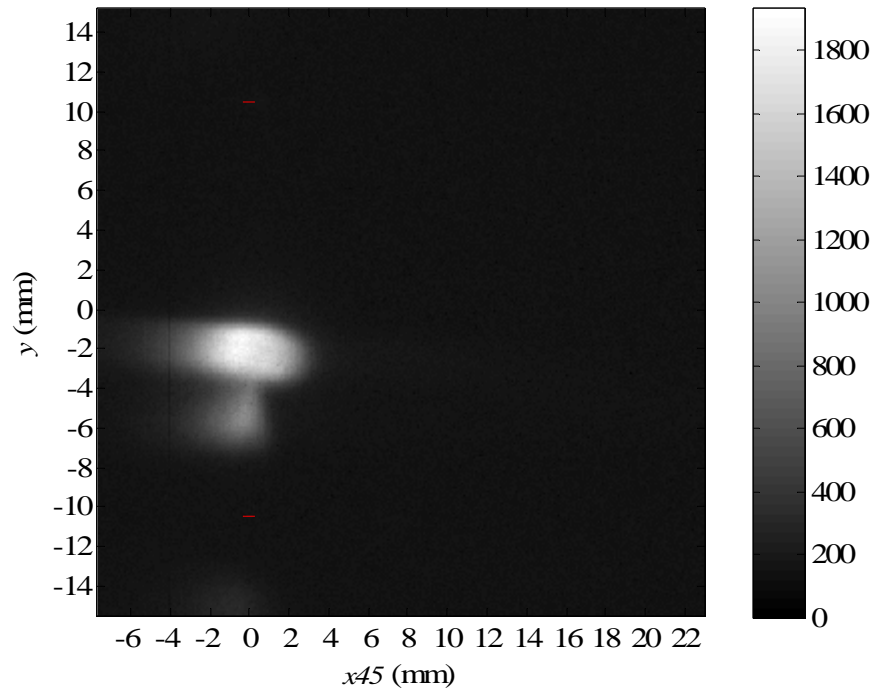


Figure 38. Ensemble average of the oblique images at $x \sim 65$ mm. Color bar units are pixel intensity.

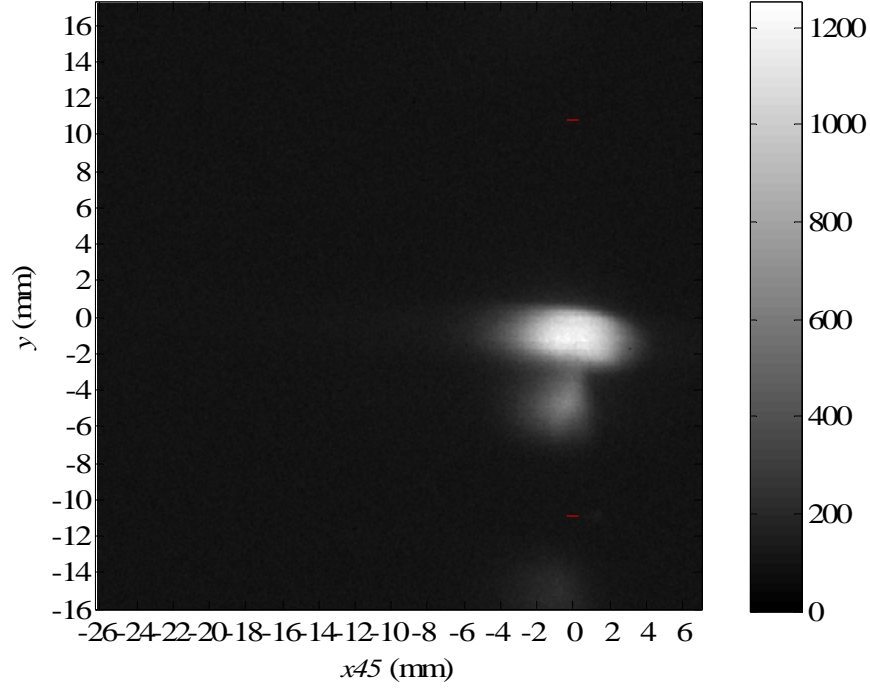


Figure 39. Ensemble average of the oblique images at $x=75$ mm. Color bar units are pixel intensity.

A pair of counter-rotating vortices is evident in the oblique images. In Figures 34 through Figure 39, a recirculation region below the counter-rotating vortex pair (CRVP) is visible as well. The height of the CRVP is increasing with downstream distance, along with the recirculation region of the jet. From Figure 39, it is evident that the jet structure extends to the centerline of the nozzle by $x = 75$ mm.

5.3 Histograms

To quantify the mixing between the jet and the primary flow, a histogram analysis was performed on both the streamwise and oblique images. Histograms display the probability density of the fluorescence intensity. For an unmixed flow, a histogram will typically be bimodal. It will have a zero-intensity peak indicating the primary, non-fluorescing flow and a

high-intensity peak indicating the injected, fluorescing flow. There also may be a third intermediate-intensity peak if the primary and secondary flows are mixing.

The intensities of the peaks will shift with downstream distance. As mixing occurs, the intermediate- and high-intensity peaks decrease with downstream distance. This indicates that the primary flow is being advected into the CRVP where it is mixed with the jet, thus reducing the fluorescence intensity of the injected flow.

5.3.1 Streamwise Images

Histograms for the ensemble-averaged streamwise images are shown in Figure 40. The normalized intensity is displayed on the abscissa, while the number of pixels at a specific intensity is displayed on the ordinate. The downstream location of each histogram is displayed on the x -axis, where the downstream location of the streamwise image is taken as the location of the center pixel. In all the histograms, a zero-intensity peak is present, representing the primary flow. The high-intensity peak in each histogram, representing iodine, occurs at lower intensity levels with downstream distance. A third, intermediate-intensity peak forms at $x = 29$ mm (red line) and moves to lower intensity levels with downstream distance. Because of the decrease in intensity levels with the high-intensity and intermediate-intensity peaks, mixing is evident with the streamwise PLIF images.

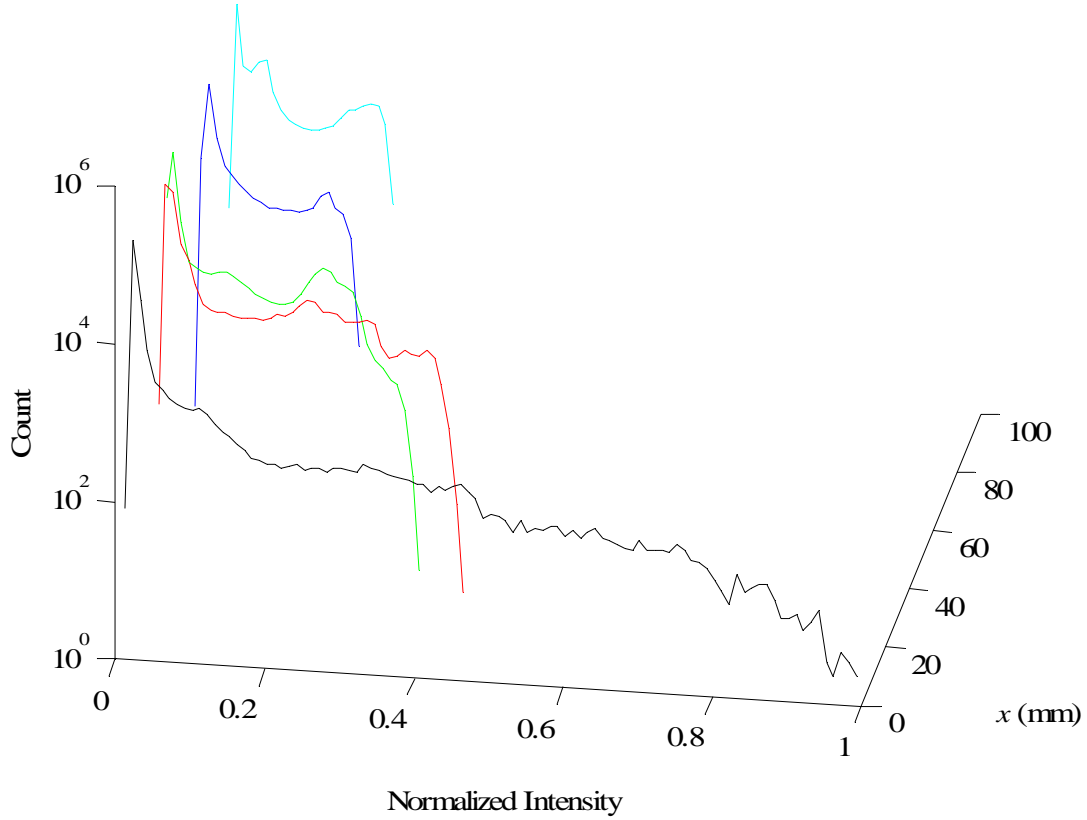


Figure 40. Histograms of the ensemble-averaged streamwise images from Figures 27 to 31. The intensity of each image is normalized by the maximum intensity in Figure 27. The x -location is measured at the center of the image.

5.3.2 Oblique Images

As with the streamwise images, a histogram analysis was performed on the ensemble-averaged oblique images. Histograms for Figures 33 through 39 are displayed in Figure 41. The zero-intensity and high-intensity peaks are discernible, but an intermediate-intensity peak is difficult to distinguish. The high-intensity peaks are decreasing with downstream distance, as with the streamwise images, indicating mixing between the primary and injected flows.

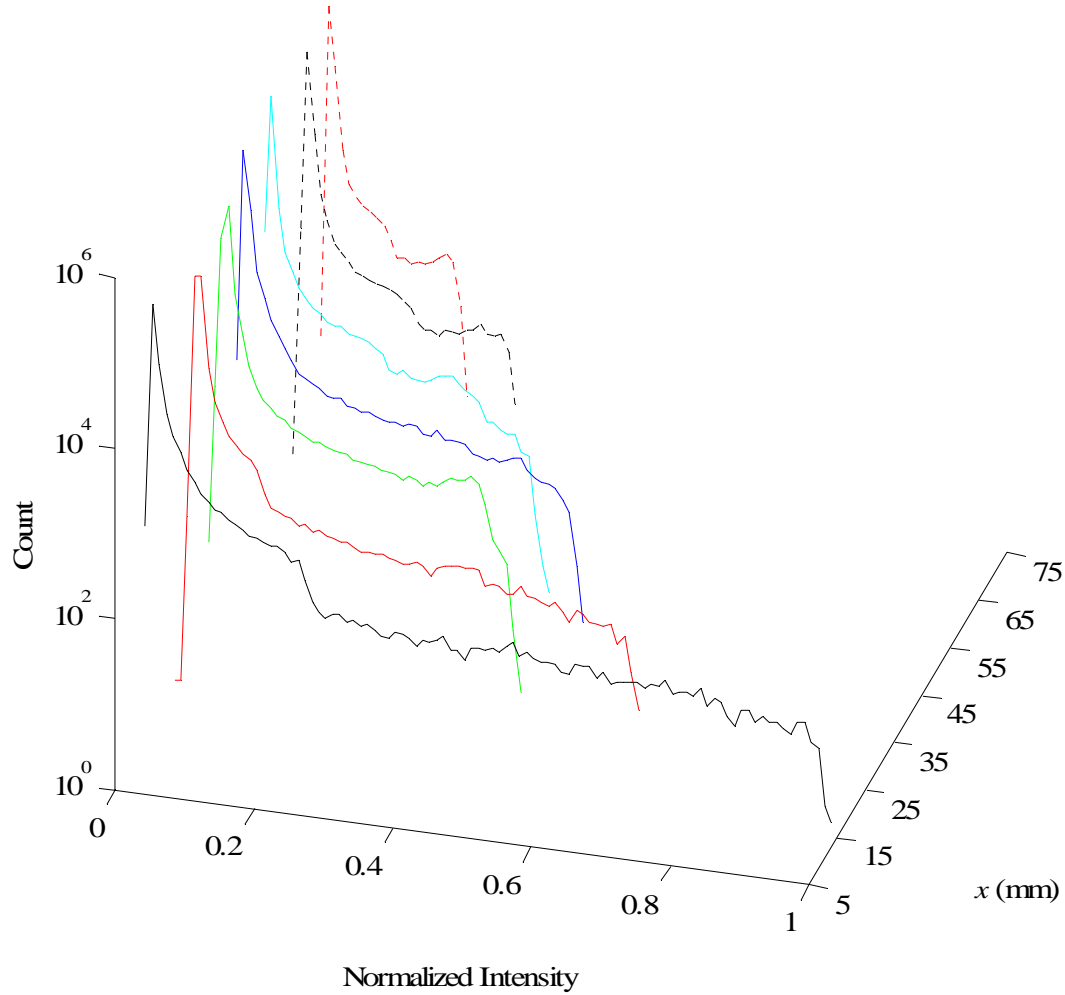


Figure 41. Histograms of the ensemble-averaged oblique images from Figures 33 to 39. The intensity of each image is normalized by the maximum intensity in Figure 33.

5.4 Structure Size

If diffusive mixing between the primary and injected flows occurs with downstream distance, the jet structure will grow in size. This size can be measured by its area or length of interface between the jet structure and primary flow.⁴⁹

To determine the area of the oblique structure, the grayscale PLIF image is converted to monochrome, with a threshold of 30% of the maximum image intensity. Figure 42 is a monochrome rendition of Figure 39 ($x = 75$ mm). The black pixels, representing all intensities

greater than or equal to 30% of the maximum image intensity, are counted, where the count is converted to square millimeters to give the structure area. The area was determined for x positions: 13 mm, 23 mm, 35 mm, 45 mm, 55 mm, 65 mm, and 75 mm. Structure area versus downstream distance from the nozzle throat is displayed in Figure 43. The area increases with downstream distance, where the area more than doubles from the $x = 13$ mm position to the $x = 75$ mm position.

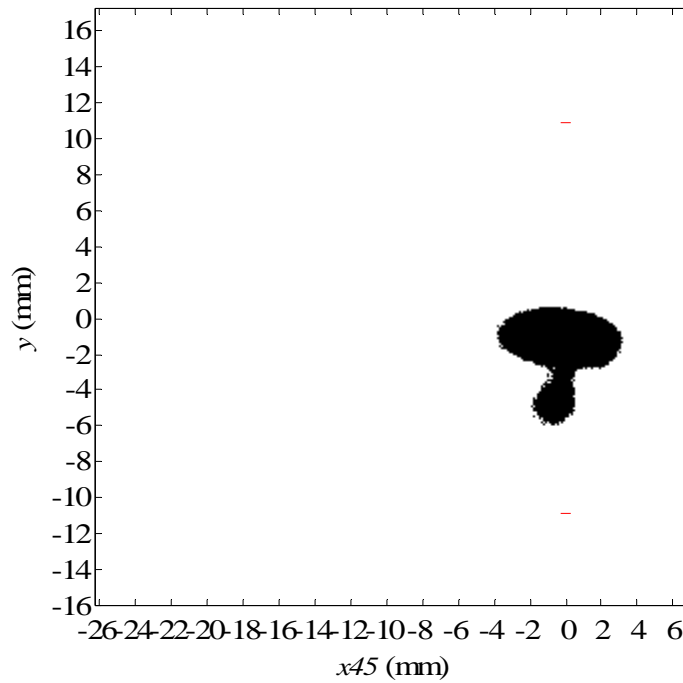


Figure 42. Black and white image of the oblique structure at $x \sim 75$ mm.

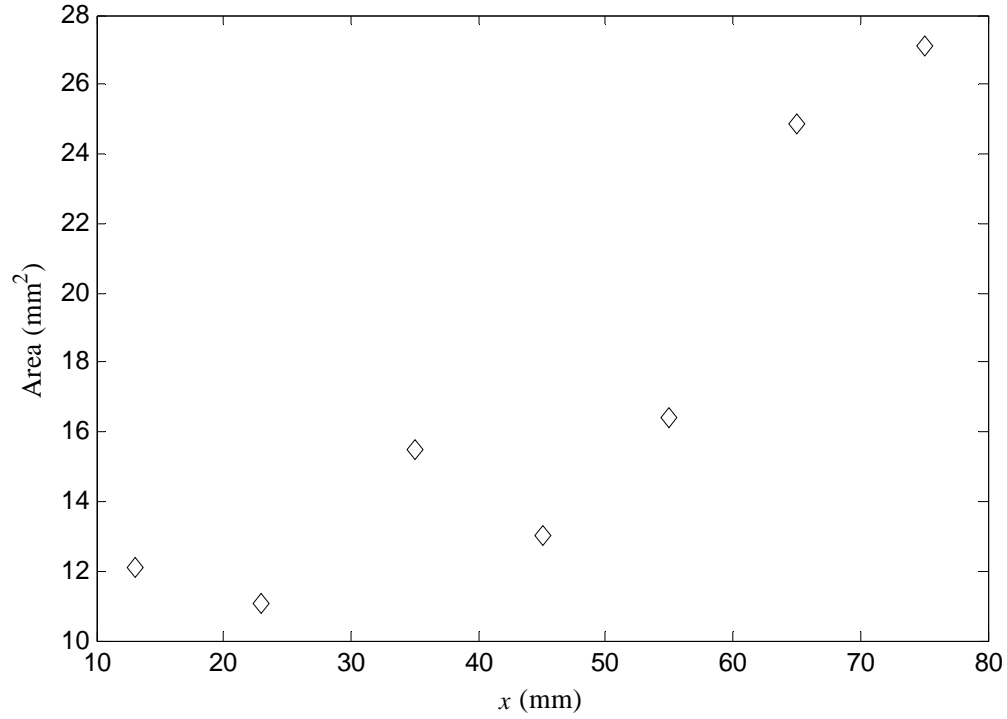


Figure 43. Areas of the oblique image structures versus downstream distance from the nozzle throat.

Outlines from the monochrome images were used to estimate the interface length of the structures in the oblique view. These were computed using the edge-detection function *Outline* in the public-domain imaging software, ImageJ.⁵⁰ This function examines each pixel in the monochrome image, and flips it from black to white if all pixels surrounding it are black. This leaves black pixels only at the edge of the structure, defining its outline. Figure 44 is an outline of the structure shown in Figure 39. The number of black pixels in the outline was counted and then converted to interface length (in millimeters) using the pixel resolution (0.05 mm/pixel). Interface length versus downstream distance from the nozzle throat is displayed in Figure 45. As with structure area, interface length increases with downstream distance.

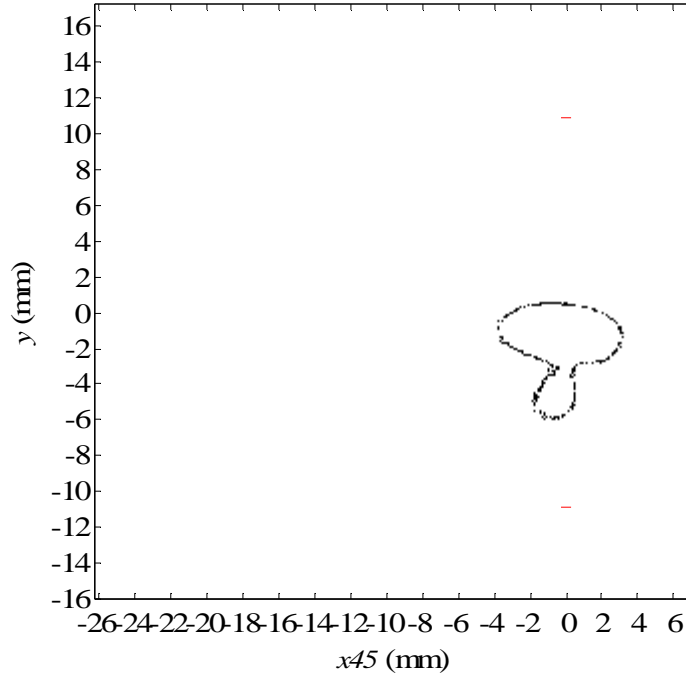


Figure 44. Outline of the black and white image from Figure 42.

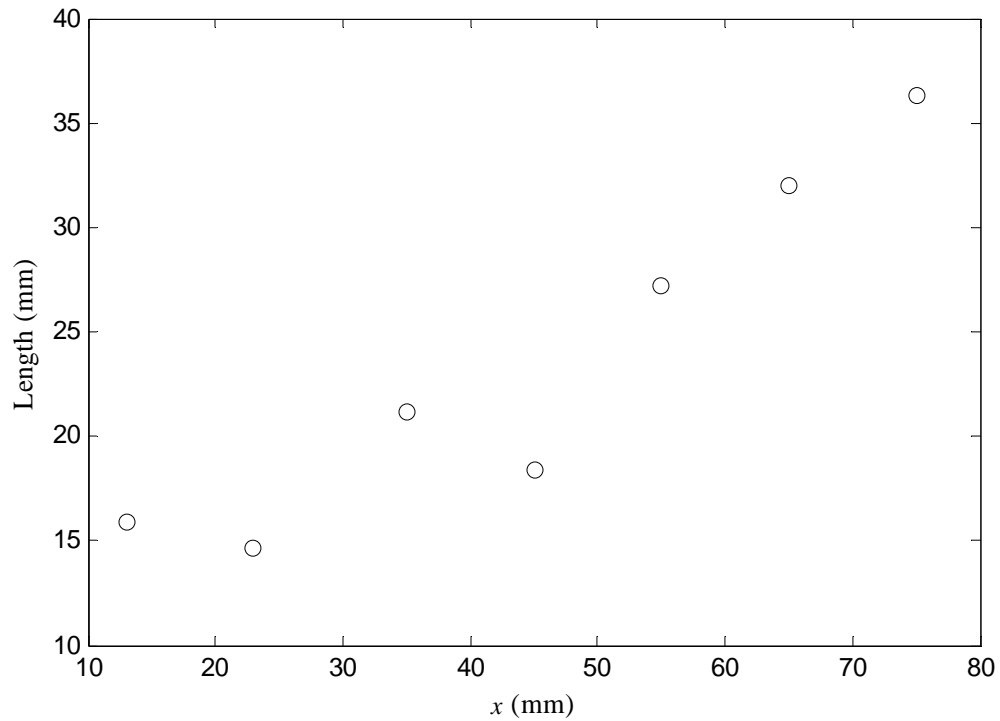


Figure 45. Interface lengths of the oblique image structures versus downstream distance from the nozzle throat.

With both interface length and structure area increasing with downstream distance, it is evident that the CRVP is increasing in size with downstream distance. This indicates that

diffusive mixing between the injected and primary flows of the nozzle is occurring. It is also suggestive that there is advection of the main flow into the CRVP.

The next chapter will discuss the investigation of other injection scenarios, where trip jets are used to perturb the flow. Along with histograms, interface length and structure areas will be used to compare the relative mixing for each of the injection scenarios.

6.0 MULTIPLE INJECTORS

6.1 Introduction

To enhance mixing between the primary and injected flows, small injectors were positioned in the wake of the single injector. These small injectors are termed *trip jets* because they are intended to disturb, or trip, the counter-rotating vortex pair of the single injector. The trip jets are 0.25 mm in diameter, angled perpendicular to the nozzle wall, and have a jet exit Mach number of 1. The diameter of each trip jet was designed to be significantly smaller than the injector, which has an effective diameter of 1.02 mm. With the sizeable thickness of the nozzle between the wall and injector plenum, the smallest diameter that could be manufactured by Wire-Tech, Inc., was 0.25 mm. Therefore, the trip jet diameters are 0.25 mm. The constant diameter of the trip jets, from the plenum to the jet exit, creates the Mach 1 design. They are angled perpendicular to the nozzle wall, or 83° to the primary flow, to allow penetration to the injector jet.

The trip jets were placed in the wake of the injector, where the flow is subsonic, to facilitate the trip jet penetration to the counter-rotating vortex pair (CRVP). The first injection scenario tested (Trip Scenario A) consists of a single injector placed along the centerline of the nozzle, with its leading edge 1.00 mm downstream of the trailing edge of the injector, which is one injector diameter. This places the center of the trip jet 4.41 mm downstream of the nozzle throat. Once this scenario was tested, Trip Scenario B was created to determine if decreasing the distance between the injector and trip would have an increased impact on the disturbance of the CRVP. The distance between the trailing edge of the injector and leading edge of the trip was

approximately halved to 0.45 mm, where the center of the trip jet is 3.96 mm from the nozzle throat. Once Trip Scenario B was tested, Trip Scenario C was created to determine if two injectors, 3.96 mm from the nozzle throat, each 0.33 mm from the centerline, could destabilize the CRVP or, at least, push the counter-rotating vortices apart. The centerline of the trip jets was positioned 0.33 mm from the centerline to hit the jet on the outer edge of each vortex core. From Figure 33, the outer edge of each vortex core (though it appears as one vortex close to the jet exit) is approximately one-third of the jet width (0.33 mm) from the centerline. Figures 46 through 48 are schematics of the injector and trip jets from Trip Scenarios A through C. Table 2 summarizes the dimensions of the Trip Scenarios.

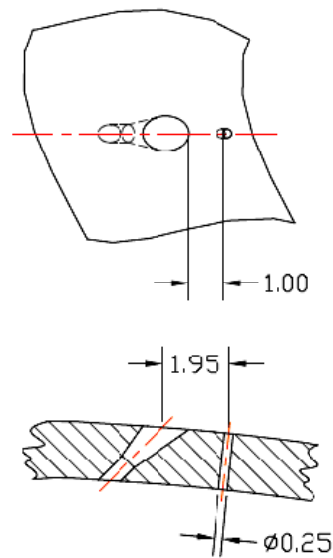


Figure 46. Top- and side-view schematic of the injector and trip jet for Trip Scenario A. Units are in millimeters and the primary flow is left to right.

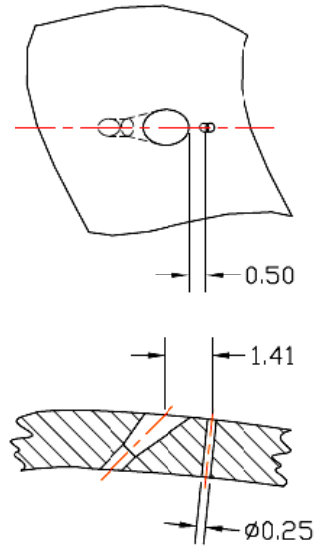


Figure 47. Top- and side-view schematic of the injector and trip jet for Trip Scenario B. Units are in millimeters and the primary flow is left to right.

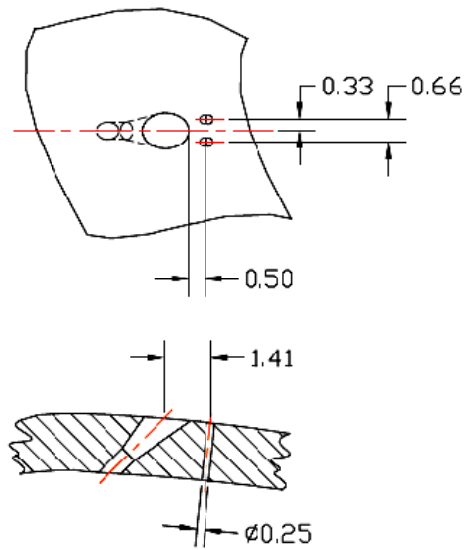


Figure 48. Top- and side-view schematic of the injector and trip jet for Trip Scenario C. Units are in millimeters and the primary flow is left to right.

Table 2. Trip Scenario specifications.

	Trip Scenario A	Trip Scenario B	Trip Scenario C
Number of Trip Jets	1	1	2
Trip Jet Diameter	0.25 mm	0.25 mm	0.25 mm
Trip Jet Mach Number	1	1	1
Distance from Nozzle Throat	4.41 mm	3.96 mm	3.96 mm
Edge-to-Edge Distance from Injector	1.00 mm	0.45 mm	0.45 mm
Distance from Nozzle Centerline	0.00 mm	0.00 mm	0.33 mm

To compare the nozzles with the trip jets to the nozzle with the single injector, streamwise and oblique PLIF images were taken. Histogram analyses were performed on the ensemble-averaged streamwise and oblique images for each trip jet scenario. Jet penetration was measured with the ensemble-averaged streamwise images while the interface length and structure areas of the oblique structures were determined for comparison to the nozzle with the single injector.

6.2 Streamwise-View Ensemble Averages

As in Chap. 5, streamwise images were collected in ensembles of 100. For each trip jet scenario, the streamwise PLIF images are normalized by the maximum intensity at the exit of the injector for that scenario. The streamwise images overlap by approximately 7 mm and are taken from the jet exit to approximately 75 mm downstream of the nozzle throat. The PLIF images for Trip Scenarios A and B were taken with a camera gain of 200, while the images for Trip Scenario C were taken with a camera gain of 100. Because the images are normalized, they can be directly compared. In each image, the flow is from left to right, the nozzle wall is drawn in

red, the x -value is the distance from the nozzle throat, and the y -value is the distance from the nozzle half-height.

6.2.1 Trip Scenario A

Ensemble-averaged streamwise PLIF images for Trip Scenario A (shown in Figure 46) are displayed in Figures 49 through 58. The camera gain is 200 for all images and each image is normalized by the maximum intensity at the injector exit. Figure 49 is a mosaic of all streamwise images, excluding Figure 54 (where the jet height did not match well with the upstream and downstream images).

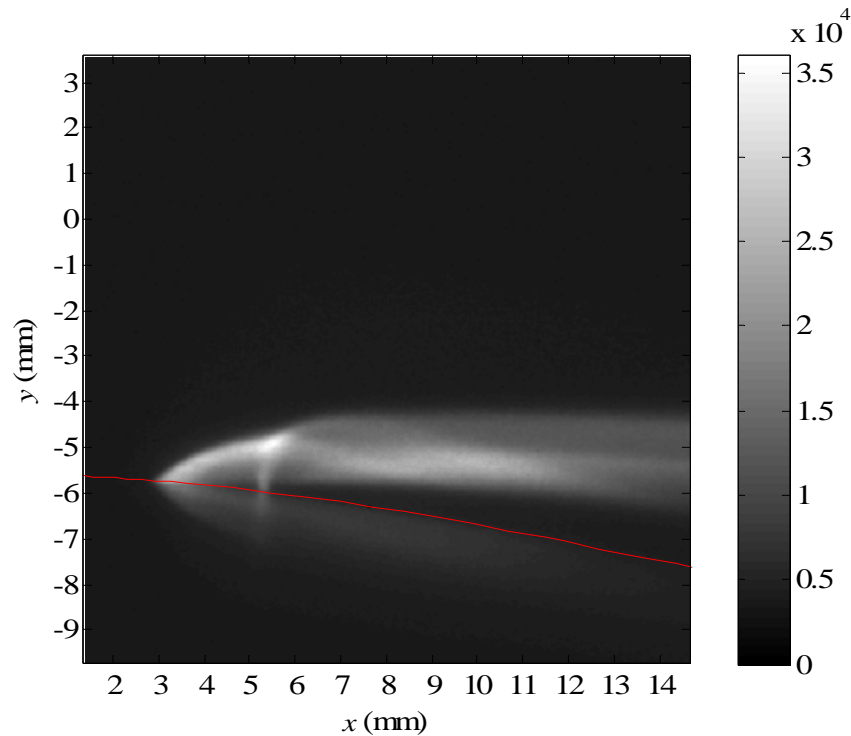


Figure 49. Ensemble average of the streamwise images at the jet exit for Trip Scenario A. Note that the iodine fluorescence is reflected from the bottom wall of the nozzle, shown under the red line. Color bar units are pixel intensity.

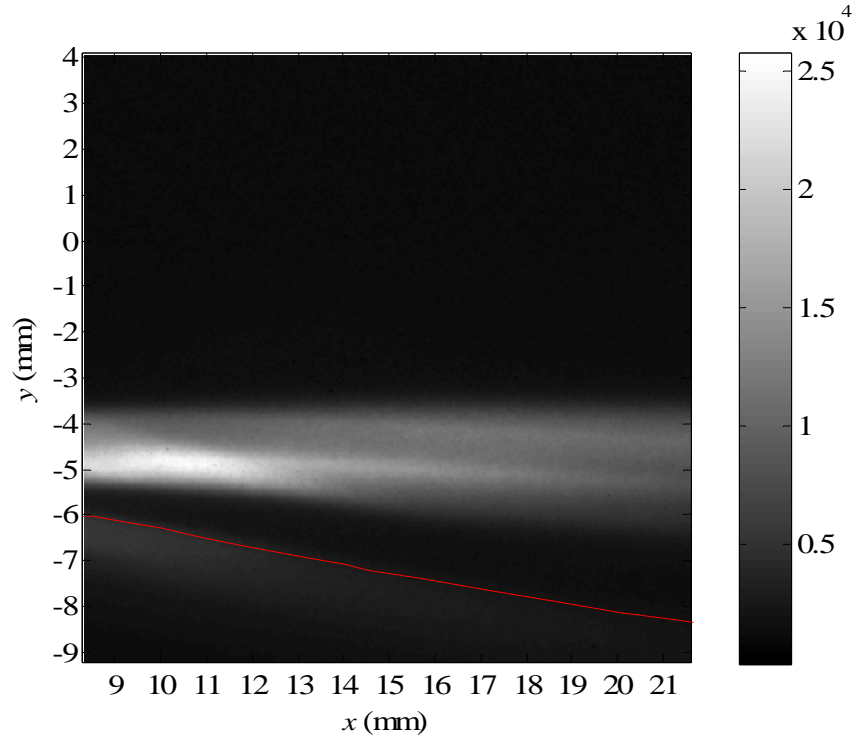


Figure 50. Ensemble average of the streamwise images of the jet from ~ 8 mm to ~ 22 mm downstream of the nozzle throat, for Trip Scenario A. Color bar units are pixel intensity.

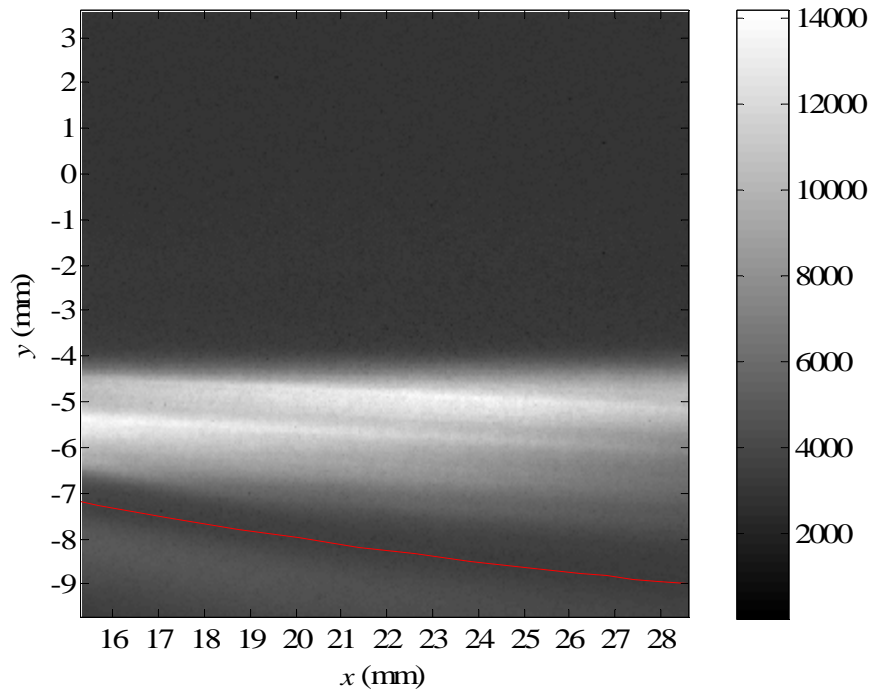


Figure 51. Ensemble average of the streamwise images of the jet from ~ 15 mm to ~ 29 mm downstream of the nozzle throat, for Trip Scenario A. Color bar units are pixel intensity.

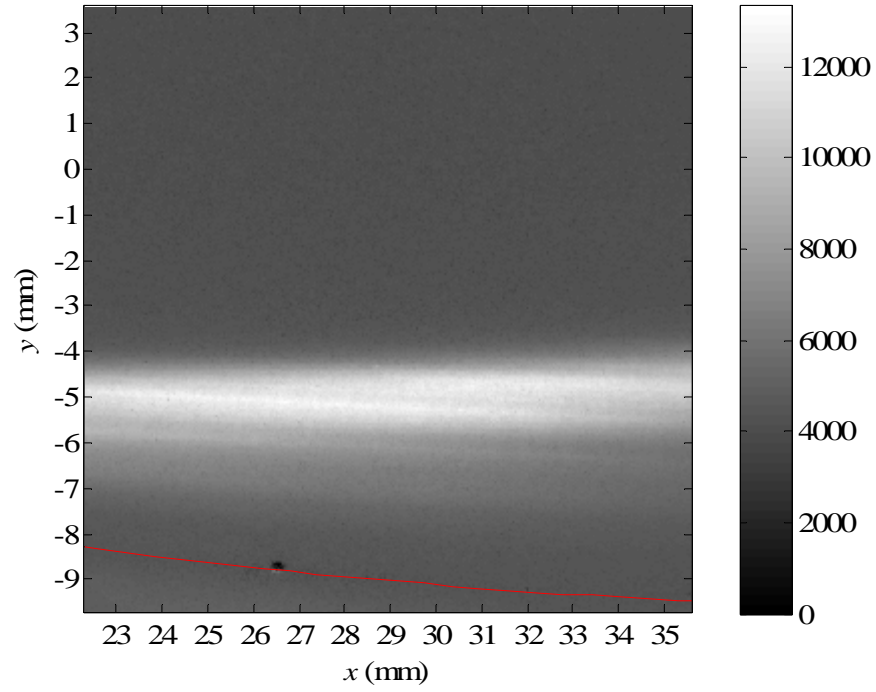


Figure 52. Ensemble average of the streamwise images of the jet from ~22 mm to ~36 mm downstream of the nozzle throat, for Trip Scenario A. Color bar units are pixel intensity.

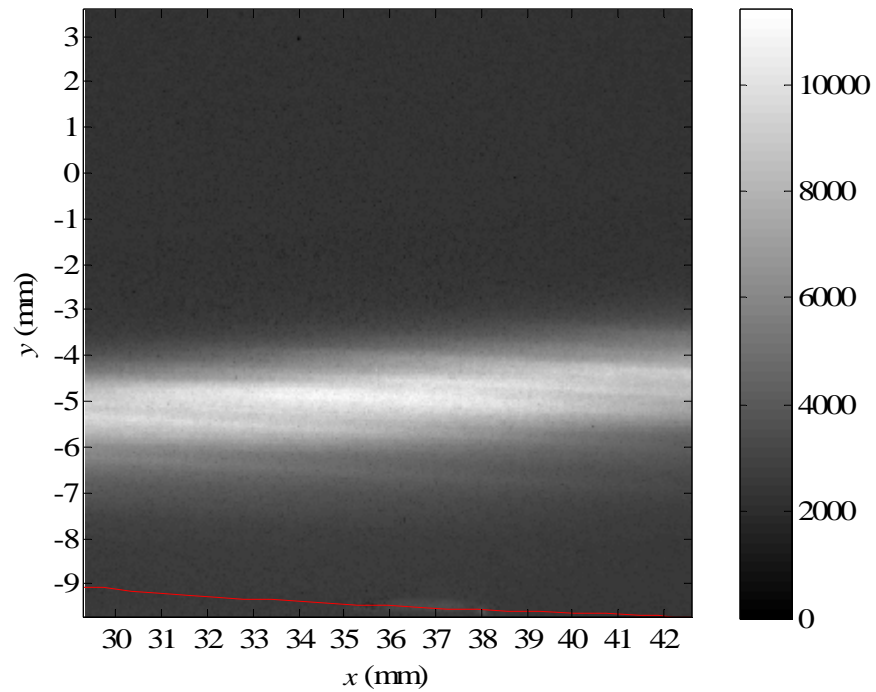


Figure 53. Ensemble average of the streamwise images of the jet from ~29 mm to ~43 mm downstream of the nozzle throat, for Trip Scenario A. Color bar units are pixel intensity.

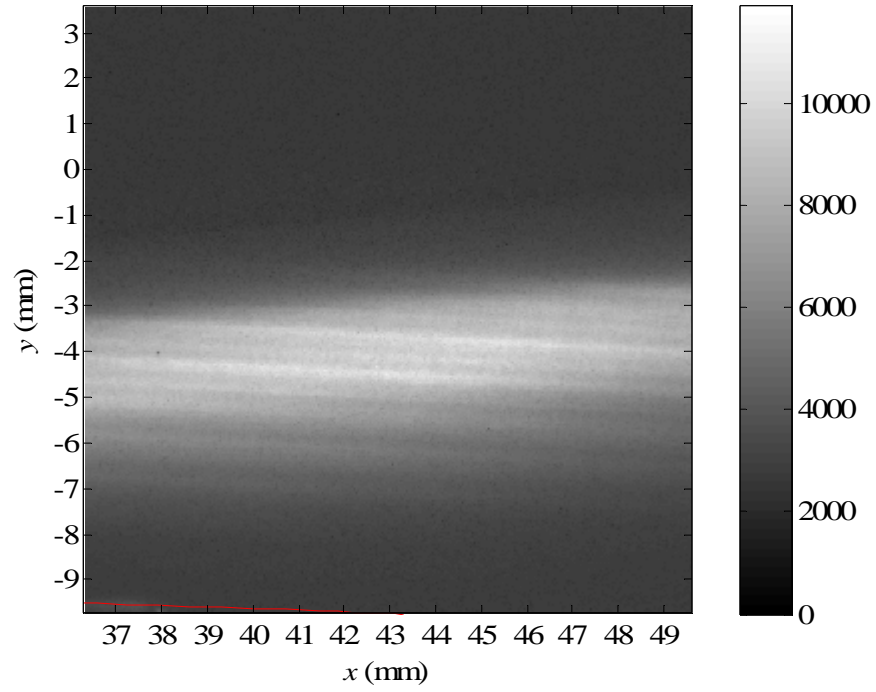


Figure 54. Ensemble average of the streamwise images of the jet from ~36 mm to ~50 mm downstream of the nozzle throat, for Trip Scenario A. Color bar units are pixel intensity.

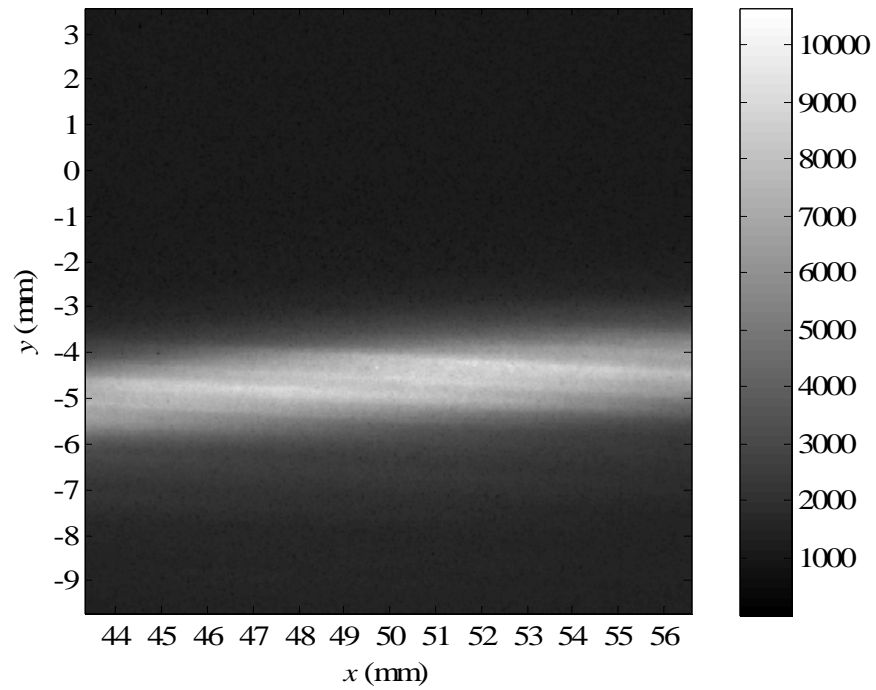


Figure 55. Ensemble average of the streamwise images of the jet from ~43 mm to ~57 mm downstream of the nozzle throat, for Trip Scenario A. Color bar units are pixel intensity.

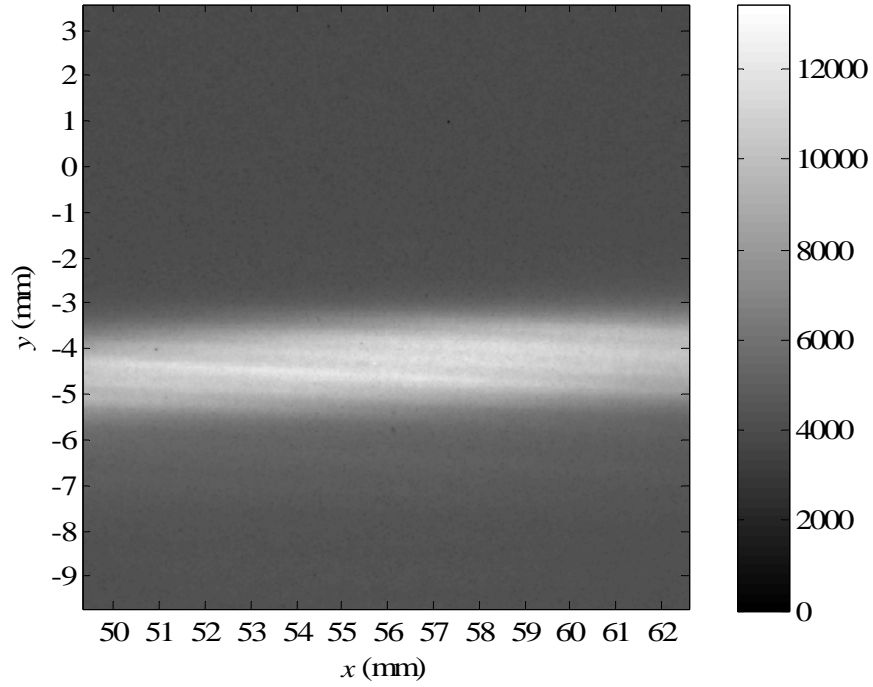


Figure 56. Ensemble average of the streamwise images of the jet from ~49 mm to ~63 mm downstream of the nozzle throat, for Trip Scenario A. Nozzle wall is not present in image. Color bar units are pixel intensity.

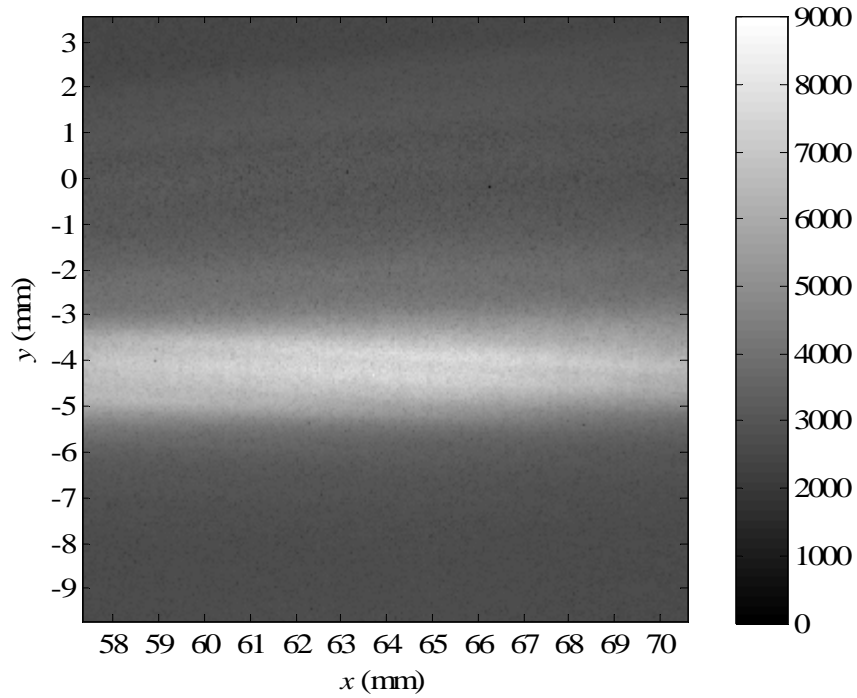


Figure 57. Ensemble average of the streamwise images of the jet from ~57 mm to ~71 mm downstream of the nozzle throat, for Trip Scenario A. Nozzle wall is not present in image. Color bar units are pixel intensity.

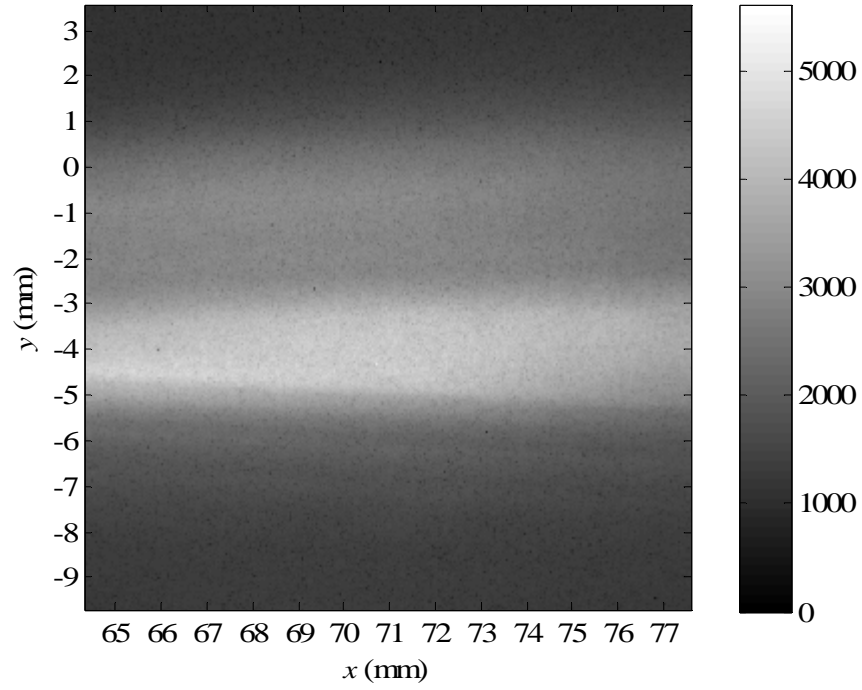


Figure 58. Ensemble average of the streamwise images of the jet from ~64 mm to ~78 mm downstream of the nozzle throat, for Trip Scenario A. Nozzle wall is not present in image. Color bar units are pixel intensity.

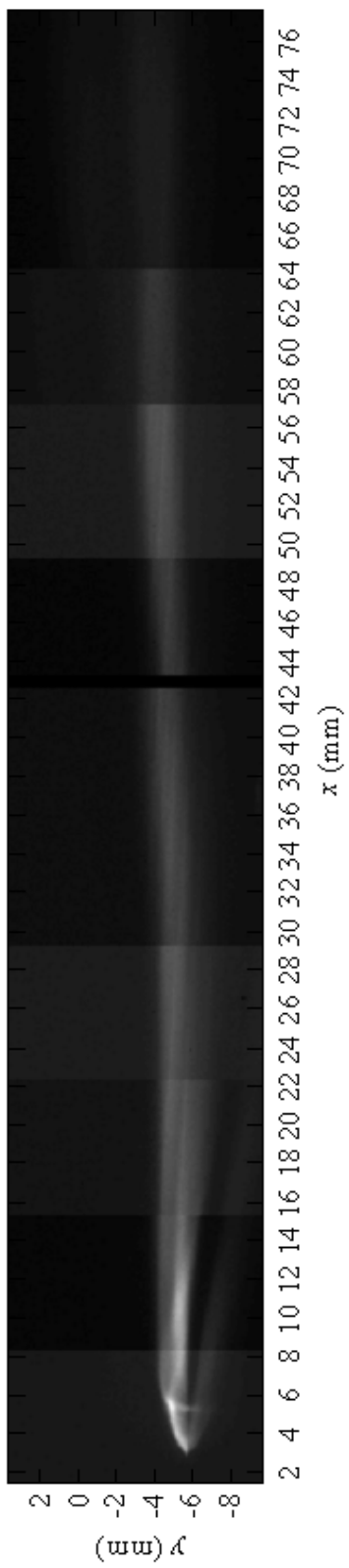


Figure 59. A mosaic of the streamwise images for Trip Scenario A.

6.2.2 Trip Scenario B

Ensemble-averaged streamwise PLIF images for Trip Scenario B (illustrated in Figure 47) are displayed in Figures 60 through 69. The camera gain is 200 for all images and each image is normalized by the maximum intensity at the injector exit. Figure 70 is a mosaic of all streamwise images.

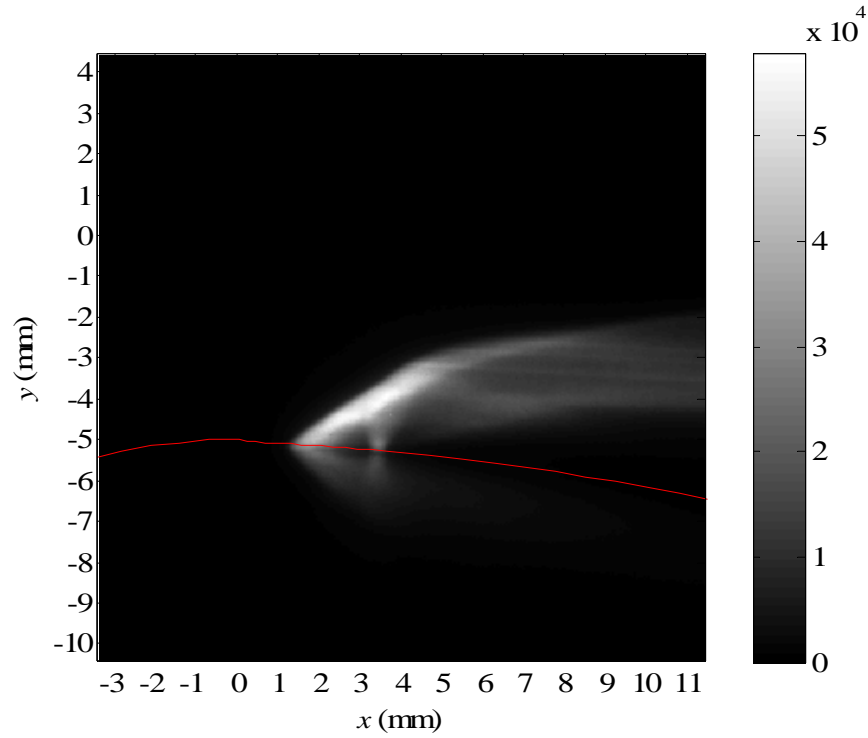


Figure 60. Ensemble average of the streamwise images at the jet exit, for Trip Scenario B. Color bar units are pixel intensity.

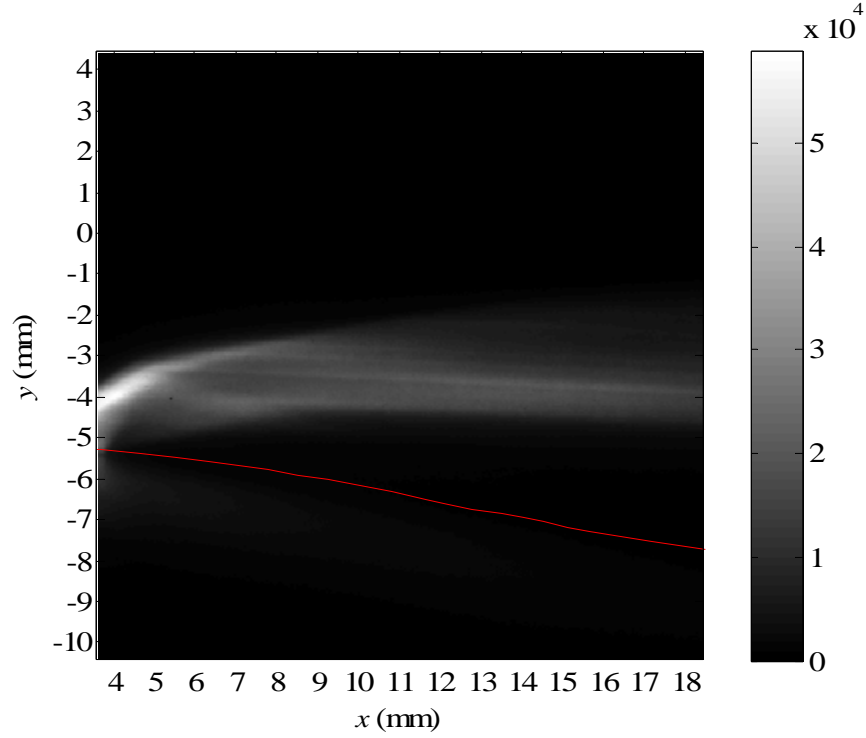


Figure 61. Ensemble average of the streamwise images of the jet from ~ 4 mm to ~ 18 mm downstream of the nozzle throat, for Trip Scenario B. Color bar units are pixel intensity.

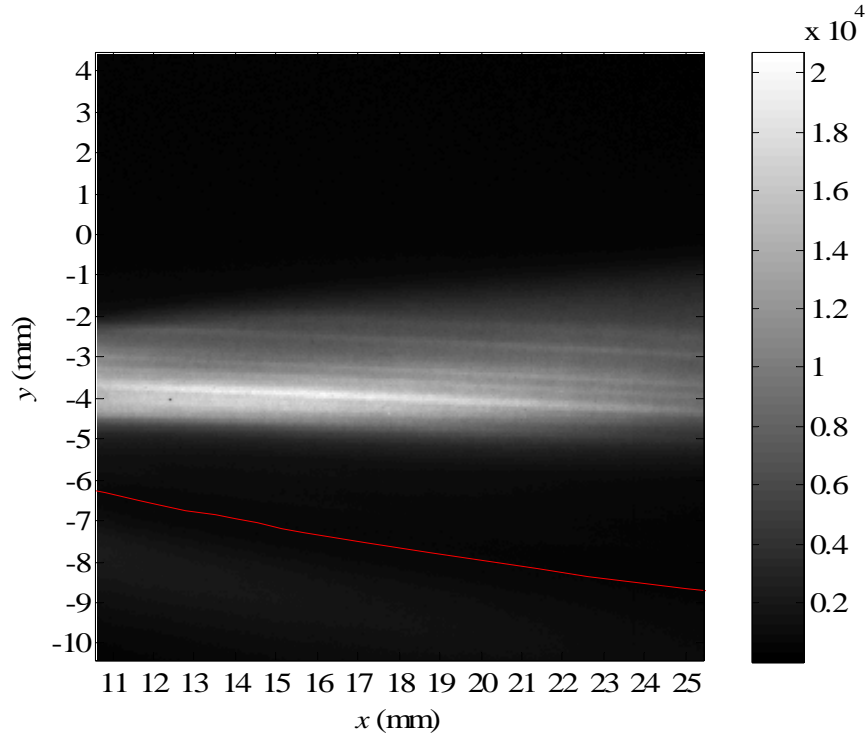


Figure 62. Ensemble average of the streamwise images of the jet from ~ 11 mm to ~ 25 mm downstream of the nozzle throat, for Trip Scenario B. Color bar units are pixel intensity.

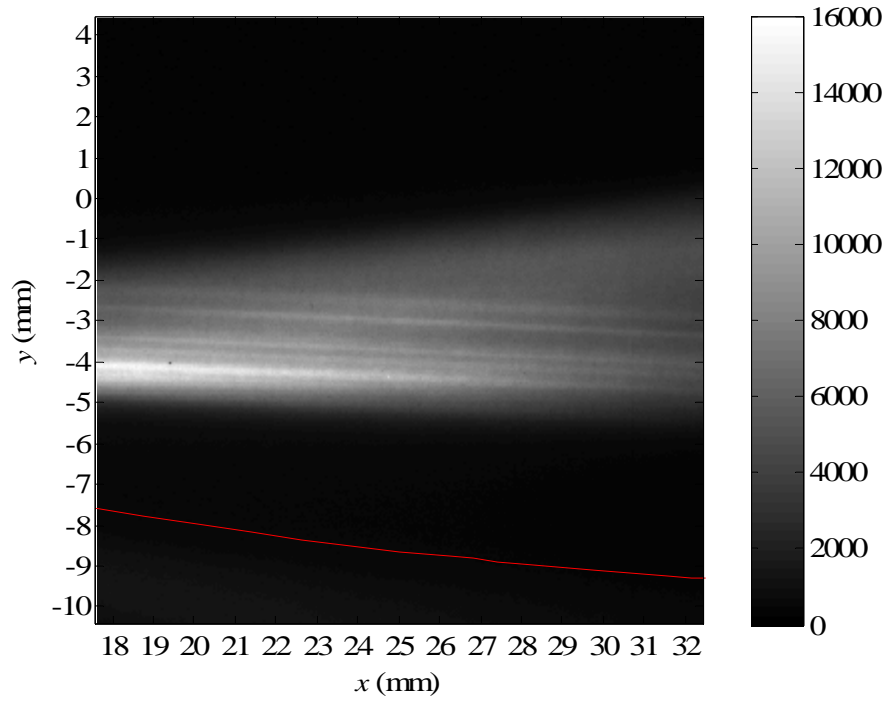


Figure 63. Ensemble average of the streamwise images of the jet from ~18 mm to ~32 mm downstream of the nozzle throat, for Trip Scenario B. Color bar units are pixel intensity.

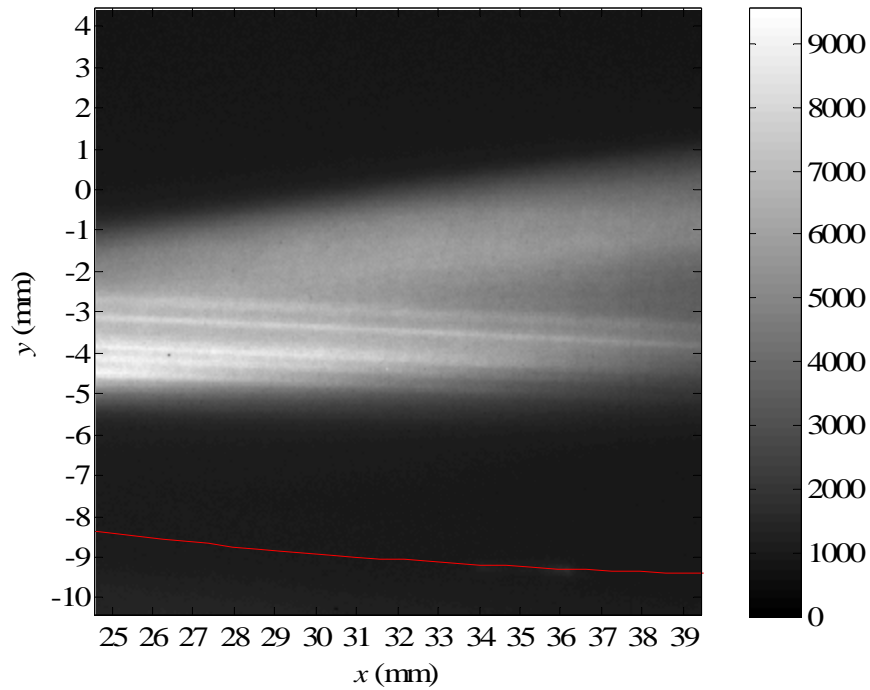


Figure 64. Ensemble average of the streamwise images of the jet from ~25 mm to ~39 mm downstream of the nozzle throat, for Trip Scenario B. Color bar units are pixel intensity.

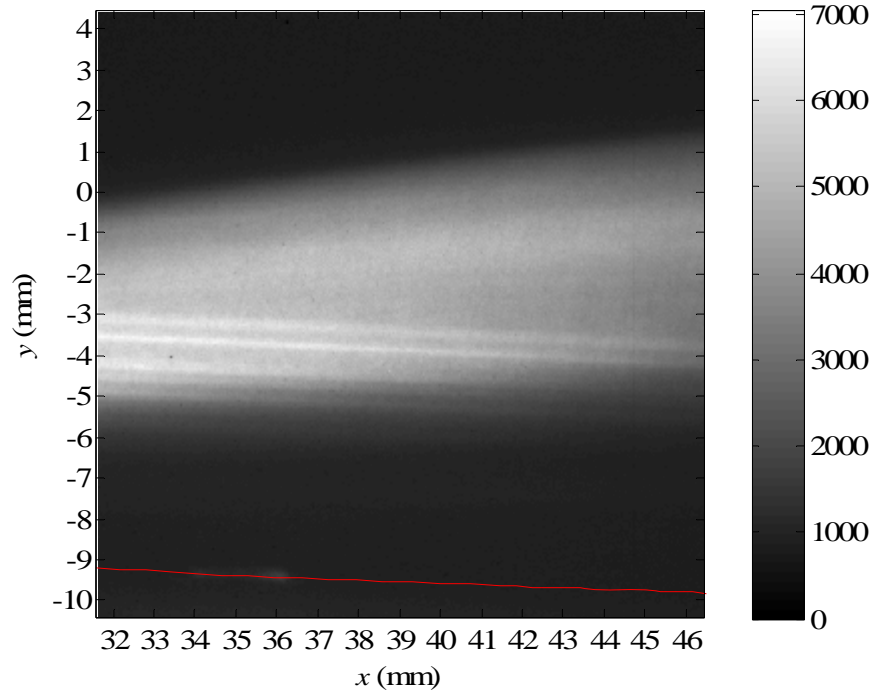


Figure 65. Ensemble average of the streamwise images of the jet from ~32 mm to ~46 mm downstream of the nozzle throat, for Trip Scenario B. Color bar units are pixel intensity.

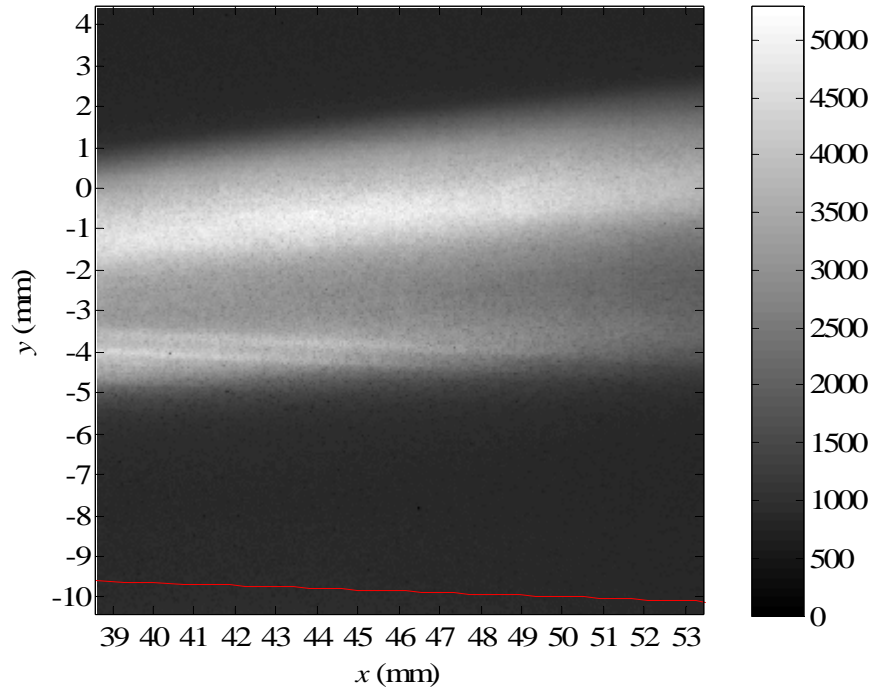


Figure 66. Ensemble average of the streamwise images of the jet from ~39 mm to ~53 mm downstream of the nozzle throat, for Trip Scenario B. Color bar units are pixel intensity.

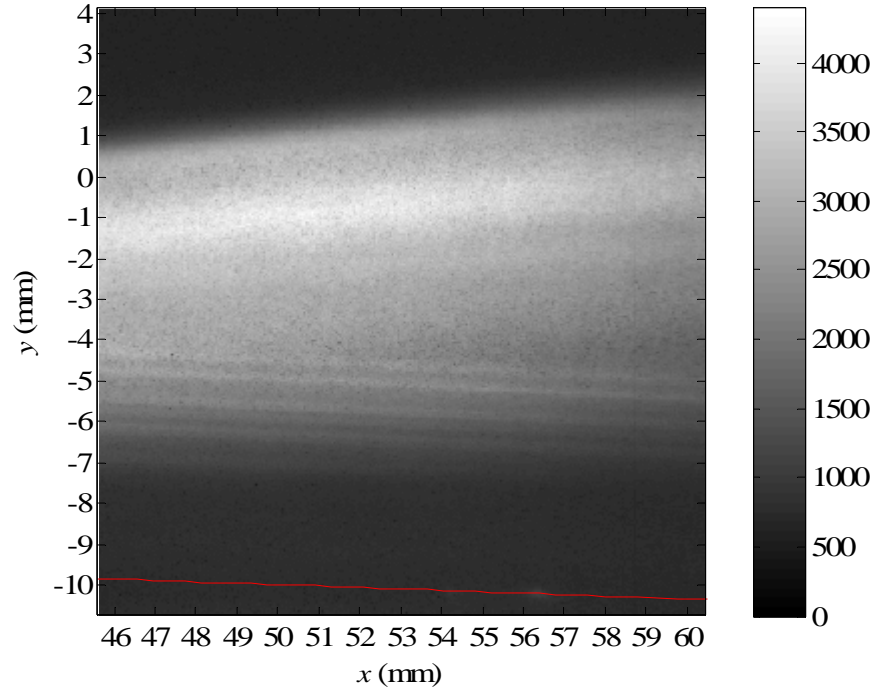


Figure 67. Ensemble average of the streamwise images of the jet from ~45 mm to ~60 mm downstream of the nozzle throat, for Trip Scenario B. Color bar units are pixel intensity.

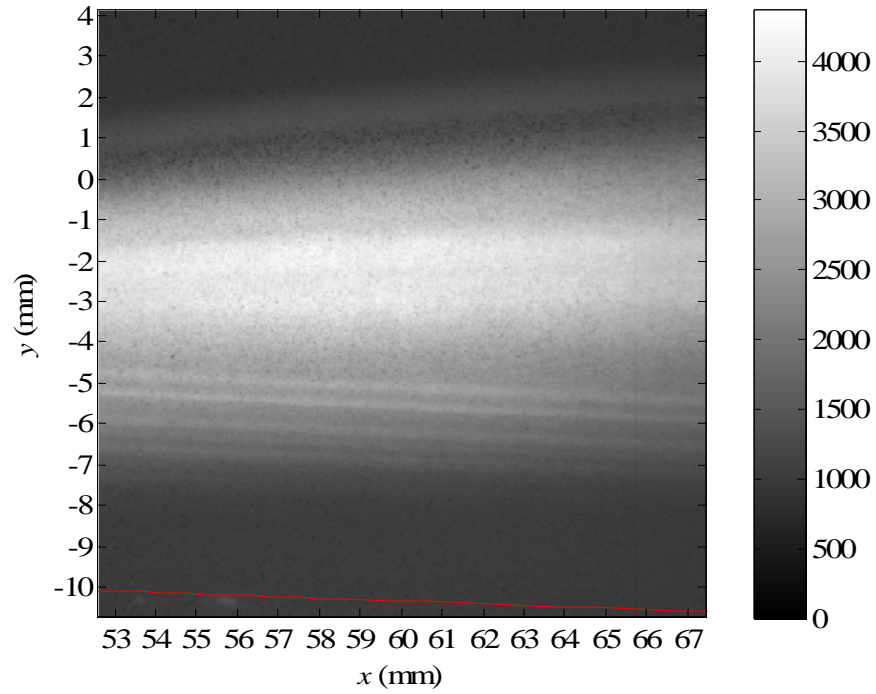


Figure 68. Ensemble average of the streamwise images of the jet from ~53 mm to ~67 mm downstream of the nozzle throat, for Trip Scenario B. Color bar units are pixel intensity.

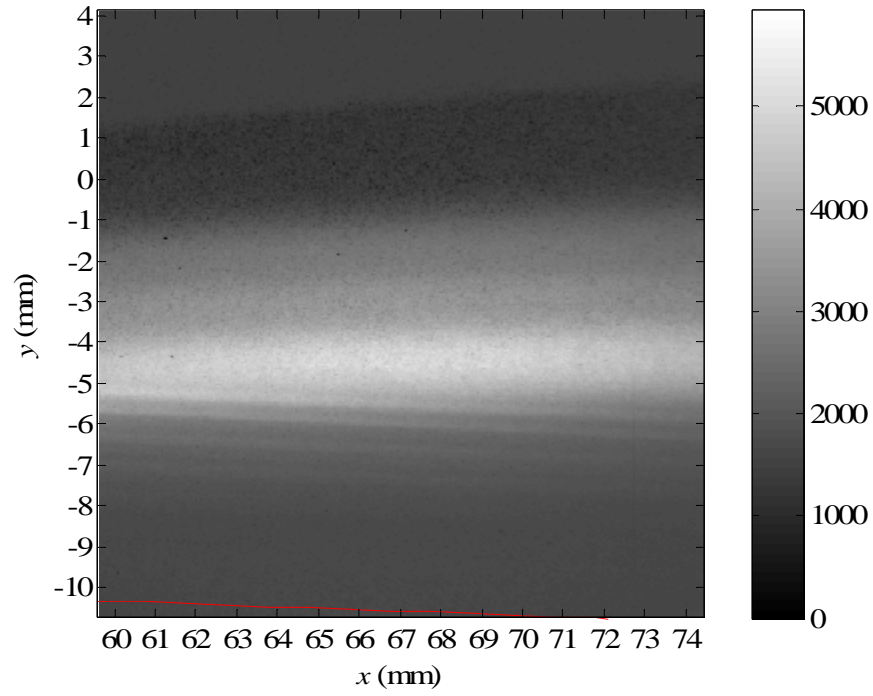


Figure 69. Ensemble average of the streamwise images of the jet from ~60 mm to ~74 mm downstream of the nozzle throat, for Trip Scenario B. Color bar units are pixel intensity.

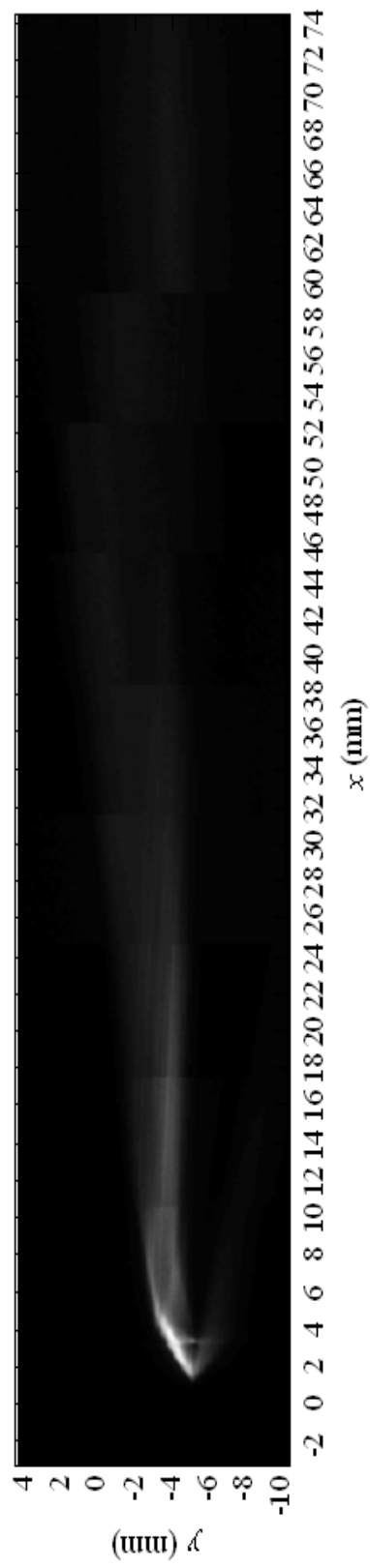


Figure 70. A mosaic of the streamwise images for Trip Scenario B.

6.2.3 Trip Scenario C

Ensemble-averaged streamwise PLIF images for Trip Scenario C (illustrated in Figure 48) are displayed in Figures 71 through 81. The camera gain is 100 for all images and each image is normalized by the maximum intensity at the injector exit. Figure 82 is a mosaic of all streamwise images.

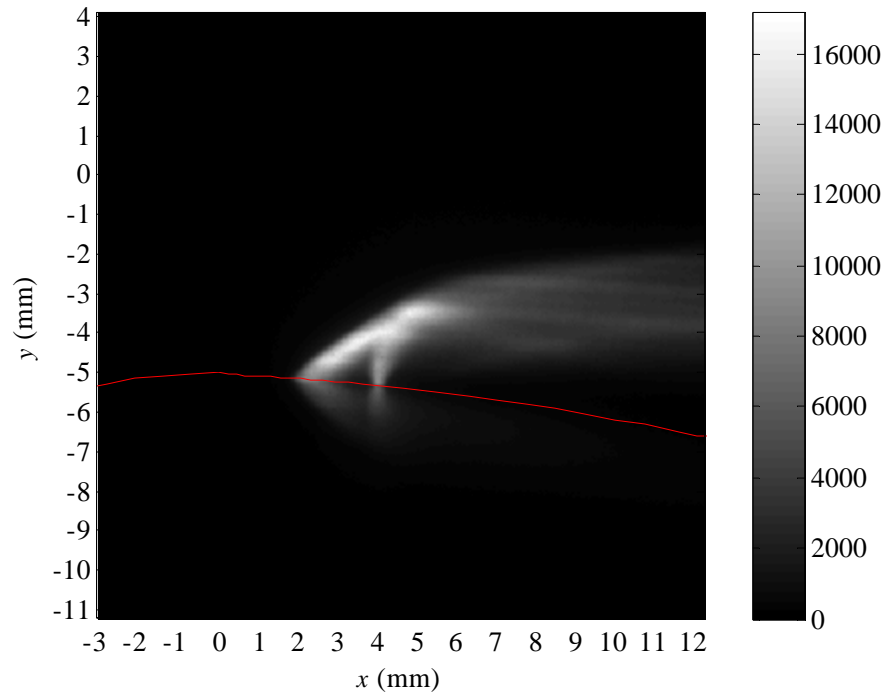


Figure 71. Ensemble average of the streamwise images at the jet exit, for Trip Scenario C. Color bar units are pixel intensity.

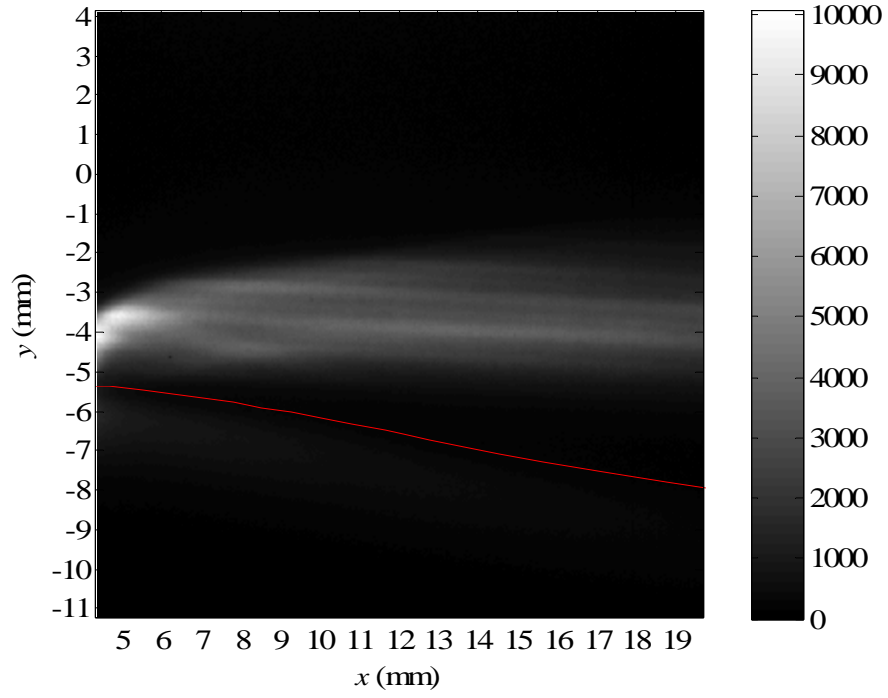


Figure 72. Ensemble average of the streamwise images of the jet from ~5 mm to ~19 mm downstream of the nozzle throat, for Trip Scenario C. Color bar units are pixel intensity.

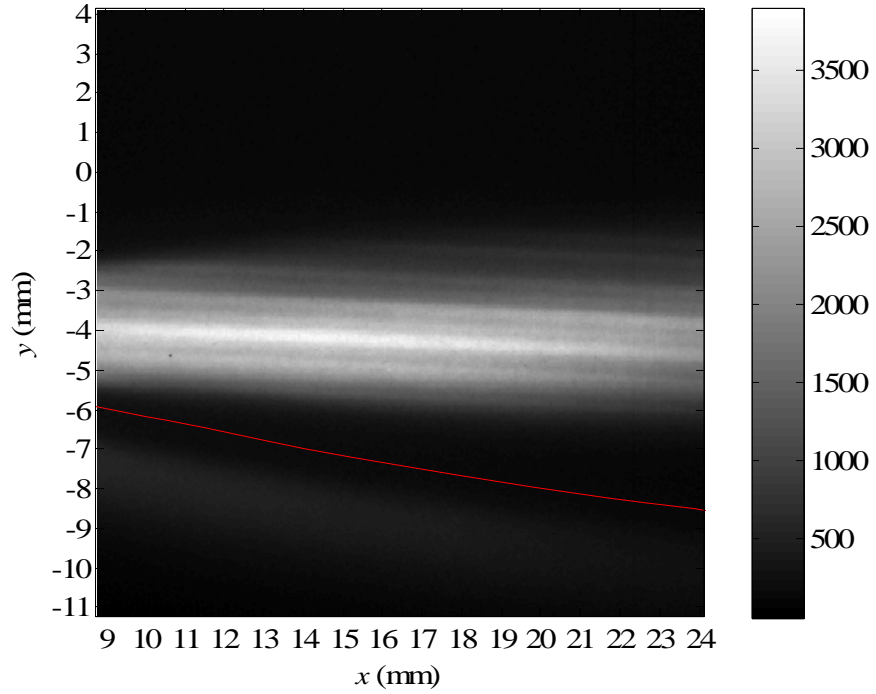


Figure 73. Ensemble average of the streamwise images of the jet from ~9 mm to ~24 mm downstream of the nozzle throat, for Trip Scenario C. Color bar units are pixel intensity.

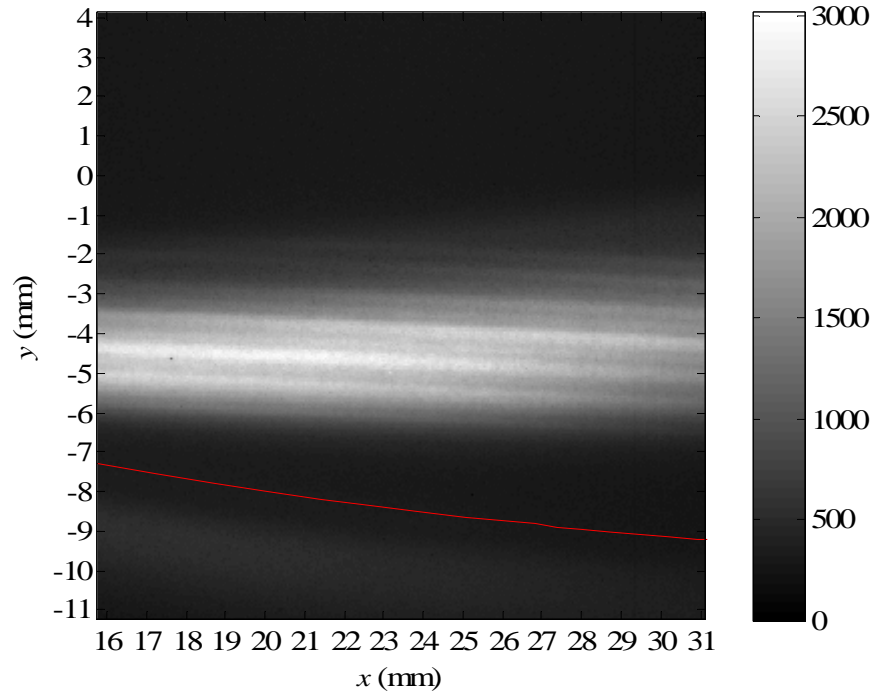


Figure 74. Ensemble average of the streamwise images of the jet from ~16 mm to ~31 mm downstream of the nozzle throat, for Trip Scenario C. Color bar units are pixel intensity.

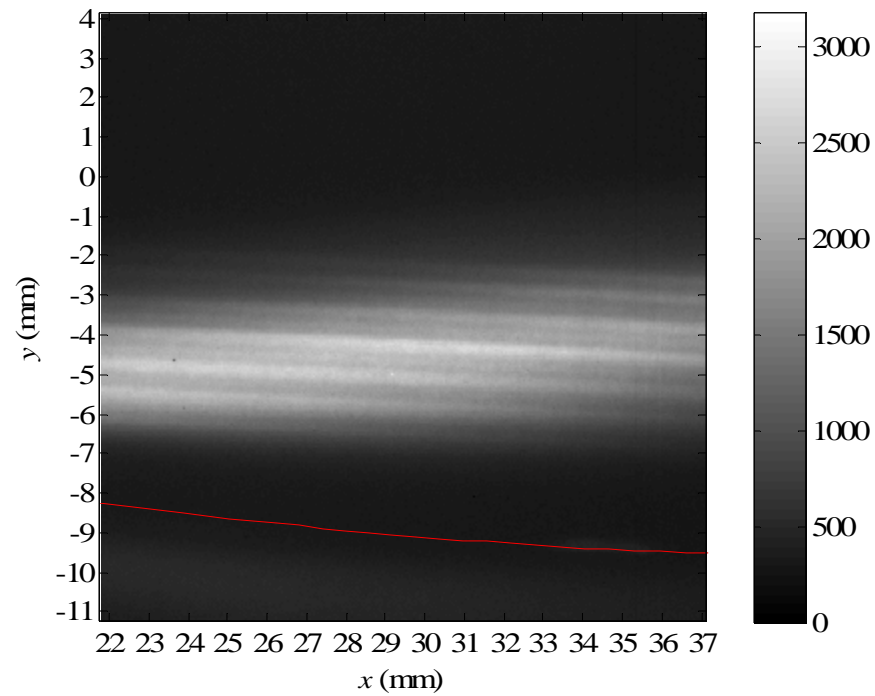


Figure 75. Ensemble average of the streamwise images of the jet from ~22 mm to ~37 mm downstream of the nozzle throat, for Trip Scenario C. Color bar units are pixel intensity.

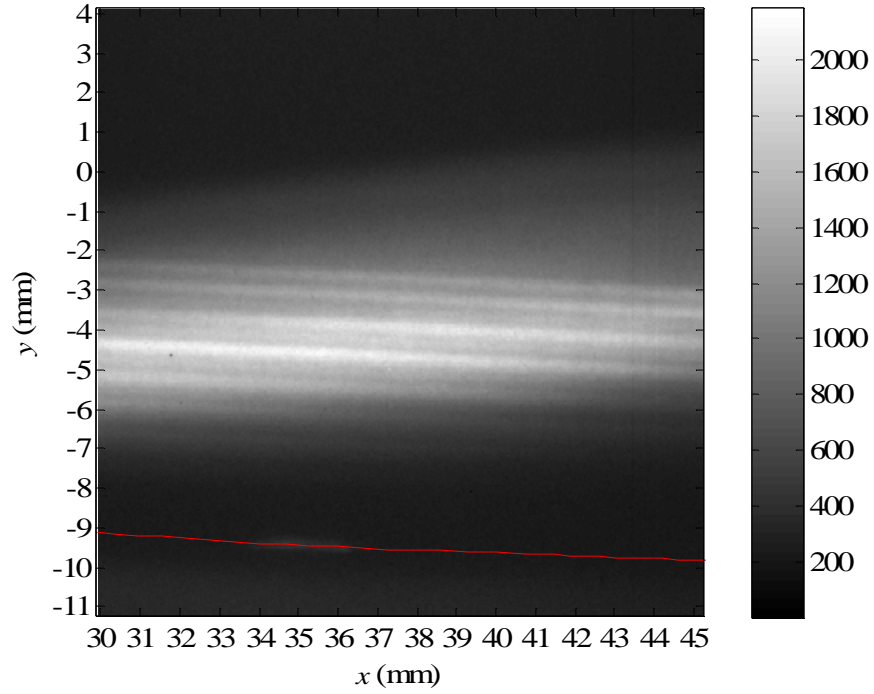


Figure 76. Ensemble average of the streamwise images of the jet from ~30 mm to ~45 mm downstream of the nozzle throat, for Trip Scenario C. Color bar units are pixel intensity.

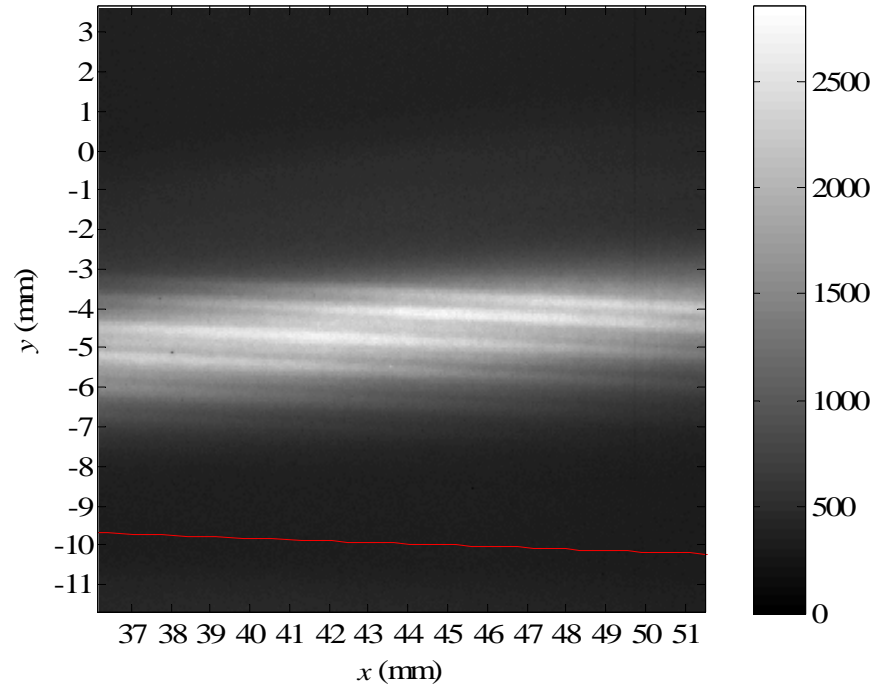


Figure 77. Ensemble average of the streamwise images of the jet from ~36 mm to ~52 mm downstream of the nozzle throat, for Trip Scenario C. Color bar units are pixel intensity.

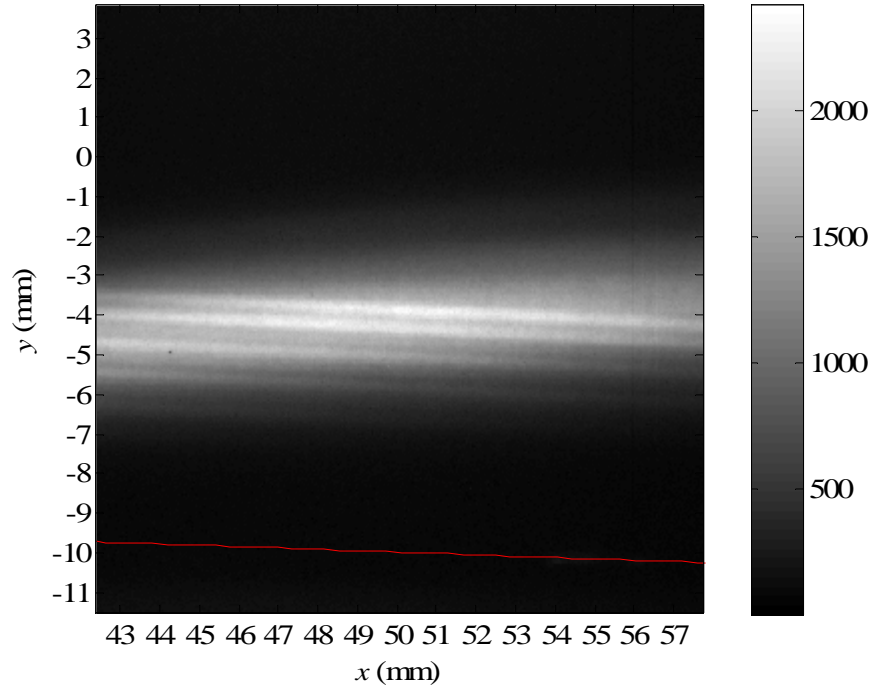


Figure 78. Ensemble average of the streamwise images of the jet from ~42 mm to ~58 mm downstream of the nozzle throat, for Trip Scenario C. Color bar units are pixel intensity.

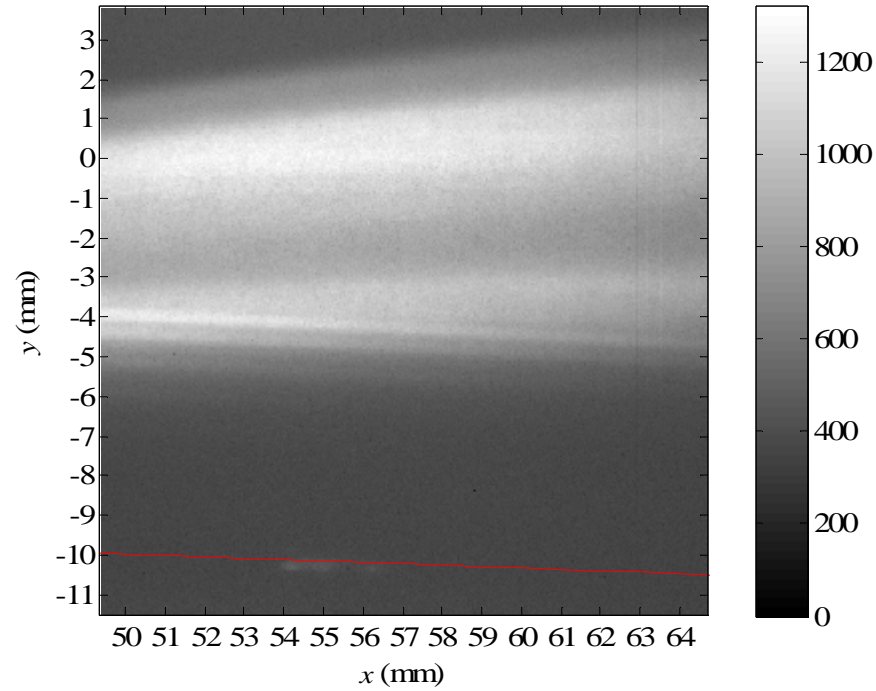


Figure 79. Ensemble average of the streamwise images of the jet from ~49 mm to ~65 mm downstream of the nozzle throat, for Trip Scenario C. Color bar units are pixel intensity.

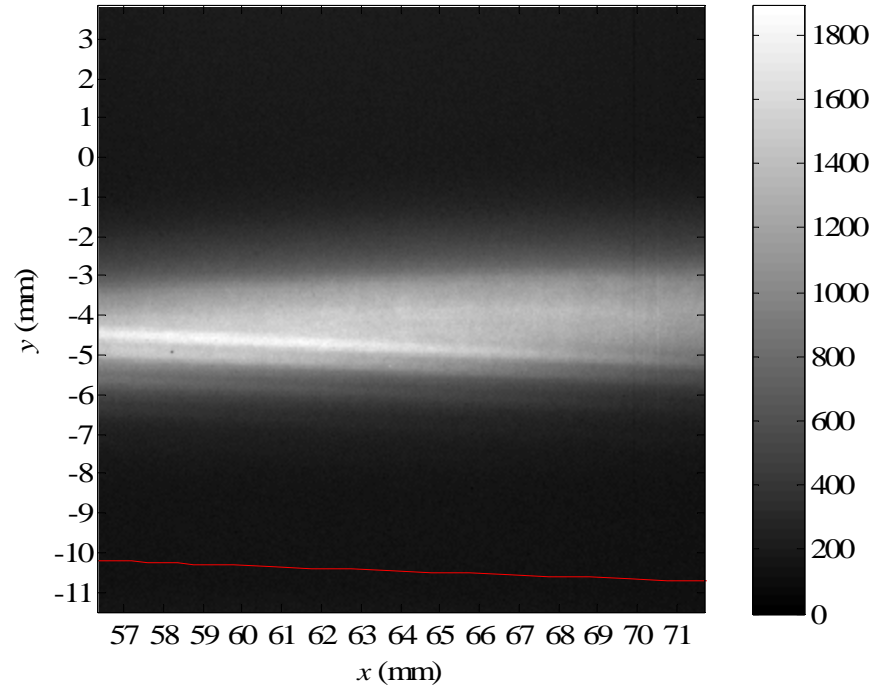


Figure 80. Ensemble average of the streamwise images of the jet from ~56 mm to ~72 mm downstream of the nozzle throat, for Trip Scenario C. Color bar units are pixel intensity.

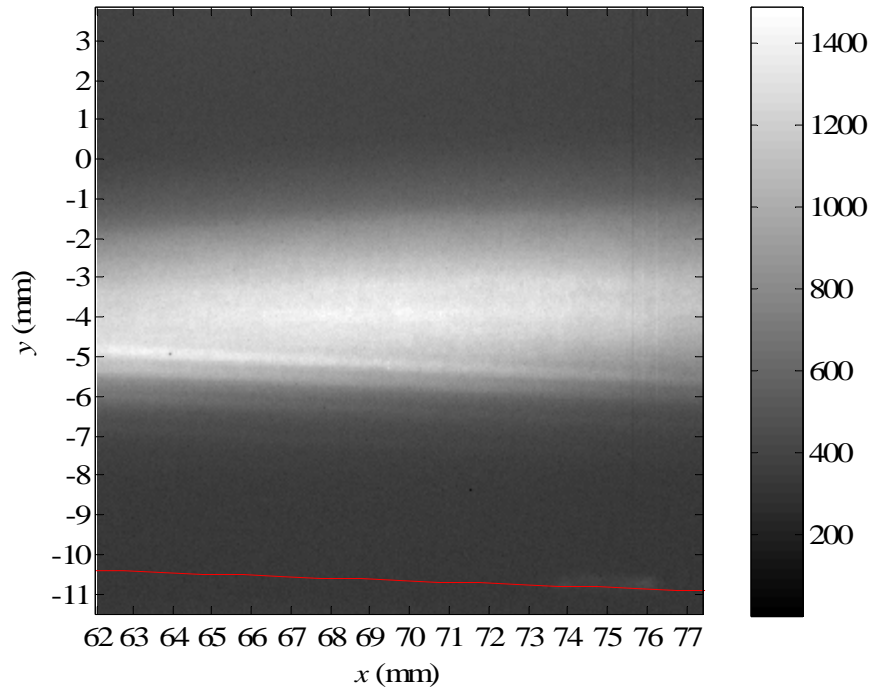


Figure 81. Ensemble average of the streamwise images of the jet from ~62 mm to ~77 mm downstream of the nozzle throat, for Trip Scenario C. Color bar units are pixel intensity.



Figure 82. A mosaic of the streamwise images for Trip Scenario C.

6.3 Oblique-View Ensemble Averages

For each trip jet scenario, oblique-view PLIF images were taken as described in Section 5.2.2. The images were taken in ensembles of 100 and averaged. For each trip jet scenario, the oblique images were normalized by the maximum intensity in the most-upstream oblique image (closest to the jet exit). When present, the top and bottom walls of the nozzle are indicated by red dashes.

6.3.1 Trip Scenario A

Ensemble-averaged oblique PLIF images for Trip Scenario A (see Figure 46) are displayed in Figures 83 through 90. The camera gain is 100 for all images except Figures 85 and 86, where the intensities are adjusted as was done in Figure 29. Each image is normalized by the maximum intensity in Figure 83.

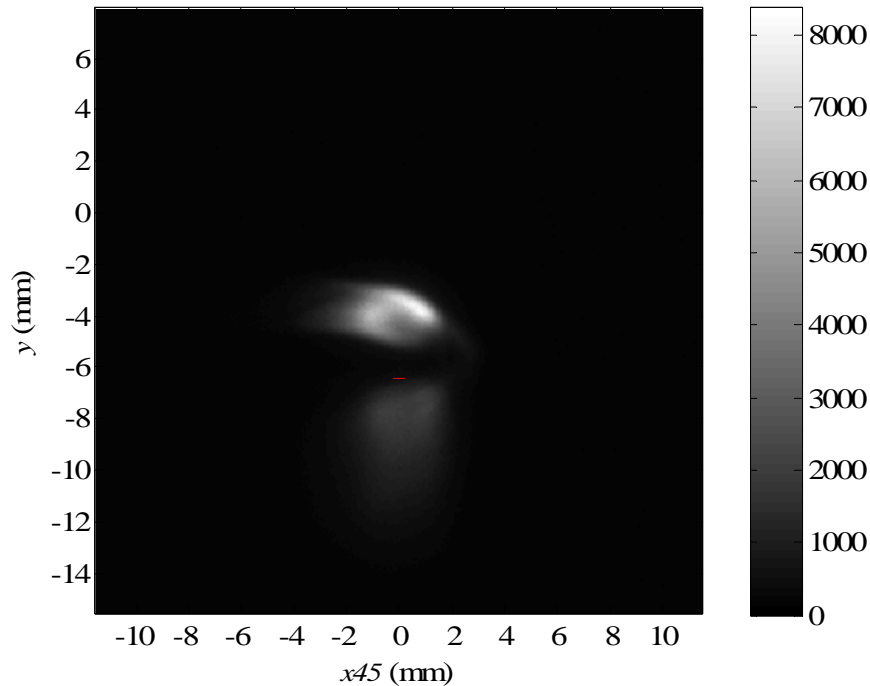


Figure 83. Ensemble average of oblique images at $x \sim 10$ mm, for Trip Scenario A. Color bar units are pixel intensity.

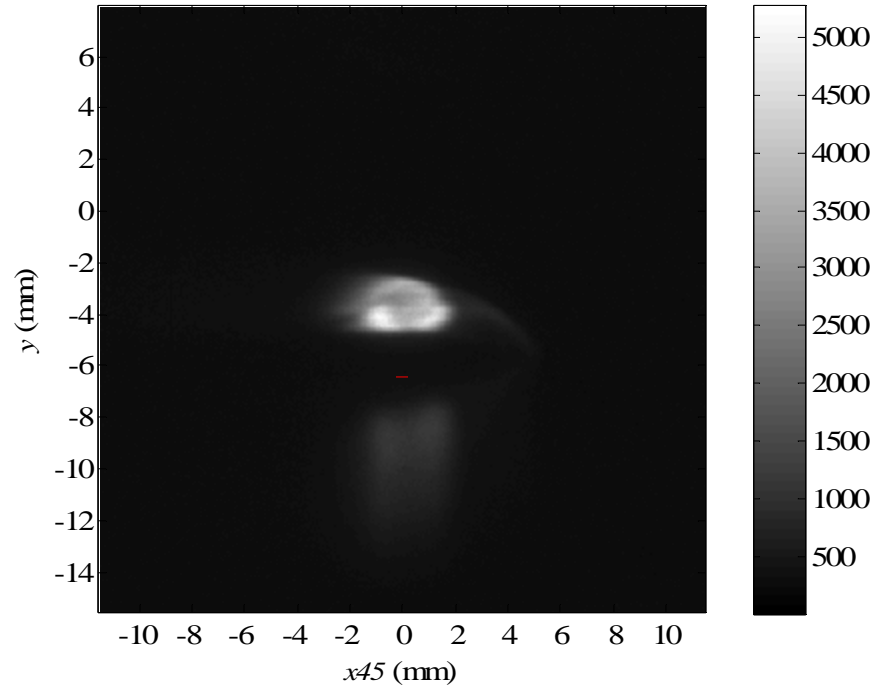


Figure 84. Ensemble average of oblique images at $x \sim 13$ mm, for Trip Scenario A. Color bar units are pixel intensity.

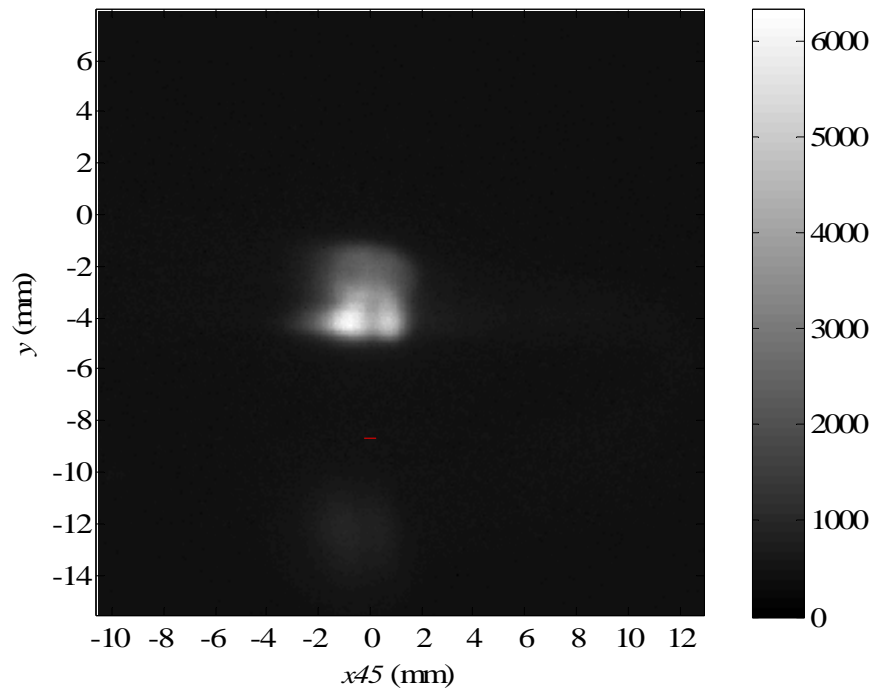


Figure 85. Ensemble average of oblique images at $x \sim 25$ mm, for Trip Scenario A. Color bar units are pixel intensity.

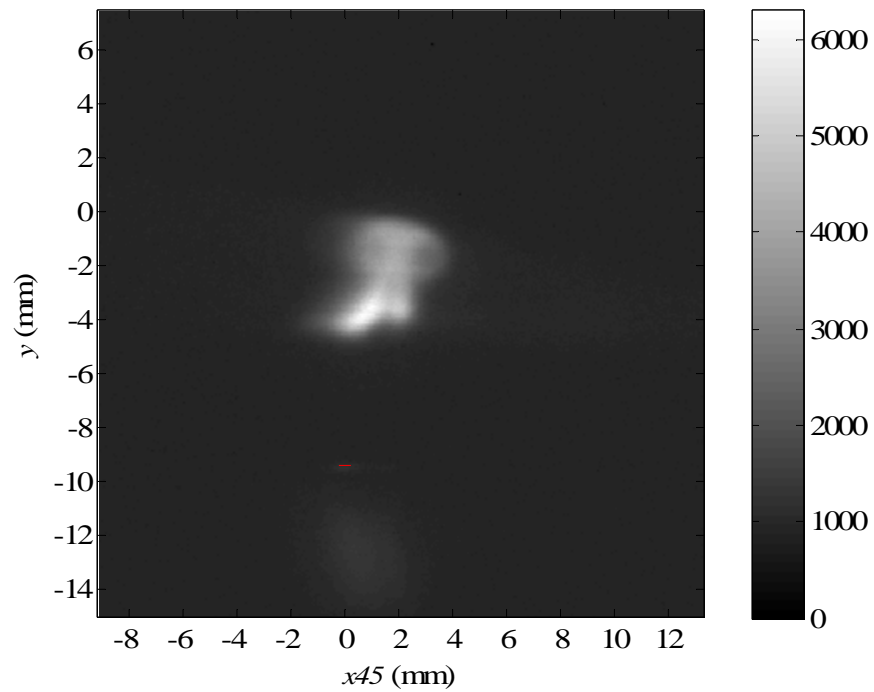


Figure 86. Ensemble average of oblique images at $x \sim 35$ mm, for Trip Scenario A. Color bar units are pixel intensity.

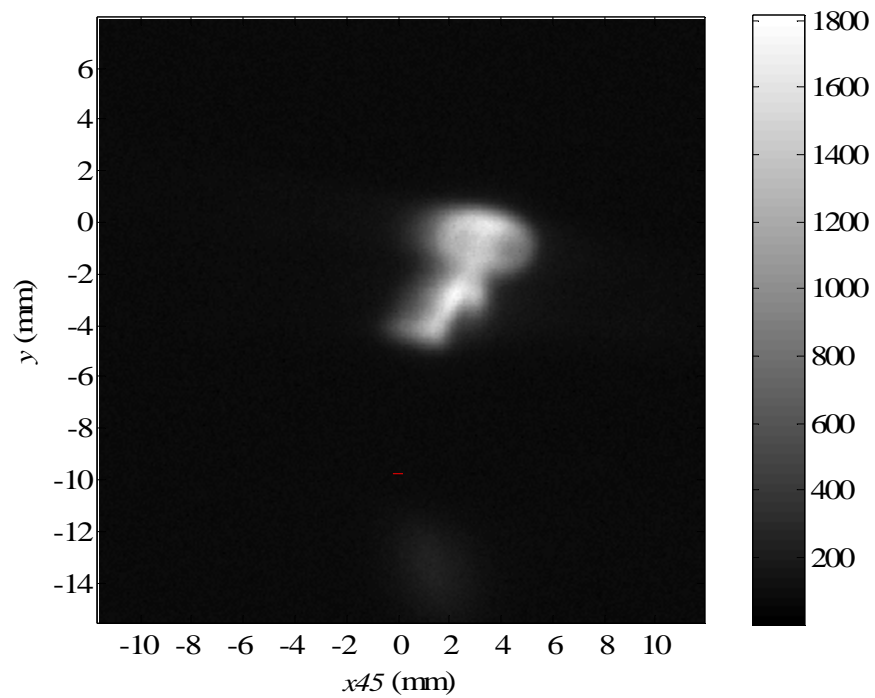


Figure 87. Ensemble average of oblique images at $x \sim 45$ mm, for Trip Scenario A. Color bar units are pixel intensity.

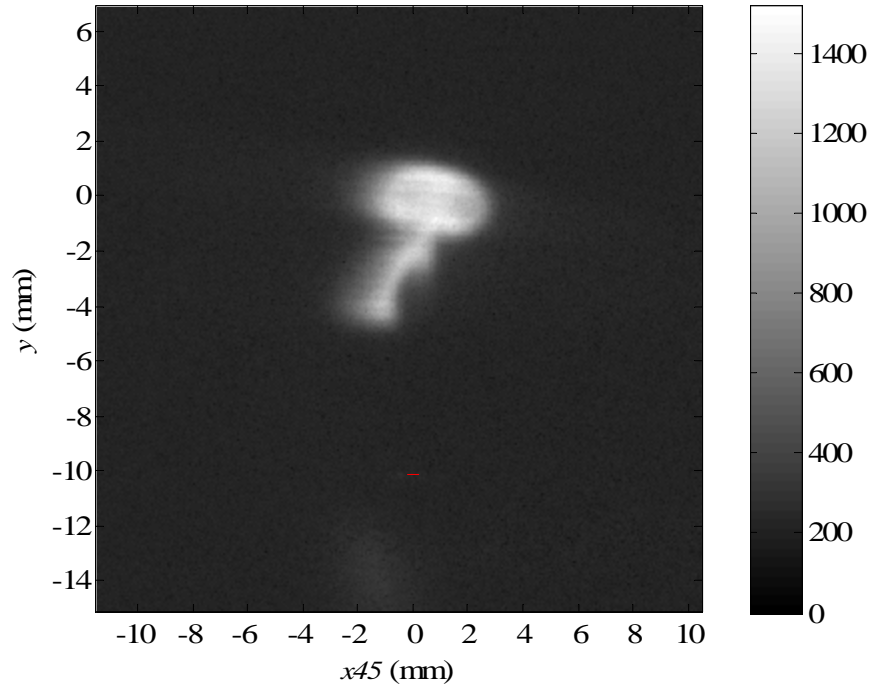


Figure 88. Ensemble average of oblique images at $x \sim 55$ mm, for Trip Scenario A. Color bar units are pixel intensity.

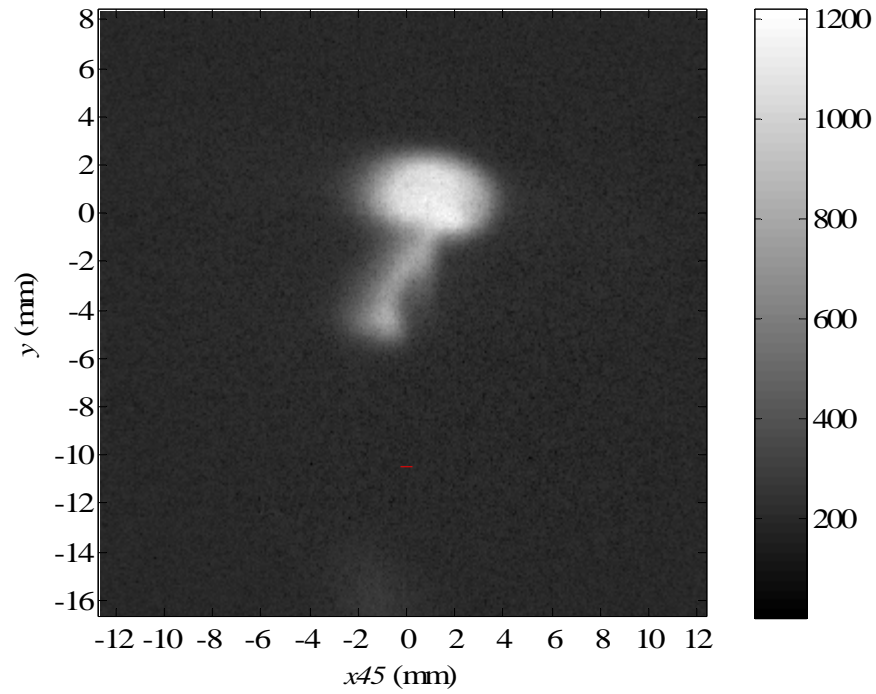


Figure 89. Ensemble average of oblique images at $x \sim 65$ mm, for Trip Scenario A. Color bar units are pixel intensity.

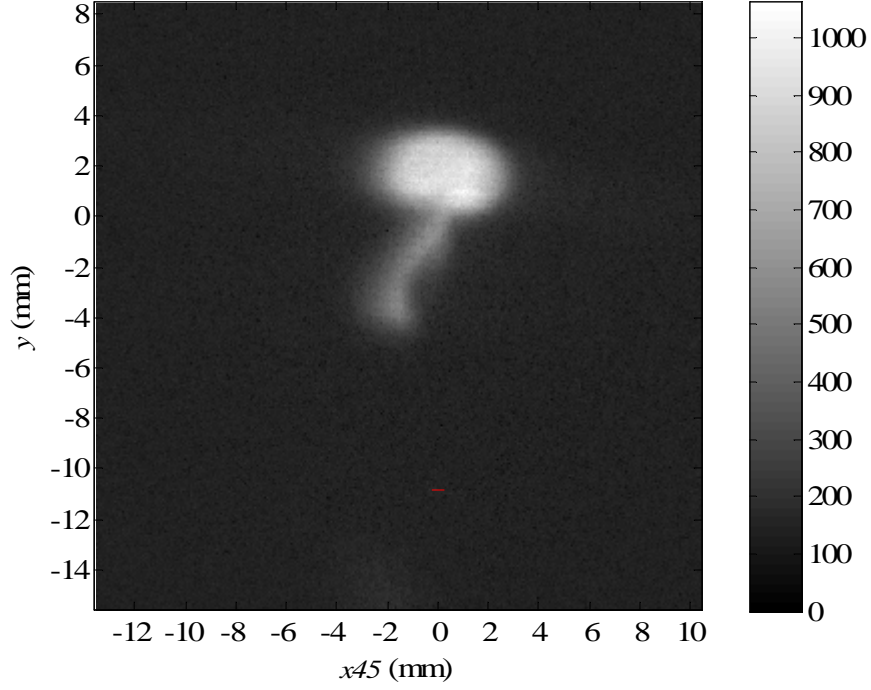


Figure 90. Ensemble average of oblique images at $x \sim 75$ mm, for Trip Scenario A. Color bar units are pixel intensity.

6.3.2 Trip Scenario B

Ensemble-averaged oblique PLIF images for Trip Scenario B (see Figure 47) are displayed in Figure 91 through 97. The camera gain is 100 for all images except Figures 96 and 97, where the intensities are adjusted as was done in Figure 29. Each image is normalized by the maximum intensity in Figure 91.

This trip jet design produced some unsteadiness in the jet. To ensemble-average the oblique structure, the structure in each image was centered using a method described by Vorobieff et al.⁵¹ For each instantaneous image, the center of intensity (x_I , y_I) is determined in the same fashion the center of gravity would be calculated in solid mechanics:

$$x_I = \frac{\sum_i \sum_j I_{i,j} x_{i,j}}{\sum_i \sum_j I_{i,j}}, \quad y_I = \frac{\sum_i \sum_j I_{i,j} y_{i,j}}{\sum_i \sum_j I_{i,j}}, \quad (11)$$

where x_{ij} is the x -pixel, y_{ij} is the y -pixel, and I_{ij} is the intensity at pixel (i,j) . Each instantaneous image was then translated to the center pixel for each of the 100 images in the ensemble. The ensemble was then averaged. The centering allows for a better representation of the oblique structure with fluctuating instantaneous images. The fluctuating ensembles were centered, but the steady ensembles were not.

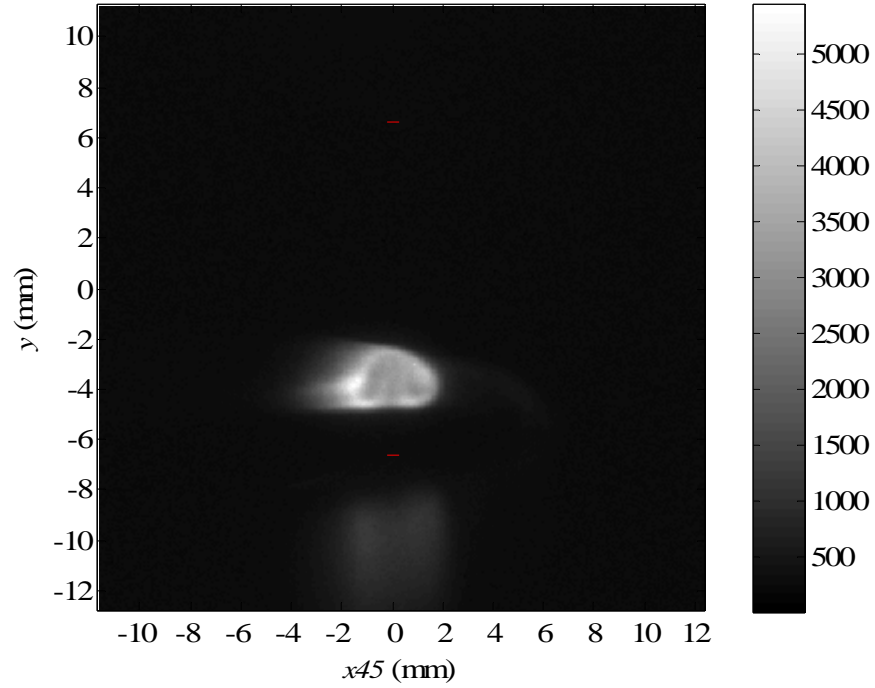


Figure 91. Ensemble average of oblique images at $x \sim 12.3$ mm, for Trip Scenario B. Color bar units are pixel intensity.

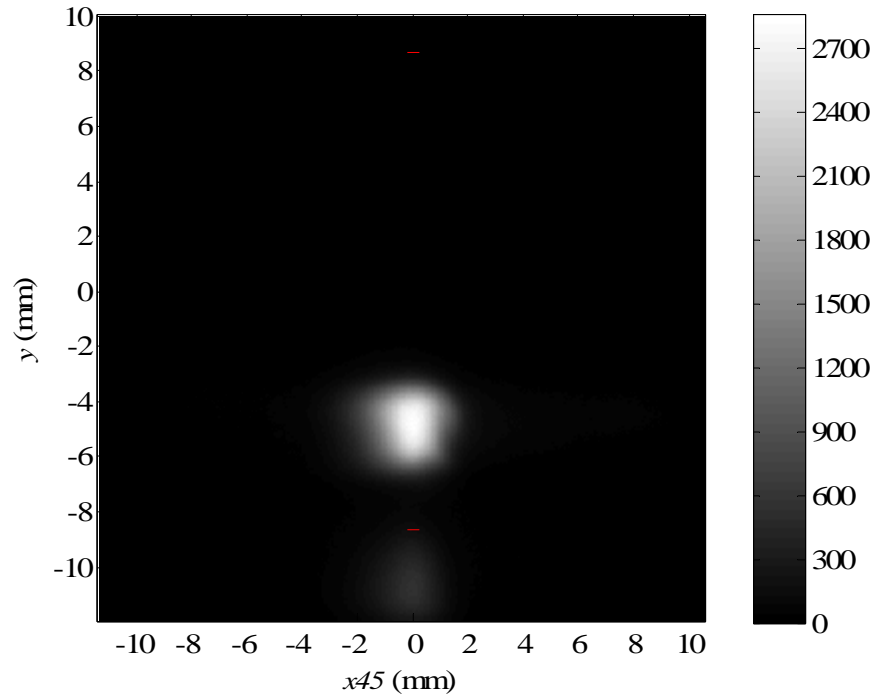


Figure 92. Ensemble average of oblique images at $x \sim 25$ mm, for Trip Scenario B. Instantaneous images were centered. Color bar units are pixel intensity.

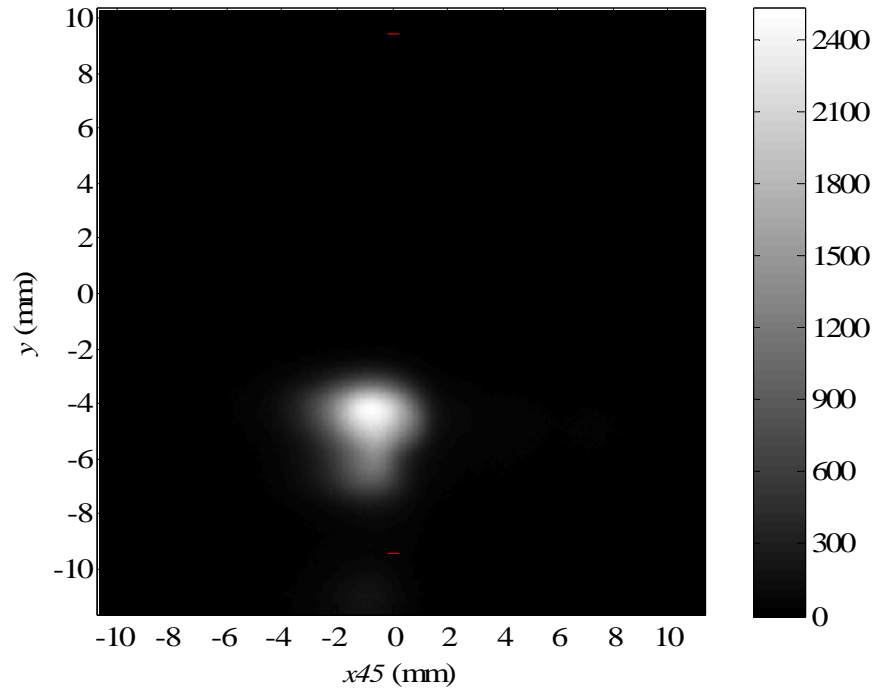


Figure 93. Ensemble average of oblique images of the jet at $x \sim 35$ mm, for Trip Scenario B. Instantaneous images were centered. Color bar units are pixel intensity.

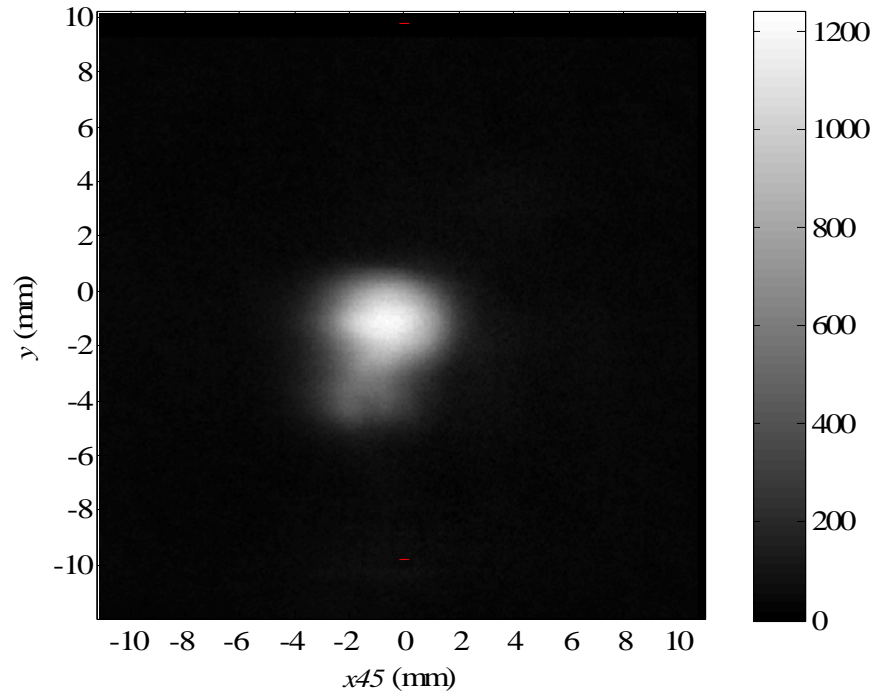


Figure 94. Ensemble average of oblique images at $x \sim 45$ mm, for Trip Scenario B. Instantaneous images were centered. Color bar units are pixel intensity.

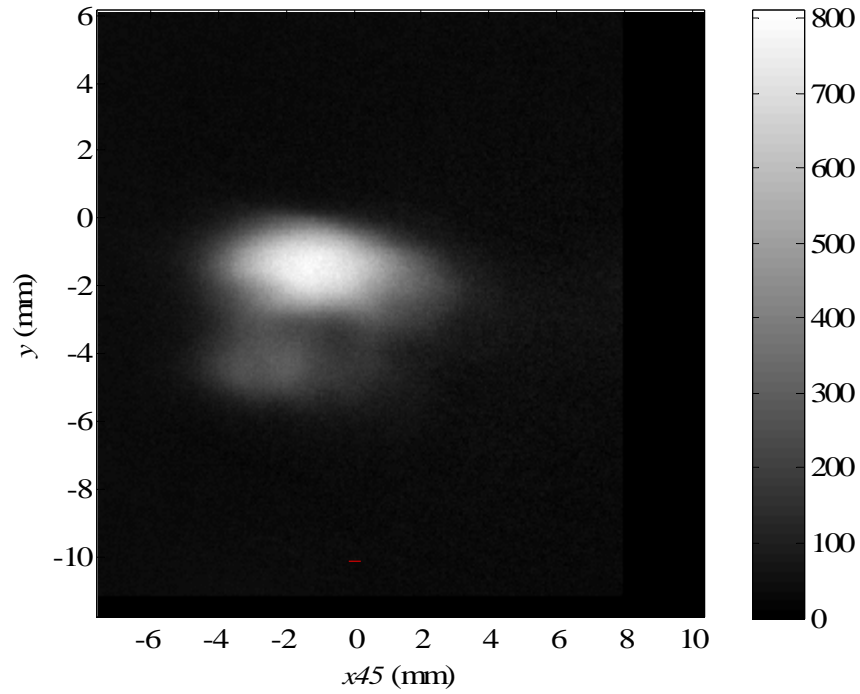


Figure 95. Ensemble average of oblique images at $x \sim 55$ mm, for Trip Scenario B. Instantaneous images were centered. Color bar units are pixel intensity.

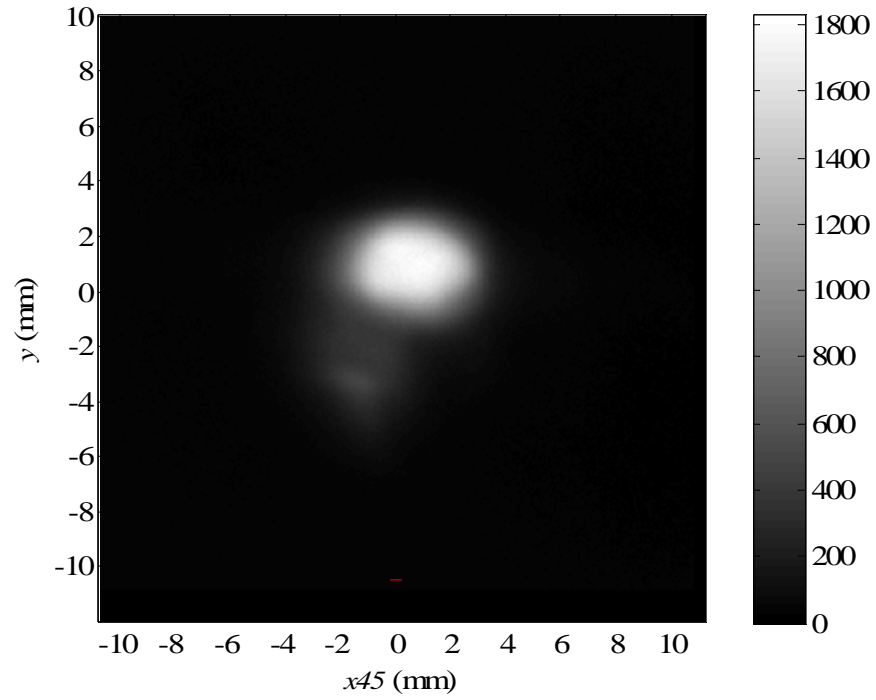


Figure 96. Ensemble average of oblique images of the jet at $x \sim 65$ mm, for Trip Scenario B. Instantaneous images were centered. Color bar units are pixel intensity.

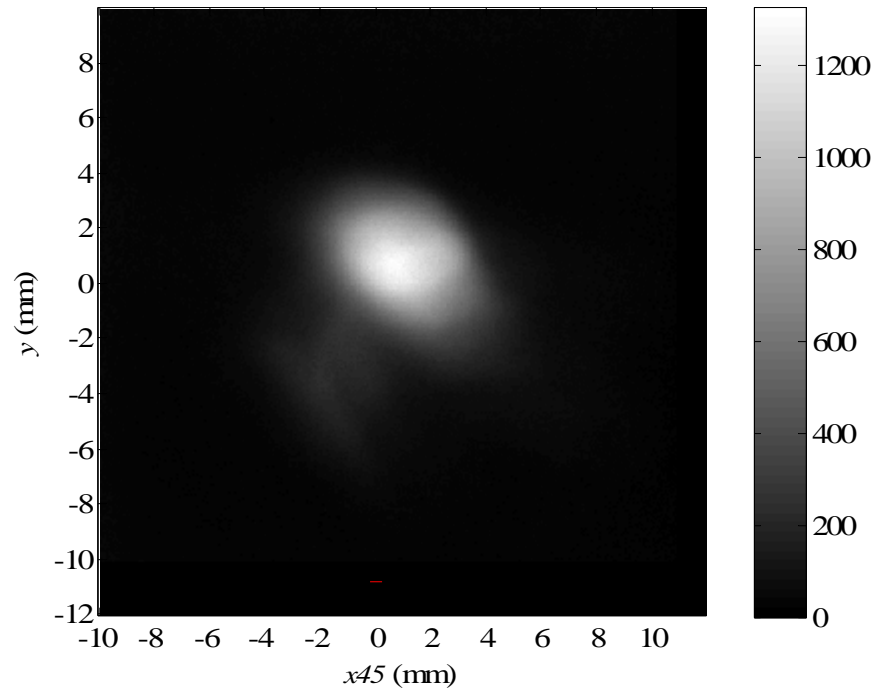


Figure 97. Ensemble average of oblique images at $x \sim 75$ mm, for Trip Scenario B. Instantaneous images were centered. Color bar units are pixel intensity.

6.3.3 Trip Scenario C

Ensemble-averaged oblique PLIF images for Trip Scenario C (see Figure 48) are displayed in Figures 98 through 105. The camera gain is 100 for all images and each image is normalized by the maximum intensity in Figure 98. Trip Scenario C also produced some unsteadiness in the jet. The ensembles with unsteady instantaneous images were centered, as described in Section 6.3.2.

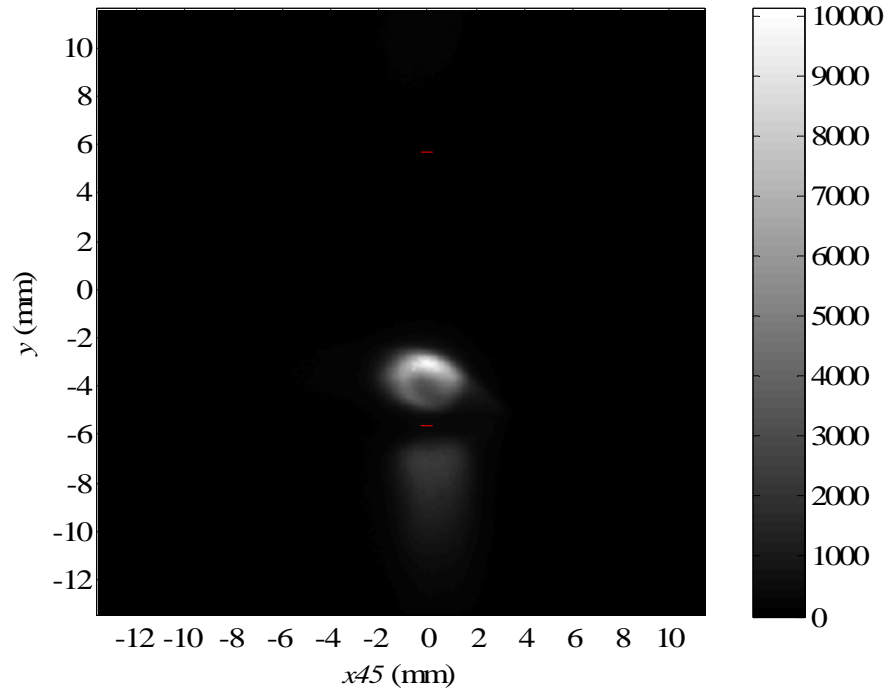


Figure 98. Ensemble average of oblique images at $x \sim 7$ mm, for Trip Scenario C. Color bar units are pixel intensity.

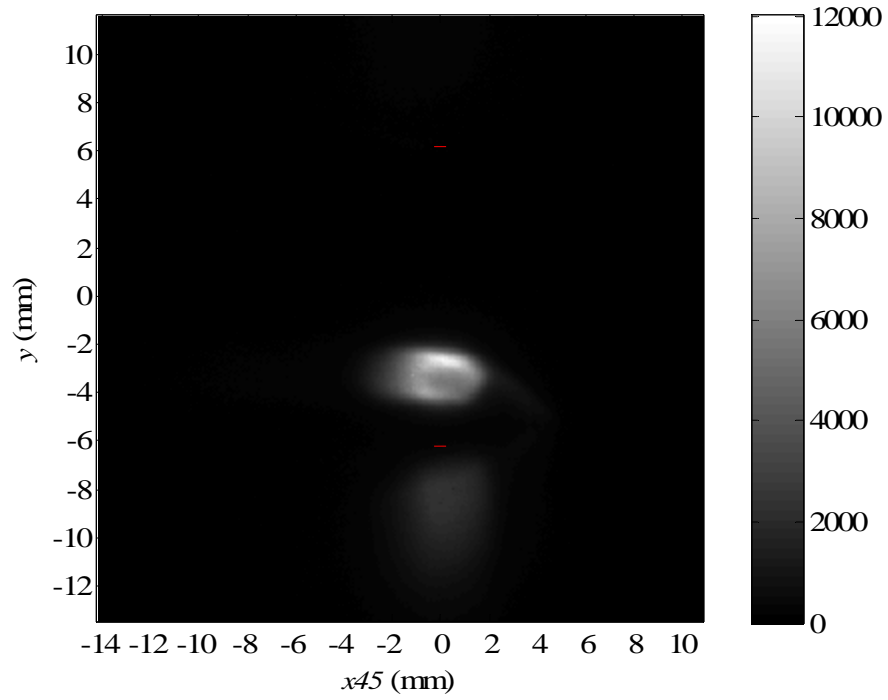


Figure 99. Ensemble average of oblique images at $x \sim 10.5$ mm, for Trip Scenario C. Color bar units are pixel intensity.

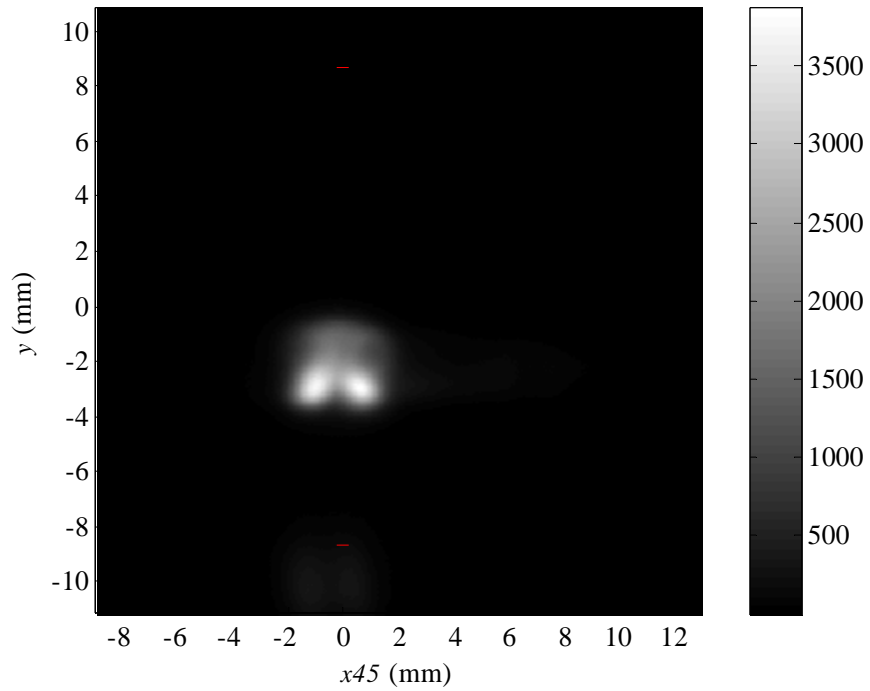


Figure 100. Ensemble average of oblique images at $x \sim 25$ mm, for Trip Scenario C. Instantaneous images were centered. Color bar units are pixel intensity.

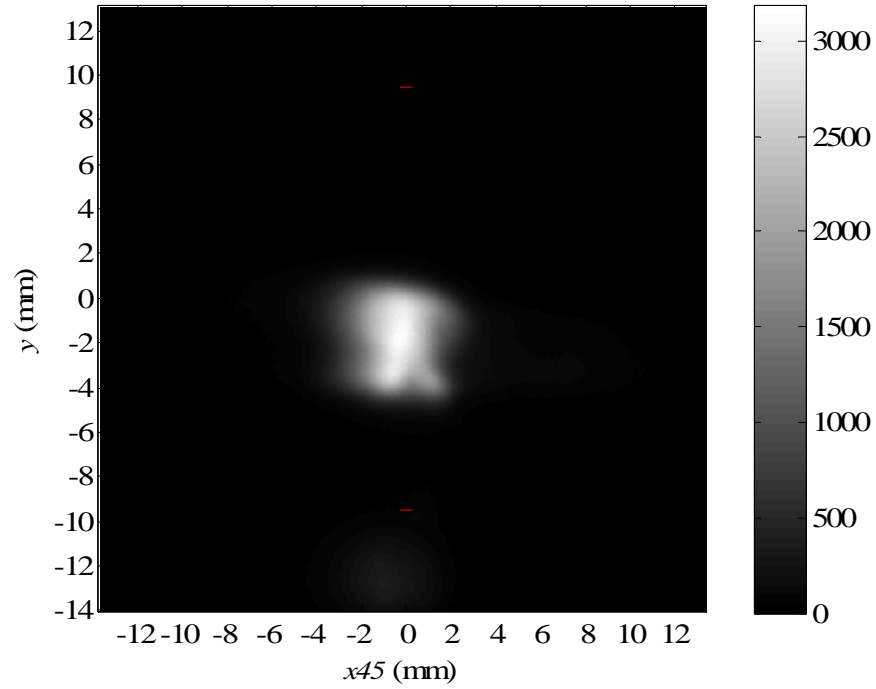


Figure 101. Ensemble average of oblique images at $x \sim 35$ mm, for Trip Scenario C. Instantaneous images were centered. Color bar units are pixel intensity.

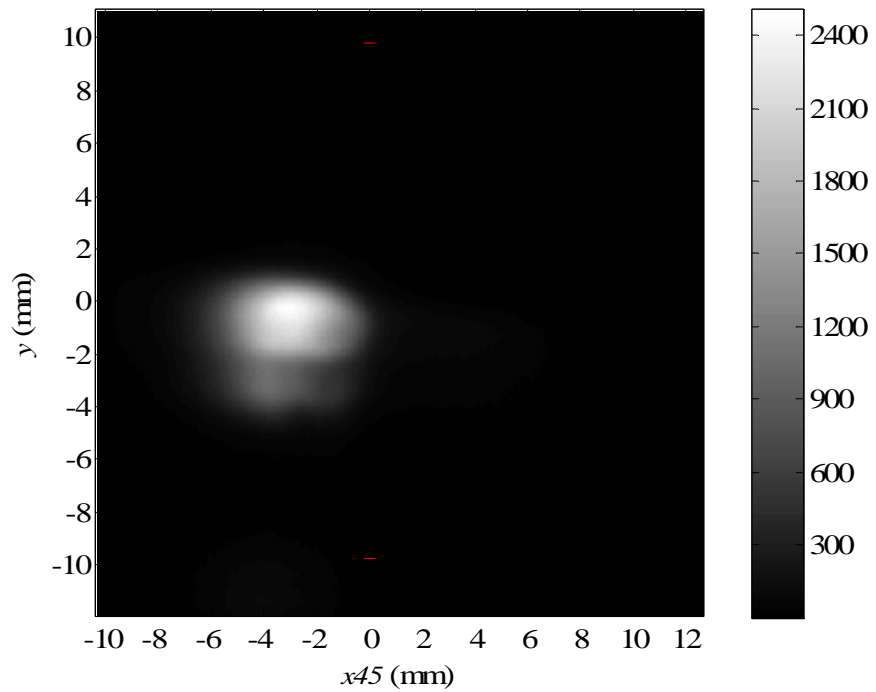


Figure 102. Ensemble average of oblique images at $x \sim 45$ mm, for Trip Scenario C. Instantaneous images were centered. Color bar units are pixel intensity.

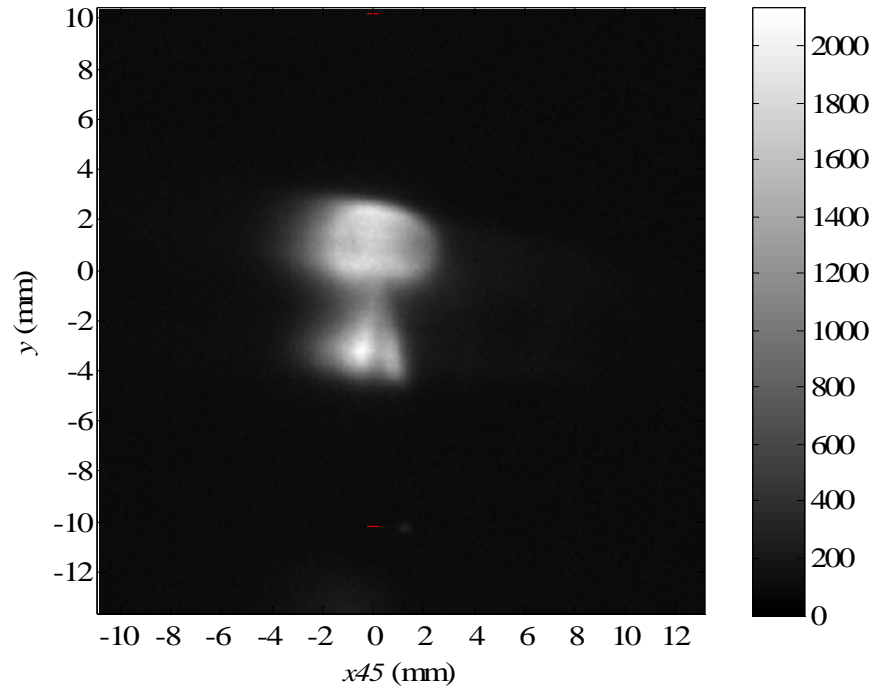


Figure 103. Ensemble average of oblique images at $x \sim 55$ mm, for Trip Scenario C. Color bar units are pixel intensity.

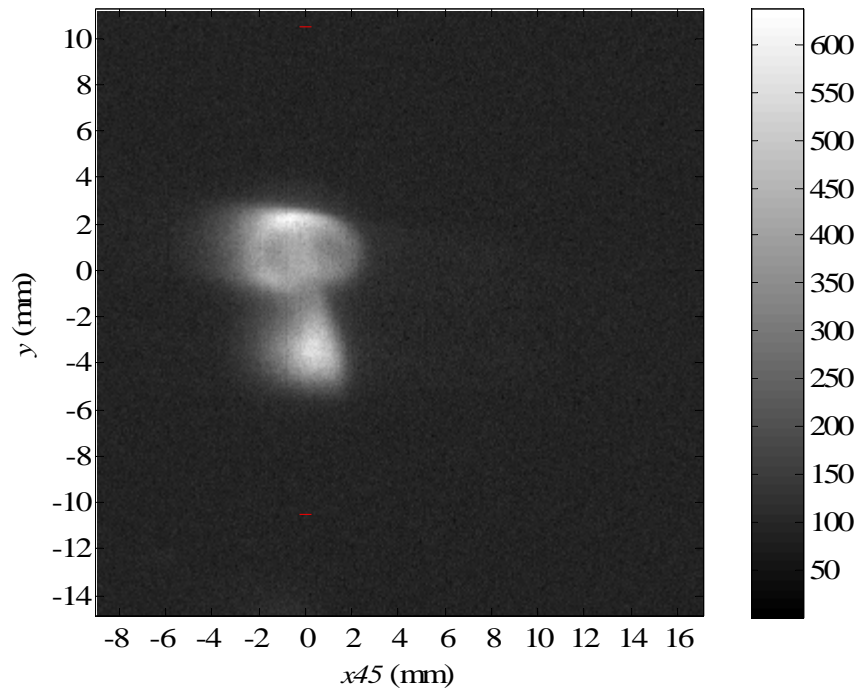


Figure 104. Ensemble average of oblique images at $x \sim 65$ mm, for Trip Scenario C. Color bar units are pixel intensity.

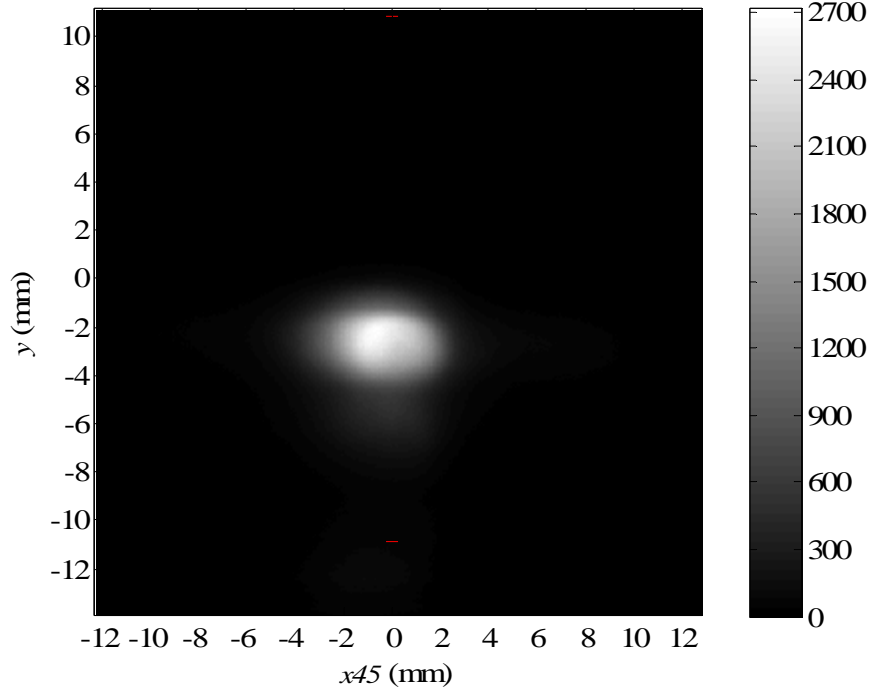


Figure 105. Ensemble average of oblique images at $x \sim 75$ mm, for Trip Scenario C. Instantaneous images were centered. Color bar units are pixel intensity.

6.4 Streamwise-View Histograms

A histogram analysis was performed on the ensemble-averaged streamwise images for Trip Scenarios A, B, and C. The analysis is described in detail in Section 5.3. The normalized intensity is displayed on the x -axis, while the number of pixels at a specific intensity is displayed on the z -axis. The downstream location of each histogram is displayed on the y -axis, where the downstream location of the streamwise image is taken as the location of the center pixel.

6.4.1 Trip Scenario A

Histograms for the ensemble-averaged streamwise images for Trip Scenario A are shown in Figure 106. In all the histograms, a zero-intensity peak is present, representing the primary flow. The high-intensity peak (representative of the injected flow) in each histogram is decreasing in intensity with downstream distance. The intensity decrease is greater than

the decrease shown in the histograms for the single injector (shown in Figure 40). This greater intensity decrease signifies that the trip jet enables greater mixing between the primary and injected flows.

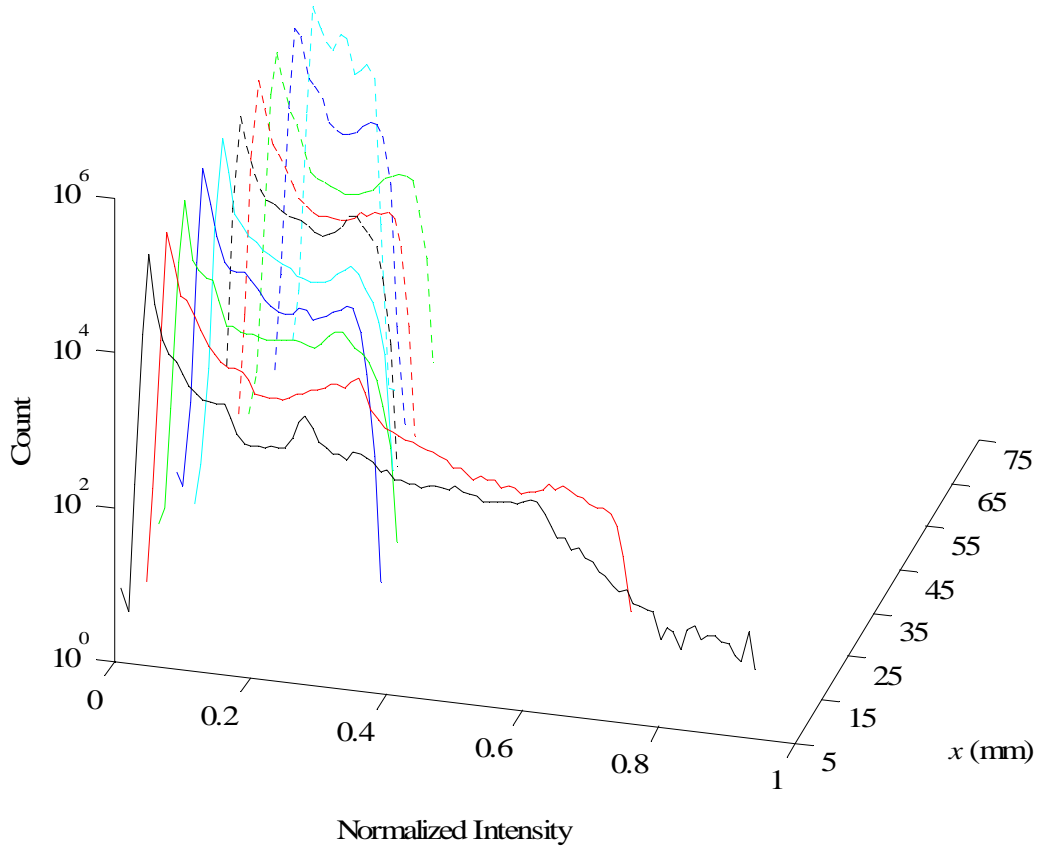


Figure 106. Histograms of the ensemble-averaged streamwise images from Figures 49 to 58, Trip Scenario A. The intensity of each image is normalized by the maximum intensity in Figure 49. The x -location is measured at the center of the image.

6.4.2 Trip Scenario B

Histograms for the ensemble-averaged streamwise images for Trip Scenario B are displayed in Figure 107. The second, high-intensity peak has an even greater decrease in intensity than the high-intensity peaks from Figure 106, which is evidence that Trip Scenario B has even greater mixing than Trip Scenario A.

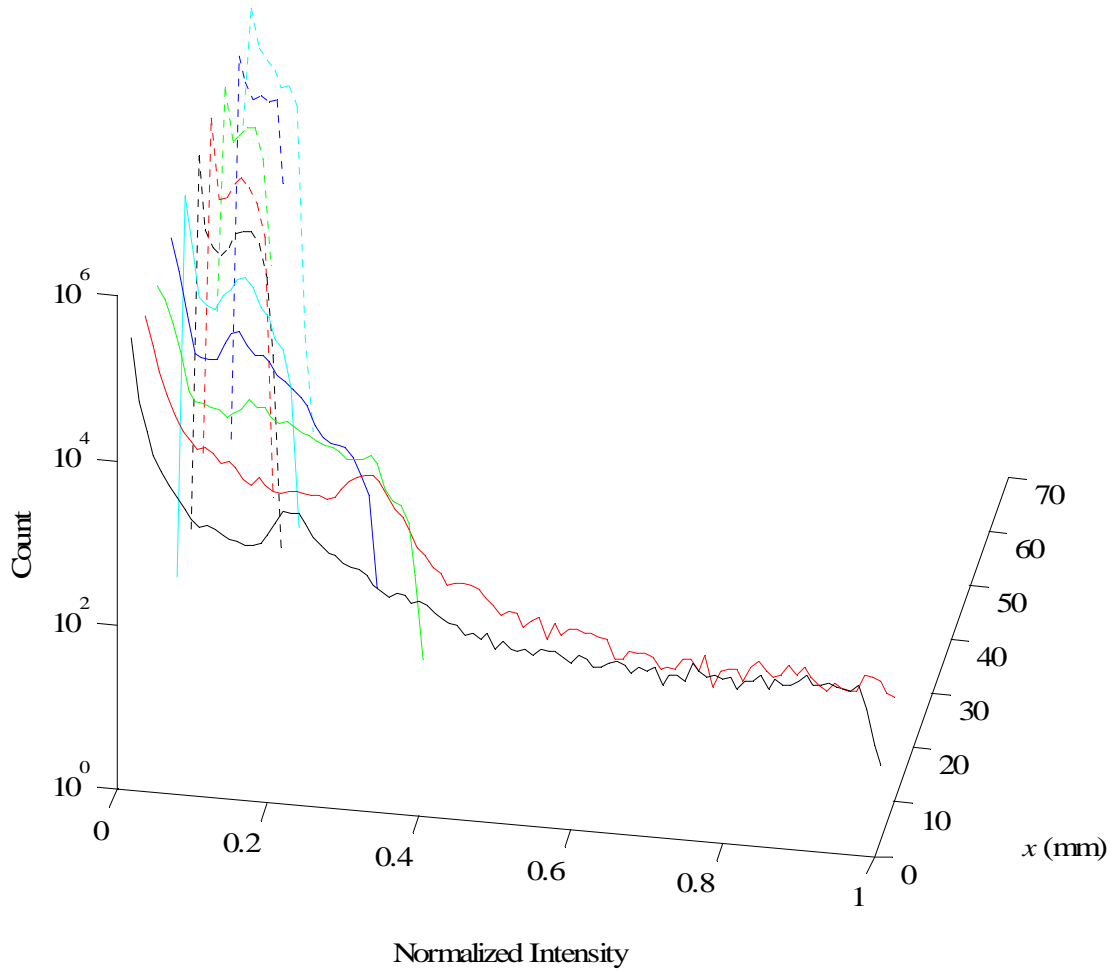


Figure 107. Histograms of the ensemble-averaged streamwise images from Figures 60 to 69, Trip Scenario B. The intensity of each image is normalized by the maximum intensity in Figure 60. The x -location is measured at the center of the image.

6.4.3 Trip Scenario C

Histograms for the ensemble-averaged streamwise images for Trip Scenario C are shown in Figure 108. The high-intensity peak has a greater decrease in intensity than with Trip Scenario A, but perhaps not as great of a decrease as Trip Scenario B. This signifies that Trip Scenario C has greater mixing between the primary and injected flows than Trip Scenario A, but no greater than Trip Scenario B.

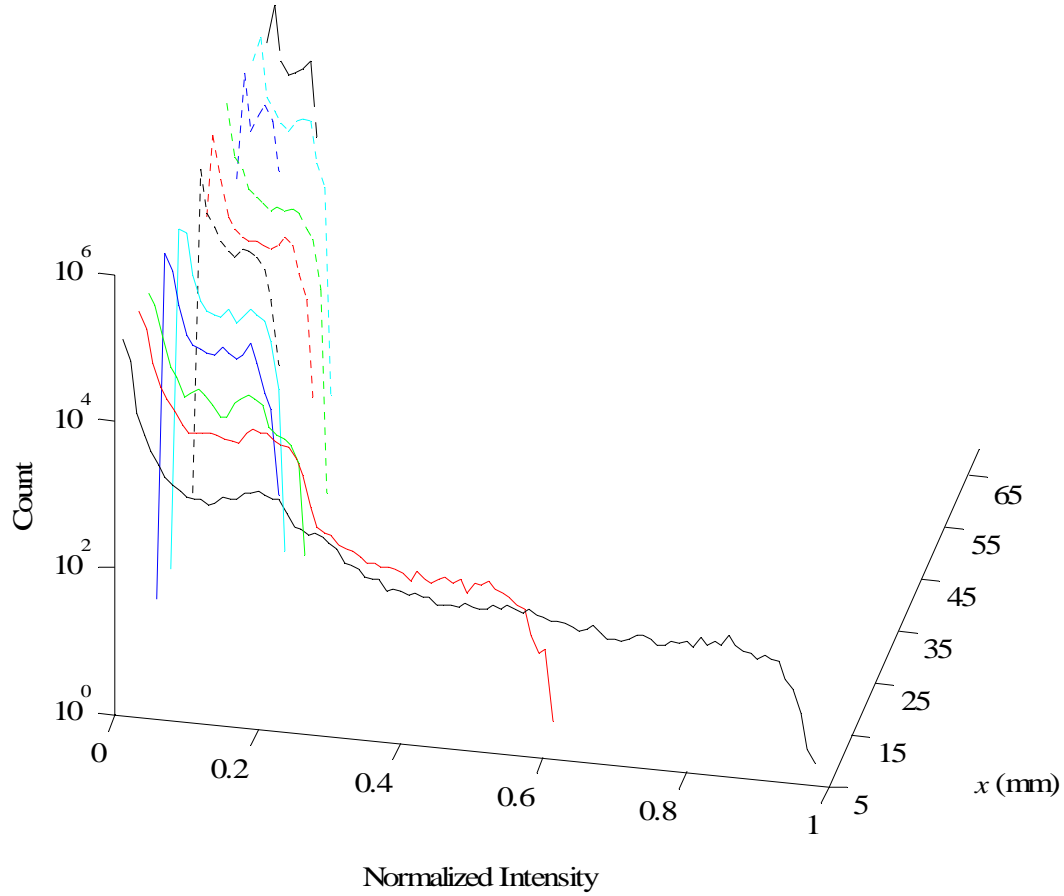


Figure 108. Histograms of the ensemble-averaged streamwise images from Figures 71 to 81, Trip Scenario C. The intensity of each image is normalized by the maximum intensity in Figure 71. The x -location is measured at the center of the image.

6.5 Oblique-View Histograms

A histogram analysis was performed on the ensemble-averaged oblique images for the three different trip jet scenarios. While the high-intensity peaks generally decrease in intensity with downstream distance for each trip jet scenario, the pattern of this decrease does not match that of the streamwise-view histograms. The oblique-view histograms indicate that Trip Scenario A has the greatest mixing between the primary and injected flows, whereas the streamwise-view histograms indicate that Trip Scenario B has the greatest mixing.

6.5.1 Trip Scenario A

Histograms for the ensemble-averaged oblique images for Trip Scenario A are shown in Figure 109. The high-intensity peak has a greater decrease in intensity, with downstream distance, than the nozzle with the single injector. This indicates that this trip jet scenario has greater mixing between the primary and injected flows than the nozzle with no trip jets.

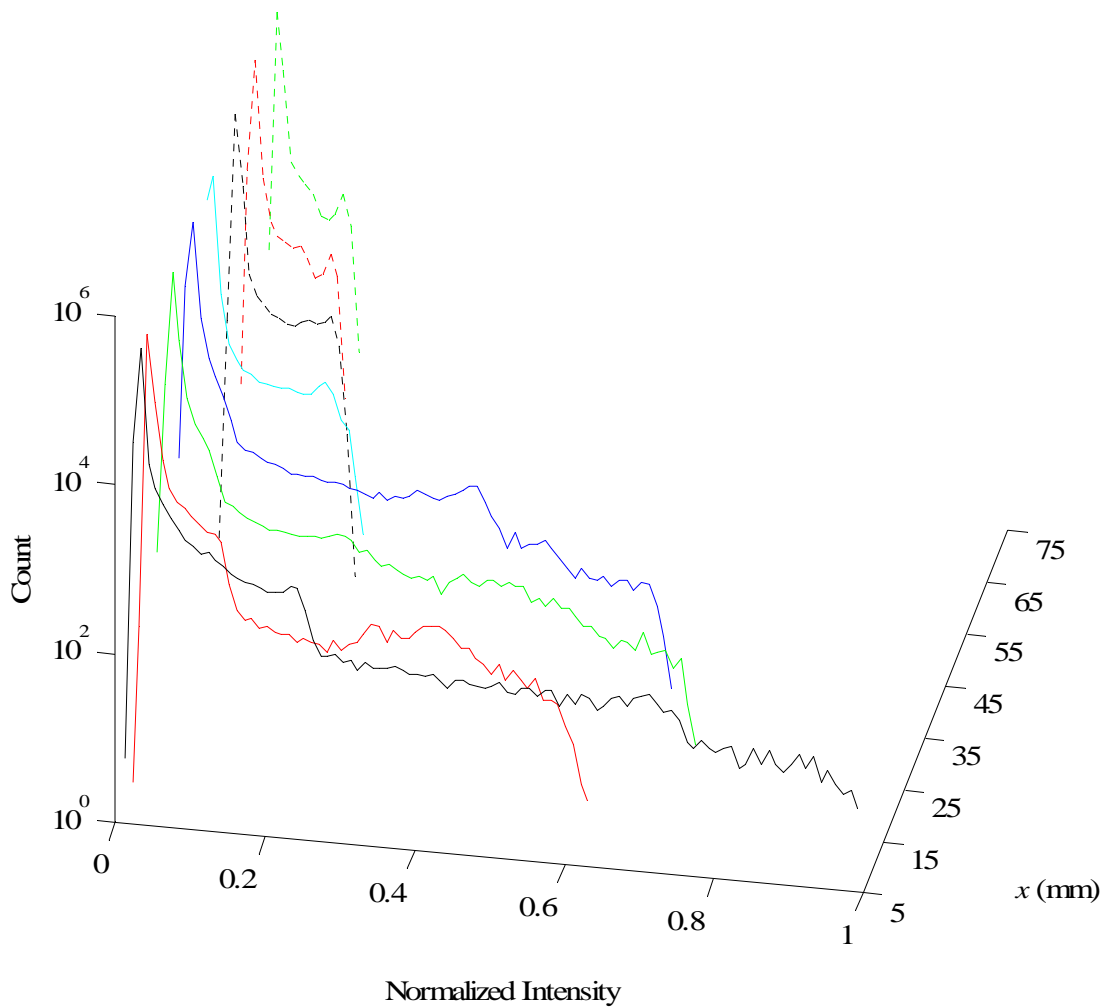


Figure 109. Histograms of the ensemble-averaged oblique images from Figures 83 to 90, Trip Scenario A. The intensity of each image is normalized by the maximum intensity in Figure 83.

6.5.2 Trip Scenario B

Histograms for the ensemble-averaged oblique images for Trip Scenario B are displayed in Figure 110. From $x = 12.3$ mm to $x = 55$ mm, the high-intensity peak decreases

in intensity with downstream distance. At $x = 65$ mm and $x = 75$ mm, the high-intensity peak actually increases in intensity. Perhaps this is because of the trip jet unsteadiness and misrepresentation of the jet structure (even though the images were centered before ensemble averaging).

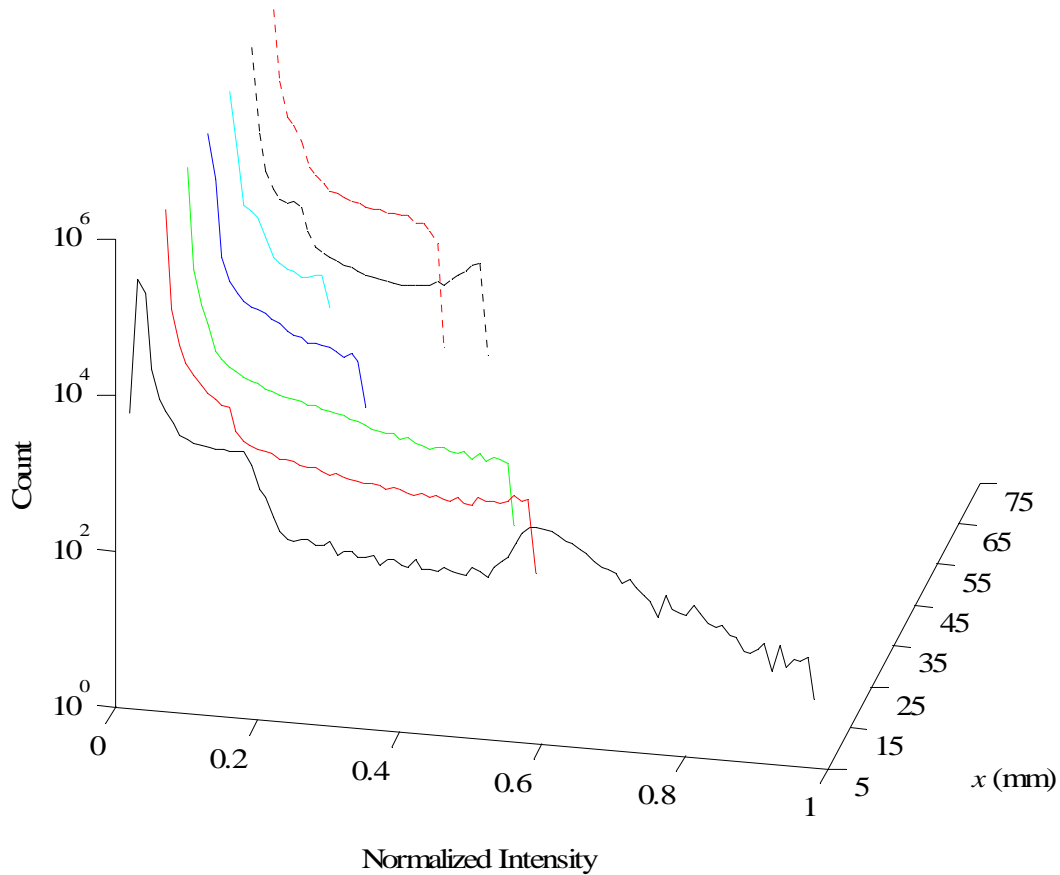


Figure 110. Histograms of the ensemble-averaged oblique images from Figures 91 to 97, Trip Scenario B. The intensity of each image is normalized by the maximum intensity in Figure 91.

6.5.3 Trip Scenario C

Histograms for the ensemble-averaged oblique images for Trip Scenario C are displayed in Figure 111. The high-intensity peak decreases in intensity from $x = 7$ mm to $x = 65$ mm, but increases at $x = 75$ mm. This is most likely from the jet unsteadiness, as with the oblique-view histograms for Trip Scenario B.

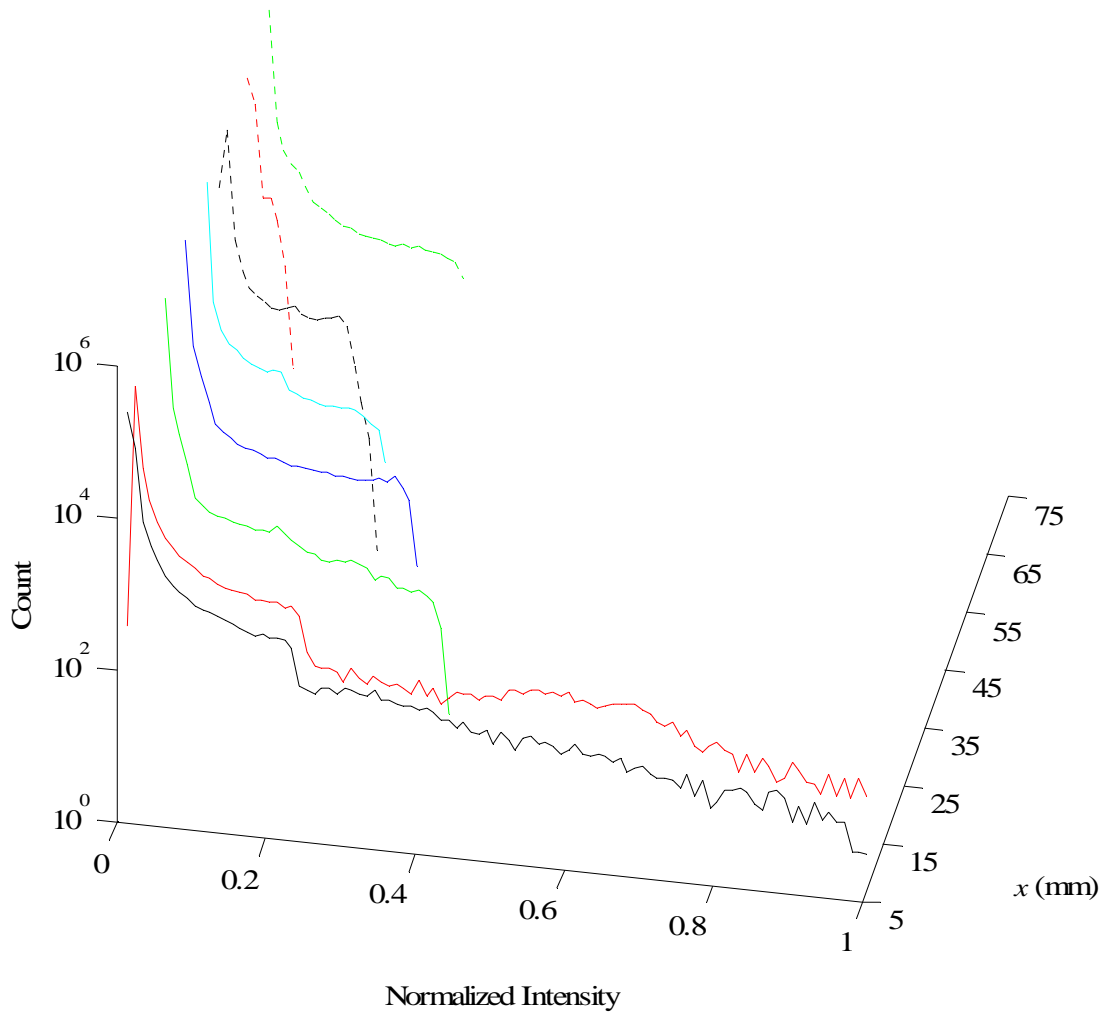


Figure 111. Histograms of the ensemble-averaged oblique images from Figures 98 to 105, Trip Scenario C. The intensity of each image is normalized by the maximum intensity in Figure 98.

6.6 Structure Size

The structure area and interface lengths of the oblique-view structures, for Trip Scenarios A, B, and C were measured. The method for measuring the area and interface length of a structure is detailed in Section 5.4. The threshold for converting the grayscale PLIF images to monochrome was set at 30%, as was done in Chap. 5. Structure area versus downstream distance is displayed in Figure 112. The values for each trip jet scenario and the single jet are

shown for comparison. Close to the jet exit ($x \leq 25$ mm), the single jet has a comparable area to the jet with trip jet(s). Trip Scenarios A and C have greater structure areas between $x = 35$ and $x = 65$, while Trip Scenario B does not have as significant of an impact on the structure area. At $x = 75$ mm, the structure areas for Trip Scenarios A and C decrease because of the jet fluctuations caused by the trip jets, which decreases the structure size in the ensemble-averaged image.

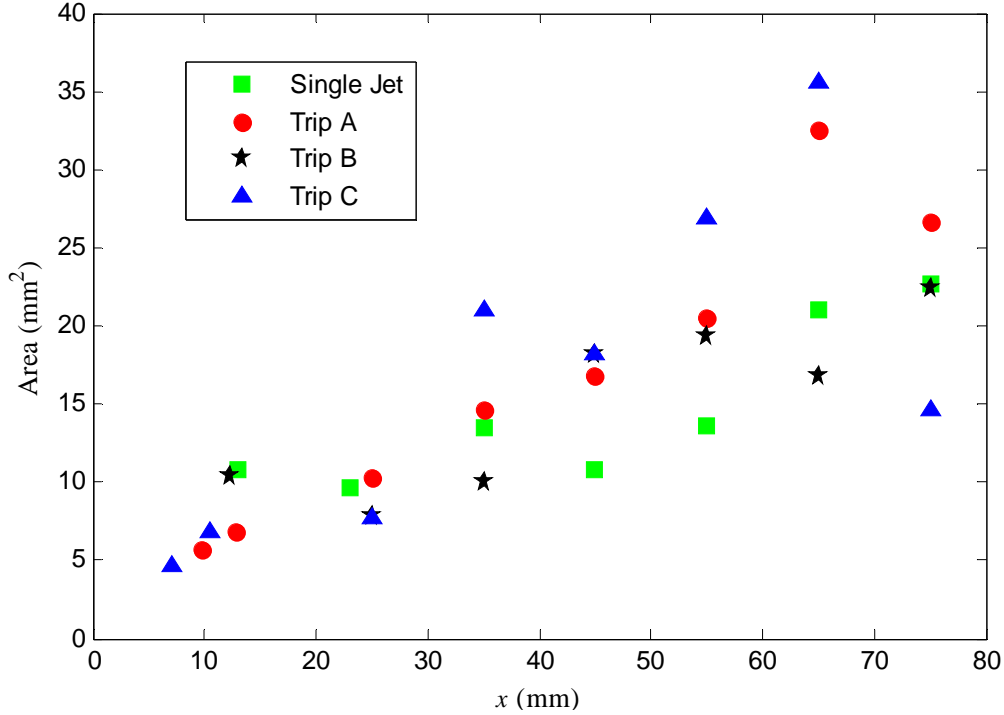


Figure 112. Structure area versus downstream distance for the single jet and Trip Scenarios A, B, and C.

Figure 113 displays the interface length versus downstream distance for the single injector and the three trip jet scenarios. Close to the exit of the injector, the oblique structure interface lengths are similar for the single jet and trip scenarios. With increasing downstream distance, Trip Scenarios A and C produce an oblique structure with much greater interface length than that of the single jet, except at $x = 75$ mm. The decrease in structure area and interface length at $x = 75$ mm could be caused by the jet unsteadiness. The ensemble-averaged oblique structures for Trip Scenarios B and C at $x = 75$ mm (Figures 97 and 105, respectively) appear significantly smaller and distorted from the averages at upstream positions, even though the

instantaneous images have been centered. This unsteadiness could cause the ensemble average (with centering) to misrepresent the structure area and interface length at downstream locations.

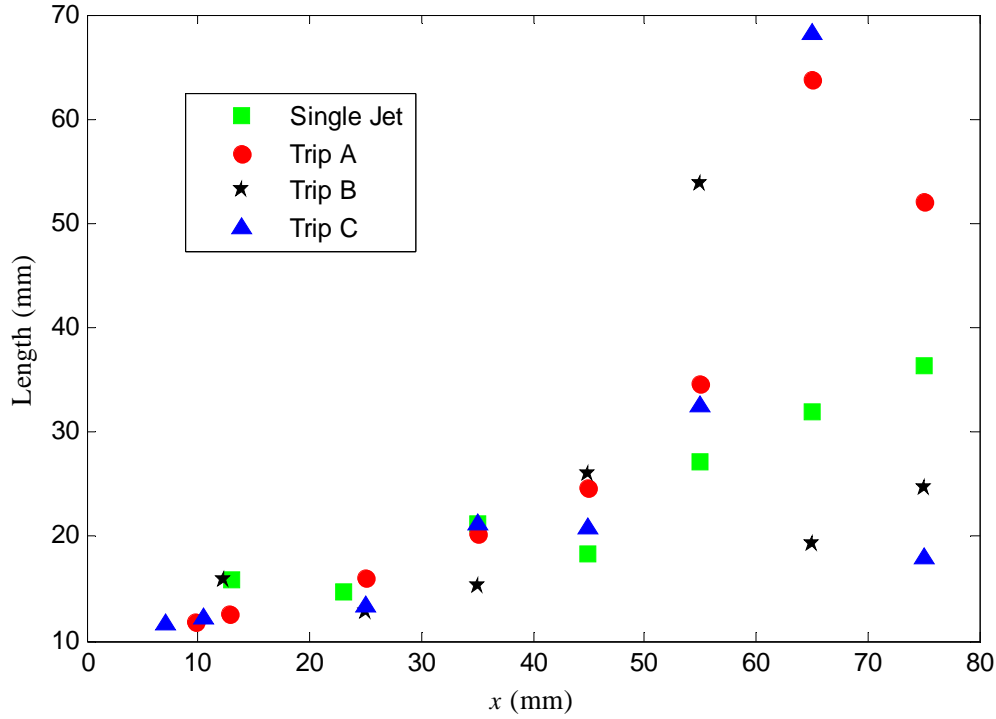


Figure 113. Interface length versus downstream distance for the single jet and Trip Scenarios A, B, and C.

6.7 Jet Penetration

With the ensemble-averaged streamwise PLIF images, jet penetration was measured. The penetration was measured as the y-location of the top of the jet. The streamwise images were converted to monochrome, with a threshold of 30% maximum intensity. The top of the jet, at each x -location, was then determined. For the single jet and the three trip jet scenarios, the jet penetration versus downstream distance is displayed in Figure 114. Although jet penetration generally increases in the x -direction, there is a decrease in penetration with the single jet at 60 mm, with Trip Scenario A at 50 mm, with Trip Scenario B at 60 mm, and Trip Scenario C at 65 mm. The decrease in penetration is most likely caused by jet unsteadiness in the nozzle. The single jet and the three jet scenarios produced a jet that eventually crossed the nozzle centerline.

Trip Scenario B crossed the centerline before the other cases and had the farthest penetration in the nozzle.

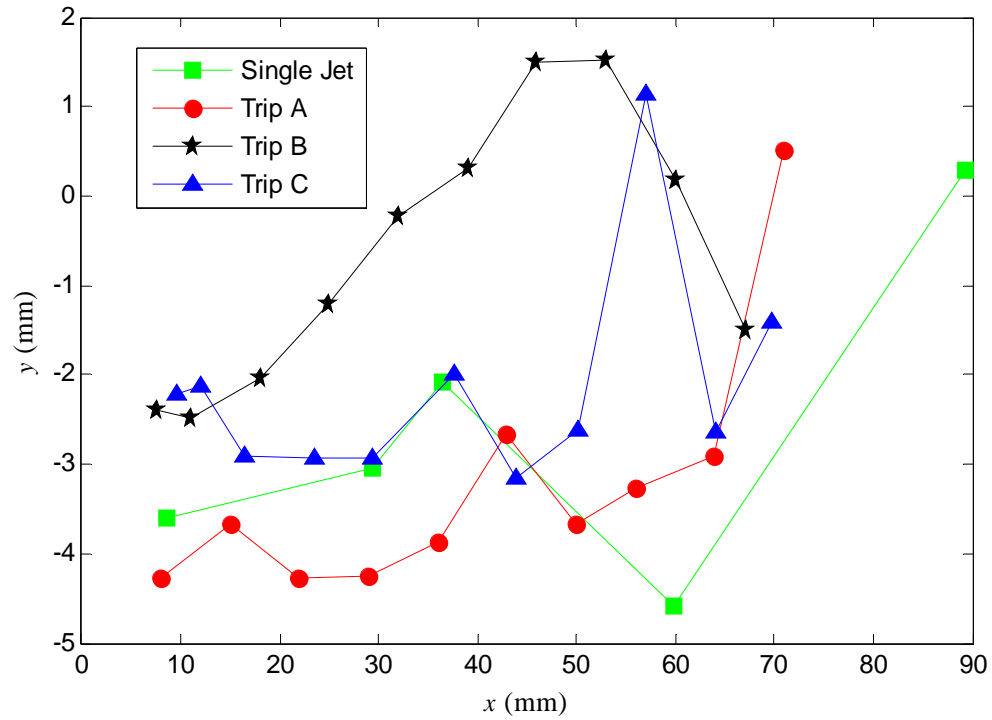


Figure 114. Jet penetration versus downstream distance for the single jet and Trip Scenarios A, B, and C. Penetration measurements are taken from the ensemble-averaged streamwise images.

7.0 CONCLUSION AND RECOMMENDATIONS

7.1 Summary of Results and Conclusions

In this study, a supersonic nozzle with COIL applications was designed and tested using PLIF imaging. The nozzle was designed with a Mach number of 2.2 at the nozzle exit plane (NEP), where the downstream distance from the nozzle throat, x , was 43 mm. Pitot tube measurements and 3-D computational fluid dynamic (CFD) computations confirmed a Mach number close to the design number at this location.

The focus of this study was to examine the influence trip jets may exert on the flow structure and mixing. To elucidate the trip jet effect on the flow, four different iodine injection scenarios were imaged with the PLIF technique. The first scenario is a single injector placed downstream of the nozzle throat. In an attempt to increase mixing between the injected and primary flows, trip jets were placed downstream of the single injector with the intention to destabilize the counter-rotating vortex pair (CRVP) of the single jet or at least push the jet farther into the centerline of the nozzle. Three different trip jet scenarios were tested: 1) Trip Scenario A, where a single trip jet (0.25 mm in diameter) is placed one injector diameter (1.00 mm) downstream of the single injector, 2) Trip Scenario B, where the single trip jet from Trip Scenario A is placed closer to the single injector (0.45 mm), and 3) Trip Scenario C, where two trip jets are placed in the same downstream location as Trip Scenario B, but each are 0.33 mm from the nozzle centerline. Each injection scenario was imaged in the streamwise and oblique views.

From the PLIF images, four different analyses were performed on the images. Histogram analyses were performed on both the streamwise- and oblique-view ensemble-averaged images. From each of the oblique-view images, the area of the oblique structure and the structure interface length were measured. The final analysis was the measurement of the jet penetration from the ensemble-averaged streamwise-view images. With these four measurement/analysis techniques, the mixing quality and penetration can be compared for the four different injection scenarios.

The histogram analysis was performed on both the streamwise- and oblique-view images. Histograms plot the probability density of the normalized fluorescence intensity. With a histogram, there are at least two peaks, the zero-intensity peak represents the primary, non-fluorescing flow, while the high-intensity peak represents the fluorescing, injected flow. Histograms for each downstream location were plotted on the same axis for each injection scenario. When mixing between the primary and injected flows occur, the normalized intensity of the high-intensity peak decreases with downstream distance (indicating a dilution of the fluorescing species). A greater decrease in normalized intensity signifies greater mixing between the two flows. From the streamwise-view images, all three trip scenarios had a greater intensity decrease in the high-intensity peak than with the single injector. With the single injector, the greatest decrease in normalized intensity for the high-intensity peak was from 1.0 to 0.2, whereas Trip Scenarios A, B, and C had peaks that decreased to 0.12, 0.06, and 0.04, respectively. This signifies that Trip Scenarios B and C had greater mixing than Trip Scenario A and the single injector. From the oblique-view images, the high-intensity peaks decreased to 0.2 for the single injector and 0.1, 0.13, and 0.04 for Trip Scenarios A, B, and C, respectively. From the oblique-

view histograms, Trip Scenario C has the greatest mixing, while Trip Scenarios A and B had comparable mixing and the single injector had the least amount of mixing.

From the oblique-view PLIF images, the structure size and length of interface between the injected and primary flows were measured. The images were converted to monochrome, with a 30% intensity threshold, to facilitate area and interface length measurement. For all injection scenarios, the structure area increased with downstream distance. Trip Scenario C had the greatest area of 36 mm^2 at $x = 65 \text{ mm}$. The maximum areas for the single injector, Trip Scenario A, Trip Scenario B, and Trip Scenario C were 23 mm^2 , 33 mm^2 , 19 mm^2 , and 23 mm^2 , respectively. The structure areas decreased at $x = 65 \text{ mm}$ for Trip Scenario B and at $x = 75 \text{ mm}$ for Trip Scenarios A and C. This decrease in area may be caused by the jet fluctuations. The interface length measurement has the same trends as the structure area. Trip Scenarios A and C had the longest length at $x = 65 \text{ mm}$, with 62 mm and 69 mm , respectively. As with structure area, the interface length decreased at $x = 65 \text{ mm}$ for Trip Scenario B and at 75 mm for Trip Scenarios A and C. Because of the jet fluctuations at the downstream locations, it is difficult to interpret this data.

With a larger structure area and interface length, the contact between the injected and primary flows is increased. This greater contact is indicative of diffusive mixing in the nozzle. However, in some cases, the jet is fluctuating so much that the ensemble-averaged structure area is smaller than the structures in each instantaneous image. The fluctuations dilute the edges of the jet structure in the ensemble averages. The fluctuations actually enable greater contact between the primary and injected flows, which increases the mixing capability. With the area and interface length plots (Figures 112 and 113), the measurements are only useful in the non-fluctuating portions of the nozzle, up to 55 mm . From the structure area measurements, the Trip

Scenarios A, B, and C all have better mixing than the single injector, with Trip Scenario C having the best results. The interface length results also indicate that the trip jets increased the mixing, but Trip Scenario B has the best results (greatest length). These results are comparable with the histogram results, where Trip Scenarios B and C had better mixing than the single injector and Trip Scenario A.

The final analysis with the PLIF images is the jet penetration measurement from the streamwise ensemble-averaged images. Jet penetration is the y -location of the top of the jet, which is defined from the monochrome image (where the intensity threshold is set at 30%). From the jet penetration plot (Figure 114), Trip Scenario B has a consistently greater penetration than Trip Scenarios A and C and the single injector. Interestingly, the jet penetration with Trip Scenario A is less than with the single injector. Jet fluctuations are evident with Trip Scenarios B and C at $x \sim 57$ -60 mm.

From the PLIF images, the mixing between the primary and injected flows was measured by four different methods: 1) histogram analysis, 2) oblique structure area, 3) oblique structure interface length, and 4) jet penetration. From these four analyses, it is evident that the trip jets did influence the single injector. The effects of the trip jet(s) included altered mixing (as measured with the histograms), considerable change in oblique structure size, and differences in the interface length between the injected and primary flows, as well as a noticeable change in the jet penetration. The trip jets also increased the jet fluctuations at a downstream distance, x , greater than 55 mm (though most notable with Trip Scenarios B and C). Trip Scenarios B and C have an increased jet penetration and greatest mixing when measured with the streamwise-view histograms. Because of the jet fluctuations, Trip Scenario B has a smaller oblique structure area,

oblique structure interface length, and less reduction in intensity with the oblique histograms than Trip Scenarios A and C.

In comparing the results of the three trip jet scenarios, it is evident that the close placement of the trip jets to the single injector in Trip Scenarios B and C increases the jet penetration more than the location of the trip jet in Trip Scenario A. Mixing, as measured with the streamwise-view histograms, is also greatest with Trip Scenarios B and C. Because the jet fluctuations are most notable with the oblique-view images, it is difficult to compare the area, interface length, and oblique-view histograms in determining the best trip jet scenario for the greatest mixing. With the increased jet fluctuations with Trip Scenario B, when compared to Trip Scenario C, a single trip jet just downstream of the injector may be more desirable than two offset injectors in destabilizing the injected flow. These studies of the trip jets are by no means exhaustive, but they serve a dual purpose, first by experimentally confirming their effectiveness, with relatively small energy input into the flow, and second, by providing experimental benchmarks for future numerical studies of the problem. Some of the likely directions for future work are summarized in the following section.

7.2 Recommendations for Future Work

The effects of single or multiple trip jets on a single injector in supersonic flow have been investigated. Three trip jet scenarios have been imaged and analyzed. To fully understand what drives jet unsteadiness, jet penetration, and mixing between the primary and injected flows, more trip jet scenarios need to be tested. In this study, a single trip jet, placed on the nozzle centerline, was tested at two different downstream locations. The trip jet placed closest to the injector increased the jet's penetration and mixing. Testing more distances would determine an optimal

trip jet distance. Also, the use of double trip jets in Trip Scenario C needs optimization. From the oblique PLIF images, it appears that the trip jets hit the outside of the counter-rotating vortices (see Figure 99), rather than the center of each vortex, as intended. Decreasing the distance from the nozzle centerline may produce the desired unsteadiness in the CRVP. Upon optimization, testing entire rows of injectors and trip jets would reveal the mixing capability in the nozzle and flow uniformity (which is desirable for applications to a COIL system).

REFERENCES

- ¹ McDermott, W. E., Pchelkin, N. R., Benard, D. J., and Bousek, R. R., "An Electronic Transition Chemical Laser," *Applied Physics Letters*, **Vol. 32**, No. 8, 1978, pp. 469-470.
- ² Truesdell, K. A., Lamberson, S. E., and Hager, G. D., "Phillips Laboratory COIL Technology Overview," *23rd AIAA Plasmadynamics and Lasers Conference*, AIAA Paper 92-3003, Jul. 1992.
- ³ Avizonis, P. V. and Neumann, D. K., "The Chemical Oxygen-Iodine Laser," *Journal of Defense Research*, 1986, pp. 511-524.
- ⁴ Avizonis, P. V., and Truesdell, K. A., "Historical Perspectives of the Chemical Oxygen-Iodine Laser (COIL)," *25th AIAA Plasmadynamics and Lasers Conference*, AIAA Paper 94-2416, 1994.
- ⁵ Madden, T. J., and Miller, J. H., "Simulation of Flow Unsteadiness in Chemical Flowfields," *42nd AIAA Aerospace Sciences Meeting and Exhibit*, AIAA Paper 2004-0805, Jan. 2004.
- ⁶ Miller, J. H., Shang, J. S., and Madden, T. J., "Parallel Computation of Chemical Oxygen/Iodine Laser Flowfields," *32nd AIAA Plasmadynamics and Lasers Conference*, AIAA Paper 2001-2869, Jun. 2001.
- ⁷ Miller, J. H., Shang, J. S., Tomaro, R. F., and Strang, W. Z., "Computation of Compressible Flows Through a Chemical Laser Device with Crossflow Injection," *Journal of Propulsion and Power*, **Vol. 17**, No. 4, Jul.-Aug. 2001, pp. 836-844.
- ⁸ Madden, T.J., and Solomon, W. C., "A Detailed Comparison of a Computational Fluid Dynamic Simulation and a Laboratory Experiment for a COIL Laser," *28th AIAA Plasmadynamics and Lasers Conference*, AIAA Paper 97-2387, Jun. 1997.
- ⁹ Masuda, W., Hishida, M., Hirooka, S., Azami, N., and Yamada, H., "Three-Dimensional Mixing/Reacting Zone Structure in a Supersonic Flow Chemical Oxygen-Iodine Laser," *JSME International Journal, Series B—Fluids and Thermal Engineering*, **Vol. 40**, No. 2, May 1997, pp. 209-215.
- ¹⁰ Madden, T. J., Hager, G. D., Lampson, A. I., and Crowell, P. G., "An Investigation of Supersonic Mixing Mechanisms for the Chemical Oxygen-Iodine Laser (COIL)," *30th AIAA Plasmadynamics and Lasers Conference*, AIAA Paper 99-3429, 1999.
- ¹¹ Rosenwaks, S., Bruins, E., Furman, D., Rybalkin, V., and Barmashenko, B. D., "Supersonic COIL with Iodine Injection in Transonic and Supersonic Sections of the Nozzle," *XIII International Symposium on Gas Flow and Chemical Lasers and High-Power Laser Conference, Proceedings of SPIE*, **Vol. 4184**, edited by A. Lapucci and M. Ciofini, 25 Jan. 2001, pp. 19-22.
- ¹² Barmashenko, B., Rybalkin, V., Katz, A., and Rosenwaks, S., "Parametric Study of the Ben-Gurion University Efficient Supersonic Chemical Oxygen-Iodine Laser," *High-Power Laser*

Ablation V, Proceedings of the SPIE, edited by C. R. Phipps, **Vol. 5448**, No. 1, 20 Sept. 2004, pp. 282-293.

¹³ Fric, T. F., and Roshko, A., "Vortical Structure in the Wake of a Transverse Jet," *Journal of Fluid Mechanics*, **Vol. 279**, 25 Nov. 1994, pp. 1-47.

¹⁴ Rivero, A., Ferré, J. A., and Giralt, F., "Organized Motions in a Jet in Crossflow," *Journal of Fluid Mechanics*, **Vol. 444**, 10 Oct. 2001, pp. 117-149.

¹⁵ Gruber, M. R., Nejad, A. S., Chen, T. H., and Dutton, J. C., "Compressibility Effects in Supersonic Transverse Injection Flowfields," *Physics of Fluids*, **Vol. 9**, No. 5, May 1997, pp. 1448-1461.

¹⁶ Voignier, F., Merat, F., and Brunet, H., "Mixing Diagnostic in a CW DF Chemical Laser Operating at High Cavity Pressure," *8th International Symposium on Gas Flow and Chemical Lasers, Proceedings of SPIE*, edited by C. M. Domingo and J. M. Orza, **Vol. 1397**, 1 Feb. 1991, pp. 297-301.

¹⁷ Cenkner, A. A., and Driscoll, R. J., "Laser-Induced Fluorescence Visualization on Supersonic Mixing Nozzles that Employ Gas-Trips," *AIAA Journal*, **Vol. 20**, No. 6, 1982, pp. 812-819.

¹⁸ Driscoll, R. J., "Mixing Enhancement in Chemical Lasers, Part I: Experiments," *AIAA Journal*, **Vol. 24**, No. 7, 1986, pp. 1120-1126.

¹⁹ Takeuchi, N., Sugimoto, D., Tei, K., Nanri, K., and Fujioka, T., "High-Pressure Nozzle Bank for a Chemical Oxygen Iodine Laser," *Japanese Journal of Applied Physics*, **Vol. 44**, No. 2, Feb. 2005, pp. 900-904.

²⁰ Murugappan, S., Gutmark, E., and Carter, C., "Control of Penetration and Mixing of an Excited Supersonic Jet into a Supersonic Cross Stream," *Physics of Fluids*, **Vol. 17**, No. 10, Oct. 2005, p. 106101.

²¹ Murugappan, S., Gutmark, E., Carter, C., Donbar, J., Gruber, M. R., and Hsu, K.-Y., "Transverse Supersonic Controlled Swirling Jet in a Supersonic Cross Stream," *AIAA Journal*, **Vol. 44**, No. 2, 2006, pp. 290-300.

²² Gruber, M. R., Nejad, A. S., and Dutton, J. C., "An Experimental Investigation of Transverse Injection from Circular and Elliptical Nozzles into Supersonic Crossflow," Tech. Rep. WL-TR-96-2102, Wright-Patterson Air Force Base, 1996.

²³ Gruber, M. R., Nejad, A. S., Chen, T. H., and Dutton, J. C., "Transverse Injection from Circular and Elliptic Nozzles into a Supersonic Crossflow," *Journal of Propulsion and Power*, **Vol. 16**, No. 3, May-Jun. 2000, pp. 449-457.

- ²⁴ Palekar, A., Truman, C. R., and Vorobieff, P. V., "Prediction of Transverse Injection of a Sonic Jet in Supersonic Crossflow," *36th AIAA Plasmadynamics and Lasers Conference*, AIAA Paper 2005-5366, 2005.
- ²⁵ Blanchard, J. N., Brunet, Y., and Merlen, A., "Influence of a Counter Rotating Vortex Pair on the Stability of a Jet in Cross Flow: An Experimental Study by Flow Visualizations," *Experiments in Fluids*, **Vol. 26**, No. 1-2, Jan. 1999, pp. 63-74.
- ²⁶ Landman, M. J., and Saffman, P. G., "The Three-Dimensional Instability of Strained Vortices in a Viscous Fluid," *Physics of Fluids*, **Vol. 30**, No. 8, Aug. 1987, pp. 2339-2342.
- ²⁷ Viti, V., Wallis, S., Schetz, J. A., Neel, R., and Bowersox, R. D. W., "Jet Interaction with a Primary Jet and an Array of Smaller Jets," *AIAA Journal*, **Vol. 42**, No. 4, 2004, pp. 1358-1368.
- ²⁸ Borg, A., Bolinder, J., and Fuchs, L., "Simultaneous Velocity and Concentration Measurements in the Near Field of a Turbulent Low-Pressure Jet by Digital Particle Image Velocimetry-Planar Laser-Induced Fluorescence," *Experiments in Fluids*, **Vol. 31**, No. 2, Aug. 2001, pp. 140-152.
- ²⁹ Ben-Yakar, A., and Hanson, R. K., "Ultra-Fast-Framing Schlieren System for Studies of the Time Evolution of Jets in Supersonic Crossflows," *Experiments in Fluids*, **Vol. 32**, No. 6, Jun. 2002, pp. 652-666.
- ³⁰ Thurber, M. C., and Hanson, R. K., "Simultaneous Imaging of Temperature and Mole Fraction Using Acetone Planar Laser-Induced Fluorescence," *Experiments in Fluids*, **Vol. 30**, No. 1, Jan. 2001, pp. 93-101.
- ³¹ Kumar, S., Orlicz, G., Tomkins, C., Goodenough, C., Prestridge, K., Vorobieff, P., and Benjamin, R., "Stretching of Material Lines in Shock-Accelerated Gaseous Flows," *Physics of Fluids*, **Vol. 17**, No. 8, Aug. 2005, p.082107.
- ³² Palma, P. C., Mallinson, S. G., O'Byrne, S. B., Danehy, P. M., and Hillier, R., "Temperature Measurements in a Hypersonic Boundary Layer Using Planar Laser-Induced Fluorescence," *AIAA Journal*, **Vol. 38**, No. 9, 2000, pp.1769-1772.
- ³³ Lee, M. P., McMillin, B. K., Palmer, J. L., and Hanson, R. K., "Planar Fluorescence Imaging of a Transverse Jet in a Supersonic Crossflow," *Journal of Propulsion and Power*, **Vol. 8**, No. 4, Jul.-Aug. 1992, pp. 729-735.
- ³⁴ Hiller, B., and Hanson, R. K., "Properties of the Iodine Molecule Relevant to Laser-Induced Fluorescence Experiments in Gas Flows," *Experiments in Fluids*, **Vol. 10**, No. 1, 1990, pp. 1-11.
- ³⁵ Hartfield, Jr., R. J., Abbitt III, J. D., and McDaniel, J. C., "Injectant Mole-Fraction Imaging in Compressible Mixing Flows Using Planar Laser-Induced Iodine Fluorescence," *Optics Letters*, **Vol. 14**, No. 16, 15 Aug. 1989, pp. 850-852.

- ³⁶ Hartfield, Jr., R. J., Hollow, S. D., and McDaniel, J. C., “Planar Measurement Technique for Compressible Flows Using Laser-Induced Iodine Fluorescence,” *AIAA Journal*, **Vol. 31**, No. 3, 1993, pp. 483-490.
- ³⁷ Donohue, J. M., and McDaniel Jr., J. C., “Computer-Controlled Multiparameter Flowfield Measurements Using Planar Laser-Induced Iodine Fluorescence,” *AIAA Journal*, **Vol. 34**, No. 8, 1996, pp. 1604-1611.
- ³⁸ Rittenhouse, T. L., Phipps, S. P., and Helms, C. A., “Performance of a High-Efficiency 5-cm Gain Length Supersonic Chemical Oxygen-Iodine Laser,” *IEEE Journal of Quantum Electronics*, **Vol. 35**, No. 6, Jun. 1999, pp. 857-866.
- ³⁹ Carroll, B.F., Dutton, J. C., and Addy, A. L., “NOZCS2: A Computer Program for the Design of Continuous Slope Supersonic Nozzles,” Department of Mechanical and Industrial Engineering, University of Illinois at Urbana-Champaign, Report No. UILU ENG 86-4007, 1986.
- ⁴⁰ Lifshitz, E. M., and Landau, L. D., *Fluid Mechanics*, 2nd ed., Course of Theoretical Physics, Vol. 6, Butterworth-Heinemann, Oxford, 1987, p. 319.
- ⁴¹ Madden, T. J., private communication, Directed Energy Directorate, Air Force Research Laboratory, Kirtland AFB, NM, 2006.
- ⁴² Zhu, X., Nur, A. H., and Misra, P., “Laser Optogalvanic Wavelength Calibration with a Commercial Hollow Cathode Iron-Neon Discharge Lamp,” *Journal of Quantitative Spectroscopy and Radiative Transfer*, **Vol. 52**, No. 2, Aug. 1994, pp. 167-177.
- ⁴³ Spectra-Physics Cobra-Stretch Sirah Dye Laser Manual, Sirah Laser- und Plasmatechnik GmbH, Kaarst, Germany.
- ⁴⁴ Heaven, M., private communication, Department of Chemistry, Emory University, Atwood Hall 410, Atlanta, GA, 2007.
- ⁴⁵ Herzberg, G., *Molecular Spectra and Molecular Structure I. Spectra of Diatomic Molecules*, 2nd ed., Krieger Publishing Company, Malabar, Florida, 1989, pp. 103-108, 122-125, 540-541.
- ⁴⁶ Capelle, G. A., and Broida, H. P., “Lifetimes and Quenching Cross Sections of $I_2(B^3\Pi_{Ou}^+)^*$,” *Journal of Chemical Physics*, **Vol. 58**, No. 10, 15 May 1973, pp. 4212-4222.
- ⁴⁷ Madden, T. J., Noren, C. A., Emmert, L., and Heaven, M., “A Model for the Prediction of I_2 Fluorescence in the Presence of Pulsed Laser Radiation Utilizing Computational Fluid Dynamic Simulation Datasets,” 38th *AIAA Plasmadynamics and Lasers Conference*, AIAA Paper 2007-4605, Jun. 2007.
- ⁴⁸ Roper Scientific Inc., Princeton Instruments Acton PI-MAX[®]/PI-MAX2[™] System Manual, Version 5.D, 2005, Copyright 2003-2005, Trenton, NJ.

- ⁴⁹ Truesdell, R. A., Vorobieff, P. V., Sklar, L. A., and Mammoli, A. A., "Mixing of a Continuous Flow of Two Fluids Due to Unsteady Flow," *Physical Review E*, **Vol. 67**, No. 6, 2003, p. 066304.
- ⁵⁰ Rasband, W., *Image J 1.40*, 2007, <<http://rsb.info.nih.gov/ij/>>.
- ⁵¹ Vorobieff, P. V., Mohamed, N. G., Tomkins, C., Goodenough, C., Marr-Lyon, M., and Benjamin, R. F., "Scaling Evolution in Shock-Induced Transition to Turbulence," *Physical Review E*, **Vol. 68**, No. 6, 2003, p. 065301.
- ⁵² Johnson, A. N., Espina, P. I., Mattingly, G. E., Wright, J. D., and Merkle, C. L., "Numerical Characterization of the Discharge Coefficient in Critical Nozzles," *National Conference of Standards Laboratories (NCSL) Workshop & Symposium*, 1998, pp. 407-422.
- ⁵³ Davis, S. J., "Halogen Mass Flow Rate Detection System," U.S. Patent 4,467,474, 21 Aug. 1984.
- ⁵⁴ Saiz-Lopez, A., Saunders, R. W., Joseph, D. M., Ashworth, S. H., and Plane, J. M. C., "Absolute Absorption Cross-Section and Photolysis Rate of I₂," *Atmospheric Chemistry and Physics*, **Vol. 4**, 1 Sep. 2004, pp. 1443-1450.
- ⁵⁵ Farell, C., and Youssef, S., "Experiments on Turbulence Management Using Screens and Honeycombs," *Journal of Fluids Engineering*, **Vol. 118**, No. 1, Mar. 1996, pp. 26-31.
- ⁵⁶ Loehrke, R. I., and Nagib, H. M., "Control of Free-Stream Turbulence by Means of Honeycombs: A Balance Between Suppression and Generation," *Journal of Fluids Engineering*, **Vol. 98**, No. 3, 1976, pp. 342-353.
- ⁵⁷ Scheiman, J., and Brooks, J. D., "A Comparison of Experimental and Theoretical Turbulence Reduction from Screens, Honeycomb, and Honeycomb-Screen Combinations," *11th Aerodynamic Testing Conference*, AIAA Paper 80-0433, 18-20 Mar. 1980.
- ⁵⁸ Laws, E. M., and Livesey, J. L., "Flow Through Screens," *Annual Review of Fluid Mechanics*, **Vol. 10**, 1978, pp. 247-266.
- ⁵⁹ Schlichting, H., *Boundary-Layer Theory*, 7th ed., McGraw-Hill, New York, 1979, pp. 135-141.
- ⁶⁰ Anderson, Jr., J. K., *Modern Compressible Flow*, 2nd ed., McGraw-Hill, Boston, MA, 1990, pp. 59, 155.
- ⁶¹ White, F. M., *Viscous Fluid Flow*, 2nd ed., McGraw-Hill International Editions, Singapore, 1991, pp. 28-29, 35.
- ⁶² AeroSoft, Inc., Blacksburg, VA, *GASP User Manual*, 2005.

Appendix A: Flow Rate Measurement and Uncertainty

A.1 Introduction

This appendix details the molar flow rate measurement and the uncertainty analysis for the measurement of the primary and carrier flow rates, including the flow rate of iodine.

Thermocouples, pressure transducers, orifices, and photometers were all used in the flow measurements and each have an uncertainty which will be included in this analysis.

The uncertainty of the iodine molar flow rate is important when analyzing the PLIF images. The fluorescence intensity is directly affected by the iodine concentration in the flow. Uncertainty in the iodine molar flow rate or iodine concentration influences the interpretation of the PLIF images.

A.2 Method to Measure Molar Flow Rate

To measure the carrier helium, primary helium, and primary oxygen molar flow rates, orifices were used to create a choke point in their flow. Pressure and temperature were measured upstream of the choke point, where the flow is considered to be stagnate (Mach number less than 0.05). With the stagnation pressure and temperature measurements, the molecular weight of the gas, and the ratio of specific heat capacities for the gas, the molar flow rate can be determined from the isentropic relationships, conservation of mass, and ideal gas law. An orifice schematic is displayed in Figure A.1, below.

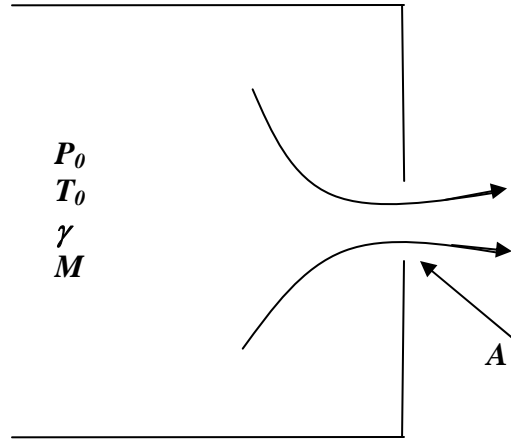


Figure A.1. A schematic of an orifice, with the flow from left to right. The pressure and temperature upstream of the orifice are stagnation values.

To calculate the molar flow rate, start with the conservation of mass equation, Eqn. A.1, where ρ is the gas density, A is the orifice area, V is the flow velocity, and \dot{m} is the mass flow rate.

$$\dot{m} = \rho AV \quad (\text{A.1})$$

From the Ideal Gas Law,

$$P = \rho RT \quad (\text{A.2})$$

where P is pressure, T is temperature, and R is the gas constant. Equation A.1 can then be written as

$$\dot{m} = \frac{PAV}{RT} \quad (\text{A.3})$$

The velocity is related to the Mach number, M , by the speed of sound, a , as

$$V = Ma \quad (\text{A.4})$$

The speed of sound is a function of temperature and the ratio of specific heats for the gas

$$a = \sqrt{\gamma RT} \quad (\text{A.5})$$

Equations A.4 and A.5 reduce Eqn. A.3 to

$$\dot{m} = PAM \sqrt{\frac{\gamma}{RT}} \quad (\text{A.6})$$

At the orifice, the Mach number is one. The temperature and pressure cannot be measured at the orifice, but could be deduced from the stagnation values by using the isentropic equations. Also, the area of the orifice needs to be adjusted for boundary layer build up. Orifices are calibrated for the actual flow rate based on the Reynolds number. They are usually calibrated by the manufacturer and given a value for the discharge coefficient, C_d , where unity is an orifice without a boundary layer.

The isentropic equations for static temperature and pressure are

$$T = T_0 \left[1 + \frac{\gamma - 1}{2} M^2 \right]^{-1} \quad (\text{A.7})$$

$$P = P_0 \left[1 + \frac{\gamma - 1}{2} M^2 \right]^{-(\gamma - 1)/\gamma} \quad (\text{A.8})$$

With the isentropic relationships, a Mach number of one at the orifice, and the C_d value incorporated to allow for the reduction in orifice area, Eqn. A.6 becomes

$$\dot{m} = C_d P_0 A \sqrt{\frac{\gamma}{RT_0}} \left(\frac{\gamma + 1}{2} \right)^{\gamma + 1 / 2(1 - \gamma)} \quad (\text{A.9})$$

Equation A.9 gives the mass flow rate, but the molar flow rate is desired. The molecular weight, \mathcal{M} , of the gas is divided through to give molar flow rate. Also, the gas constant is replaced by the Universal Gas Constant, \mathcal{R} , divided by molecular weight. Therefore, the molar flow rate is

$$\dot{N} = C_d P_0 A \sqrt{\frac{\gamma}{\mathcal{R}M T_0}} \left(\frac{\gamma + 1}{2} \right)^{\gamma+1/2(1-\gamma)} \quad (\text{A.10})$$

With Eqn. A.10, the molar flow rate of a flow can be determined by the gas molecular weight, ratio of specific heats, orifice area and discharge coefficient, and the pressure and temperature upstream of the orifice.

A.3 Primary and Carrier Molar Flow Rate Uncertainties

When determining the molar flow rate, uncertainty may arise from the accuracy of the measured pressure and temperature of the gas and from the measured discharge coefficient of the orifice (which takes into account the uncertainty in the orifice diameter). For simplicity in the uncertainty calculations, Eqn. A.10 can be reduced to

$$\dot{N} = \frac{C_d P_0}{\sqrt{T_0}} B \quad (\text{A.11})$$

where

$$B = A \sqrt{\frac{\gamma}{\mathcal{R}M}} \left(\frac{\gamma + 1}{2} \right)^{\gamma+1/2(1-\gamma)} \quad (\text{A.12})$$

The uncertainty in the molar flow rate is given by $\Delta \dot{N}$, where Δ refers to the uncertainty of a specified measurement.

$$\Delta \dot{N} = \sqrt{\left(\frac{\partial \dot{N}}{\partial C_d} \Delta C_d \right)^2 + \left(\frac{\partial \dot{N}}{\partial P_0} \Delta P_0 \right)^2 + \left(\frac{\partial \dot{N}}{\partial T_0} \Delta T_0 \right)^2} \quad (\text{A.13})$$

where

$$\frac{\partial \dot{N}}{\partial C_d} = \frac{P_0}{\sqrt{T_0}} B \quad (\text{A.14})$$

$$\frac{\partial \dot{N}}{\partial P_0} = \frac{C_d}{\sqrt{T_0}} B \quad (\text{A.15})$$

$$\frac{\partial \dot{N}}{\partial T_0} = -\frac{1}{2} \frac{C_d}{T_0^{3/2}} B \quad (\text{A.16})$$

The uncertainty in the pressure transducers is 0.25%. The uncertainty in the thermocouples is a conservative 1% on the Kelvin scale. The discharge coefficient, C_d , has uncertainty from a few different factors. An orifice is usually calibrated with air. Using the orifice with another gas species introduces uncertainty in the measured discharge coefficient value. The uncertainty of the discharge coefficient with the calibrated species is 0.25%. From Johnson et al., using a gas that differs from the calibration gas can change the discharge coefficient by 2%.⁵² From the calibration uncertainty, the fact that the gas species is different than that used for calibration, and the uncertainty in the orifice diameter, the orifice discharge coefficient uncertainty was set at a conservative 5%.

Table A.1 displays a sample of measured and calculated values used in calculating the flow rate uncertainties for carrier and primary helium and primary oxygen. In each case, the flow rate uncertainty is 5%, with the uncertainty in the orifice discharge coefficient being the dominant factor.

Table A.1. Sample calculation of carrier and primary gas flow rates and uncertainties.

	Carrier Helium	Primary Helium	Primary Oxygen
Orifice Diameter	0.055 in 1.40 mm	0.070 in 1.78 mm	0.075 in 1.91 mm
γ	1.66	1.66	1.40
\mathcal{M}	4 g/mol	4 g/mol	32 g/mol
C_d	0.967 ± 0.048	1.032 ± 0.052	1.024 ± 0.051
P_0	46.70 ± 0.12 psia $3.220\text{E}5 \pm 800$ N/m ²	124.38 ± 0.31 psia $8.576\text{E}5 \pm 2100$ N/m ²	68.55 ± 0.17 psia $4.726\text{E}5 \pm 1200$ N/m ²
T_0	294 ± 3 K	292 ± 3 K	295 ± 3 K
$\frac{\partial \dot{N}}{\partial C_d} \Delta C_d$	5.53 mmol/s	25.55 mmol/s	5.33 mmol/s
$\frac{\partial \dot{N}}{\partial P_0} \Delta P_0$	0.28 mmol/s	1.28 mmol/s	0.27 mmol/s
$\frac{\partial \dot{N}}{\partial T_0} \Delta T_0$	-0.55 mmol/s	-2.56 mmol/s	-0.53 mmol/s
\dot{N}	110.7 ± 5.6 mmol/s	511.1 ± 25.7 mmol/s	106.6 ± 5.4 mmol/s
$\frac{\Delta \dot{N}}{\dot{N}}$	5%	5%	5%

A.4 Iodine Flow Rate and its Uncertainty

The iodine molar flow rate is determined by the molar flow rate of the carrier helium and the concentration of iodine in the carrier flow. The concentration of iodine is measured using the absorbance of an argon-ion laser beam that passes through the flow of carrier helium and iodine. This method is detailed and patented by Davis.⁵³ The concentration measurement and uncertainty in the concentration and iodine flow rate will be described below.

A.4.1 Iodine Concentration Measurement

The iodine concentration is measured using the absorbance of an argon-ion laser that passes through the helium carrier and iodine flow, using Beer's Law. A form of Beer's Law is

$$I_T = I_0 e^{-N\sigma L} \quad (\text{A.17})$$

N is the number density of absorbing iodine molecules, σ is the absorbance cross section of iodine, L is the path length of the laser beam through the flow, and I_0 and I_T are the laser intensities before and after passing through the flow. At 488 nm, the absorption cross section was measured to be $1.70 \times 10^{-18} \text{ cm}^2$ by Davis and $1.68 \times 10^{-18} \text{ cm}^2$ by Saiz-Lopez et al.⁵³⁻⁵⁴

Beer's law, rearranged to give the number density, N , is

$$N = \frac{1}{\sigma L} \ln \frac{I_0}{I_T} \quad (\text{A.18})$$

The concentration of iodine in the flow is the number density divided by Avogadro's constant, N_A ,

$$[I_2] = \frac{1}{\sigma L N_A} \ln \frac{I_0}{I_T} \quad (\text{A.19})$$

Figure A.2 is a schematic of the diagnostic setup. The argon-ion laser beam exits the laser, passes through a 100-Hz optical chopper, and a beam splitter sends 50% of the beam to the I_0 photometer and the other 50% is coupled into a fiber optic cable. The fiber optic cable is routed to the iodine and helium pipe, where a cell with windows is attached. The laser beam passes through the windowed cell (which has a path length of 1.27 cm) and is coupled into another fiber optic cable. The beam is then directed to the I_T photometer. The signals from the photometers are amplified by lock-in amplifiers. A baseline reading of I_T/I_0 is taken

with no iodine present in the flow. The ratio is multiplied by a factor to result in a ratio of 1.

This factor is used in the measurements when iodine is present.

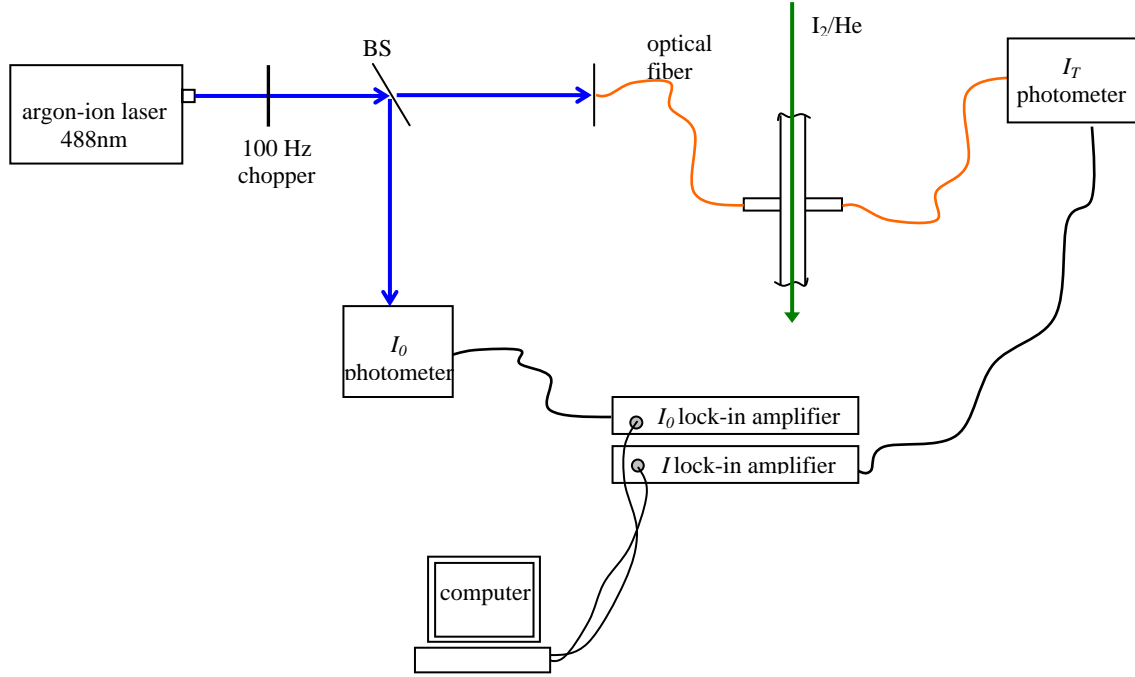


Figure A.2. A schematic of the diagnostic setup to measure iodine concentration in the iodine/helium flow.

A.4.2 Iodine Concentration Measurement Uncertainty

The uncertainty of the iodine concentration is determined by the uncertainty of the photometer measurements and the path length of the cell. Iodine uncertainty is

$$\Delta[I_2] = \sqrt{\left(\frac{\partial[I_2]}{\partial I_0} \Delta I_0\right)^2 + \left(\frac{\partial[I_2]}{\partial I_T} \Delta I_T\right)^2 + \left(\frac{\partial[I_2]}{\partial L} \Delta L\right)^2} \quad (\text{A.20})$$

where

$$\frac{\partial[I_2]}{\partial I_T} = \frac{1}{\sigma L N_A I_0} \quad (\text{A.21})$$

$$\frac{\partial[I_2]}{\partial I_0} = \frac{-1}{\sigma L N_A I_T} \quad (\text{A.22})$$

$$\frac{\partial[I_2]}{\partial L} = \frac{-1}{\sigma L^2 N_A} \ln \frac{I_0}{I_T} \quad (\text{A.23})$$

Based on the measurement standard of deviation, the uncertainty in the photometer signal is $\pm 1\%$. With fabrication tolerances, the uncertainty in the cell path length is ± 0.02 cm. Table A.2 displays two samples of measured and calculated values used in determining the iodine concentration and its uncertainty. There is more iodine concentration in the helium carrier flow with Sample Data 2, which has significantly less uncertainty. With a higher concentration of iodine, the laser intensity after passing through the flow, I_T , is reduced, reducing the uncertainty in I_T . It is therefore advantageous to have a higher concentration of iodine in the flow to reduce the concentration uncertainty.

Table A.2. Sample calculation of iodine concentration and uncertainties.

	Sample Data 1	Sample Data 2
I_0	100 ± 1	100 ± 1
I_T	97.0 ± 1.0	19.0 ± 0.2
L	1.27 ± 0.02 cm	1.27 ± 0.02 cm
$\frac{\partial[I_2]}{\partial I_0} \Delta I_0$	7.69	7.69
$\frac{\partial[I_2]}{\partial I_T} \Delta I_T$	-7.93	-40.6
$\frac{\partial \dot{N}}{\partial L} \Delta L$	-1.17	-20.1
$[I_2]$	23.4 ± 11.1 mmol/m ³	1280 ± 50 mmol/m ³
$\frac{\Delta[I_2]}{[I_2]}$	47%	4%

A.4.3 Iodine Molar Flow Rate Measurement

The iodine molar flow rate is determined by Dalton's Law of Partial Pressures, definition of mole fraction, and the ideal gas law. Per Dalton's Law of Partial Pressures,

$$P_{Total} = P_{I_2} + P_{He} \quad (A.24)$$

The mole fraction of iodine is then

$$x_{I_2} = \frac{P_{I_2}}{P_{Total}} \quad (A.25)$$

The total pressure is measured in the iodine concentration diagnostic cell, but the partial pressure of iodine cannot be measured. However, the ideal gas law can be used to represent the partial pressure as a function of temperature and iodine concentration. The temperature is measured with a thermocouple and the iodine concentration is calculated from the argon-ion laser beam absorbance,

$$P_{I_2} = RTn/V = RT[I_2] \quad (A.26)$$

Therefore, the iodine mole fraction is

$$x_{I_2} = \frac{RT[I_2]}{P_{Total}} \quad (A.27)$$

Now that the iodine mole fraction can be calculated, the iodine molar flow rate must be determined. The iodine mole fraction is also a function of the helium and iodine flow rates, where \dot{N} is a molar flow rate

$$x_{I_2} = \frac{\dot{N}_{I_2}}{\dot{N}_{I_2} + \dot{N}_{He}} \quad (A.28)$$

Equation A.28 can be solved for iodine molar flow rate as a function of the helium molar flow rate and iodine mole fraction

$$\dot{N}_{I_2} = \dot{N}_{He} \left(\frac{x_{I_2}}{1 - x_{I_2}} \right) \quad (\text{A.29})$$

Inserting Eqn. A.27 into Eqn. A.29 for mole fraction gives

$$\dot{N}_{I_2} = \dot{N}_{He} \left(\frac{P_{Total}}{[I_2]RT} - 1 \right)^{-1} \quad (\text{A.30})$$

Equation A.30 gives the iodine molar flow rate as a function of the measured pressure, temperature, and iodine concentration in the diagnostic cell and the helium molar flow rate.

A.4.4 Iodine Molar Flow Rate Measurement Uncertainty

The uncertainty of the iodine molar flow rate is determined by the uncertainties of the iodine concentration, measured pressure and temperature in the iodine diagnostic cell, and helium flow rate. Iodine molar flow rate uncertainty is

$$\Delta \dot{N}_{I_2} = \sqrt{\left(\frac{\partial \dot{N}_{I_2}}{\partial [I_2]} \Delta [I_2] \right)^2 + \left(\frac{\partial \dot{N}_{I_2}}{\partial P_{Total}} \Delta P_{Total} \right)^2 + \left(\frac{\partial \dot{N}_{I_2}}{\partial T} \Delta T \right)^2 + \left(\frac{\partial \dot{N}_{I_2}}{\partial \dot{N}_{He}} \Delta \dot{N}_{He} \right)^2} \quad (\text{A.31})$$

where

$$\frac{\partial \dot{N}_{I_2}}{\partial [I_2]} = \dot{N}_{He} \frac{P_{Total} / [I_2]^2 RT}{(P_{Total} / [I_2] RT - 1)^2} \quad (\text{A.32})$$

$$\frac{\partial \dot{N}_{I_2}}{\partial P_{Total}} = -\dot{N}_{He} \frac{1/[I_2]RT}{(P_{Total} / [I_2] RT - 1)^2} \quad (\text{A.33})$$

$$\frac{\partial \dot{N}_{I_2}}{\partial T} = \dot{N}_{He} \frac{P_{Total} / [I_2] RT^2}{(P_{Total} / [I_2] RT - 1)^2} \quad (\text{A.34})$$

$$\frac{\partial \dot{N}_{I_2}}{\partial \dot{N}_{He}} = \frac{1}{P_{Total} / [I_2] RT - 1} \quad (A.35)$$

Table A.3 displays the measured and calculated values, along with their uncertainties, used in calculating the iodine molar flow rate and its uncertainty. Two sample calculations were done, both of which correspond to the sample calculations from Table A.2. The calculation from Sample Data 2 has a significantly smaller uncertainty percentage than that from Sample Data 1. This is because the percentage of uncertainty in the iodine concentration is significantly smaller in Sample Data 2.

Table A.3. Two sample calculations of iodine molar flow rate and their uncertainties.

	Sample Data 1	Sample Data 2
$[I_2]$	$23.4 \pm 11.1 \text{ mmol/m}^3$	$1280 \pm 50 \text{ mmol/m}^3$
P_{Total}	$7.82 \pm 0.02 \text{ psia}$ $53900 \pm 140 \text{ N/m}^2$	$13.90 \pm 0.03 \text{ psia}$ $95800 \pm 240 \text{ N/m}^2$
T	402 ± 4	429 ± 4
\dot{N}_{He}	$110.7 \pm 5.6 \text{ mmol/s}$	$79.7 \pm 4.0 \text{ mmol/s}$
$\frac{\partial \dot{N}_{I_2}}{\partial [I_2]} \Delta [I_2]$	$7.60 \times 10^{-3} \text{ mmol/s}$	$1.50 \times 10^{-1} \text{ mmol/s}$
$\frac{\partial \dot{N}_{I_2}}{\partial P_{Total}} \Delta P_{Total}$	$4.03 \times 10^{-4} \text{ mmol/s}$	$1.04 \times 10^{-2} \text{ mmol/s}$
$\frac{\partial \dot{N}_{I_2}}{\partial T} \Delta T$	$1.61 \times 10^{-3} \text{ mmol/s}$	$4.18 \times 10^{-2} \text{ mmol/s}$
$\frac{\partial \dot{N}_{I_2}}{\partial \dot{N}_{He}} \Delta \dot{N}_{He}$	$8.09 \times 10^{-3} \text{ mmol/s}$	$2.00 \times 10^{-1} \text{ mmol/s}$
\dot{N}_{I_2}	$0.16 \pm 0.08 \text{ mmol/s}$	$3.98 \pm 0.25 \text{ mmol/s}$
$\frac{\Delta \dot{N}_{I_2}}{\dot{N}_{I_2}}$	50%	6%

A.5 Injector Molar Flow Rate

To accurately deliver a relatively small quantity of iodine and carrier helium, it is best to flow a large quantity (at the desired ratio of iodine to helium) and fractionate the flow so that the desired fraction of this flow is delivered to the injectors whereas the rest is passed through to the vacuum. The iodine and carrier helium flow is delivered at an approximate rate of 125 mmol/s of helium and 1.9 mmol/s of iodine. For a single injector, for example, only 1% of the flow should be delivered to the injector, while 99% of the flow is sent to the vacuum. As seen in Eqn. A.10, the flow rate is dependent on the area of an orifice. In the situation where flow needs to be fractionated, two orifice areas, one area from the injector(s) and another from the bypass orifice, make up the total area used in Eqn. A.10. The molar flow rate based on the sum of a single bypass orifice, A_{bp} , and the injector throat area, A_{inj} , is

$$\dot{N} = C_d P_o (A_{bp} + A_{inj}) \sqrt{\frac{\gamma}{\mathcal{R}M T_o}} \left(\frac{\gamma + 1}{2} \right)^{\gamma+1/2(1-\gamma)} \quad (\text{A.36})$$

For simplicity, this equation is simplified with a constant, B'

$$\dot{N} = \frac{C_d P_o}{\sqrt{T_o}} B' (A_{bp} + A_{inj}) \quad (\text{A.37})$$

where

$$B' = \sqrt{\frac{\gamma}{\mathcal{R}M}} \left(\frac{\gamma + 1}{2} \right)^{\gamma+1/2(1-\gamma)} \quad (\text{A.38})$$

The ratio of injected molar flow to the total molar flow is

$$\frac{\dot{N}_{inj}}{\dot{N}} = \frac{\frac{C_d P_o}{\sqrt{T_o}} B' A_{inj}}{\frac{C_d P_o}{\sqrt{T_o}} B' (A_{bp} + A_{inj})} = \frac{A_{inj}}{A_{bp} + A_{inj}} \quad (\text{A.39})$$

With area directly proportional to the square of the orifice (or injector) throat diameter, the injector molar flow rate is written as

$$\dot{N}_{inj} = \dot{N} \frac{d_{inj}^2}{d_{bp}^2 + d_{inj}^2} \quad (\text{A.40})$$

where d_{inj} and d_{bp} are the injectors' effective throat diameter and the bypass throat diameter, respectively.

A.6 Injector Molar Flow Rate Uncertainty

The uncertainty in the injector and bypass diameters and the uncertainty in the helium and iodine molar flow rate dictate the uncertainty in the injector flow rate, \dot{N}_{inj} . The uncertainty for the injector molar flow rate is

$$\Delta \dot{N}_{inj} = \sqrt{\left(\frac{\partial \dot{N}_{inj}}{\partial d_{inj}} \Delta d_{inj} \right)^2 + \left(\frac{\partial \dot{N}_{inj}}{\partial d_{bp}} \Delta d_{bp} \right)^2 + \left(\frac{\partial \dot{N}_{inj}}{\partial \dot{N}} \Delta \dot{N} \right)^2} \quad (\text{A.41})$$

where

$$\frac{\partial \dot{N}_{inj}}{\partial d_{inj}} = \frac{2d_{bp}^2 d_{inj}}{(d_{bp}^2 + d_{inj}^2)^2} \quad (\text{A.42})$$

$$\frac{\partial \dot{N}_{inj}}{\partial d_{bp}} = \frac{2d_{inj}^2 d_{bp}}{(d_{bp}^2 + d_{inj}^2)^2} \quad (\text{A.43})$$

$$\frac{\partial \dot{N}_{inj}}{\partial \dot{N}} = \frac{d_{inj}^2}{d_{bp}^2 + d_{inj}^2} \quad (\text{A.44})$$

$$\Delta \dot{N} = \sqrt{(\Delta \dot{N}_{He})^2 + (\Delta \dot{N}_{I_2})^2} \quad (\text{A.45})$$

Sample Data 2 did not fractionate the flow, but Sample Data 1 did. Table A.4 displays values used in calculating the injector flow rate. The uncertainty of 5% is relatively small.

Table A.4. Sample calculation of an injector molar flow rate and its uncertainty.

	Sample Data 1
d_{inj}	$0.020 \pm 0.001 \text{ in}$
d_{bp}	$0.160 \pm 0.001 \text{ in}$
\dot{N}	$110.9 \pm 5.6 \text{ mmol/s}$
$\frac{\partial \dot{N}_{inj}}{\partial d_{inj}} \Delta d_{inj}$	$1.51 \times 10^{-3} \text{ mmol/s}$
$\frac{\partial \dot{N}_{inj}}{\partial d_{bp}} \Delta d_{bp}$	$1.89 \times 10^{-4} \text{ mmol/s}$
$\frac{\partial \dot{N}_{inj}}{\partial \dot{N}} \Delta \dot{N}$	$8.57 \times 10^{-2} \text{ mmol/s}$
\dot{N}_{inj}	$1.71 \pm 0.09 \text{ mmol/s}$
$\frac{\Delta \dot{N}_{inj}}{\dot{N}_{inj}}$	5%

A.7 Injector Mole Fraction Uncertainty

Now that the total flow rate through the injector is known, the mole fractions of iodine and helium, with the corresponding uncertainties must be determined. The mole fractions are calculated with the molar flow rates. The mole fractions for helium and iodine, respectively, are

$$x_{He} = \frac{\dot{N}_{He}}{\dot{N}_{He} + \dot{N}_{I_2}} \quad (\text{A.46})$$

$$x_{I_2} = \frac{\dot{N}_{I_2}}{\dot{N}_{He} + \dot{N}_{I_2}} \quad (\text{A.47})$$

The uncertainties for the mole fractions are

$$\Delta x_{He} = \sqrt{\left(\frac{\partial x_{He}}{\partial \dot{N}_{He}} \Delta \dot{N}_{He} \right)^2 + \left(\frac{\partial x_{He}}{\partial \dot{N}_{I_2}} \Delta \dot{N}_{I_2} \right)^2} \quad (\text{A.48})$$

$$\Delta x_{I_2} = \sqrt{\left(\frac{\partial x_{I_2}}{\partial \dot{N}_{He}} \Delta \dot{N}_{He} \right)^2 + \left(\frac{\partial x_{I_2}}{\partial \dot{N}_{I_2}} \Delta \dot{N}_{I_2} \right)^2} \quad (\text{A.49})$$

where

$$\frac{\partial x_{He}}{\partial \dot{N}_{He}} = \frac{\dot{N}_{I_2}}{(\dot{N}_{He} + \dot{N}_{I_2})^2} = -\frac{\partial x_{I_2}}{\partial \dot{N}_{He}} \quad (\text{A.50})$$

$$\frac{\partial x_{He}}{\partial \dot{N}_{I_2}} = \frac{-\dot{N}_{He}}{(\dot{N}_{He} + \dot{N}_{I_2})^2} = -\frac{\partial x_{I_2}}{\partial \dot{N}_{I_2}} \quad (\text{A.51})$$

Table A.5. Sample calculation of the injector mole fractions and their uncertainties.

	Sample Data 1
\dot{N}_{I_2}	0.16 ± 0.08 mmol/s
\dot{N}_{He}	110.7 ± 5.6 mmol/s
$\frac{\partial x_{He}}{\partial \dot{N}_{He}} \Delta \dot{N}_{He}$	7.29×10^{-5}
$\frac{\partial x_{He}}{\partial \dot{N}_{I_2}} \Delta \dot{N}_{I_2}$	-6.89×10^{-5}
$\frac{\partial x_{I_2}}{\partial \dot{N}_{He}} \Delta \dot{N}_{He}$	-7.29×10^{-5}
$\frac{\partial x_{I_2}}{\partial \dot{N}_{I_2}} \Delta \dot{N}_{I_2}$	6.89×10^{-5}
x_{He}	0.99858 ± 0.00069
x_{I_2}	0.00076 ± 0.00069

Appendix B: Flow Straightener

B.1 Introduction

The primary flow delivered to the nozzle is a mixture of helium and oxygen. To adequately mix the two gases, an in-line mixer is used to induce swirl in the flow. Once the two gases are mixed, the turbulence generated by the in-line mixer is no longer desired. Mesh wire screens and honeycomb can be placed in the flow to suppress turbulence. However, care must be taken in choosing the mesh size of the screens, honeycomb size, honeycomb length, and relative placement between screens and honeycomb because more turbulence can be produced than suppressed if these design elements are not chosen with care.

B.2 Flow Straightener Design

The mixture of gases is delivered in a pipe that has a diameter of 1.0 in to a plenum that is rectangular in shape, with a width of 1.669 in and a height of 2.204 in. A transition stage is used to expand the circular pipe to a rectangular cross section, matching the dimensions of the plenum. The elements used to reduce the flow turbulence are placed between this transition stage and the entrance of the plenum.

Farell and Youssef recommend placing a combination of honeycomb and mesh screens to reduce both lateral and axial turbulence.⁵⁵ The honeycomb reduces swirl and large-scale eddy motions while the mesh screens reduce the axial variations in velocity. In their study, the best combination for reducing turbulence was a coarse screen, honeycomb, fine mesh screen, and even finer mesh screen. In their study, the turbulence intensities (ratio of velocity fluctuations to

average velocity) were reduced from 12 to 2 percent. They tried other combinations of honeycombs and screens, but this configuration had the most significant effect on decreasing turbulence.

Loehrke and Nagib studied the effect honeycomb size had on suppressing turbulence.⁵⁶ While a relatively long honeycomb reduces internal turbulence more than shorter honeycomb, the long honeycomb generates turbulence through the shear layer instability, such that the net reduction of turbulence by the long honeycomb is less than with a shorter honeycomb. They recommend the honeycomb length to be less than 10 cell sizes long (though their best results had a length to cell diameter ratio of 6). Their results include the turbulence decay length for honeycomb of various sizes, where the honeycomb with the length to cell ratio of 6 had a decay length of about 6 cell lengths. They also recommend using a mesh screen downstream of the honeycomb, placed less than 5 cell sizes downstream. Scheiman and Brooks studied honeycomb and mesh screen combinations for reducing flow turbulence and conclude that the honeycomb that is used to reduce lateral turbulence should be followed by a screen to reduce the axial turbulence created by the honeycomb.⁵⁷ With their published data, it is evident that a finer mesh screen has greater turbulence reduction. Two mesh screens equal in size, or in cascade starting with the largest mesh first, can be used to suppress the axial turbulence. Laws and Livesey recommend the second screen to be twice as fine.⁵⁸ They also recommend placing the screens 500 mesh lengths apart to allow the turbulence from the first screen to decay before approaching the second screen.

With the recommendations from Farell and Youssef, Loehrke and Nagib, Scheiman and Brooks, and Laws and Livesey,⁵⁵⁻⁵⁸ the flow straightening system was designed with a honeycomb (HC) positioned at the exit of the transition stage to take out the initial swirl of the

in-line mixer, a spacer longer than the decay rate of the honeycomb (S1), another honeycomb of the same size to suppress any remaining swirl, a fine mesh screen (FS1), a spacer of about 500 mesh lengths (S2), and an even finer mesh screen (FS2). The second mesh screen is positioned at the entrance of the plenum. The plenum is longer than the decay rate of the second mesh screen. The properties for the flow straightening elements are displayed in Table B.1. Figures B.1 and B.2 display a schematic and a picture of the flow-straightening elements.

The effective diameter of the plenum is 1.90 in, as determined by

$$d_{eff} = \frac{4A}{P},$$

where A is the area and P is the perimeter of the plenum. The honeycomb cell diameter is 6.6% of the effective plenum diameter, which is similar to the 5.7% honeycomb cell to pipe diameter used by Farrell and Youssef. The cell length to diameter is 6.4, which is recommended by Loehrke and Nagib. The spacer, S1, is 6.25 honeycomb cell diameters long, which is the measured decay length in Loehrke and Nagib's work. The second fine mesh screen (FS2) is about twice as fine as the mesh in FS1, as recommended by Laws and Livesey. In choosing the sizes of the honeycomb and mesh screens, it was important to choose elements that would not decrease the plenum area too much to have a significant pressure drop. The finest mesh screen (FS2) restricts the area the most with an open area of 36% of the plenum area, increasing the Mach number from 0.12 to 0.33, which is still reasonable for the upstream portion of the plenum.

Table B.1. Flow straightening element properties.

	Length (in)	Cell/Mesh Size (in)	Foil/Wire Thickness (in)
HC	0.8	0.125	0.004
S1	5.0	N/A	N/A
FS1	N/A	0.0041	0.0026
S2	2.0	N/A	N/A
FS2	N/A	0.0024	0.0016

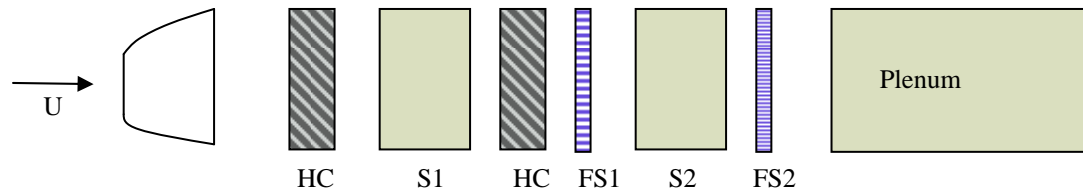


Figure B.1. A schematic of the flow straightening elements.

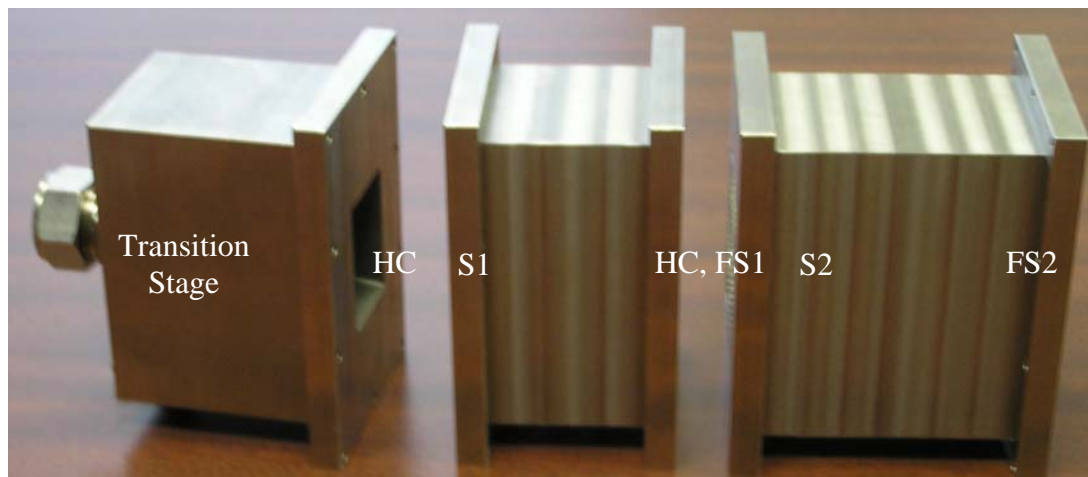


Figure B.2. A picture of the flow straightening elements.

Appendix C: Nozzle Design

C.1 Introduction

The nozzle profile was designed to have a contour on the top and bottom of the nozzle but flat sidewalls. The nozzle profile was calculated and then corrected to account for the boundary layer that would build up on it. In this appendix, the design of the nozzle contour and boundary layer correction, from the nozzle throat to nozzle exit plane, is discussed.

C.2 Nozzle Design

The contour of the nozzle was designed using a computer program developed at the University of Illinois at Urbana-Champaign.³⁹ The computer program is written in FORTRAN and implements a method of characteristics design analysis for a supersonic nozzle that has a continuous slope at the throat. Input conditions include the ratio of specific heats for the gas used in the design nozzle, desired Mach number, throat height, radius of curvature at the throat, and wall shape (hyperbolic or parabolic). The program calculates a nozzle contour that results in a uniform exit flow aligned with the nozzle axis. For the nozzle used in this research, the input conditions are displayed in Table C.1 and the nozzle contour is plotted in Figure C.1.

Table C.1. Nozzle design code inputs.

	Code Input
γ	1.587
M	2.2
Throat Height	10mm
Throat Radius of Curvature	50mm
Initial Wall Shape	Hyperbolic

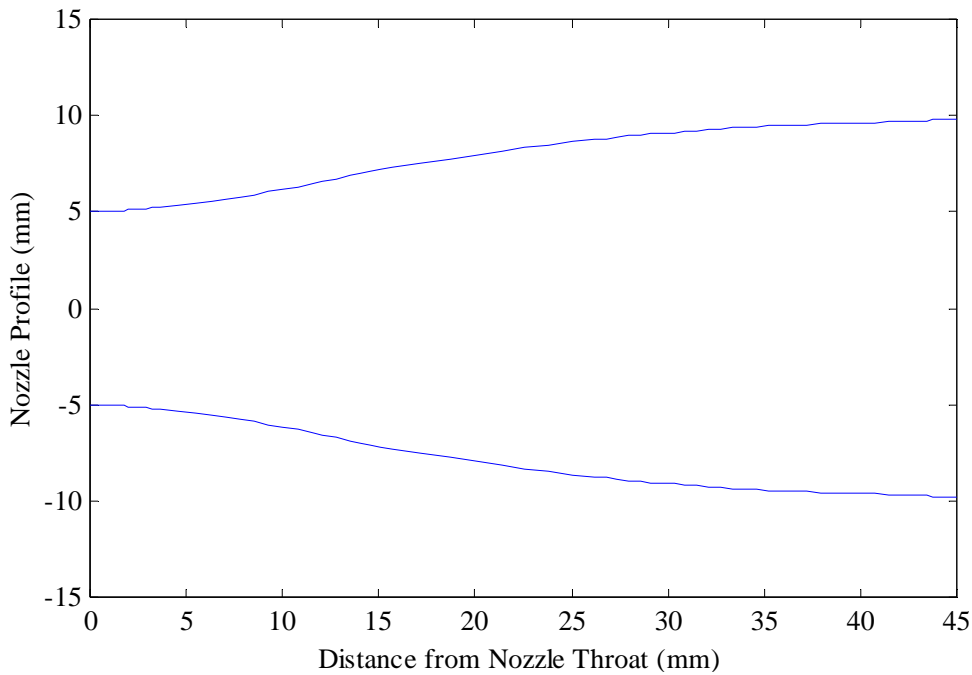


Figure C.1. Nozzle contour from method of characteristics code.

C.3 Boundary Layer Correction

To maintain the design Mach number, the nozzle contour was adjusted to account for a boundary layer that would build up on the sidewalls and contour. The boundary layer build-up was calculated by estimating the nozzle sidewalls and contour as flat plates. Using Blasius' flat

plate theory, the boundary layer displacement thickness, δ , is calculated at each point along the contour and sidewalls and is a function of the distance from the throat, x , freestream velocity at x , U_∞ , and kinematic viscosity at x , ν .⁵⁹ It can also be rewritten as a function of, Re_x , the Reynolds number based on x , as

$$\delta = 1.7208 \sqrt{\frac{\nu x}{U_\infty}} = 1.7208 \frac{x}{\sqrt{Re_x}} \quad (C.1)$$

The displacement thickness is a good measure for expanding the contour because it is the displacement thickness of the external potential field of the flow caused by the reduction of velocity in the boundary layer.

The freestream velocity is a function of the nozzle Mach number, M , and the speed of sound, a . The speed of sound is a function of the ratio of specific heats, the gas constant, R , and temperature

$$U_\infty = Ma = M\sqrt{\gamma RT} \quad (C.2)$$

For the 20% oxygen and 80% helium mixture, γ is 1.587 and R is 866 N-m/kg-K. The Mach number and temperature are functions of γ and the area ratio of the nozzle at x and at the throat ($x = 0$), A/A^* . Isentropic relationships for A/A^* and T/T_0 as a function of M , where T_0 is the plenum (stagnation) temperature,⁶⁰ are

$$\frac{A}{A^*} = \frac{1}{M} \left[\frac{2}{\gamma + 1} \left(1 + \frac{\gamma - 1}{2} M^2 \right) \right]^{\gamma+1/2(\gamma-1)} \quad (C.3)$$

$$\frac{T}{T_0} = \frac{1}{\left(1 + \frac{\gamma - 1}{2} M^2 \right)} \quad (C.4)$$

For this nozzle contour, the Mach number as a function of x is plotted in Figure C.2 and the temperature (with a plenum temperature of 300K) is plotted in Figure C.3. The velocity (as calculated in Eqn. C.2) is plotted in Figure C.4.

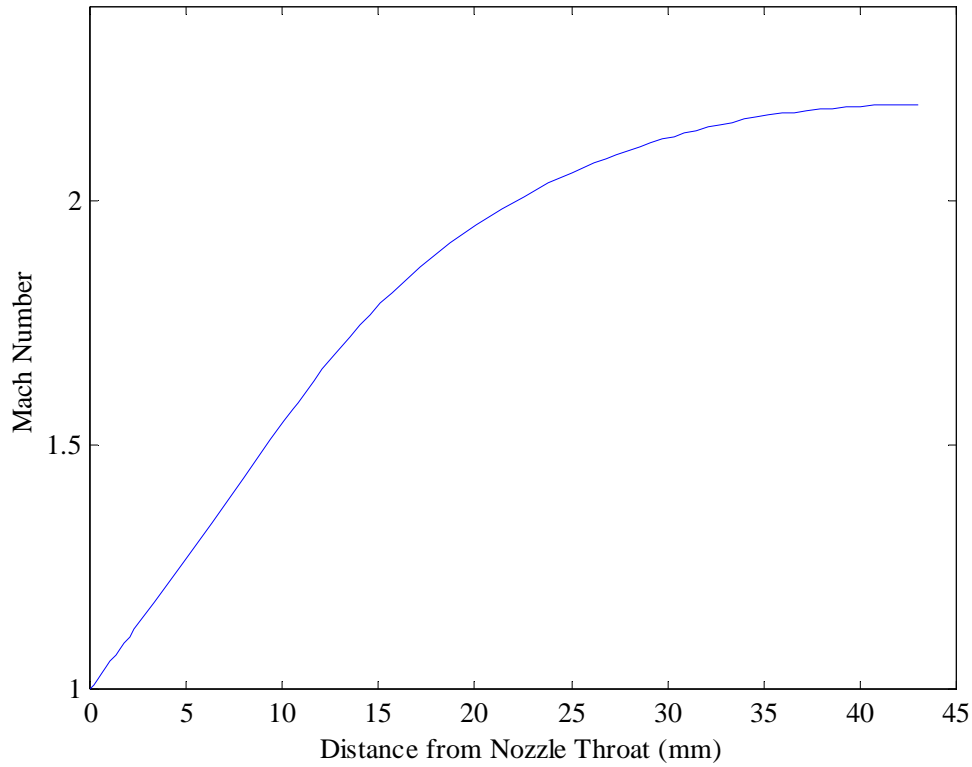


Figure C.2. Mach number versus distance from nozzle throat.

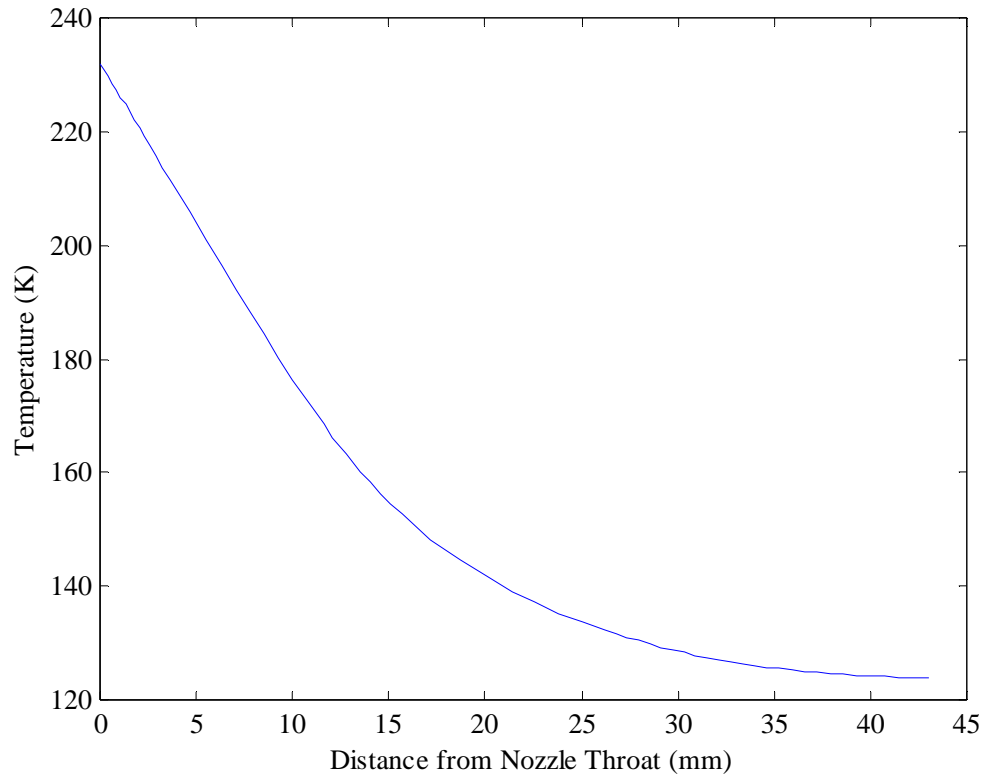


Figure C.3. Temperature versus distance from nozzle throat, with plenum temperature of 300 K.

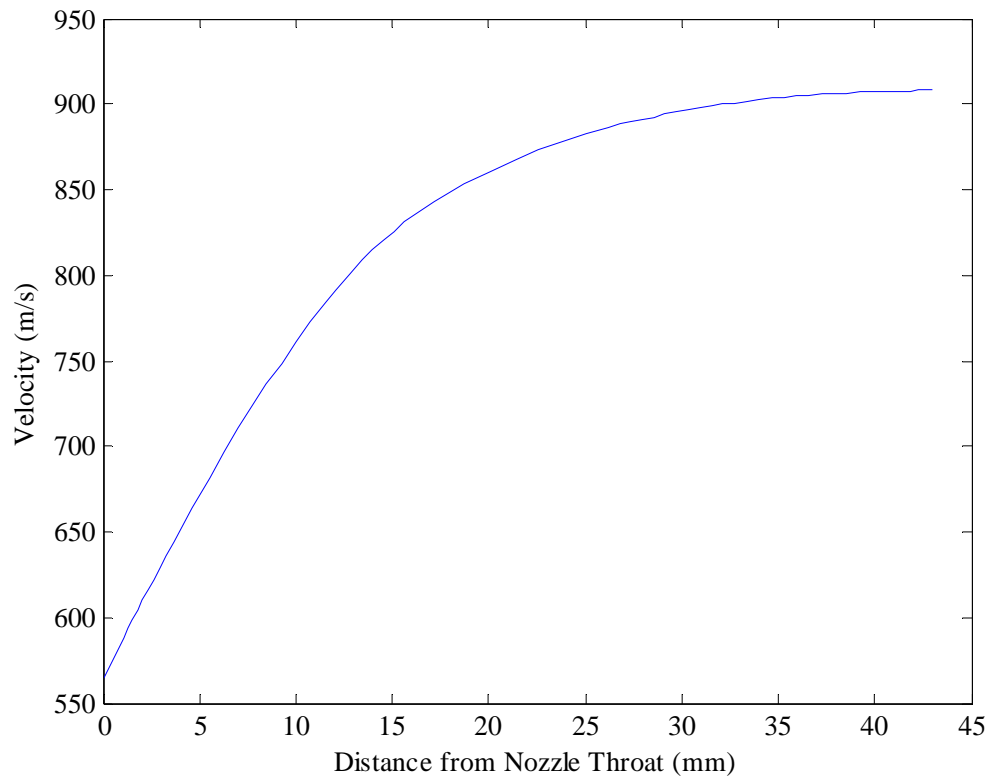


Figure C.4. Freestream velocity versus distance from nozzle throat.

The final variable needed to calculate the displacement thickness is the kinematic viscosity, ν

$$\nu = \frac{\mu}{\rho} \quad (C.5)$$

which is viscosity, μ , divided by the gas density, ρ . The density is calculated as a function of x using the Ideal Gas Law

$$\rho = \frac{P}{RT} \quad (C.6)$$

where pressure, P was determined using the isentropic relationship between the pressure, stagnation pressure, and Mach number.

$$\frac{P}{P_0} = \left(1 + \frac{\gamma - 1}{2} M^2 \right)^{\gamma / (1 - \gamma)} \quad (C.7)$$

The plenum pressure is 65 Torr (8666 Pa). Plots of the pressure and density are shown in Figures. C.5 and C.6, respectively.

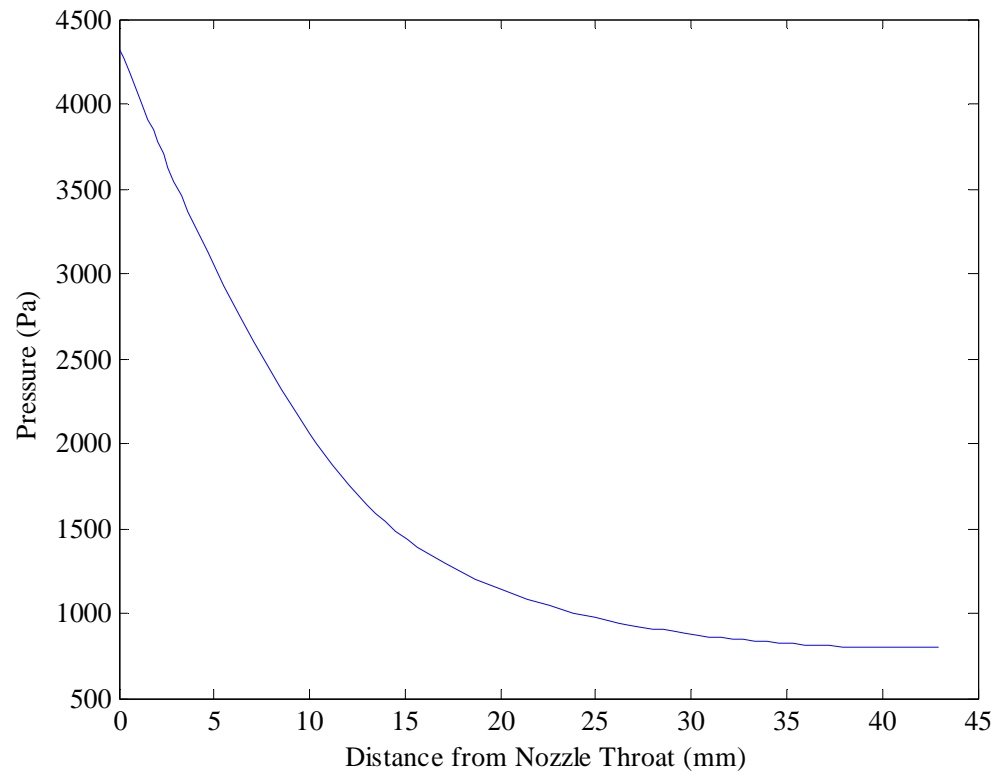


Figure C.5. Freestream pressure versus distance from nozzle throat.

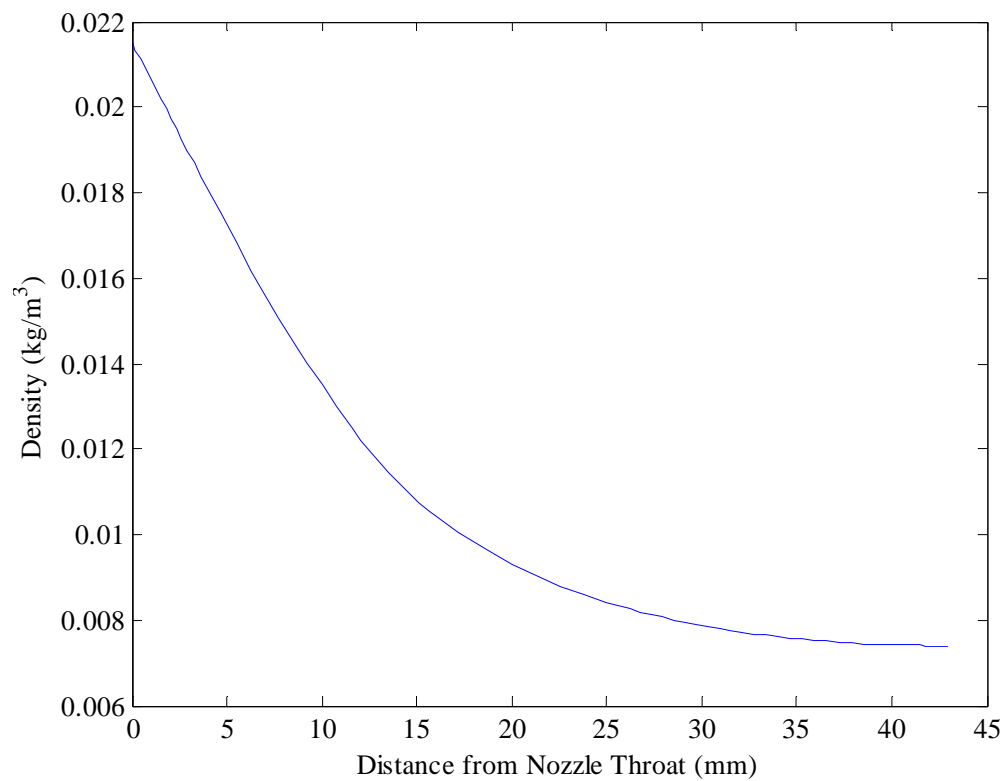


Figure C.6. Freestream density versus distance from nozzle throat.

The viscosity is calculated for the mixture of oxygen and helium. Using Sutherland's Law, the viscosity for each gas is determined as a function of temperature and the Sutherland constant, S ⁶¹

$$\frac{\mu}{\mu_0} \approx \left(\frac{T}{T_0} \right)^{3/2} \frac{T_0 + S}{T + S} \quad (\text{C.8})$$

For oxygen and helium, the Sutherland-law viscosity parameters are displayed in Table C.2. The viscosities for each gas are plotted in Figure. C.7.

Table C.2. Sutherland-law viscosity parameters. ⁶²

	Helium	Oxygen
T_0 (K)	273	273
μ_0 (N-s/m ²)	2.04E-5	1.92E-5
S (K)	36	139

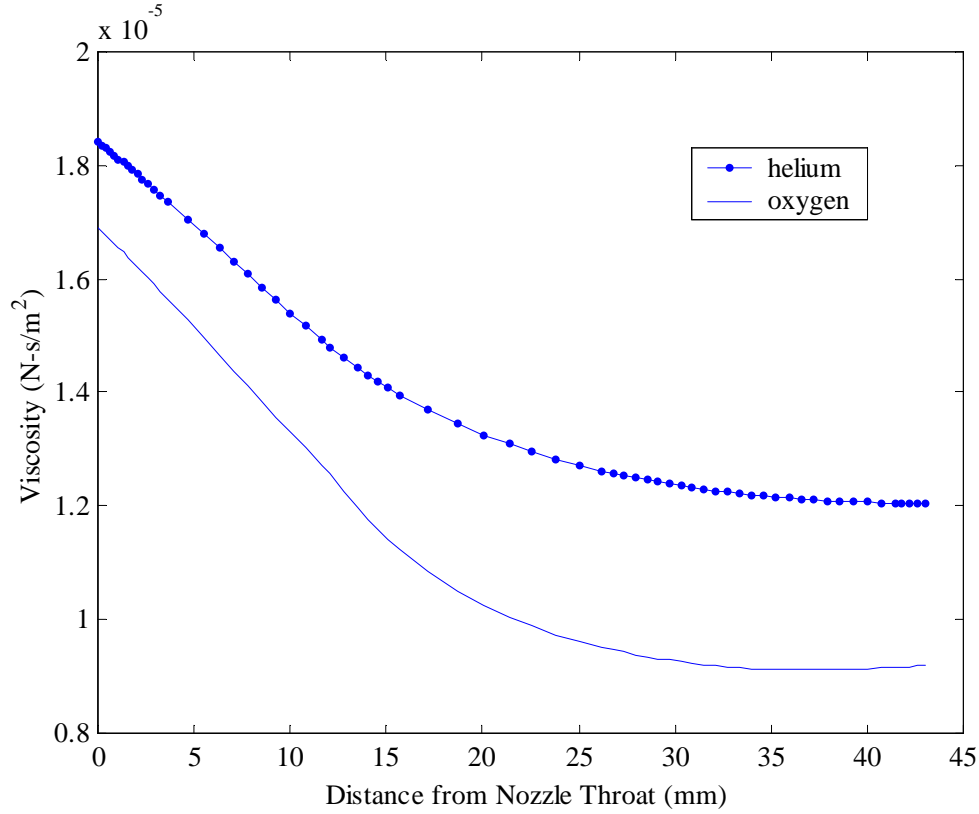


Figure C.7. Viscosity for the oxygen and helium gases versus distance from nozzle throat.

Wilke's formula for calculating the viscosity for a mixture of gases was used, where n is the number of gases present and i, j of 1 represents oxygen and i, j of 2 represents helium⁶¹

$$\mu_{mix} \approx \sum_{i=1}^n \frac{x_i \mu_i}{\sum_{j=1}^n x_j \phi_{ij}} \quad (C.9)$$

where

$$\phi_{ij} = \frac{\left[1 + (\mu_i / \mu_j)^{1/2} (M_j / M_i)^{1/4}\right]^2}{(8 + 8M_i / M_j)^{1/2}} \quad (C.10)$$

For the situation when $i = j$, Eqn. C.10 reduces to $\phi = 1$. The values for ϕ_{12} and ϕ_{21} are plotted in Figure C.8 and the viscosity for the oxygen and helium mixture is plotted in Figure C.9. The kinematic viscosity is plotted in Figure C.10.

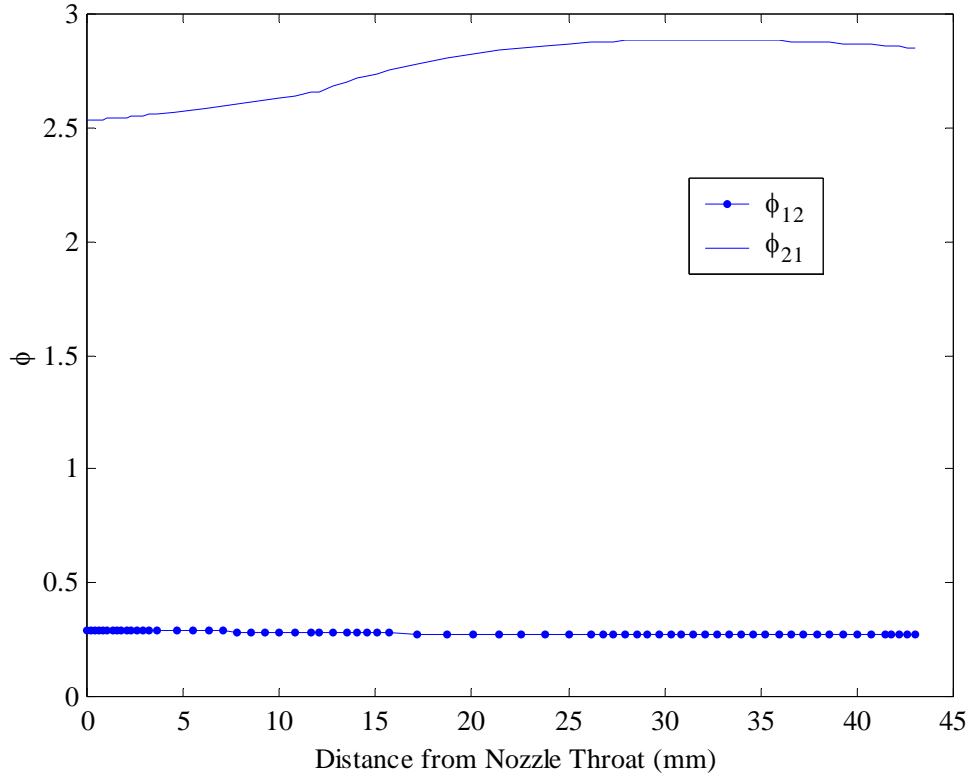


Figure C.8. Values for ϕ_{12} and ϕ_{21} versus distance from nozzle throat.

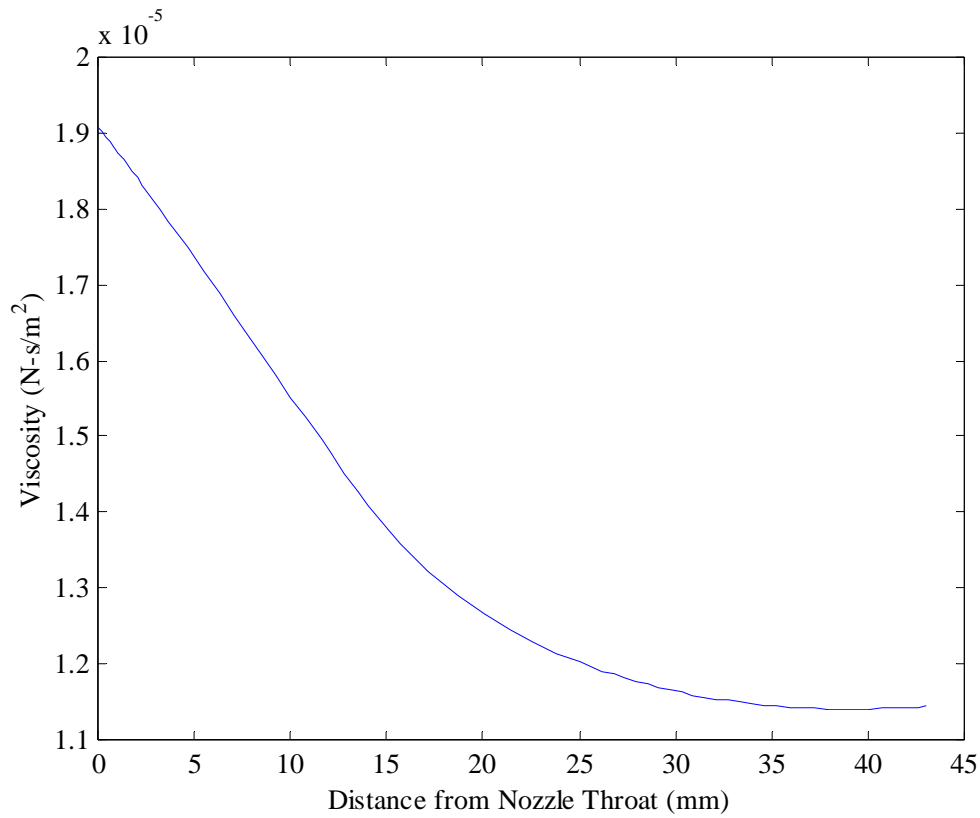


Figure C.9. Viscosity for the helium/oxygen mixture versus distance from nozzle throat.

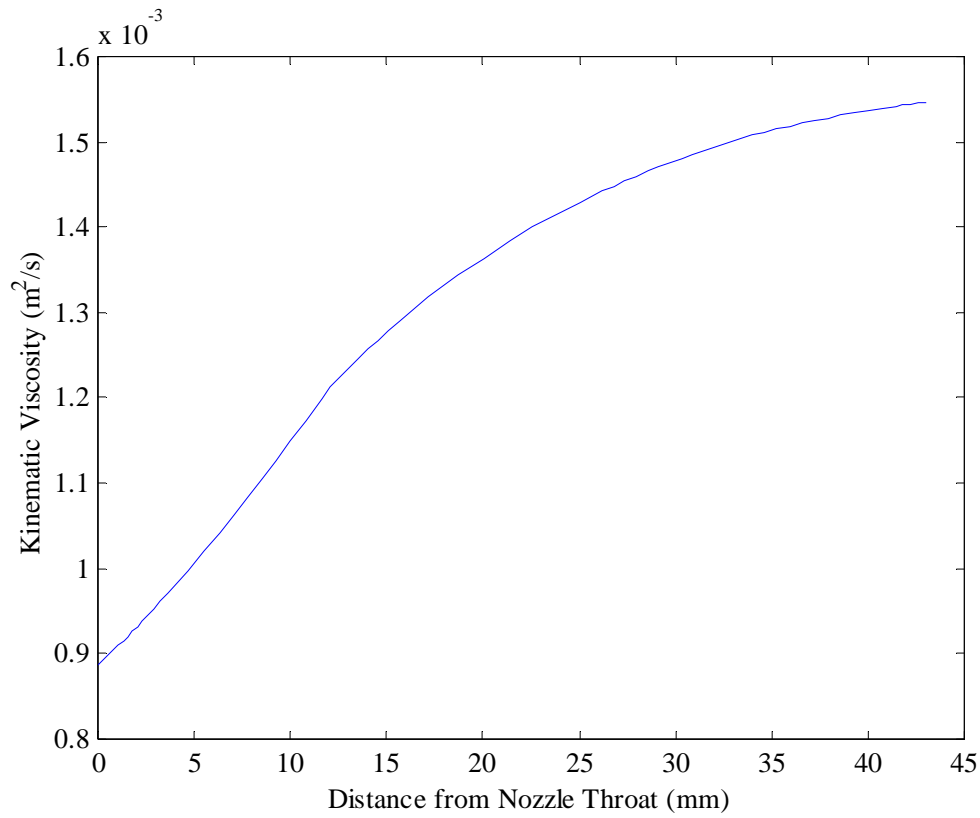


Figure C.10. Kinematic viscosity for the helium/oxygen mixture versus distance from nozzle throat.

With the freestream velocity and kinematic viscosity, the Reynolds number based on the distance from the nozzle throat, x , can be calculated, as shown in Figure C.11.

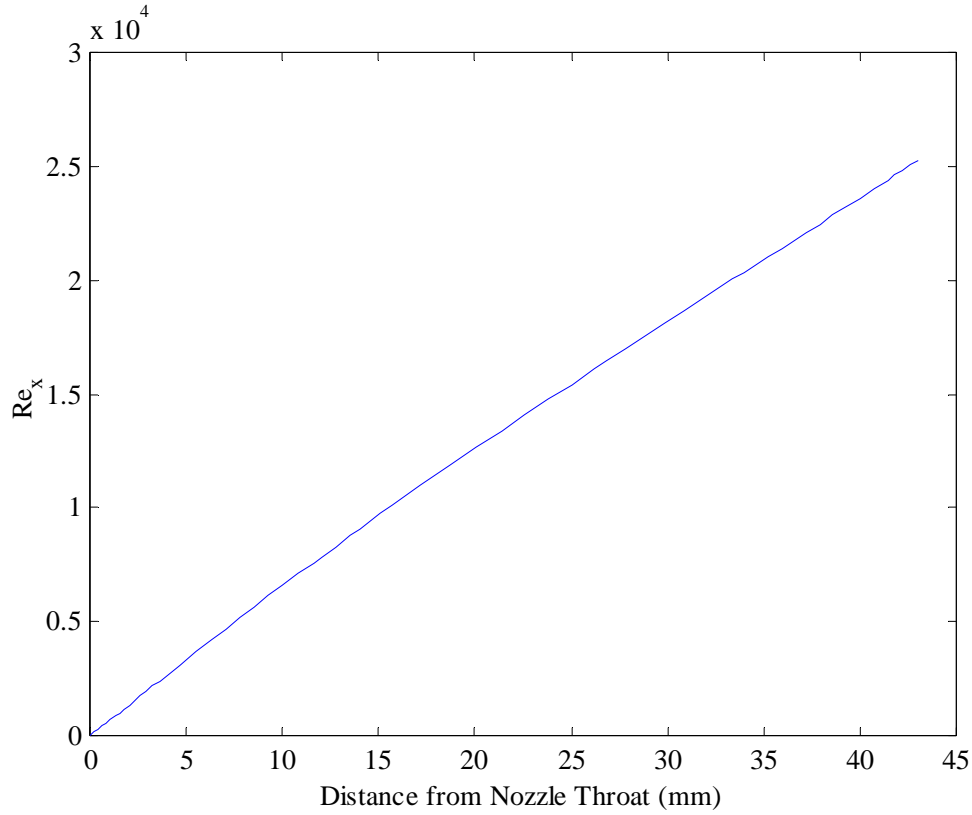


Figure C.11. Re_x versus distance from nozzle throat.

From Eqn. C.1, the displacement thickness can now be determined, which is plotted in Figure C.12. Figure C.13 displays the original nozzle profile (as plotted in Figure C.1) and the nozzle profile that is corrected by the boundary layer displacement thickness.

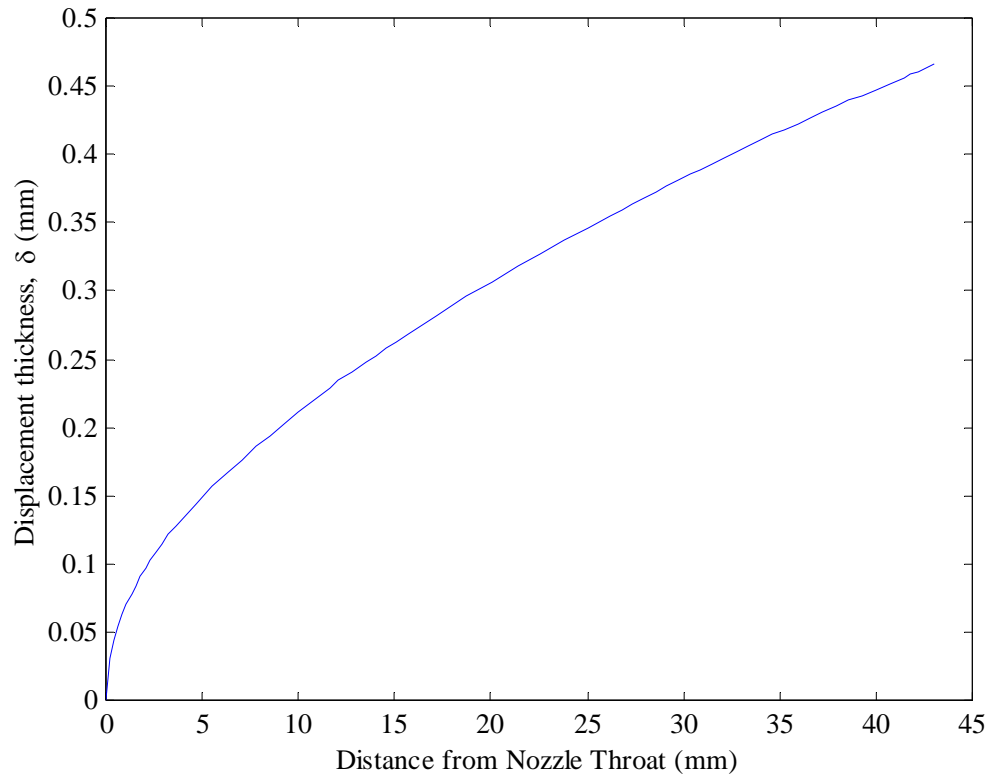


Figure C.12. Displacement thickness versus distance from nozzle throat.

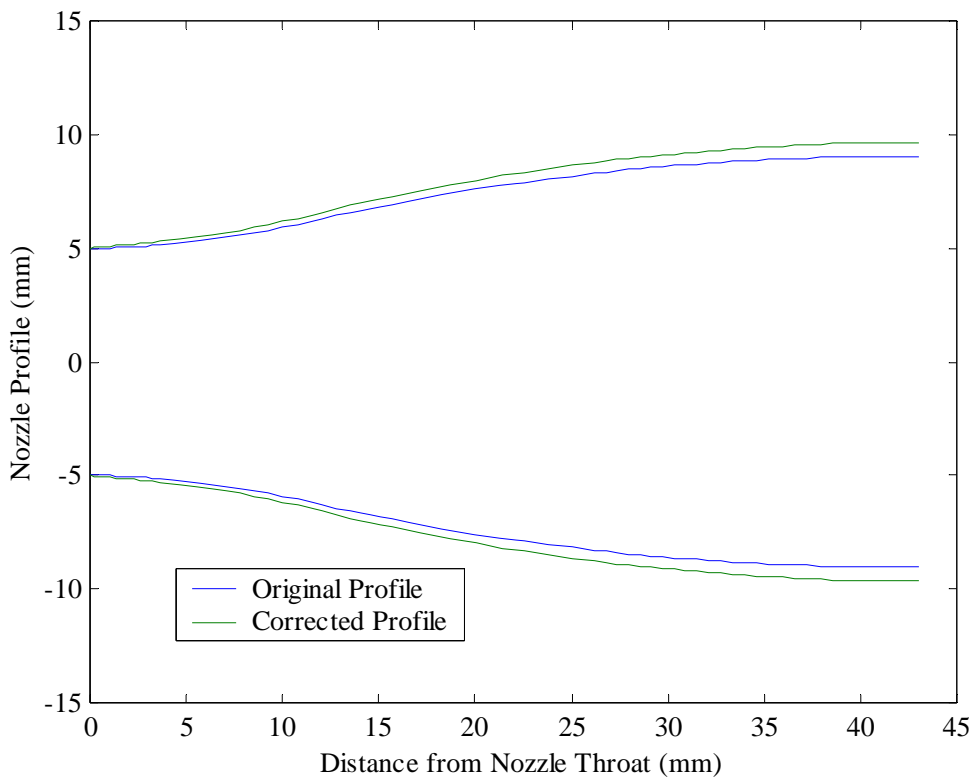


Figure C.13. Original nozzle profile and nozzle profile corrected by the displacement thickness of the boundary layer.

DISTRIBUTION LIST

DTIC/OCF

8725 John J. Kingman Rd, Suite 0944

Ft Belvoir, VA 22060-6218

1 cy

AFRL/RVIL

Kirtland AFB, NM 87117-5776

2 cys

Official Record Copy

AFRL/RDLC/Carrie A. Noren

1 cy

This page intentionally left blank